OKLAHOMA TRANSPORTATION CENTER

ECONOMIC ENHANCEMENT THROUGH INFRASTRUCTURE STEWARDSHIP

SOIL-STRUCTURE INTERACTION STUDIES FOR UNDERSTANDING THE BEHAVIOR OF INTEGRAL ABUTMENT BRIDGES

KANTHASAMY K. MURALEETHARAN, PH.D., P.E.,G.E.
GERALD MILLER, PH.D., P.E.
KARRTHIK KIRUPAKARAN
DANIEL KRIER, PH.D.
BRYCE R. HANLON

OTCREOS7.1-37-F

Oklahoma Transportation Center
2601 Liberty Parkway, Suite 110
Midwest City, Oklahoma 73110

Phone: 405.732.6580
Fax: 405.732.6586
www.oktc.org

DISCLAIMER

The contents of this report reflect the views of the authors, who are responsible for the facts and accuracy of the information presented herein. This document is disseminated under the sponsorship of the Department of Transportation University Transportation Centers Program, in the interest of information exchange. The U.S. Government assumes no liability for the contents or use thereof.

TECHNICAL REPORT DOCUMENTATION PAGE

1. REPORT NO.	2. GOVERNMENT ACCESSION NO.	3. RECIPIENTS CATALOG NO.
OTCREOS7.1-37-F		

4. TITLE AND SUBTITLE	5. REPORT DATE
Soil-Structure Interaction Studies for Understanding the Behavior of Integral Abutment Bridges	March 31, 2012
	6. PERFORMING ORGANIZATION CODE

7. AUTHOR(S)	8. PERFORMING ORGANIZATION REPORT
Kanthasamy K. Muraleetharan, Gerald A. Miller, Karrthik Kirupakaran, Daniel Krier, Bryce R. Hanlon	

9. PERFORMING ORGANIZATION NAME AND ADDRESS	10. WORK UNIT NO.
The University of Oklahoma School of Civil Engineering and Environmental Science 202 W. Boyd St., Room 334, Norman, OK 73019	11. CONTRACT OR GRANT NO. DTRT06-G-0016

12. SPONSORING AGENCY NAME AND ADDRESS	13. TYPE OF REPORT AND PERIOD COVERED
The Oklahoma Transportation Center (Fiscal) 201 ATRC, Stillwater, OK 74078 (Technical) 2601 Liberty Parkway, Suite 110, Midwest City, OK 73110	Final, August 2008 – March 2012
	14. SPONSORING AGENCY CODE

15. SUPPLEMENTARY NOTES
University Transportation Center

16. ABSTRACT
Integral Abutment Bridges (IAB) are bridges without any joints within the bridge deck or between the superstructure and the abutments. An IAB provides many advantages during construction and maintenance of a bridge. Soil-structure interactions at the abutments occurring during thermal loading of a bridge are complex, especially in skewed and long span IABs. The uncertainties in understanding these interactions affect the ability to properly predict the long term behavior of these bridges. This project was developed to understand the complex interactions in an IAB and to propose design guidelines to build new IABs with longer lengths and larger skew angles. Two computer simulation tools, TeraGrande and TeraDysac, were validated in Phase I. Phase II of the project involved instrumenting an Oklahoma IAB to collect data to study the behavior of IABs under Oklahoma weather conditions and construction practices. So far more than 30 months of data from the Oklahoma IAB has been collected. The field measured bridge temperatures for Oklahoma IAB agree with the temperature range specified in AASHTO LRFD Bridge Design Specifications. Earth pressure measurements show that fairly significant amount of abutment back pressures occur during summer. Crackmeter and tiltmeter measurements show that the majority of bridge translation is accommodated by the abutment pile movements in IABs. Abutment piles of IABs are experiencing bending moments beyond the yield bending moment at shallow depths. The behavior of the Oklahoma IAB was also studied with the use of computer programs LPILE and GROUP. The computed bending moments for abutment piles confirm that piles have yielded at shallow depths. The three-dimensional model developed in GROUP shows biaxial bending of abutment piles in skewed IABs. Field measured bending moments for the south abutment pile have lower values than the computed bending moments; very likely due to the installation of these piles in pre-drilled holes. In order to accommodate the thermal movement in IABs and to reduce the bending moments in the abutment piles, a smaller pile section should be placed in weak axis bending and in pre-drilled holes with low stiffness material, especially at shallow depths. Using longer spans with larger girders will increase the axial load on the abutment piles and therefore long-span IABs should be designed with caution. Biaxial bending of abutment piles in skewed IABs increases stresses in the concrete superstructure and therefore structural components for IABs with larger skew angles have to be designed carefully to accommodate the thermally induced deformations.

17. KEY WORDS	18. DISTRIBUTION STATEMENT
Soil-Structure Interaction, Integral Abutment Bridges, Finite Element Analysis, Instrumented Abutments	No restrictions. This publication is available at www.oktc.org and from the NTIS

19. SECURITY CLASSIF. (OF THIS REPORT)	20. SECURITY CLASSIF. (OF THIS PAGE)	21. NO. OF PAGES	22. PRICE
Unclassified	Unclassified	219 + covers	

SI (METRIC) CONVERSION FACTORS

Approximate Conversions to SI Units

Symbol	When you know	Multiply by	To Find	Symbol
	LENGTH			
in	inches	25.40	millimeters	mm
ft	feet	0.3048	meters	m
yd	yards	0.9144	meters	m
mi	miles	1.609	kilometers	km
	AREA			
in^2	square inches	645.2	square millimeters	mm
ft^2	square feet	0.0929	square meters	m^2
yd^2	square yards	0.8361	square meters	m^2
ac	acres	0.4047	hectares	ha
mi^2	square miles	2.590	square kilometers	km^2
	VOLUME			
fl oz	fluid ounces	29.57	milliliters	mL
gal	gallons	3.785	liters	L
ft^3	cubic feet	0.0283	cubic meters	m^3
yd^3	cubic yards	0.7645	cubic meters	m^3
	MASS			
oz	ounces	28.35	grams	g
lb	pounds	0.4536	kilograms	kg
T	short tons (2000 lb)	0.907	megagrams	Mg
	TEMPERATURE (exact)			
°F	degrees Fahrenheit	(°F-32)/1.8	degrees Celsius	°C
	FORCE and PRESSURE or STRESS			
lbf	poundforce	4.448	Newtons	N
lbf/in^2	poundforce per square inch	6.895	kilopascals	kPa

Approximate Conversions from SI Units

Symbol	When you know	Multiply by	To Find	Symbol
	LENGTH			
mm	millimeters	0.0394	inches	in
m	meters	3.281	feet	ft
m	meters	1.094	yards	yd
km	kilometers	0.6214	miles	mi
	AREA			
mm^2	square millimeters	0.00155	square inches	in^2
m^2	square meters	10.764	square feet	ft^2
m^2	square meters	1.196	square yards	yd^2
ha	hectares	2.471	acres	ac
km^2	square kilometers	0.3861	square miles	mi^2
	VOLUME			
mL	milliliters	0.0338	fluid ounces	fl oz
L	liters	0.2642	gallons	gal
m^3	cubic meters	35.315	cubic feet	ft^3
m^3	cubic meters	1.308	cubic yards	yd^3
	MASS			
g	grams	0.0353	ounces	oz
kg	kilograms	2.205	pounds	lb
Mg	megagrams	1.1023	short tons (2000 lb)	T
	TEMPERATURE (exact)			
°C	degrees Celsius	9/5+32	degrees Fahrenheit	°F
	FORCE and PRESSURE or STRESS			
N	Newtons	0.2248	poundforce	lbf
kPa	kilopascals	0.1450	poundforce per square inch	lbf/in^2

ACKNOWLEDGEMENTS

The support of the Oklahoma Transportation Center (Award OTCREOS7.1-37) for this project is gratefully acknowledged. The assistance provided by the Oklahoma Department of Transporation Bridge Engineer, Mr. Bob Rusch, and the Assistant Bridge Engineer, Mr. Walt Peters, in identifying an Oklahoma intergral abutment bridge to instrument and coordinating the instrumentation work with the bridge construction is also gratefully acknowledged.

SOIL-STRUCTURE INTERACTION STUDIES FOR UNDERSTANDING THE BEHAVIOR OF INTEGRAL ABUTMENT BRIDGES

Final Report

March 2012

Kanthasamy K. Muraleetharan, Ph.D., P.E., G.E.
Gerald A. Miller, Ph.D., P.E.
Karrthik Kirupakaran
Daniel Krier, Ph.D.
Bryce R. Hanlon

The University of Oklahoma
School of Civil Engineering and Environmental Science
202 W. Boyd St., Room 334, Norman, OK 73019

Oklahoma Transportation Center
Project Number: OTCREOS7.1-37
201 ATRC
Stillwater, OK 74078

TABLE OF CONTENTS

LIST OF TABLES

LIST OF FIGURES

EXECUTIVE SUMMARY

Integral Abutment Bridges (IAB) or jointless bridges are bridges without any joints within the bridge deck or between the superstructure (decks and girders) and the abutments. An IAB provides many advantages during construction and maintenance of a bridge. Joints and bearings in a conventional bridge with expansion joints are expensive to install. Leaking joints in a conventional bridge lead to deterioration of girders and bearings and therefore higher maintenance costs. IABs also provide superior performance during extreme loading events such as earthquakes and blast loading. Due to these reasons, IABs are being built by agencies at an increasing rate in U.S. The complex interactions in an IAB between the superstructure, abutments, piers, foundations, and soils are, however, still poorly understood. Because of the uncertainties in understanding these interactions, many Departments of Transportations (DOTs) have been reluctant to build longer and skewed IABs. These uncertainties also affect the ability of the agencies to properly understand the long-term behavior of these bridges.

The main objectives of this project are: (i) to validate two computer simulation tools, TeraGrande (ANATECH 2005) and TeraDysac (Muraleetharan et al. 2003, Ravichandran 2005), for studying the interactions in an IAB using field data collected at a Minnesota Department of Transportation (Mn/DOT) bridge site; (ii) to instrument an Oklahoma IAB and collect data that can be utilized to validate the simulation tools for Oklahoma conditions and construction practices; and (iii) to use the validated computer simulation tools to understand the long-term performance of existing IABs and propose design guidelines to build new IABs with longer lengths and larger skew angles.

The Mn/DOT study involved an instrumented IAB in Rochester, Minnesota (Huang et al. 2004). Mn/DOT Bridge #55555 is a three-span prestressed concrete bridge with a total length of 216.6 ft. Phase I of this project involved the calibration and validation of the simulation tools TeraGrande and TeraDysac using the Mn/DOT study. TeraGrande can model the bridge superstructure accurately, including concrete cracking. TeraDysac can model the soil-structure interactions accurately, including the nonlinear behavior of soils and piles. The calibration and validation of TeraGrande and TeraDysac involved the following activities: (i) prediction of camber in a Mn/DOT bridge girder during prestressing to validate the structural modeling aspects of TeraGrande; (ii) confirming the assumption that the bridge superstructure will behave in a linear manner during the expected temperature increases and decreases using detailed structural modeling in TeraGrande; and (iii) validation of TeraDysac by comparing its predictions with the field measurements from the Mn/DOT study.

Phase II of the project involved selecting and instrumenting an Oklahoma IAB to collect data to study the behavior of IABs under Oklahoma weather conditions and construction practices. The North bound I-44 Bridge over the Medicine Bluff Creek in Comanche County near Lawton, Oklahoma, a 210 feet long, three span IAB with a 10^0 skew, was instrumented with pile strain gages, earth pressure cells, crackmeters, tiltmeters, and thermistors. The data collection started on June 23, 2009 and so far more than 30 months of data from this bridge has been collected. This is the first time such a comprehensive set of data is being collected for an Oklahoma IAB.

The bridge temperature decreases for a six month duration (from July to January) and then increases for the next six month duration (January to July). This

cyclic behavior continues from year to year. The average temperature change that the bridge superstructure experienced over a six month period of time is 90 – 95 ^{0}F. The field measured bridge temperatures agree with the temperature range specified in AASHTO LRFD Bridge Design Specifications. Earth pressures on the abutments increase as the temperature increases and decrease as the temperature decreases. Maximum changes in earth pressures are recorded at the obtuse corner of the north abutment. Earth pressure measurements show that fairly significant amounts of abutment back pressures occurred during summer. Recorded readings from the earth pressure cells, tiltmeters, and crackmeters are consistent with the expected behavior of abutments rotating outward during heating and rotating inward during cooling. Crackmeter and tiltmeter measurements show the majority of bridge translation is accommodated by the abutment pile movements in IABs. Abutment pile strains seem to be accumulating and then stabilizing after a certain time. Furthermore, the abutment piles appear to be experiencing bending moments beyond the yield bending moments at shallow depths.

Behavior of the Oklahoma IAB was also studied with the use of computer programs LPILE and GROUP. Computed bending moments for abutment piles confirm that piles have yielded at shallow depths. The three-dimensional model developed in GROUP shows biaxial bending of abutment piles occurs due to skew of the bridge. Field measured bending moments for the south abutment pile have lower values than the computed bending moments; very likely due to the installation of these piles in pre-drilled holes. A parametric study was conducted in order to propose design guidelines for IABs. According to this study, in order to accommodate thermal movement in IABs

and to reduce bending moments in abutment piles, a smaller HP pile section should be placed in weak axis bending and in pre-drilled holes with low stiffness material, especially at shallow depths. Abutment piles for IABs should be checked for capacities under combined axial force and bending moments. Using longer spans with larger girders will increase the axial load on the abutment piles and therefore long-span IABs should be designed with caution. Biaxial bending of abutment piles in skewed IABs increases stresses in the concrete superstructure and therefore the structural components for IABs with larger skew angles have to be designed carefully to accommodate the thermally induced deformations.

1 INTRODUCTION

1.1 PROBLEM

Conventional bridges are constructed with joints along the bridge deck to allow for movement caused by thermal loading. Though conventional bridges have been for the most part effective, they do have several problems during their service life. First of all, roadway runoff can pass through the open or leaking deck joints, which leads to the deterioration of the underlying girders and bearings. Additionally, if water freezes in the deck joints, the joint performance may be impacted, thus not properly accommodating the necessary contraction and expansion the bridge requires for proper functionality. Due to these factors, conventional bridges tend to have rather high maintenance costs. To reduce problems caused by the presence of joints, integral abutment bridges (IABs) are being built by agencies at an increasing rate in the U.S. Integral abutment bridges accommodate thermal contraction and expansion by movement of the abutments. The simpler joints between the approach slabs and pavements accommodate the relative movement between the bridge and the roadway. Because of their design, integral abutment bridges have less maintenance costs when compared to conventional bridges. Additionally, IABs have been found to be better for seismic and blast loading when compared to conventional bridges. Even though there are several benefits, several questions of interest to engineers regarding integral abutment bridges remain unanswered. In Oklahoma, IABs longer than 400 feet or skewed IABs are not considered as there is a lack of local knowledge on the long-term behavior of IABs. Figure 1.1 shows how a skewed bridge varies from a non-skewed bridge.

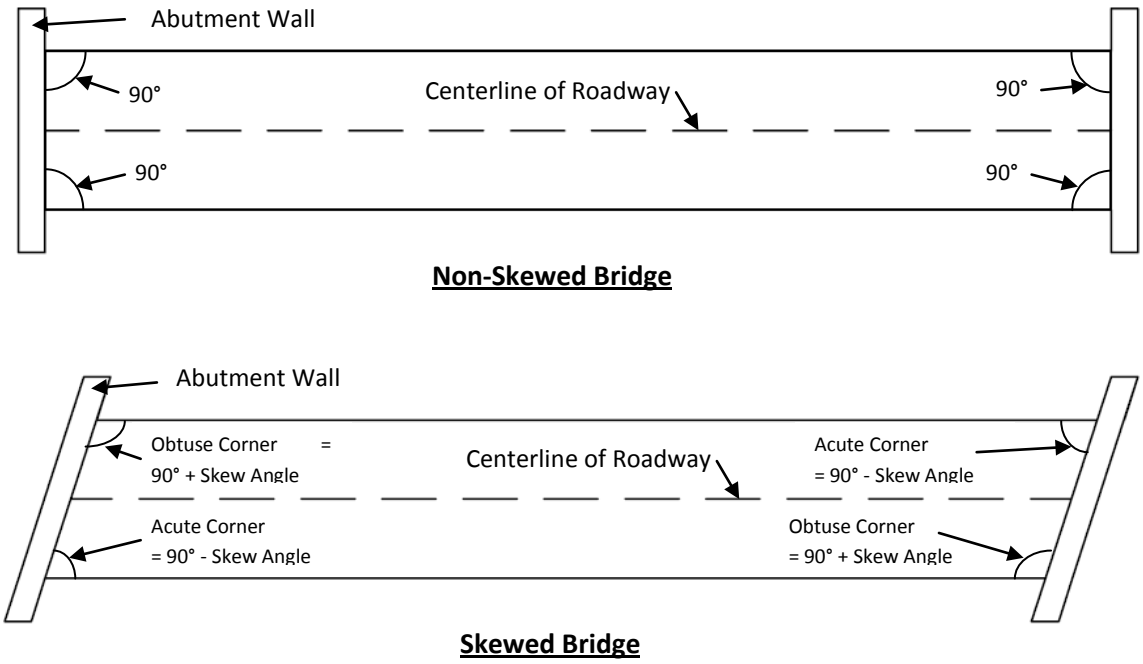

Figure 1.1: Difference between a Non-Skewed and a Skewed Bridge

Engineers in Oklahoma have been reluctant to push the limits of integral abutment bridge design because there is a lack of local experience, design history, and understanding of the soil-structure interactions at the integral abutments.

1.2 PURPOSE

Because of uncertainties related to the complex soil-structure interaction in IABs, Oklahoma Department of Transportation (ODOT) has been reluctant to build longer and skewed IABs. This project provides valuable insight into the complex soil-structure interactions occurring in IABs. The insights gained through this project will lead to better understanding of the long-term performance of existing IABs. These insights will also provide the transportation engineers with the confidence necessary to build new IABs with longer lengths and larger skew angles.

1.3 SCOPE AND OBJECTIVES

The scope of this project is to understand the complex interactions in an IAB and to propose design guidelines to build new IABs with longer lengths and larger skew angles. The main objectives of this project are: (i) to validate two computer simulation tools, TeraGrande (ANATECH 2005) and TeraDysac (Muraleetharan et al. 2003, Ravichandran 2005), for studying the interactions in an IAB using field data collected at a Minnesota Department of Transportation (Mn/DOT) bridge site; (ii) to instrument an Oklahoma IAB and collect data that can be utilized to better understand IAB behavior and validate the simulation tools for Oklahoma conditions and construction practices; and (iii) to use the computer simulation tools to understand the long-term performance of existing IABs and propose design guidelines to build new IABs with longer lengths and larger skew angles.

1.4 CHAPTER OVERVIEW

Chapter 2 provides a literature review considering previous and relevant work to the behavior of IABs. Chapter 3 presents the validation of the computer simulation tool TeraGrande. It describes TeraGrande finite element analyses in which bridge superstructure is effectively modeled incorporating reinforcement details. Chapter 4 provides the validation of the computer simulation tool TeraDysac. Minnesota IAB details are used for TeraDysac modeling and the numerical results are compared with field measurements. Chapter 5 presents the description of the Oklahoma IAB instrumentation, including details of all the instruments used and data collected. Chapter 6 provides the behavior of the Oklahoma IAB for daily temperature variations. Chapter 7 presents the behavior of the Oklahoma IAB for seasonal temperature variations.

Chapter 8 presents the numerical modeling of Oklahoma IAB, which provides the insight into long-term behavior of Oklahoma IAB. Chapter 9 provides the parametric study conducted to extend the results of the Oklahoma IAB to more general IABs. Chapter 10 contains concluding remarks and recommendations.

2 BACKGROUND

2.1 INTEGRAL ABUTMENT BRIDGES

In traditional bridges (Figures 2.1 and 2.2), structural releases are provided in bridges to permit thermal expansion and contraction. These joints lead to water-tightness problems. Water runoff into newly opened deck joints can cause extensive damage. Water corrodes the underlying steel elements (girders, supports, connection hardware, etc), damages the concrete, and corrodes reinforcing steel. This problem is magnified in states subject to heavy snow storms, where sodium chloride and calcium chloride are commonly used in de-icing applications. The joint problems first emerged in the 1960s as traffic loads increased in speed, volume, and weight. The cost of maintenance or replacement of expansion joints is a considerable portion of the total money spent by state Departments of Transportation (DOTs) every year. Joints and bearings in traditional bridges have emerged as major sources of bridge maintenance problems (Wolde-Tinsae and Greimann 1988).

In an IAB (Figures 2.3 and 2.4), there are no girder bearings at the abutments. Instead, the girder ends are cast integrally with the abutment, hence the terminology integral abutment bridge. These bridges have been commissioned for some time. States like Ohio, Oregon, and South Dakota have been employing IABs since the 1930s (Hassiotis and Roman 2005). IABs have a lower construction cost and much lower life cycle costs because of minimal maintenance. Retrofitting traditional bridges with IAB features has also shown to be cost effective (Nickerson 1996).

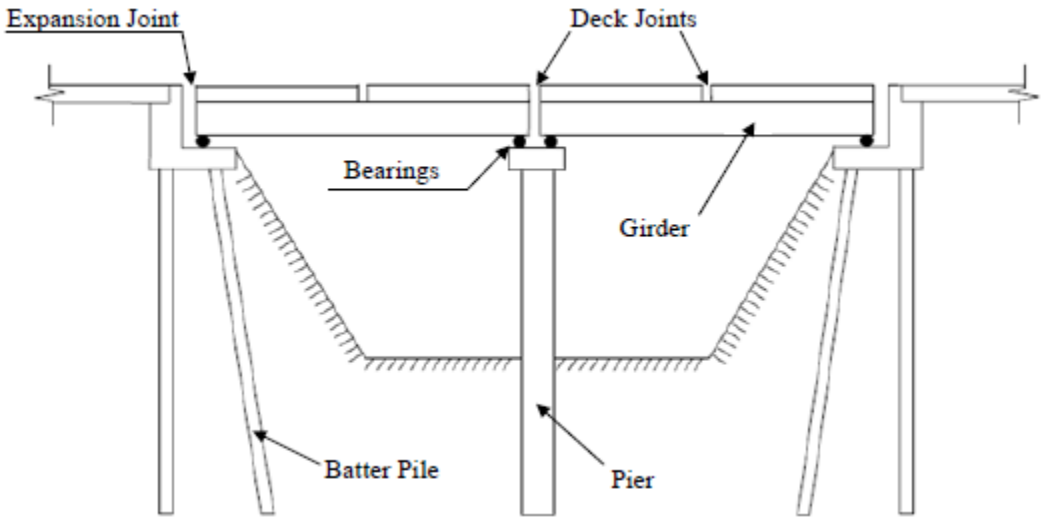

Figure 2.1: Schematic Drawing of a Traditional Bridge

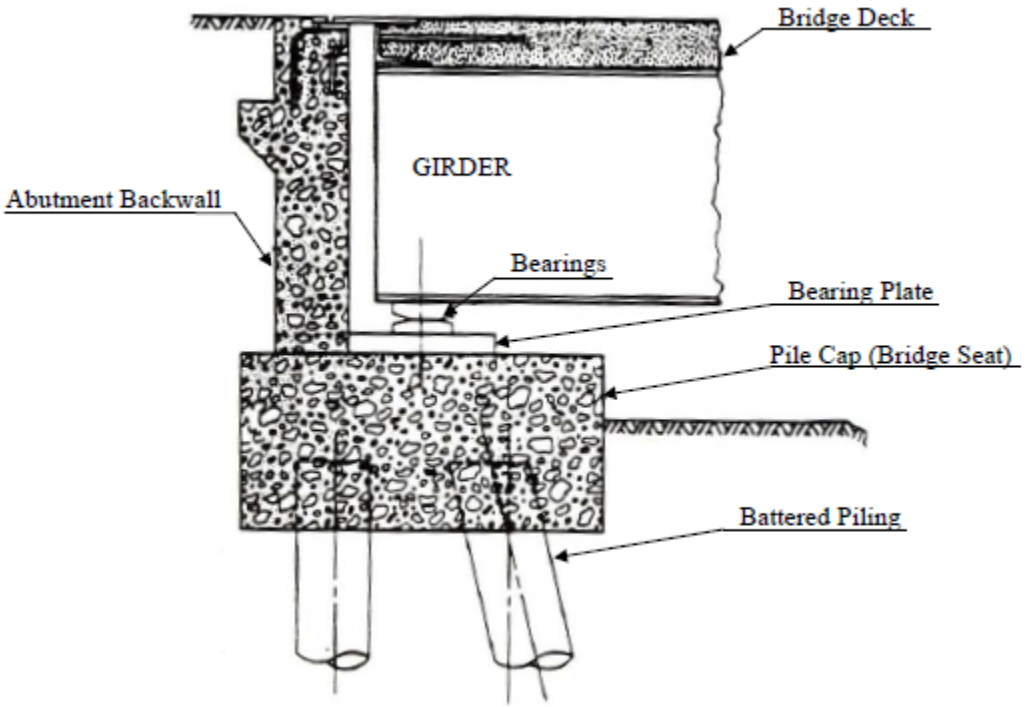

Figure 2.2: Abutment Details for a Traditional Bridge (Soltani 1990)

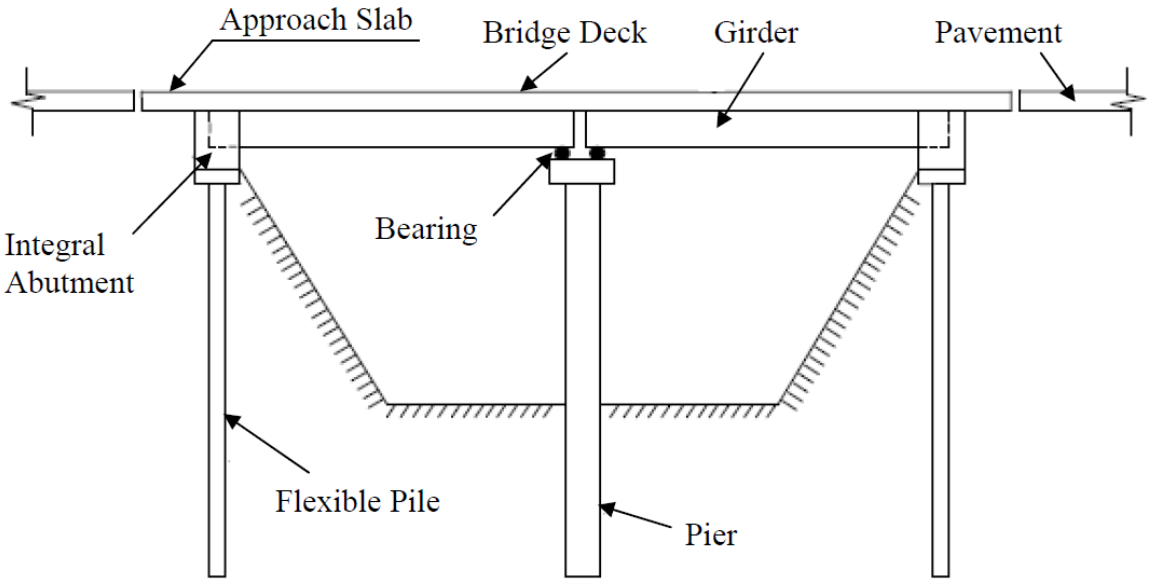

Figure 2.3: Schematic Drawing of an Integral Abutment Bridge

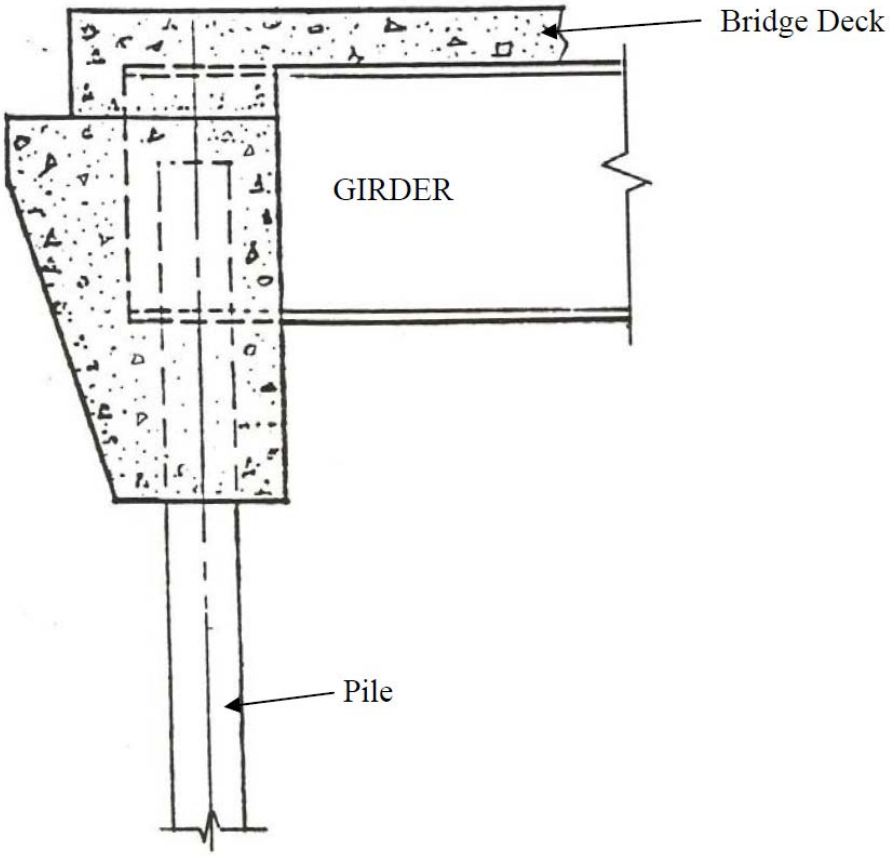

Figure 2.4: Abutment Details for an Integral Abutment Bridge (Soltani 1990)

In IABs, the thermal loading causes bending in the piles supporting the abutments. Flexibility at the abutment is provided by the use of a stub abutment supported by a single row of piles in weak-axis bending. In some cases, piles are placed in predrilled holes and then filled with sandy material. Approach slabs are usually poured behind integral abutments in order to prevent compaction of backfill soils by traffic loading and to offer a smooth transition to the bridge (Arockiasamy et al. 2004).

A numerical study conducted by Yang et al. (1985) investigated the effect that predrilled oversized holes have on abutment pile response. A finite element model of beam-column elements and nonlinear soil springs were used for the study. The work revealed that oversized holes, especially holes drilled to significant depths did much to alleviate overstressing the steel H-piles used under the abutment. Piles without oversized holes in harder materials such as stiff clay or compacted fill were shown to develop plastic hinges much quicker for prescribed transverse tip displacement than their counterparts with predrilled holes.

IABs have proven to be economical and effective in eliminating joint maintenance issues, but they are not without problems. When the bridge expands and contracts during thermal loading, soil behind the abutment is disturbed. Ground subsidence adjacent to abutments (under the approach slabs) has been observed. Subsidence behind the abutment wall can cause structural problems in the approach slab if bending loads are significant as vehicles pass over the slab. In the long term, these bridges can cause a buildup of lateral earth pressures on the abutments due to the soil-mechanics phenomenon known as ratcheting (Horvath 2004).

In some cases, special additions are made to IAB systems to alleviate high pressures behind the abutments and high stresses in the abutment piles. A field experiment was conducted in North Dakota which addressed this issue (Jorgenson 1983). A 137 m IAB with concrete box girders was instrumented and monitored for a period of one year. Ten-centimeter thick strips of compressible pressure relief material were placed in a slot between the abutments and the granular backfill. Five-centimeter layers of the material were placed on both sides of the abutment pile webs. These piles were in oversized holes filled with sand. This method was shown to be effective, as little yielding of the abutment piles was observed and plastic hinges did not form.

2.2 CURRENT PRACTICES

IABs have been in use for many years, but there still is no comprehensive design procedure. Each state highway department manages its own integral abutment program and establishes guidelines with regard to design and construction. Not having an organized design and construction procedure leads to variation in the analysis, design, and construction practices of IABs between states (Arockiasamy et al. 2004).

An excellent survey on current practices in the United States and Canada was conducted by Kunin and Alampalli (2000). The responses from 39 states and Canadian provinces provided insight into the differences in IAB design and construction practices. With the exception of one state, the opinion about IABs was positive. Due to some expensive repair operations on bridge approaches, Arizona did not recommend IAB use. Most agencies were found to use AASHTO recommendations for temperature variation according to their region and the following formula to calculate the estimated bridge thermal movement:

$$\Delta L = \alpha \Delta T L \tag{2.1}$$

where α is the coefficient of linear thermal expansion of the superstructure, ΔT is the temperature change, and L is the bridge length. Passive soil pressure was commonly used behind the abutments, but some states use an active and passive combination. Three agencies reported not considering earth pressure in their designs. A majority of the responses revealed that skew effects are not considered with respect to soil pressure. A significant number of agencies (almost half) design piles solely for axial loads. The p-y program LPILE (ENSOFT 2007) was used by some of the agencies for their pile design. In addition to soil nonlinearity, LPILE can consider structural nonlinearity (e.g. loss of bending stiffness in the piles).

2.3 SKEWED IABS

A skewed IAB is one in which the abutments are not perpendicular to the roadway centerline (see Figure 2.5). A comprehensive survey of highway departments in all 50 states was conducted to determine design practices and performance of skewed IABs (Greimann et al. 1983). This survey revealed 26 states were using skewed IABs, but designing them primarily based on local experience. No theoretical or computational methods were used in most of the designs. There was noticeable variation in the practices from state to state, including abutment pile orientation and the use of batter piles for certain skew angles.

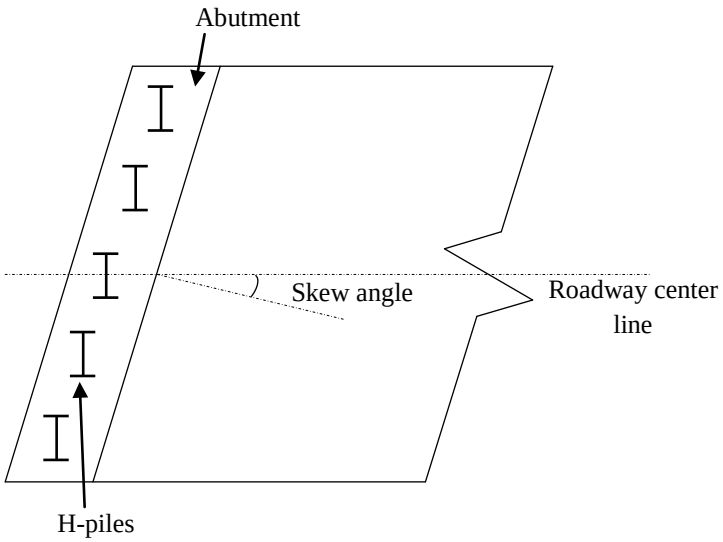

Figure 2.5: Skew Angle Depiction

A field experiment on a Maine IAB with a 20° skew angle showed the backfill pressure behind the abutments is affected by skew angle (Sandford and Elgaaly 1993). Pressure cells were mounted behind abutments to monitor skew effects. The study lasted for 33 months and revealed that the backfill behind the obtuse corners of IABs experienced significantly higher pressure (more than double in some locations) than the backfill behind the acute corners. Figure 2.6 depicts the obtuse and acute angles in an IAB.

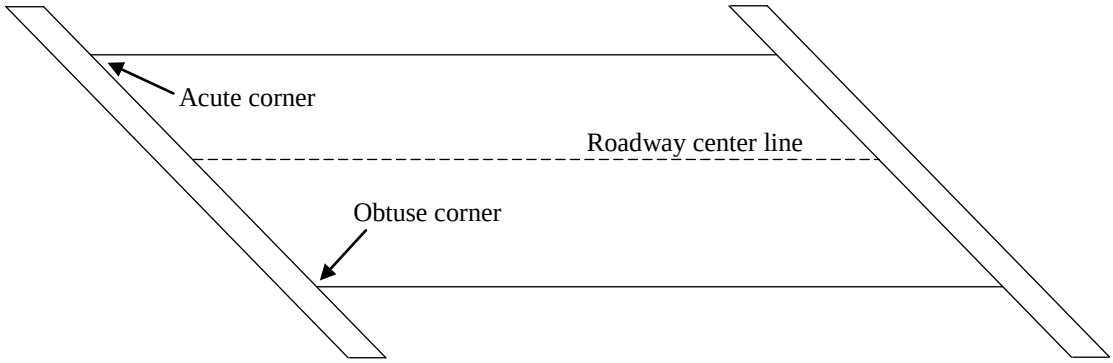

Figure 2.6: Obtuse and Acute Corners in IABs

Alampalli and Yannotti (1998) performed an in-service evaluation of IABs in New York. IABs were graded based on the New York State DOT condition rating scale for bridges. Bridge ratings were lower for both steel and concrete superstructures when the IABs were skewed. A recommendation of a maximum bridge skew angle of 30° was made pending further study. In a paper by Comstock and Dagher (1993), rearranging the longitudinal reinforcement in the bridge was shown to delay cracking in the deck near the abutment walls. By placing more steel in the obtuse corners, the bending moment and shear force capacities in the obtuse corners of the bridge were increased. This delayed cracking in the obtuse corners ultimately led to a more uniform crack pattern across the deck.

In a study conducted by Steinberg et al. (2004) on two Ohio skewed semi-integral abutment bridges, the forces developed in the wingwalls were found to be significant. It was recommended that these forces be considered in the design process, as opposed to designing the wingwalls simply as retaining walls. A subsequent finite element analysis showed the reaction at the wingwalls increased with the bridge skew angle.

2.4 SOIL-STRUCTURE INTERACTION

In analyzing soil-structure interaction problems, sometimes interface elements are used in finite element programs to simulate behavior at the interface. The important phenomena at the interface are relative slipping and shear resistance (tangential behavior) and bearing and gapping (normal behavior). Two dimensional (2D) elements or 'Zero Thickness Elements' have been around for years (e.g. Goodman et al. 1968, Beer 1985). Zero thickness elements using a Mohr-Coulomb failure criterion have been shown to model interface behavior of retaining walls with good accuracy, but numerical stability issues emerge in some problems (Day and Potts 1994). Three dimensional (3D) elements with a finite thickness or 'Thin-Layer Elements' have also been used to model soil-structure interfaces (e.g. Desai et al. 1984). These elements require a constitutive model for implementation. Usually experiments and simple lab tests are performed on the soil and the interface (e.g. a direct shear test between concrete and clay) to obtain various parameters such as the normal and tangential stiffness. Another approach models the structure and soil separately, but uses constraint equations to maintain compatibility of force and displacement between the two. This so-called 'Hybrid Method' can accommodate the relevant modes at the interface and also has been shown to be more numerically stable than the above mentioned methods because there are no vastly different values in the stiffness matrix (Lai and Booker 1991). In this project we used tied contact between shared soil and structure nodes to simulate soil-structure interaction in IABs. Although this procedure has its limitations, the coupling of soil and structural elements is a good first step to modeling soil-structure interaction.

For modeling IABs for thermal loading and associated small displacements, tied contact should be acceptable.

2.5 INSTRUMENTATION PROJECTS

There have been numerous IAB instrumentation projects reported in the literature (e.g. Fennema et al. 2005 and Sandford et al. 2006). Fennema et al. (2005) instrumented and analyzed a three-span bridge (52.4 m bridge length, zero skew angle) in Pennsylvania. This project examined several uncertainties of IAB design, performed field-monitoring, and analyzed the bridge with three levels of numerical modeling. The analysis levels included laterally loaded pile models using commercially available software, 2D single bent models, and 3D finite element models. Multilinear spring stiffnesses were developed through a sequence of linear regressions to fit p-y curves at depths corresponding to locations of soil springs defined in the bridge structural analysis model. The instrument data from the bridge site was used to refine the numerical models. The models were then used to predict IAB behavior of other Pennsylvania bridges of similar construction.

A field monitoring effort during the construction of an IAB in Maine (30 m bridge length, 35° skew angle) revealed bending stresses from dead loads are quite important (Sandford et al. 2006). Some agencies explicitly calculate bending effects, but many neglect dead load bending in piles. This monitoring effort revealed stresses from bending by abutment rotation due to dead load should be included in the design process. If the bridge is skewed, bending in piles perpendicular to the centerline should also be computed.

Major work has been done in the field of IAB instrumentation, monitoring, and analysis by the University of Minnesota (see Huang et al. 2004). An IAB located in Rochester, Minnesota (65.6 m bridge length, zero skew angle) was monitored from the beginning of construction through several years of service. More than 180 instruments, including tiltmeters, strain gauges, and pressure cells, were installed in and around the bridge during construction to monitor loading effects. Various weather recording devices were also set up at the bridge site to monitor temperature and solar radiation. The primary movement of the abutment was found to be a horizontal translation to accommodate superstructure expansion and contraction due to seasonal changes. There was a net inward movement of the abutments over time. An extensive numerical study was also performed. The numerical modeling showed that the p-y method could simulate soil-pile interaction reasonably well. This work provided good insight into IAB performance and a wealth of results from instrumentation, some of which were used to validate computational simulation tools in this project.

2.6 IMPORTANT LOADING CASES

There are many factors to be considered when designing these complicated systems. Static, live, cyclic, and dynamic loading scenarios are all possible. Because of the size and weight of highway bridges, the effect of gravity loading alone is an important load case. As discussed previously, thermal loading is of major importance in IABs. In a paper by Paul et al. (2005), the thermal forces developed in prestressed girder IABs were found to be comparable in magnitude to those caused by live load. Their work showed the largest thermally induced superstructure forces to be found near the abutments. After studying several parameters that influence thermal loading, they

concluded that bridge length and abutment height strongly influence thermal forces. Taller abutments have a larger cross-sectional area exposed to the backfill soil, so upon bridge expansion there is a greater passive soil resistance leading to higher superstructure forces. In addition to traffic loads and creep of the superstructure, earthquakes and blast loading may also need to be considered.

3 VALIDATION OF THE COMPUTER SIMULATION TOOL: TERAGRANDE

3.1 GENERAL

The structural elements implemented in TeraDysac are low order linear elastic elements. To validate the use of these elements, several thorough analyses of the superstructure were performed using the finite element application TeraGrande (ANATECH 2005). The program considers all the material nonlinearity applicable to reinforced concrete modeling. In addition to stress and deformation outputs, concrete cracking can be monitored. The purpose of this section of the report is to illustrate that although cracking does occur during the thermal loading cycles, the cracking is only minimal and therefore linear elements are acceptable for IAB analyses in TeraDysac. The instrumented Minnesota bridge is used as an example. The TeraGrande User's Manual (ANATECH 2005) should be consulted for a full description of the features available in and theory behind the TeraGrande computer program. A cursory explanation of the pertinent details to this project is presented in the following five sections.

3.1.1 Explicit Dynamics

This project used the explicit dynamics procedure available within TeraGrande for all analyses. The equations of motion of a body are integrated through time using an explicit central difference integration rule given by the following:

$$\ddot{u}_i = P_i - I_i \tag{3.1}$$

$$\dot{u}_{i+\frac{1}{2}} = \dot{u}_{i-\frac{1}{2}} + \frac{(\Delta t_i + \Delta t_{i+1})}{2}\ddot{u}_i \tag{3.2}$$

$$u_{i+1} = u_i + \Delta t \dot{u}_{i+\frac{1}{2}} \tag{3.3}$$

where u_i are the nodal displacements at time increment i, $\dot{u}_{i+\frac{1}{2}}$ are the nodal mean velocities at the mid-increment, $\ddot{u}_i$ are the nodal accelerations at time increment i, P_i are the external applied loads, and I_i are the internal forces (due to stresses) at time increment i. The time increment, Δt_i , changes as the body deforms and is governed by the damped Courant stability limit of the mesh given by:

$$\Delta t_{cr} \leq \frac{2}{\omega_{\max}}(\sqrt{1+\xi^2} - \xi \tag{3.4}$$

where $\omega_{\max}$ is the highest natural frequency of the mesh and ξ is the fraction of critical damping in the highest mode. The time steps used in the various analysis runs presented here were quite small. Analysis times of 0.5 seconds (or thereabouts) required hundreds of thousands of time steps.

3.1.2 ANATECH Concrete Model

The smeared-crack finite element technology used in the model was developed by the founder of ANATECH Corp., Dr. Y.R. Rashid (Rashid 1968). The compressive strength of concrete (f_c') is the only input required from the user for the concrete constitutive model. All other model parameters are obtained using correlations to f_c'. This nonlinear model has been shown to accurately predict laboratory tests of

reinforced concrete bridge components, capturing cracking, plasticity, and hysteresis among other phenomena (Dunham et al. 1991, Dameron and Dunham 1992). For f_c' = 40.68 * 10^3 kPa (5900 psi), the generated curves representing the concrete constitutive behavior are given Figures 3.1 and 3.2. This is the value of compressive strength at the time of prestress transfer for the example that follows.

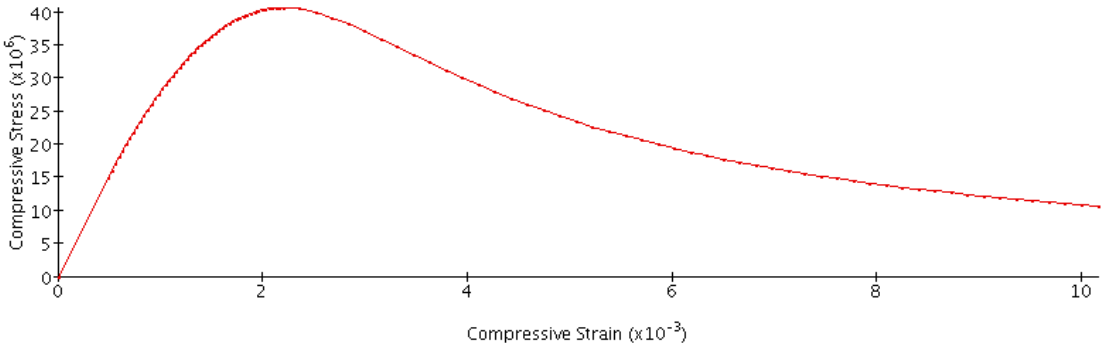

Figure 3.1: Compressive Stress (Pa)-Strain Curve

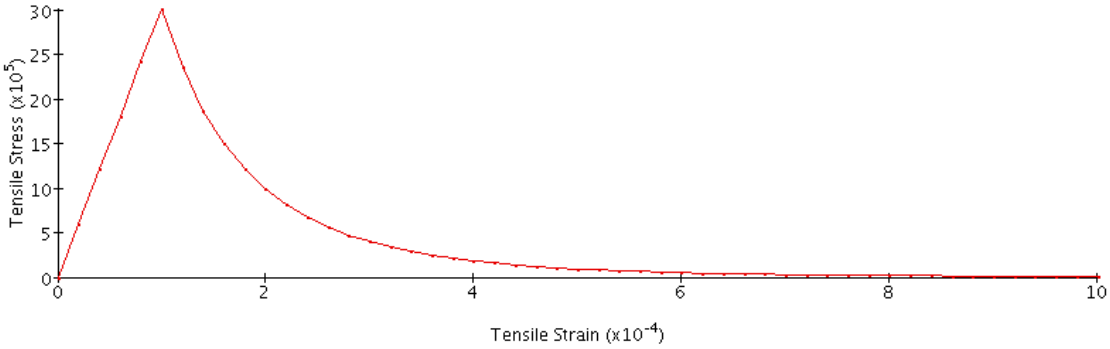

Figure 3.2: Tensile Stress (Pa)-Strain Curve

3.1.3 Concrete Cracking

The Young's modulus for the concrete is computed in the TeraGrande input file, although a user-furnished Young's modulus option is available. The value of Young's modulus for the concrete is computed using Equation 3.5 in accordance with ACI 318-02.

$$E = 57000\sqrt{f_c'} \tag{3.5}$$

where the units of f_c' and E are in psi.

The girder concrete compressive strength was given in the bridge plans (f_c' = 5900 psi). Therefore,

$$E = 57000\sqrt{5900} = 4.378 * 10^6\ psi = 30.19 * 10^6\ kPa$$

The tensile cracking strain is specified in the input file as 10^{-4}. The tensile cracking stress is determined using Young's modulus (see Figure 3.3).

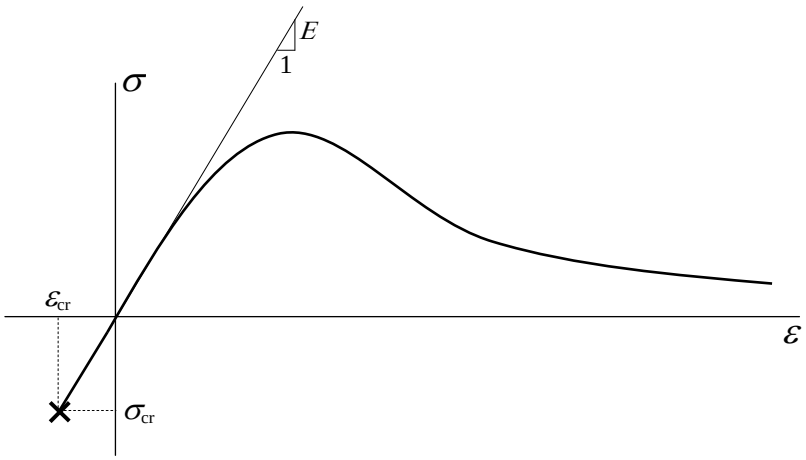

Figure 3.3: Concrete Stress-Strain Diagram

The initial slope of the concrete stress-strain curve is Young's modulus. The cracking stress occurs at the specified tensile cracking strain following the slope of the curve. The concrete cracking stress is given by:

$$\sigma_{cr} = E\varepsilon_{cr} = 30.19 * 10^6\ kPa * 10^{-4} = 3.019 * 10^3\ kPa$$

This value of cracking stress agrees with the figure furnished by TeraGrande (Figure 3.2). The tensile strength of the concrete quickly diminishes after the cracking

stress is reached. Cracking behavior is treated at the element integration stations using the smeared crack model. Cracks are assumed to form perpendicular to the directions of largest tensile strains which exceed the cracking strain. The crack direction remains fixed although the crack can close, resist compression, and re-open under load reversals (ANATECH 2005).

3.1.4 Reinforcement Modeling

TeraGrande allows the user to model individual rebar strands. Uniaxial rebar strands (2D line elements) pierce the concrete elements (3D hexagonal 8-node bricks). Figure 3.4 shows the finite element mesh of one of the bridge girders.

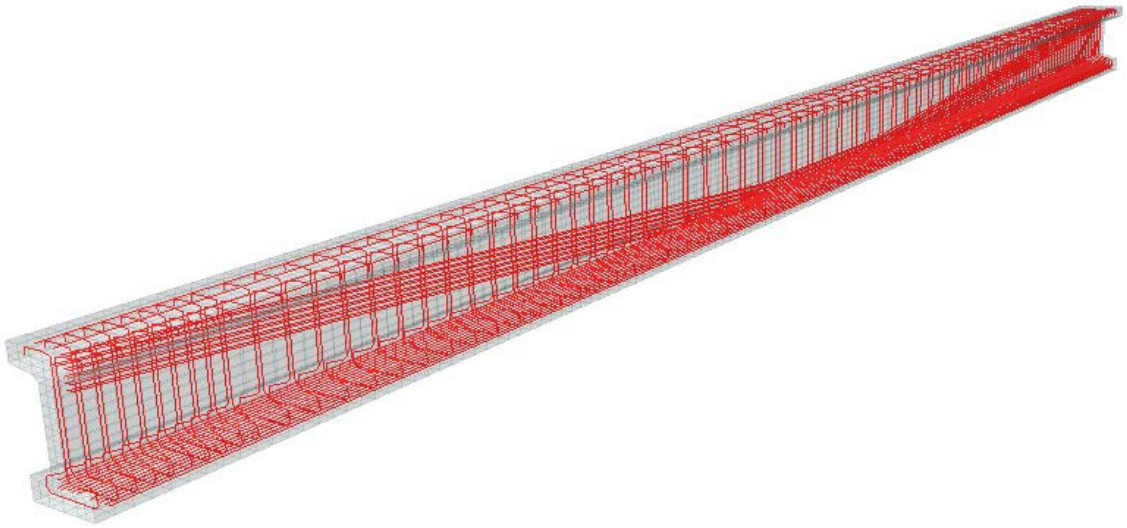

Figure 3.4: Bridge Girder Mesh

Figure 3.4 illustrates that the rebar can be accurately modeled in TeraGrande. The stirrups, prestressed rebar strands, and longitudinal reinforcement (no prestress) are all shown in the beam.

3.1.5 Tied Contact

The bridge model is built by connecting 3D mesh instances. An instance is an individual component of the bridge (i.e. a girder or a bent cap). When rebar is connecting instances (i.e. the girder connection to the deck), tied contact is used between the instances. A simple example of tied contact is shown in Figure 3.5. Three instances (two flat blocks and a bar) are connected using tied contact. The red nodes are shared nodes between instances. When the problem gets meshed, a set of shared node sets on each side of the bar is merged out and three mesh instances become one mesh assembly.

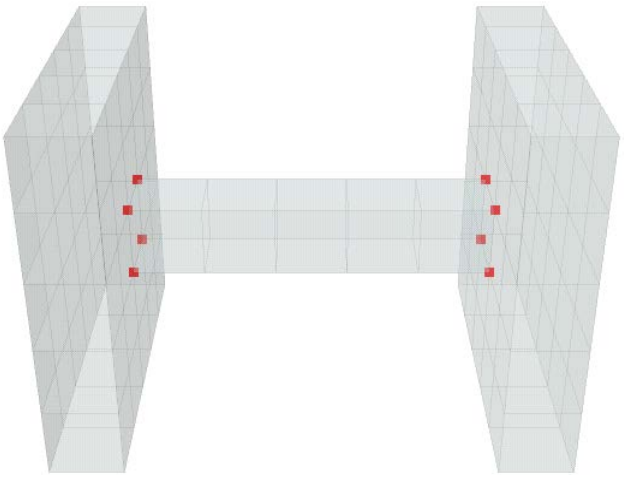

Figure 3.5: Tied Contacts between Mesh Instances

3.2 PRESTRESSED GIRDER MODELING

To show the accuracy that a reinforced concrete analysis in TeraGrande yields, the analysis of a prestressed girder from the bridge model is presented here. Figure 3.6 shows the tendons subjected to prestressing. The draped strands are located in the girder web.

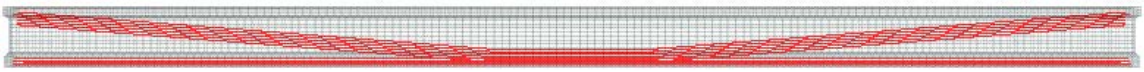

Figure 3.6: Prestressed Tendons in Bridge Girder

A set of plans was available from the IAB project. In addition to the design details (rebar layout, section geometry, etc), the plans provided design strengths, prestress loading magnitude, and camber information. The compressive strength at the time of the transfer of prestress (f_c') was 40.68 * 10^3 kPa. 12.7 mm steel plates were merged on to the girder ends (see Figure 3.7). The plates help support elements near the girder ends as the prestress load develops.

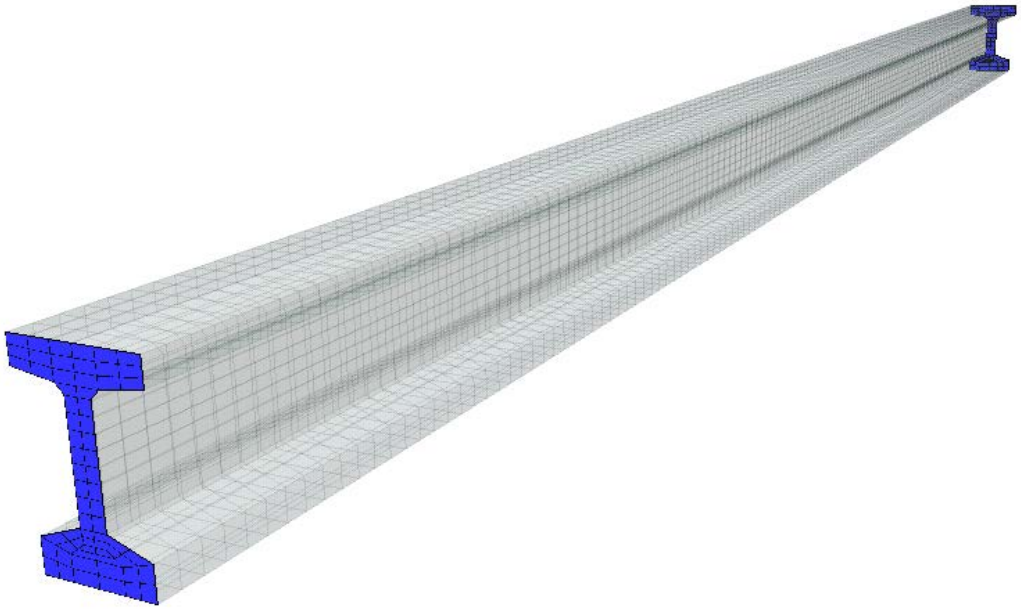

Figure 3.7: Girder End Caps

An explicit dynamics analysis was performed on the girder with two procedures. The prestress was added to mesh followed by the self-weight of the girder. The loading scheme is presented in Figure 3.8.

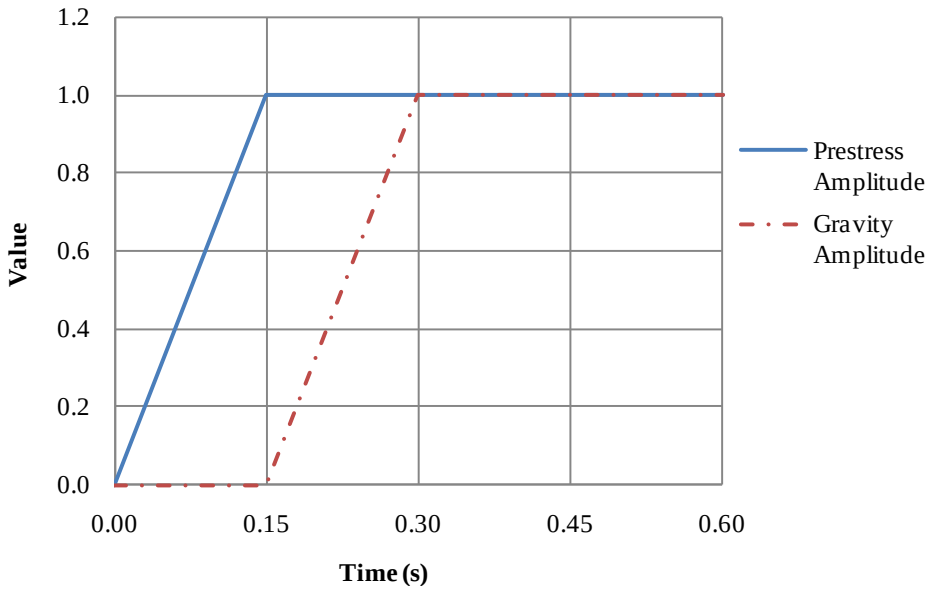

Figure 3.8: Loading Amplitudes for Girder Analysis

The y-axis value in Figure 3.8 is a portion of the loading magnitude. Therefore, when the value is 0.0 there is no load and when it is 1.0, the load is applied fully. It is apparent that the loads are each ramped up over 0.15 seconds. The first procedure (prestressing) lasts for 0.15 s. Immediately after the prestress amplitude reaches its full value, this procedure ends and the gravity procedure begins. TeraGrande allows procedures to import mechanical states from other procedures. So at 0.15 s, the gravity loading begins with the full prestress load already developed in the girder. The gravity ramps up and reaches its full value at 0.3 s. The loads are then held at their full values for another 0.3 s. Figure 3.9 shows the node sets pertinent to the analysis. The boundary nodes on the left are fixed in both the vertical and longitudinal direction of the girder and the nodes on the right are fixed in the vertical direction only. The middle node shown is at the girder midspan on the top of the girder. A nodal displacement-time history was written for this node.

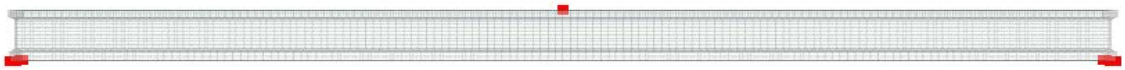

Figure 3.9: Important Node Sets for Girder Analysis

The cracking pattern was tracked during the analysis. Figures 3.10 and 3.11 show the cracked girder at 0.15 s and 0.6 s, respectively. A red marking indicates there is an open tension crack. A blue marking indicates that a once open tension crack is now closed in compression. The displacement is magnified by a factor of 5.

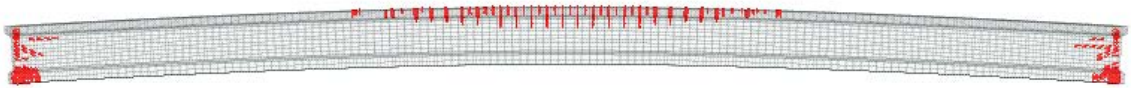

Figure 3.10: Crack Pattern at 0.15 s

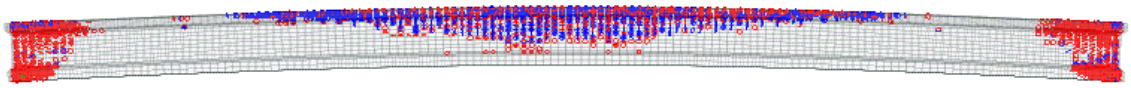

Figure 3.11: Crack Pattern at 0.6 s

It is apparent that there is significant cracking near the beam ends. Focusing on the cracking away from the beam ends, the crack pattern agrees with intuition. There are open tension cracks at the end of the prestressing. The gravity loading subsequently closes most of these cracks, as indicated by the blue markings. Although the cracking pattern looks ominous, it is important to realize that the red makers simply mean the cracking strain has been reached in the concrete. Since over 5200 kN (1.1 million lbs.) of prestress force and 215 kN (24.2 tons) of self-weight are transferred to the beam, cracking is expected. An important check on the validity of the results is found with a nodal displacement-time history. A nodal displacement history of a node at the top-center of the beam at midspan reveals information about the beam deflection and residual camber. According to the bridge plans, the residual camber in the beam is about 6 cm. Figure 3.12 shows the displacement-time history.

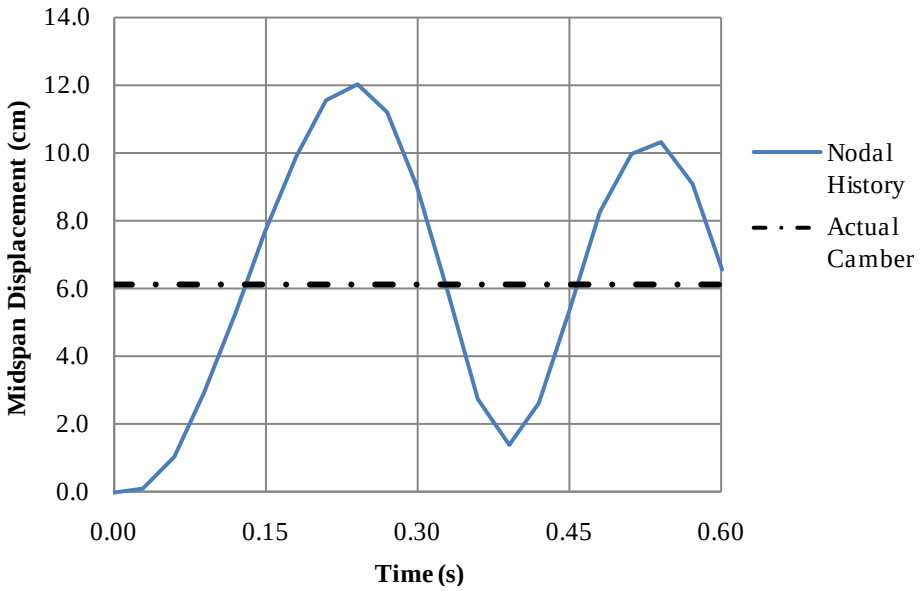

Figure 3.12: Midspan Displacement-Time History from Girder Analysis

Although there is still some oscillation left to occur in the girder, it is apparent that the midspan deflection is converging to the residual camber specified by the bridge plans. This analysis is an excellent check on the reinforced concrete analysis in TeraGrande. Considering the mesh size (9216 concrete elements, 9820 rebar elements), the model complexity, and the load magnitude, it is a very encouraging result to have the nodal displacement so close to the actual camber observed in the field.

3.3 SUPERSTRUCTURE MODEL

A full 3D model of the Minnesota bridge was created in TeraGrande (see Figure 3.13). However, the model was reduced to only the superstructure (girders and deck) for several reasons. Mainly, the analysis was designed to only study the superstructure response to abutment movements. As the girder ends sit on elastomeric bearing pads, abutment movement does not elicit any appreciable response in the piers and pier piles.

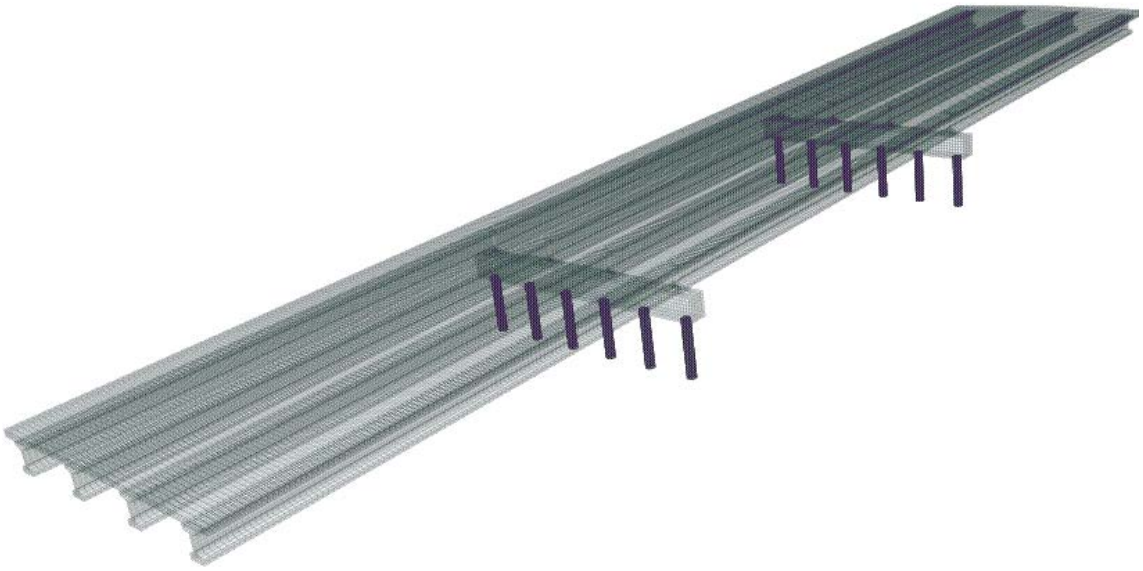

Figure 3.13: Minnesota IAB Model (Piers and Pier Piles Included)

Also, some of the elements in the pier piles above grade had very poor aspect ratios. Figure 3.14 shows a 2D view of the cross section. The red element block is steel and the blue element block is concrete. The thin steel casing around the piles and the piles themselves are quite thin (~10 mm). To make reasonable element aspect ratios for these elements would make the model size grow significantly.

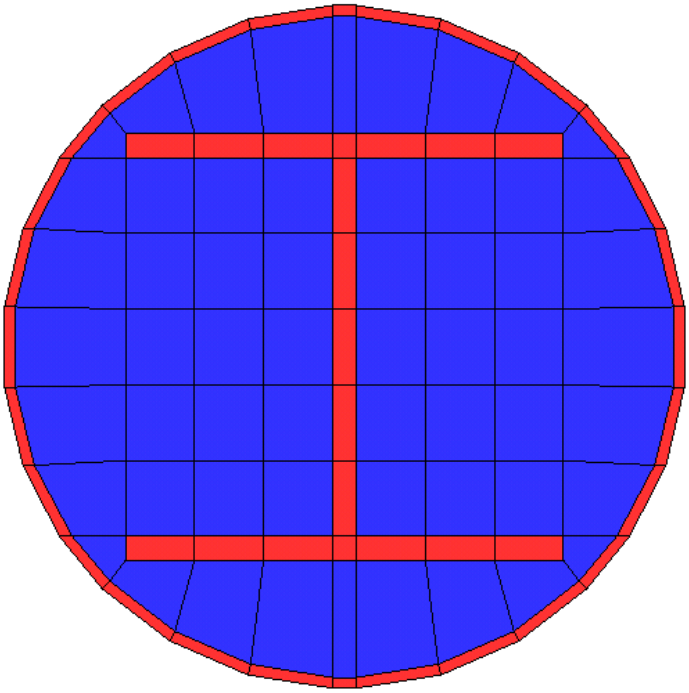

Figure 3.14: Pier Piles (Above Grade) Mesh

Removing the pier caps and the pier piles above grade resulted in a superstructure model with 366,272 elements. The element count includes 193,908 uniaxial rebar elements (see Figure 3.15).

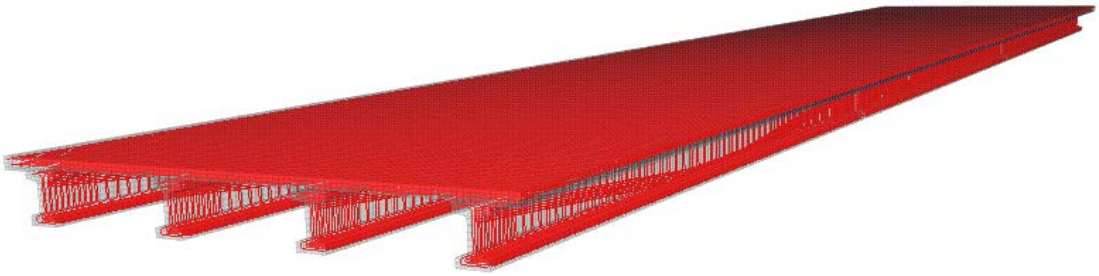

Figure 3.15: Minnesota IAB Superstructure Model (Rebar Shown)

The important regions for boundary condition application in the superstructure model include the locations of the bearing pads and the abutments in the field. A node set is created at the girder ends on the superstructure interior (shown as red squares in

Figure 3.16). These nodes are fixed in the vertical direction only to simulate resting on bearing pads. Translation in the longitudinal direction of the bridge is allowed.

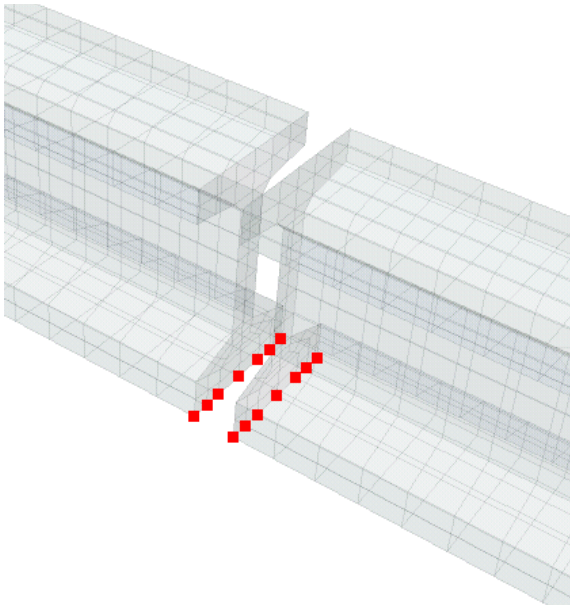

Figure 3.16: Superstructure Interior Nodes

The girder ends and deck are cast integrally into the bridge abutments. Because of the rigidity in this region, the abutment boundary conditions can be applied directly to the ends of the superstructure model. A portion of the superstructure end node set is shown as red squares in Figure 3.17.

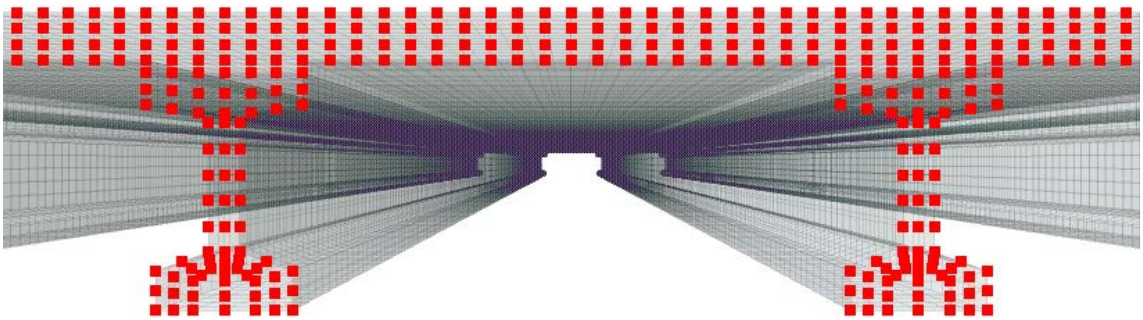

Figure 3.17: Superstructure End Node Set

The ultimate goal of the TeraGrande modeling in this work is to show that significant nonlinear behavior (e.g. concrete cracking) is not occurring during the

thermal loading of the IAB. This section is meant to show that the linear structural elements developed for TeraDysac are acceptable for the thermal analysis of IABs.

3.4 THERMAL ANALYSIS

Because the abutment movements due to the thermal loading are known from the instrumentation, a thermal analysis does not need to be performed on the superstructure. Instead the measured abutment displacements can be applied directly to the node sets on the ends of the superstructure.

3.4.1 Temperature Increase

A 10°F increase in the bridge temperature induced abutment translations of 2 mm at each abutment. This displacement was applied to each superstructure end to simulate the thermal event used for the TeraGrande validation. These histories were applied to a pristine bridge model. A model with no cracks or residual stress is used so that the observed stress, strain, cracks, etc are all due to the loading in question. Figures 3.18 and 3.19 show the crack pattern in the bridge deck and the bridge girders at the end of the loading.

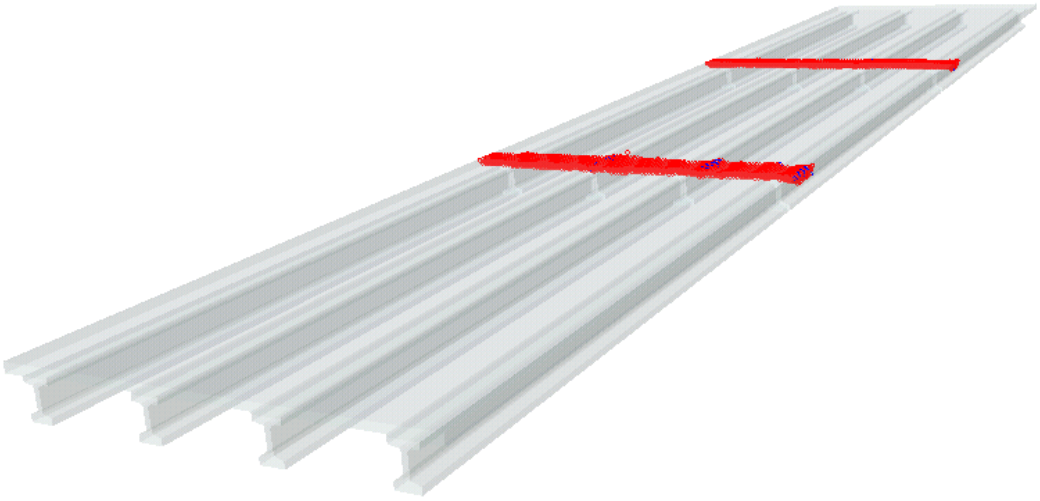

Figure 3.18: Superstructure Crack Pattern for Temperature Increase

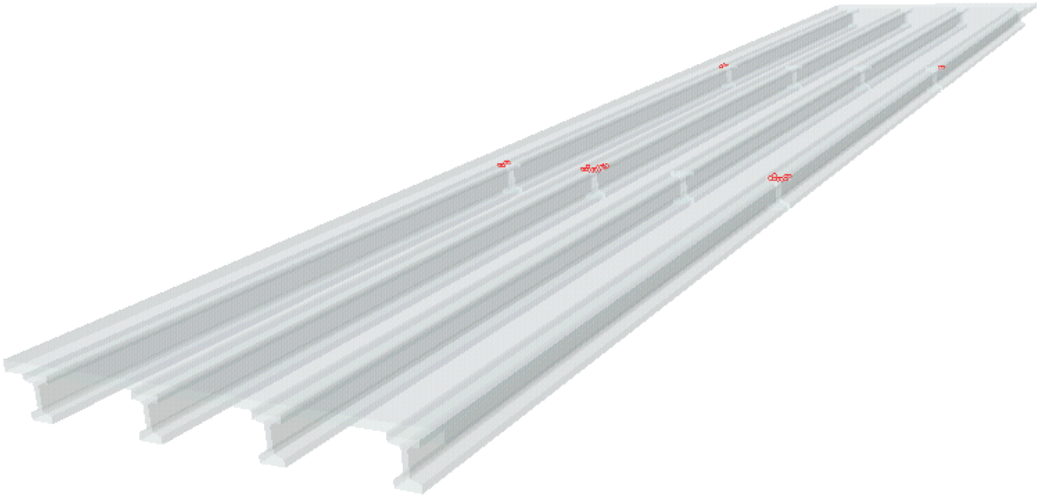

Figure 3.19: Girder Crack Pattern for Temperature Increase

There is negligible cracking in the bridge girders. As these girders are free to translate in the longitudinal direction (their interior ends are resting on bearing pads), there is relatively no induced tensile strain. The applied displacement boundary conditions have led to tension cracks at the locations of the bridge pier caps. Intuitively, crack accumulation here makes sense because the section is reduced at these locations because the girder ends are separated. The strain contours in the superstructure (longitudinal direction, ZZ) are shown in Figures 3.20 and 3.21.

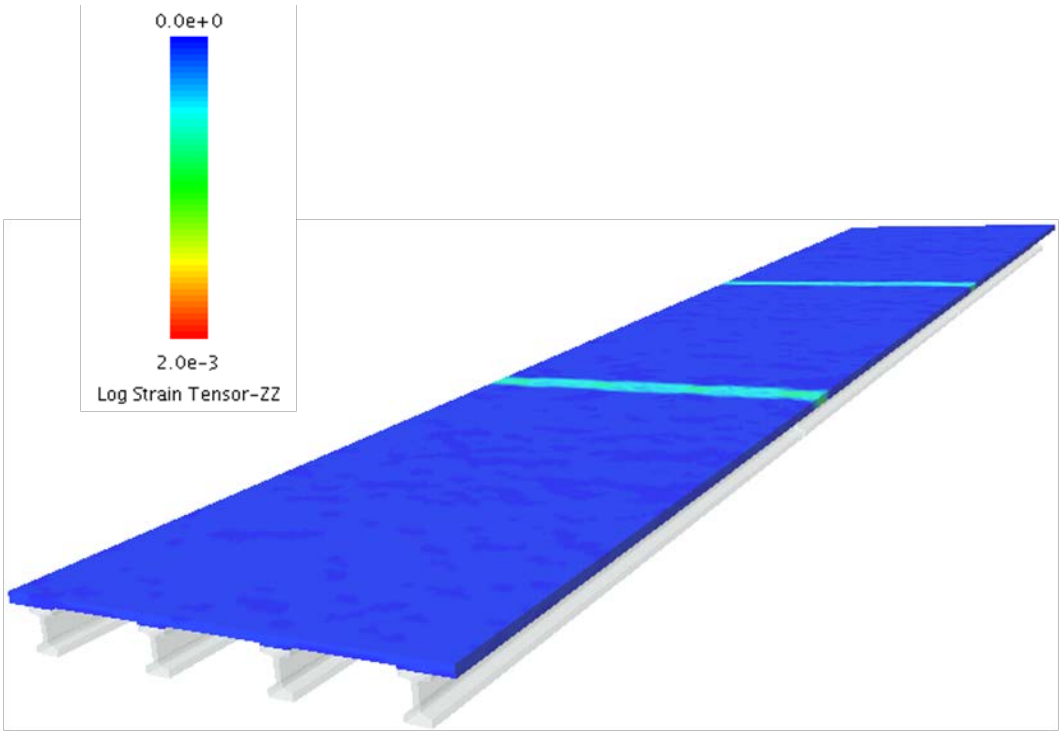

Figure 3.20: Strain Contours for Temperature Increase

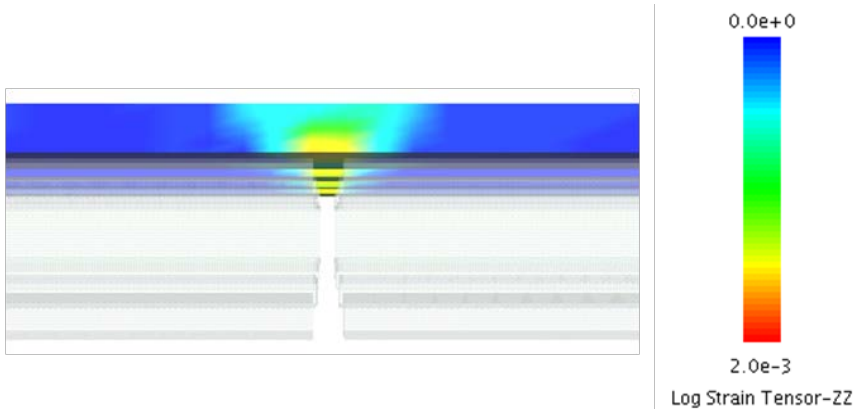

Figure 3.21: Strain Contours for Temperature Increase (Close-Up)

It is apparent that in the three spans of the superstructure, the tensile strain has not been reached. This is evident because there are no red markers in main spans and the strain contours show the tensile strain to be low. The crack pattern and strain contours illustrated in Figures 3.18-3.21 are conservative. The finite element model of

the deck is continuous and uniform across the gap between the bridge girders. In the field, a saw cut and a V-joint are used at the piers (see Figure 3.22).

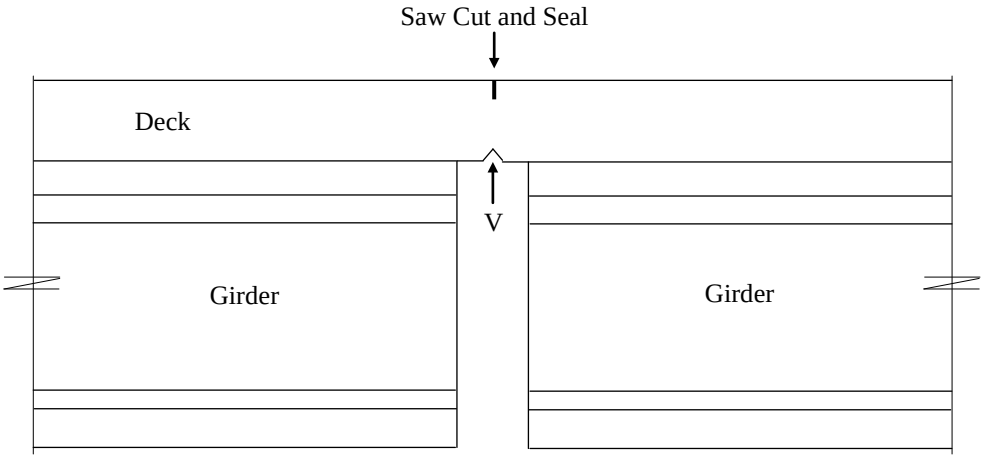

Figure 3.22: Deck Schematic at Pier Locations

Reducing the section even further with the joints will ensure that any cracking in the deck will occur under the saw cut and because it is sealed, there will be little trouble with degradation (water tightness, de-icing salts seeping into the deck). If the saw cut and V-joint were modeled in the TeraGrande analysis, the width of the crack pattern shown in Figure 3.18 would be trimmed. Considering the crack-free main spans of the bridge deck and conservative crack portrayal at the pier locations, it is concluded that the superstructure is not experiencing severe nonlinear behavior. However, this is only the case for the displacement-time history applied at the superstructure ends, which directly relates to an actual temperature change, in this case a temperature increase of 10°F. For a temperature increase of this magnitude (or less), the linear elements developed for TeraDysac should be satisfactory.

3.4.2 Temperature Decrease

A temperature drop at the bridge site was also investigated. In a two-week period in January 1998, the bridge temperature dropped by 8°F. The resulting abutment movements measured by the horizontal extensometers (1.6 mm) were applied to the superstructure end node sets (similar to the bridge heating analysis). Again, a pristine model was used. The stress contours (longitudinal, ZZ) are shown in Figures 3.23 and 3.24.

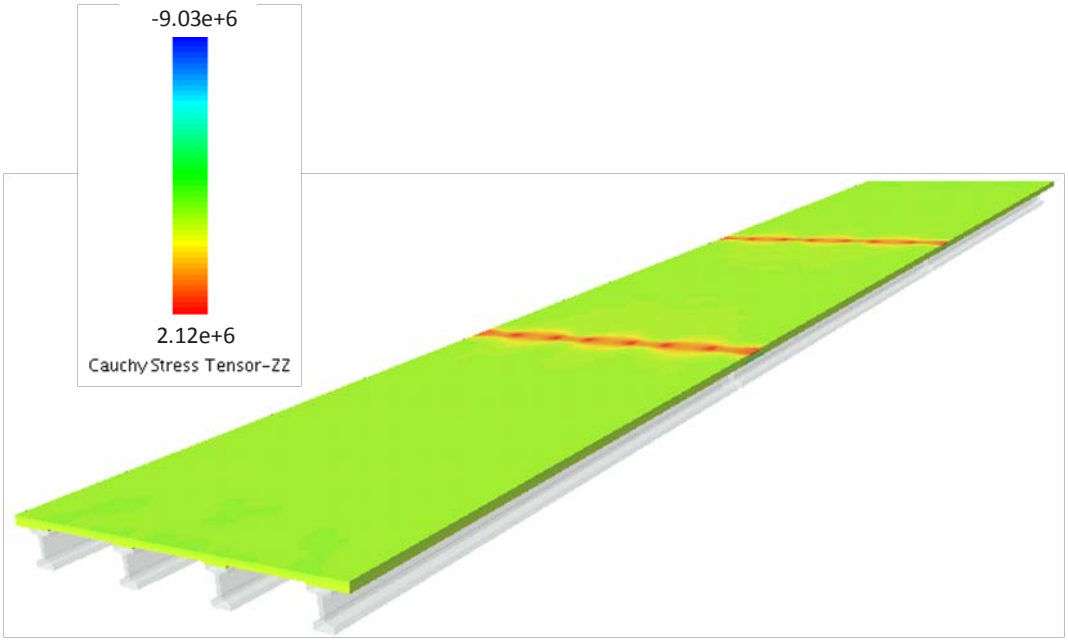

Figure 3.23: Bridge Deck Stress (Pa) Contours for Temperature Decrease

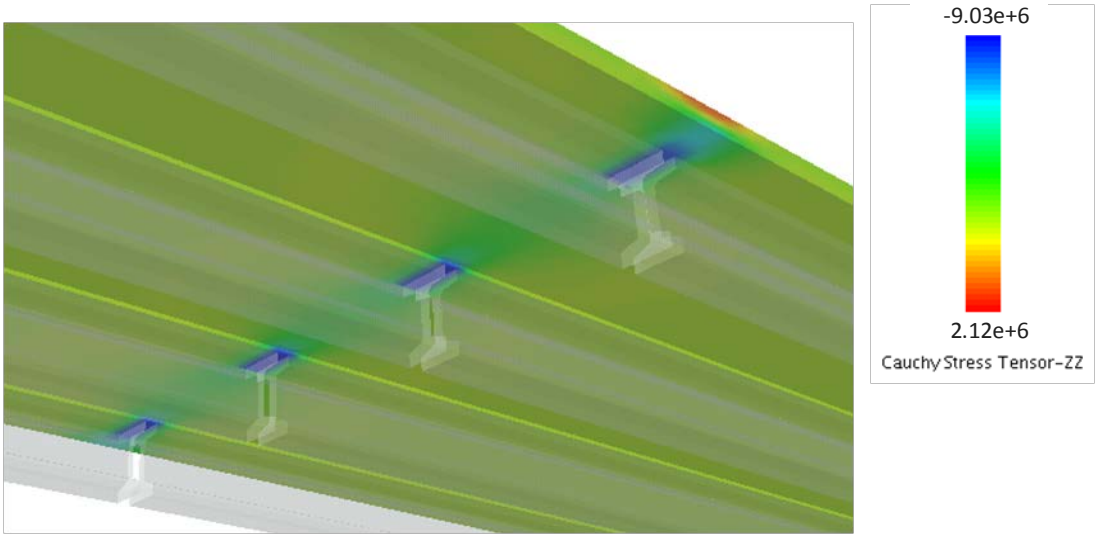

Figure 3.24: Stress (Pa) Contours Viewed from Beneath the Bridge

Again, the response is quite uniform in the main spans and there are some stress concentrations in the pier regions. Figure 3.24 shows a view from below the superstructure which reveals the highest regions of compression are on the bottom side of the deck between girder ends. A small tension zone exists on the top side of the deck in this region. This minor tension resulted in a crack pattern shown in Figure 3.25.

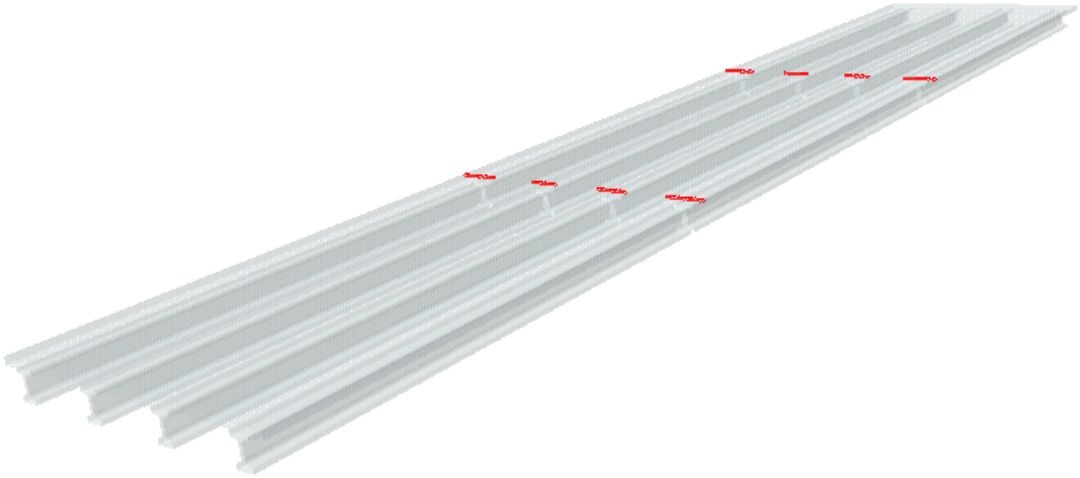

Figure 3.25: Deck Crack Pattern for Temperature Decrease

The compressive strength of the deck concrete (f_c') is 39.99 MPa (5800 psi). The ANATECH generated compressive stress-strain curve is given in Figure 3.26.

Added to the curve are two indicators: the ∇ marks the maximum compressive stress in the deck and the x marks the compressive stress in the deck as indicated by the lime coloring in Figures 3.23 and 3.24.

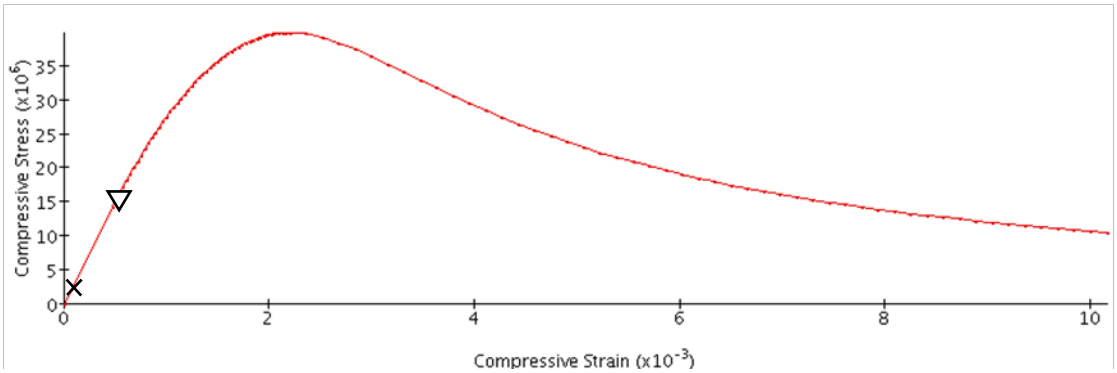

Figure 3.26: Deck Compressive Stress (Pa)-Strain Curve

Figure 3.26 illustrates that for the cooling modeled, the compressive stress in the deck does not enter the nonlinear range (i.e. it is consistent with the slope Young's modulus provides on the stress-strain curve). A majority of the compressive stress in the superstructure is quite small when compared with the compressive strength of the concrete. The compressive stress in the superstructure as indicated by the lime coloring is around 1.9 MPa (about 275 psi). Upon studying the stress-strain curve for the deck concrete and knowing the cooling-induced compressive stresses, it is concluded that the linear plate element developed in TeraDysac is acceptable to model the superstructure in this temperature range. For the temperature drop of 8°F to be modeled in TeraDysac, the developed linear elements should be satisfactory.

4 VALIDATION OF THE COMPUTER SIMULATION TOOL: TERADYSAC

4.1 PROBLEM DESCRIPTION

To validate the developed technology in TeraDysac, results from a project conducted at the University of Minnesota (Huang et al. 2004) were used. The published report provided a detailed description of the bridge site, soil testing results, and numerous instrumentation results. Bridge #55555, located in Rochester, Minnesota is a reinforced concrete IAB with prestressed girders and no skew angle. The details of the bridge are shown in Figures 4.1- 4.3.

Figure 4.1: Concrete IAB (Huang et al. 2004)

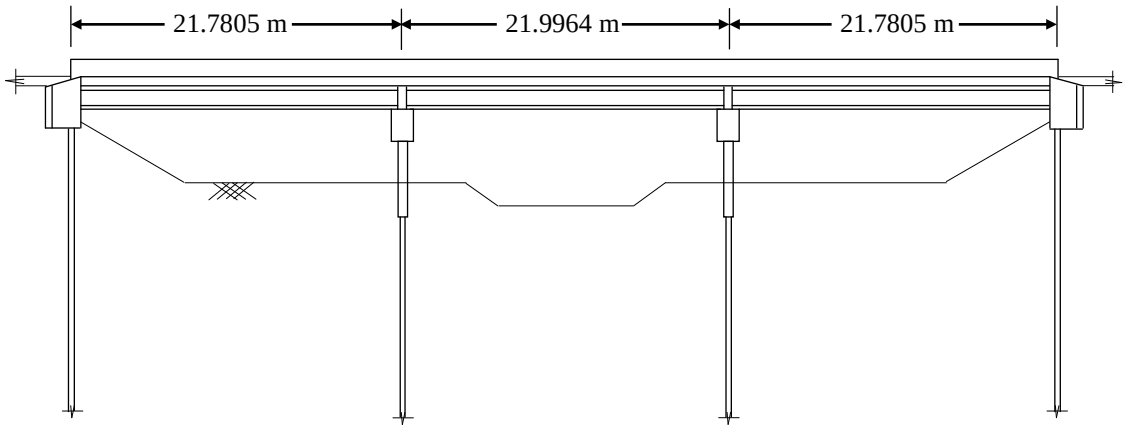

Figure 4.2: Elevation View of the Minnesota IAB

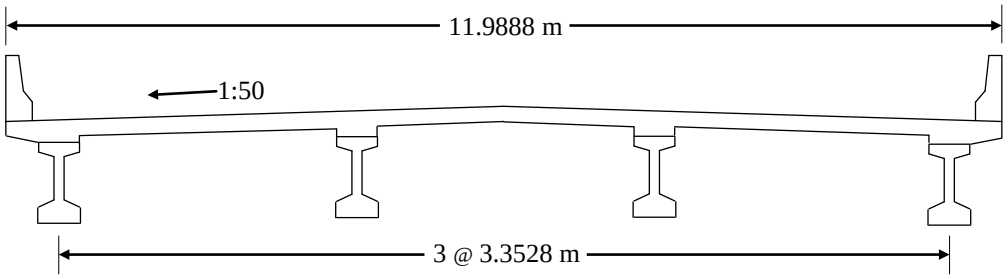

Figure 4.3: A Transverse Section (Through Deck) for the Minnesota IAB

The monitoring effort was carried out from bridge construction in 1996 to 2004. Report-furnished air temperature, abutment translation, abutment rotation, and abutment pile curvature from the year 1998 were used in the validation of the proposed modeling scheme. Results used in the analysis came from a weather station, horizontal extensometers, tiltmeters, and vibrating wire strain gages, respectively. The report also included the soil testing results from the bridge site which provided stratigraphy information and standard penetration test (SPT) results. A set of bridge plans was also obtained from the Minnesota Department of Transportation (Mn/DOT). The bridge is built over the Zumbro River in southeastern Minnesota. The water table is located about 4.5 m below the abutments, but the soils are assumed to be saturated in this work.

4.2 SOIL PROPERTIES

Two sets of analyses were carried out in 2D. The first assumes all of the soil is linear elastic. The second uses a combination of a bounding surface clay model and a sand model. In the 3D analyses (skewed vs. zero skew), only linear elastic soil properties are used. The soil exploration reported the blows per foot (BPF) from the SPT (N-value). For the linear elastic problems, only Young's modulus and Poisson's ratio are required. Poisson's ratio was set to 0.3 for all soils. Young's modulus was computed in accordance with the method described in the Naval Facilities Engineering Command design manual (NAVFAC 1986). With the exception of the two relatively thin clay layers at the site, the soils are loose and poorly graded sands. The method described in the design manual provides Young's modulus (E) as a function of N-value, where the units of E are tsf.

Table 4.1: Young's Modulus as a Function of N-Value (NAVFAC 1986)

Soil Type	E/N
Silts, sandy silts, slightly cohesive silt-sand mixtures	4
Clean, fine to medium sands and slightly silty sands	7
Coarse sands and sands with little gravel	10
Sandy gravels and gravel	12

Figure 4.4 shows the stratigraphy at the bridge site with the values of E/N used in the linear elastic analysis. In both the linear elastic and the bounding surface

analysis, pore pressure effects were captured by setting the value of the combined bulk modulus of soil grains and pore water (Γ) as 2.2 * 10^6 kPa.

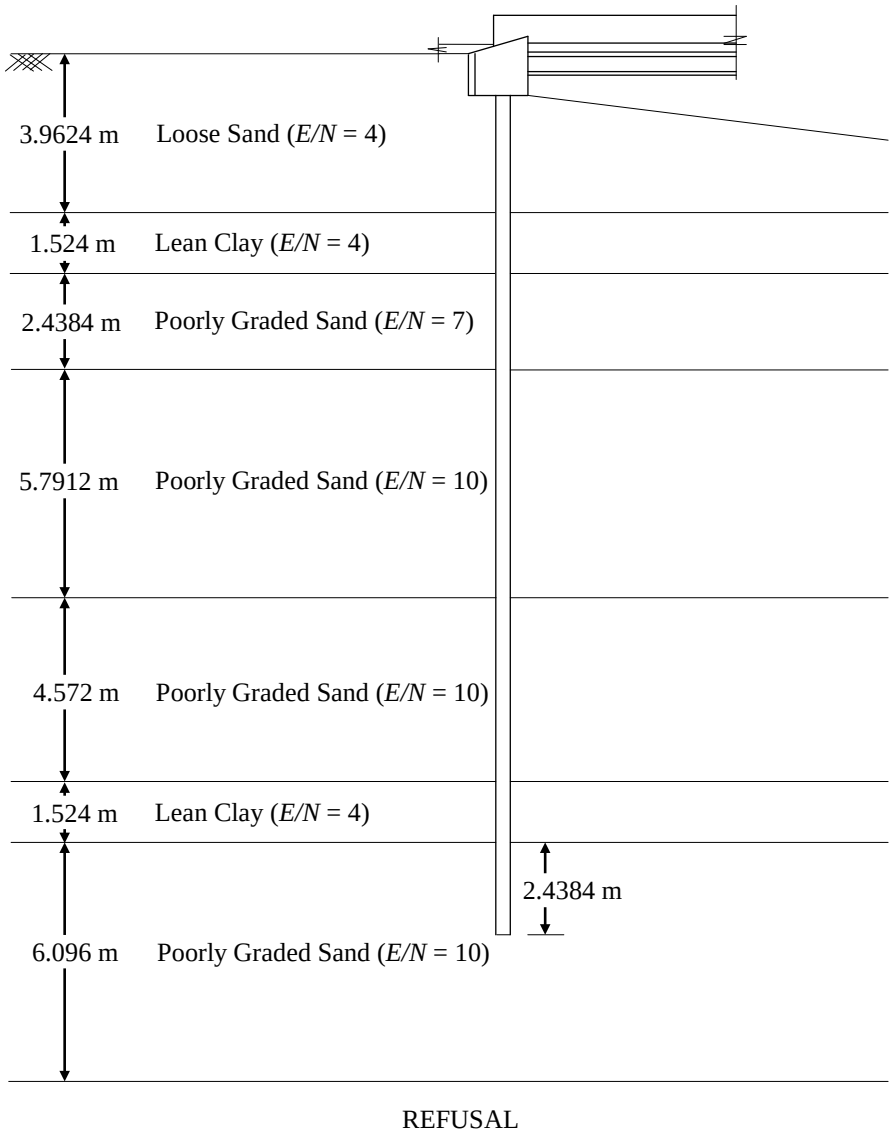

Figure 4.4: Soil Stratigraphy with Used E/N Ratios

4.3 STRUCTURAL PROPERTIES

The bridge deck, bridge girders, abutments, pier caps, and the pier piles above grade are all combinations of concrete and steel. The bridge deck, girders, abutments, and pier caps are made of reinforced concrete. The pier piles above grade and to a

depth of about 1.524 m below grade are encased in concrete and steel pipes. Because these components consist of two materials, a weighted average approach was used to obtain the material properties input for the beam and plate elements.

4.3.1 Weighted Average Example

The piles supporting the piers are HP 10 x 57 sections in strong-axis bending surrounded by concrete and steel shells (see Figure 4.5). At about 1.5 m below the ground surface, the concrete and shells end and only the piles continue to significant depth.

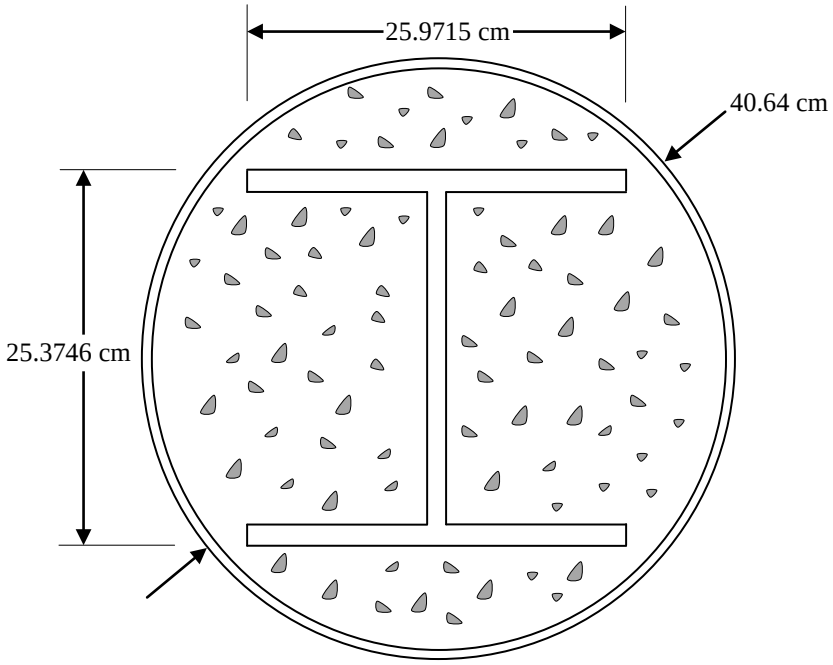

Figure 4.5: Cross-Section Pier Piles above Grade

The required beam element properties for the TeraDysac input include Young's modulus (E), Poisson's ratio (ν), area (A), strong axis moment of inertia (I_x), weak axis moment of inertia (I_y), and the coefficient of thermal expansion (α).

These properties were obtained as follows:

The modulus of concrete and the coefficients of thermal expansion for the steel and concrete at the site were reported in the Huang et al. (2004) study. The subscripts c, s, and t designate concrete, steel, and total respectively.

To calculated the composite properties, the following are used: $E_c = 30.3*10^6 kPa$, $E_s = 200*10^6 kPa$, $A_c = 1110.52cm^2$, $A_s = 186.65cm^2$, $\rho_c = 2.4Mg/m^3$, $\rho_s = 7.85Mg/m^3$, $\nu_c = 0.2$, $\nu_s = 0.3$, $\alpha_c = 6.15*10^{-6}/^0 F$, $\alpha_s = 6.7*10^{-6}/^0 F$. The bending stiffness EI is different in the strong and weak axis directions.

$$(EI)_x = (E_s I_{pile})_x + (E_s I_{shell})_x + (E_c I_c)_x = 88{,}150.75 kNm^2$$

$$(EI)_y = (E_s I_{pile})_y + (E_s I_{shell})_y + (E_c I_c)_y = 74{,}819.71 kNm^2$$

$$E_t = \frac{E_s A_s + E_c A_c}{A_t} = 54.72*10^6 kPa$$

$$I_x = \frac{(EI)_x}{E} = 0.00161 m^4$$

$$I_y = \frac{(EI)_y}{E} = 0.00137 m^4$$

The composite beam density, Poisson's ratio, and coefficient of thermal expansion were also found using this weighted average approach. The obtained values are:

$$\rho_t = 3.18 Mg/m^3$$

$$\nu_t = 0.214$$

$\alpha_t = 6.23 * 10^{-6} / ^0 F$

4.3.2 Set-Up for Plane Strain Analysis

The obtained properties described in the above example are input directly for the beams and plates in the 3D analyses. In the 2D analyses, another calculation is needed. The 2D version of TeraDysac uses plane strain theory for the soil elements. Across the width of the bridge, there are four girders and six piles at each abutment and bent. Because the soil is represented by a unit width, the section properties (A and I) for the girders and piles are spread over the bridge width. For example, the moment of inertia for an abutment pile was found to be 5.218 * 10^{-6} m^4. Across the bridge width, the six abutment piles combined have a total moment of inertia equal to 6 * 5.218 * 10^{-6} m^4 = 3.131 * 10^{-6} m^4. To find an approximate value of this moment of inertia over a unit width, the value is divided by the bridge width (3.131 * 10^{-6} m^4 / 11.9888 m = 2.611 * 10^{-5} m^4/m). In the 2D model, the 'Deck/Girder' element block (see Figures 4.11 and 4.12 and Table 4.2) is a weighted average combination of the roadway and the four girders which support it. The abutments are uniform across the bridge width, so the abutment section properties are based a unit width.

4.3.3 Set-Up for 3D Analysis

Significant reinforcement is used to connect the girders to the bridge deck. In the 3D bridge model, the girder elements are meshed directly into the deck via tied contact. The bent cap is also merged into the plane of the deck. This is not entirely accurate because the girder ends are sitting on elastomeric bearing pads which rest on the pier caps (see Figure 4.6). The diaphragms which connect the girder webs at midspan were neglected in the model. This work is concerned with the thermal response of the bridge,

especially behind the abutments so unnecessary elements were not modeled. The parapet wall (concrete railing) on either side of the roadway was also neglected. The railing is divided into roughly 6 m sections with cork deflection joints. This rail was deemed to only marginally influence the response of the bridge deck. The meshed superstructure is shown if Figure 4.7.

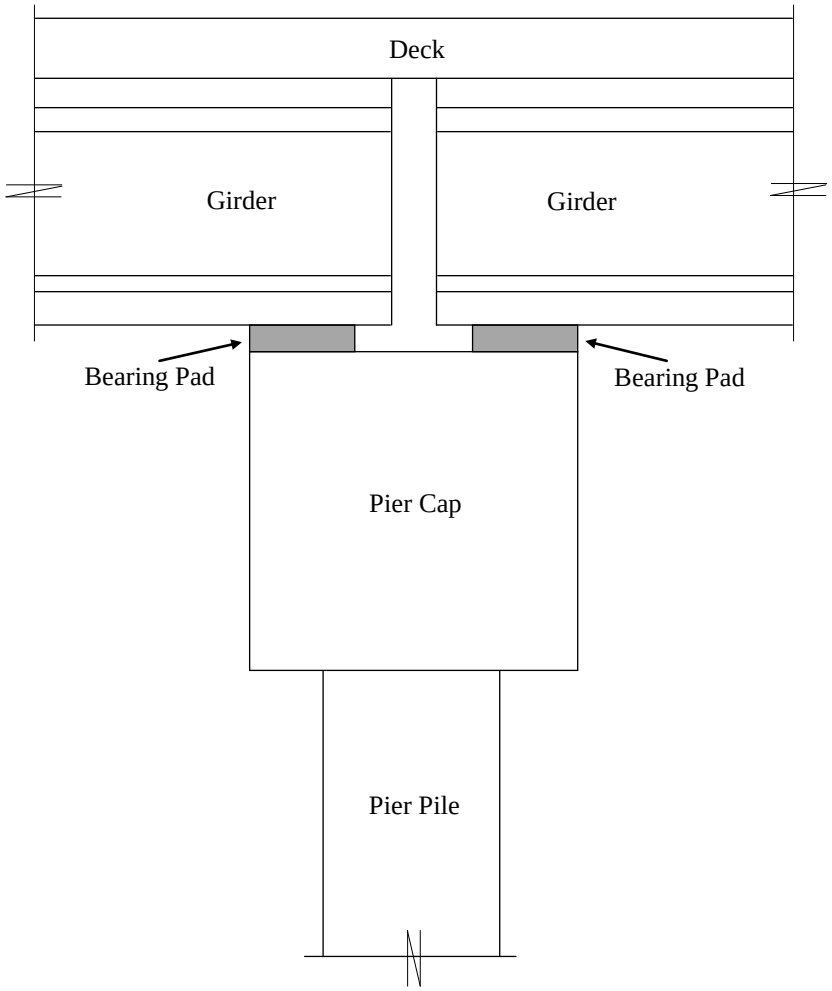

Figure 4.6: Bridge Details at Pier Locations

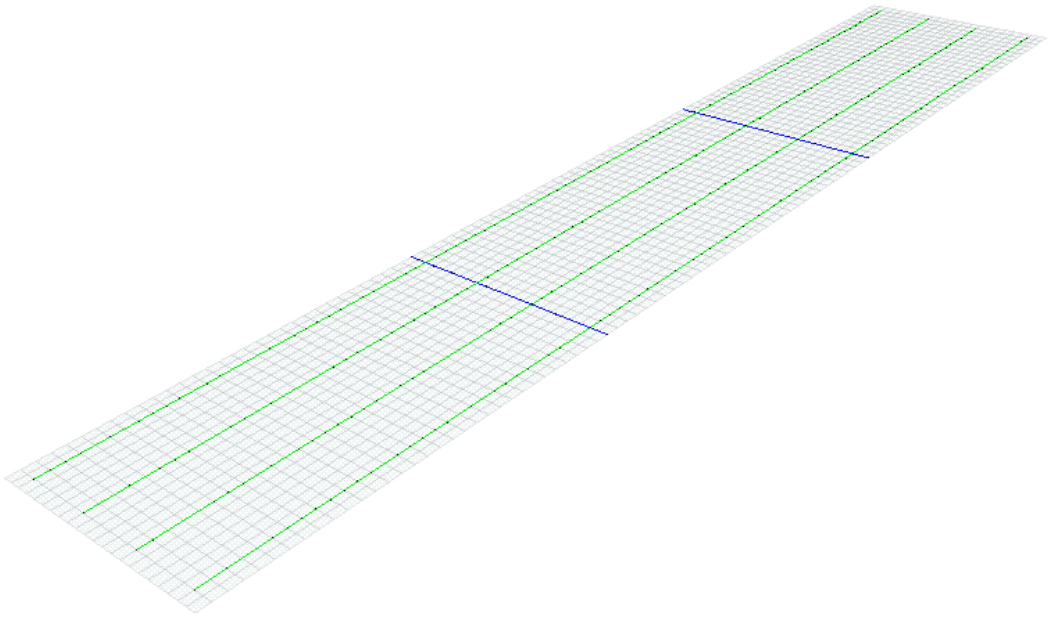

Figure 4.7: 3D TeraDysac Superstructure Model

In the above figure, the girders are colored in green and the bent caps are colored in blue. The three element blocks (deck, girders, and bent caps) are meshed together via tied contact.

4.4 APPLIED THERMAL LOADING

In the study conducted by Huang et al. (2004), thermocouples were installed in the superstructure cross-section to develop temperature profiles through the deck and girders. Figures 4.8 and 4.9 show the temperature profiles for a sunny summer day and a cloudy winter day, respectively. The figures were obtained from an electronic version of the Minnesota report (Huang et al. 2004).

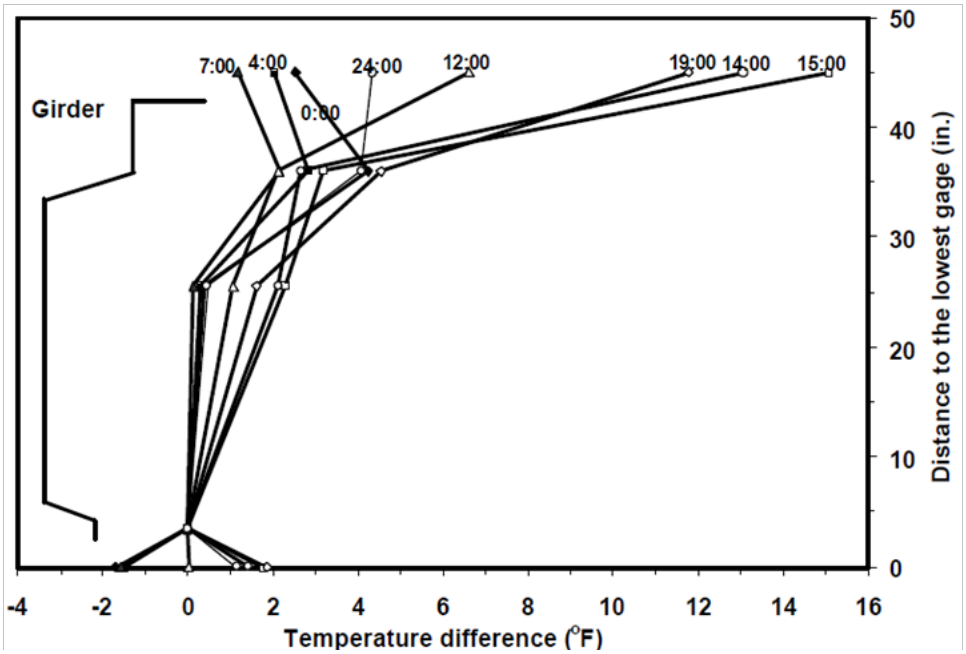

Figure 4.8: Temperature Gradient (Sunny Summer Day, After Huang et al. 2004)

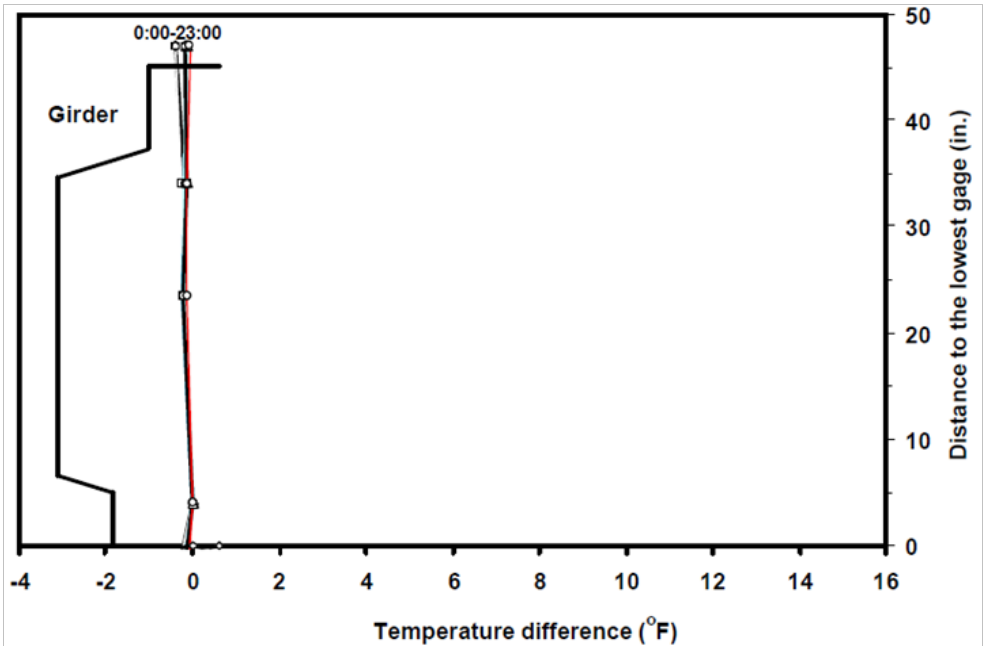

Figure 4.9: Temperature Gradient (Cloudy Winter Day, After Huang et al. 2004)

It is apparent that on sunny summer days there is an appreciable temperature difference through the superstructure, especially in the afternoon. Included in the instrumentation plan on the Minnesota bridge were pyranometers used to measure

solar radiation. On the two days in question (Figures 4.8 and 4.9), solar radiation was high in the afternoon on the summer day and relatively minimal throughout the winter day.

4.4.1 Validation Technique

For the results comparison, temperature loading was applied to the TeraDysac models and the abutment rotation, displacement, and pile curvature were compared to the instrumental data from the Minnesota report. Abutment movement was reported in two week intervals from horizontal rod extensometers during the year 1998. The bridge temperature, abutment rotation, and pile curvature were reported on a more frequent basis (every 6 hours) through the use of data loggers and a computer. A two-week period in June was selected for the temperature increase TeraDysac analysis and a two-week period in January was selected for the temperature decrease analysis.

In the summer analysis, a temperature gradient was applied through the superstructure. The bridge temperature change from the beginning to the end of the two weeks (10°F) was applied at the mid-depth of the composite superstructure. The exact temperature distribution during this time was not reported, so the gradient was estimated based on the observed temperature distribution during similar times of the year (see Figure 4.8). The temperature loading input to TeraDysac is shown in Figure 4.10.

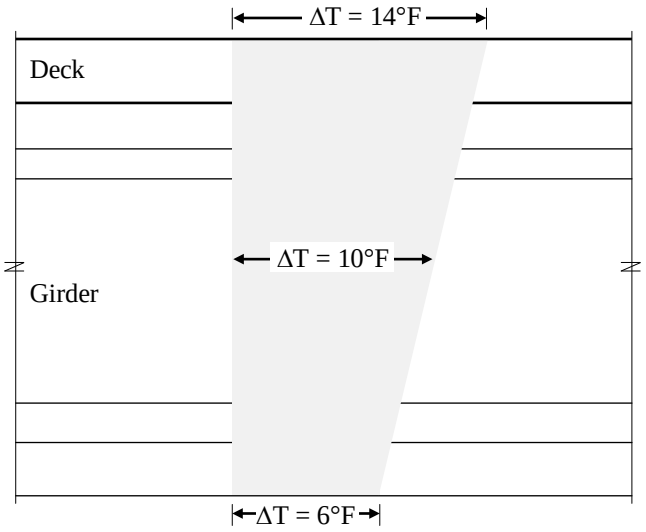

Figure 4.10: Superstructure Temperature Input (Heating)

In the temperature drop analysis, the bridge temperature change from the beginning to the end of the two weeks (8°F) was applied throughout the superstructure. Consistent with Figure 4.9, no thermal gradient was used. The thermal loading was ramped up over 1.0 s and then held to allow any oscillations in the solution to level off. Note that the obtained pore water pressure contours presented for the subsequent analyses are a function of the load duration. As a two-week event is simulated over 1.0 s of problem time, the obtained pore water pressures may not reflect field values. The ability to track pore water pressure generation is a nice feature of TeraDysac and the results are presented to provide insight into what soil regions may experience gains or losses in pore water pressure during the simulated event. The obtained abutment displacement, abutment rotation, and pile curvature from the TeraDysac analysis were compared with the respective values incurred over the two weeks of analysis.

4.5 LINEAR ELASTIC ANALYSIS

The first analysis performed on the bridge model uses the calculated Young's modulus values in a linear elastic saturated soil model. Several analyses were used to ensure the mesh has a minimum size (spatially) with minimal effect from the soil boundaries. The finite element model is shown in Figure 4.11. There are 316 line elements (structure) and 7302 quadrilateral elements (soil) in the mesh.

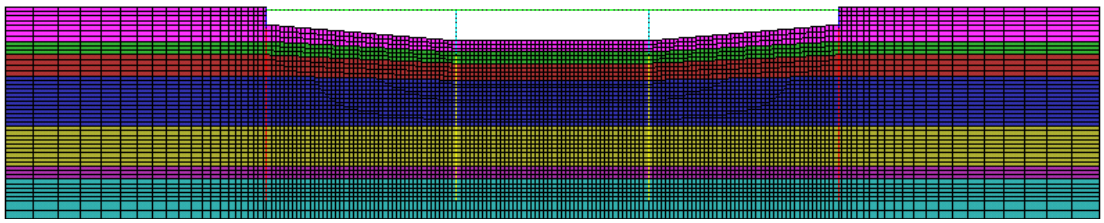

Figure 4.11: 2D IAB Finite Element Model

A gradient is applied away from the abutments on each side to reduce the model size without sacrificing accuracy near the bridge. Figure 4.12 shows a zoomed in view of the bridge with the various element blocks colored.

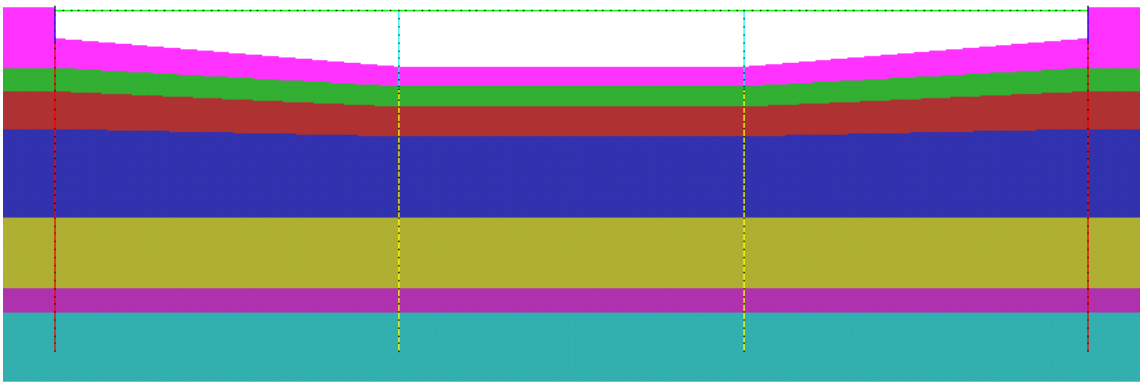

Figure 4.12: Element Block View

The various colors in Figures 4.11 and 4.12 represent the element blocks given in Tables 4.2 and 4.3.

Table 4.2: Soil Element Block by Color

Color	*Element Block*
Pink	Fill / Loose Sand
Green	Lean Clay
Maroon	Poorly Graded Sand
Blue	Poorly Graded Sand
Gold	Poorly Graded Sand
Purple	Lean Clay
Turquoise	Poorly Graded Sand

Table 4.3: Structure Element Block by Color

Color	*Element Block*
Green	Deck/Girder
Blue	Abutment
Red	Abutment Pile
Aqua	Pier Piles (Above Grade)
Yellow	Pier Piles (Below Grade)

The various poorly graded sand layers are differentiated by locations where the SPT values changed significantly in the soil exploration. The nodal equivalence scheme allows for two nodes at the same location to be merged together. The deck is merged into the abutment and the pile sections change at locations away from soil nodes (see Figure 4.13).

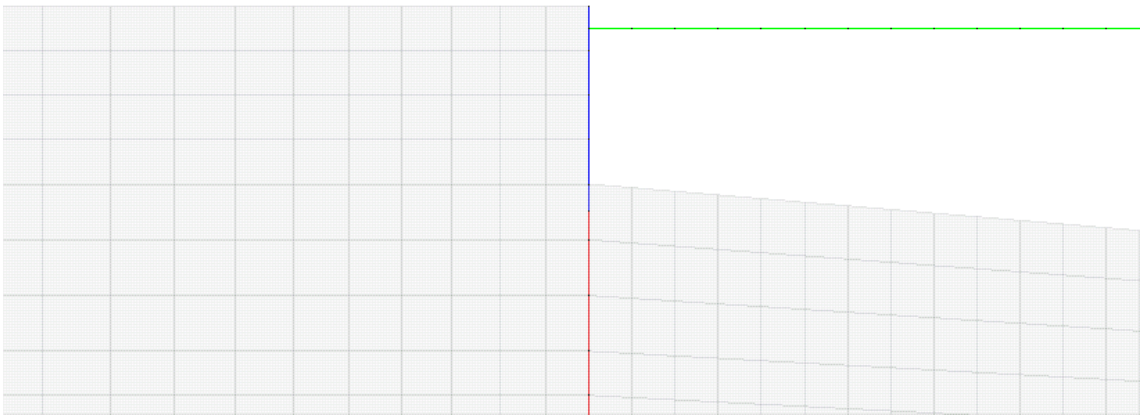

Figure 4.13: Structure Assembly at Abutment

The entire soil stratum is assumed to be saturated. The applied boundary conditions for the model include fixing the solid and fluid displacement in both the horizontal and vertical directions on the bottom soil nodes and in the horizontal direction only on the side soil nodes. Figure 4.14 highlights the boundary nodes.

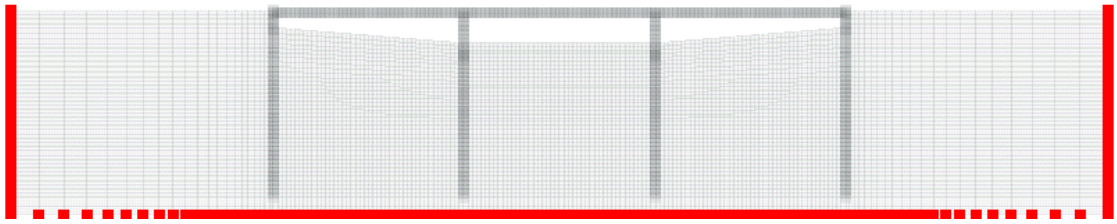

Figure 4.14: Boundary Nodes for 2D Analysis

4.5.1 Temperature Increase

The first linear elastic analysis considers the temperature rise measured during a two-week period in the summer of 1998. Figure 4.15 shows the deformed shape of the bridge (magnified by 100).

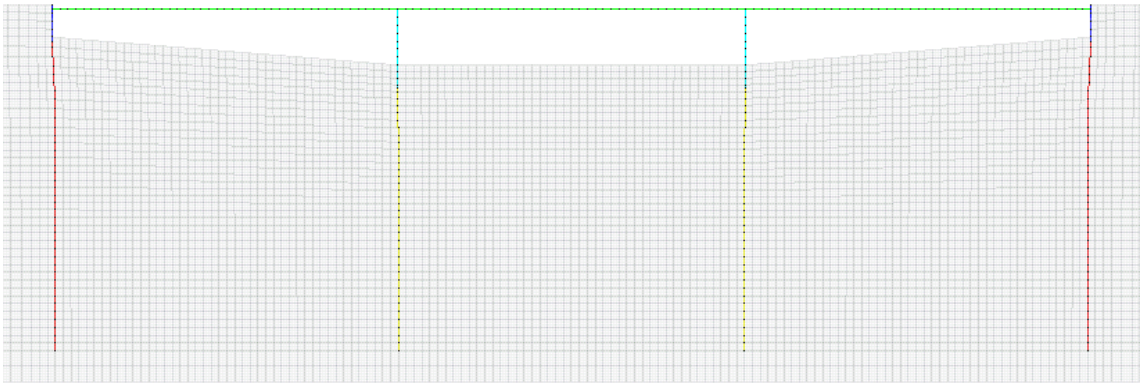

Figure 4.15: IAB Deformed Shape for Temperature Increase

A more accurate depiction of the abutment and abutment pile deformation is presented in Figure 4.16. During the two weeks of temperature variation at the IAB site, the horizontal extensometers revealed an abutment movement of about 2 mm. Figure 4.16 shows the TeraDysac displacement results to be in good agreement this value.

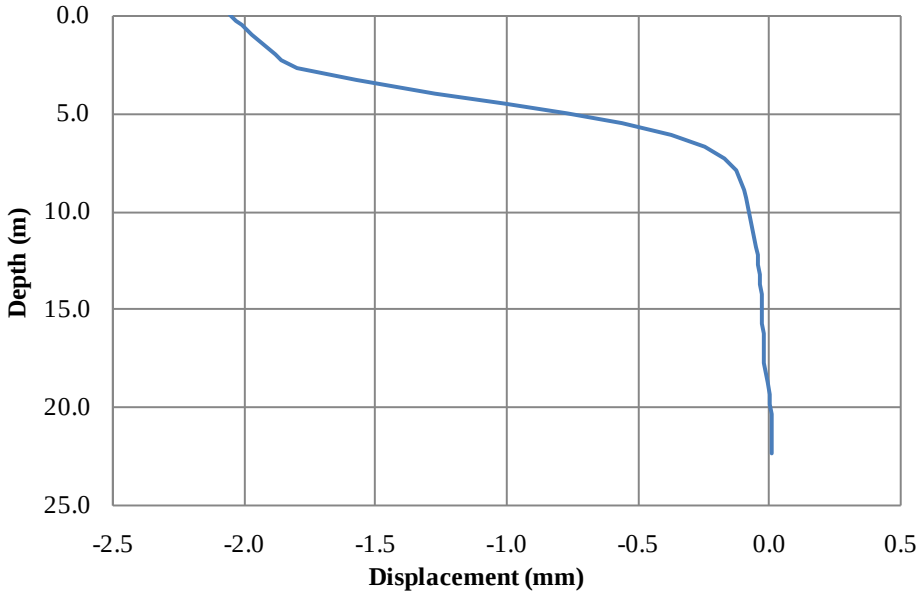

Figure 4.16: Abutment and Abutment Pile Displacement for Temperature Increase

The transition from the abutment to the abutment pile occurs at a depth of 2.35 m. The abutment is moving as a rigid unit. Knowing the length of the bridge deck in the model, the coefficient of thermal expansion, and the applied temperature change, a free

expansion calculation revealed an abutment displacement of about 2 mm. It is apparent the relatively high stiffness of the composite superstructure (deck and girder) to the soil stiffness allows the abutment movement to approach a free expansion. A free expansion would lead to a stress-free superstructure and a fully restrained loading (zero abutment movement) would lead to maximum thermal superstructure stresses, with the field behavior residing somewhere in between the two. As the field response is much closer to a free expansion, the thermal superstructure stresses are low.

In addition to the abutment displacement, abutment rotation was checked against tiltmeter-measured abutment rotation in the field. The abutment rotated away from the river by 0.014° over the two week period. Because the abutment is comprised of beam elements, there is a nodal rotation output for each node. The values of nodal rotation for the seven abutment nodes ranged from 0.0046° to 0.0050°. As Figure 4.16 illustrates, there appears to be no significant bending in the abutment (it rotated as a unit), so these rotation values are expected to be very close. Another approach to obtain the abutment rotation is to treat the abutment as a straight line that has deviated from vertical by some angle. This angle, which can be easily calculated, is the abutment rotation. Using the top and the bottom of the abutment as the line endpoints, the calculated abutment rotation is 0.0048°.

The Minnesota study also reported the abutment pile curvatures. After the piles were driven, arc-weldable strain gages were installed at depths of 15 cm and 91 cm below the bottom of the abutment. The bending moment value for each abutment pile node was obtained in the analysis. Using Equation 4.1, the pile curvature at various locations can be calculated.

$$\frac{M}{\phi} = EI \tag{4.1}$$

The reported pile curvature change over the two weeks was $866 \frac{\mu\varepsilon}{m}$. Using Equation 4.1, the curvature immediately below the abutment was found to be $552 \frac{\mu\varepsilon}{m}$. Considering the assumptions made (linear elastic soil and structure) and techniques used (weighted average approach for structural properties, SPT values to obtain Young's modulus), the results from the linear elastic analysis are encouraging. The obtained abutment translations agree with the field values. The abutment rotation and abutment pile curvature are both under-estimated.

In addition to the results already discussed, one of the main advantages of using TeraDysac is that the pore water pressure development during loading can be captured. Figure 4.17 shows the pore pressure contours at the end of the analysis run. As the bridge deck is heated, it expands pushing the abutments into the backfill soil. This loading creates a positive pore pressure buildup in the backfill soils. On the interior sides of the abutments, negative pore pressure has developed. This stems from the tied contact between the soil and structure elements. The pore pressure variations are small, with range of only about 0.9 kPa.

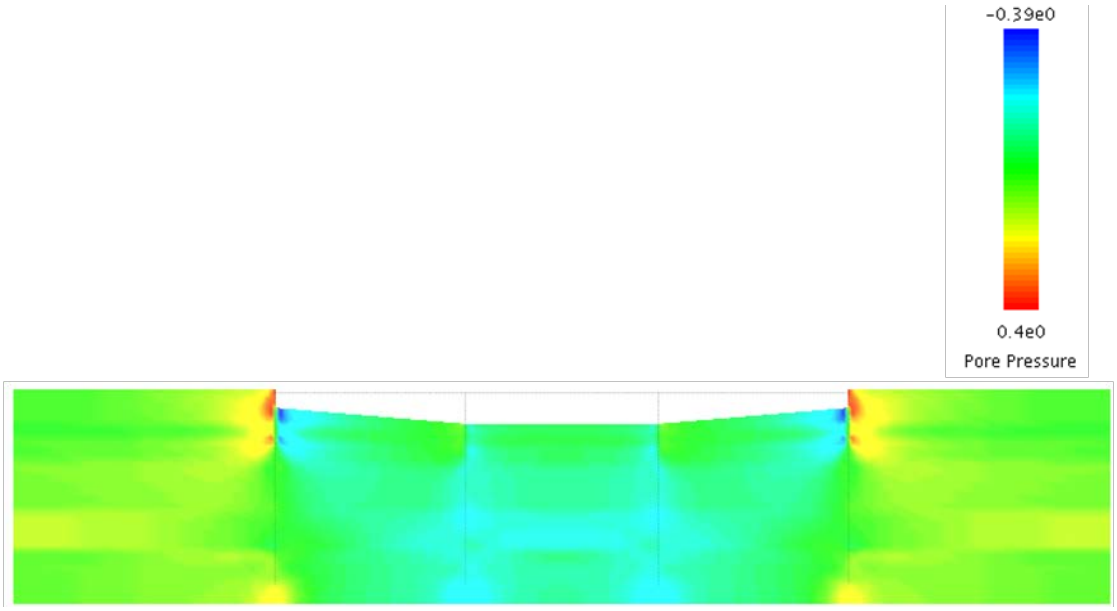

Figure 4.17: Developed Pore Water Pressure (kPa) During Temperature Increase

4.5.2 Temperature Decrease

The second linear elastic analysis considered the bridge temperature drop measured during a two-week period in the winter of 1998. Figure 4.18 shows the deformed shape of the bridge (magnified by 100).

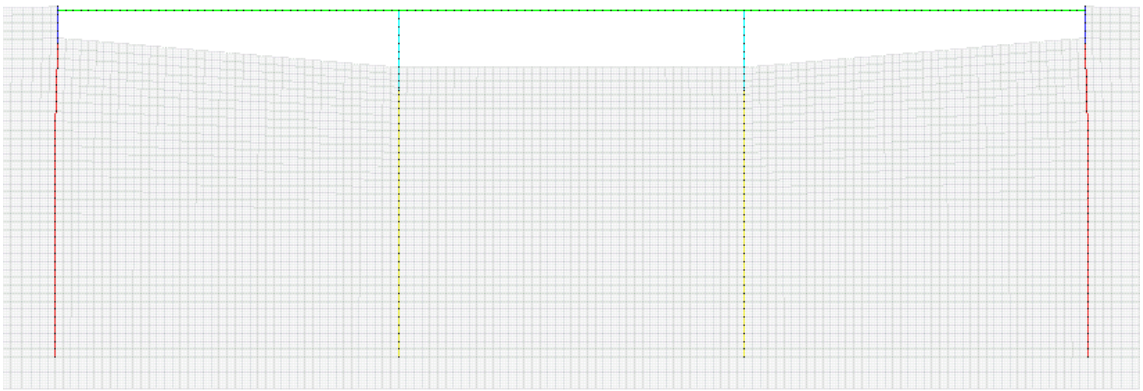

Figure 4.18: IAB Deformed Shape for Temperature Decrease

A more accurate depiction of the abutment and abutment pile deformation is presented in Figure 4.19. During the two weeks of temperature variation at the IAB site,

the horizontal extensometers revealed an abutment movement of about 1.6 mm. Figure 4.19 shows the TeraDysac displacement results to be in good agreement this value.

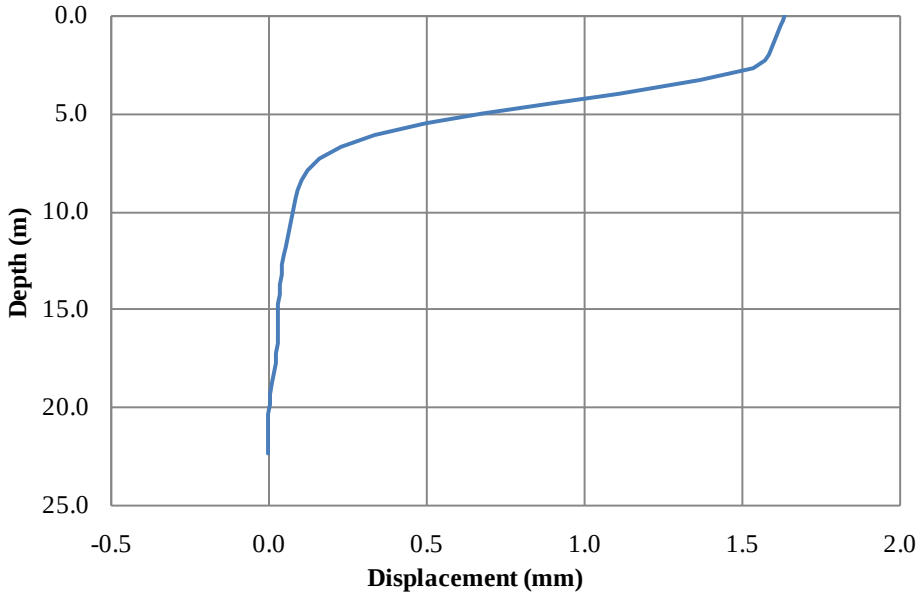

Figure 4.19: Abutment and Abutment Pile Displacement for Temperature Decrease

In addition to the abutment displacement, abutment rotation was checked against tiltmeter-measured abutment rotation in the field. The abutment rotated toward the river by about 0.01° over the two week period. As Figure 4.19 illustrates there appears to be no significant bending in the abutment (it rotated as a unit). The abutment rotation using the top and the bottom of the abutment as the endpoints of straight line, the calculated abutment rotation is 0.0015°. The reported pile curvature change over the two weeks was $709\frac{\mu\varepsilon}{m}$. Using Equation 4.1, the curvature immediately below the abutment was found to be $515\frac{\mu\varepsilon}{m}$. Again, the linear elastic analysis results are encouraging. The obtained abutment translations agree with the field values. The abutment rotation is still under-estimated, but the calculated pile curvature is closer to

the measured curvature than in the heating analysis. This could be attributable to the uncertainty in the gradient applied in the heating analysis. Gradients are low in the winter (for this analysis, no gradient was used) so the uncertainty is reduced.

Figure 4.20 shows the pore pressure contours at the end of the analysis. As the bridge deck is cooled, it contracts pulling the abutments toward the river. This loading creates a negative pore pressure buildup in the backfill soils and positive pore pressure on the interior sides of the abutments.

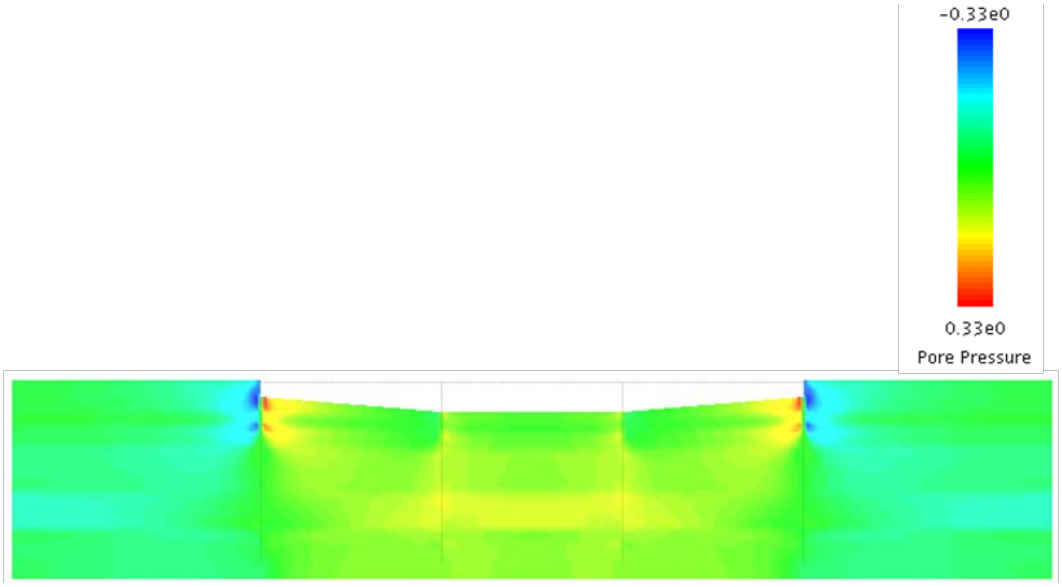

Figure 4.20: Developed Pore Water Pressure (kPa) During Temperature Decrease

4.6 ELASTOPLASTIC ANALYSIS

4.6.1 Bounding Surface Properties

The soil stratum at the bridge site consists of two relatively thin layers of soft clay, but is mostly comprised of loose and poorly graded sands (see Figures 4.4 and 4.12). The soil exploration revealed the soil classification and the SPT N-values. Lab testing of the site soils would have provided more detailed information and made

determining the bounding surface model parameters easier. But as this was not the case, some engineering judgment was used to determine what bounding surface properties to input for the data model. The clay at the bridge site was soft based on low N-values. The parameters for Speswhite Kaolin, a soft clay with calibrated parameters (see Muraleetharan et al. 1994 and Table 4.3) were used in the finite element model. The N-values in the sand layers were used to determine the relative densities using the method outlined in Tokimatsu and Seed (1986). The calibrated bounding surface properties for Nevada Sand with relative densities of 40 and 60% are available (see Muraleetharan 1995). The sand at the bridge site was assumed to be Nevada Sand and the bounding surface properties for the respective layers were set based on the relative densities for the sand layers at the bridge site. Bounding surface model parameters for the denser sand layers (D_r = 82% and 84%) were estimated based on the calibrated values of Nevada Sand (D_r = 40% and 60%). Figure 4.21 shows the soil stratum with the obtained relative densities for the sand layers. The OCRs used in the analysis for the clay layers are also shown. The OCR sets the initial bounding surface size which controls the soil response. A higher OCR corresponds to a stiffer clay. The top clay layer was softer than the layer at depth, so it was assumed to be slightly less over-consolidated than the deep layer.

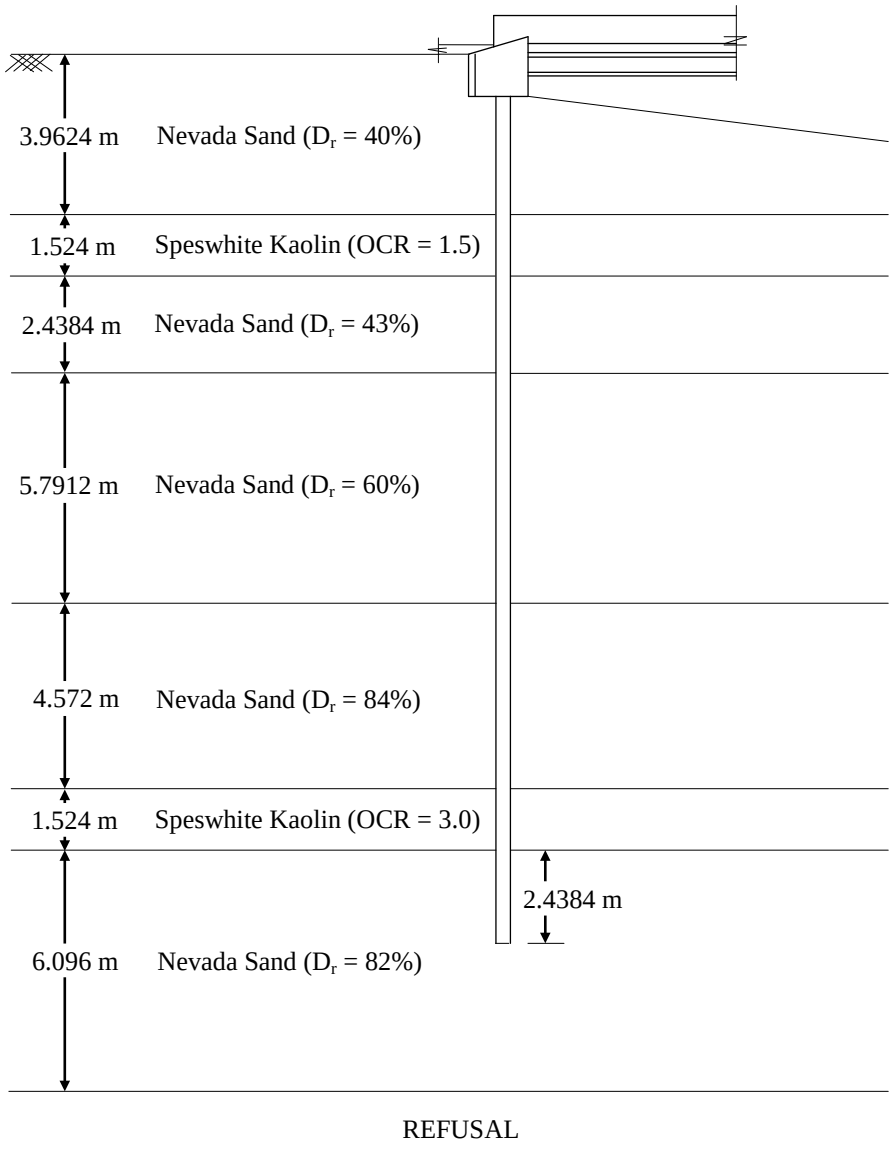

Figure 4.21: Assumed Soil Profile at the Bridge Site for Elastoplastic Analysis

The five sand layers break into three distinct groups with relative densities near 40, 60, and 80%. The calibrated bounding surface properties for 40 and 60% relative density were used directly and the values for 80% relative density were estimated. The bounding surface properties for the sand layers are given in Table 4.4.

Table 4.4: Bounding Surface Model Parameters for Speswhite Kaolin

Property		Value
Liquid limit		69%
Plasticity index		31%
Specific gravity		2.62
Permeability (m/s)		$1.7*10^{-9}$
Traditional Model Parameters		
Slope of isotropic consolidation line on $e - \ln p'$ plot	λ	0.25
Slope of elastic rebound line on $e - \ln p'$ plot	κ	0.05
Slope of critical state line in $q - p'$ space (compression)	M_C	0.88
Ratio of extension to compression value of M	M_e / M_C	1.0
Poisson's ratio	ν	0.3
Bounding Surface Configuration Parameters		
Value of parameter defining ellipse 1 in compression	R_C	2.4
Value of parameter defining the hyperbola in compression	A_C	0.01
Parameter defining ellipse 2 (the tension zone)	T	0.01
Projection center parameter	C	0.0
Elastic nucleus parameter	S	1.0
Ratio of triaxial extension to triaxial compression value of A	A_e / A_c	1.2
Hardening Parameters		
Shape hardening parameter in triaxial compression	h_C	3.0
Ratio of triaxial extension to triaxial compression value of h	h_e / h_c	1.0

Property		Value
Shape hardening parameter on the I -axis	h_2	2.0

Notes:

e = void ratio, $p' = (\sigma_1' + 2\sigma_3')/3$, $q' = \sigma_1' - \sigma_3'$

Table 4.5: Bounding Surface Properties for Sand Layers

Property		Nevada Sand (D_r = 40%)	Nevada Sand (D_r = 60%)	Nevada Sand (D_r = 80%)
Traditional Model Parameters				
Slope of isotropic consolidation line on $e - \ln p'$ plot	λ	0.017	0.009	0.007
Slope of elastic rebound line on $e - \ln p'$ plot	κ	0.003	0.002	0.0014
Bounding Surface Configuration Parameters				
Slope of line OA (Fig. 3) in $q - p'$ space (compression)	M_C	0.89	0.89	0.89
Ratio of extension to compression value of M	M_e / M_C	0.61	0.61	0.61
Value of R in triaxial compression	R_C	1.5	1.5	1.5
Related to gradient of ellipse 2 on I -axis	α	5.0	5.0	5.0
Parameter defining the initial size of the bounding surface	I_o / I	1.5	1.5	2.5

Property		Nevada Sand (D_r = 40%)	Nevada Sand (D_r = 60%)	Nevada Sand (D_r = 80%)
Plastic Potential Surface Configuration Parameter				
Slope of critical state line (compression) in $q - p'$ space	$(M_u)_c$	1.33	1.44	1.55
Hardening Parameters During Loading				
Shape hardening parameter in triaxial compression	h_C	2.0	2.0	2.0
Ratio of triaxial extension to triaxial compression value of h	h_e / h_c	0.05	0.05	0.05
Deviatoric hardening parameter	β_1	0.5	0.4	0.4
Hardening Parameters During Unloading				
Unloading hardening parameter	H_u	0.2	0.2	0.2

Notes:

e = void ratio, $p' = (\sigma_1' + 2\sigma_3')/3$,
$q' = \sigma_1' - \sigma_3'$

The initial stress state is important when using the bounding surface models. The initial stress state provides the starting location inside the bounding surface. Assuming a saturated soil stratum and using the soil unit weights, the initial stress state was calculated by hand. After the mesh was created, the mid-element depths were used to find the effective stresses. A K_0 value of 0.5 was assumed. Figure 4.22 shows the initial effective stress in the vertical direction.

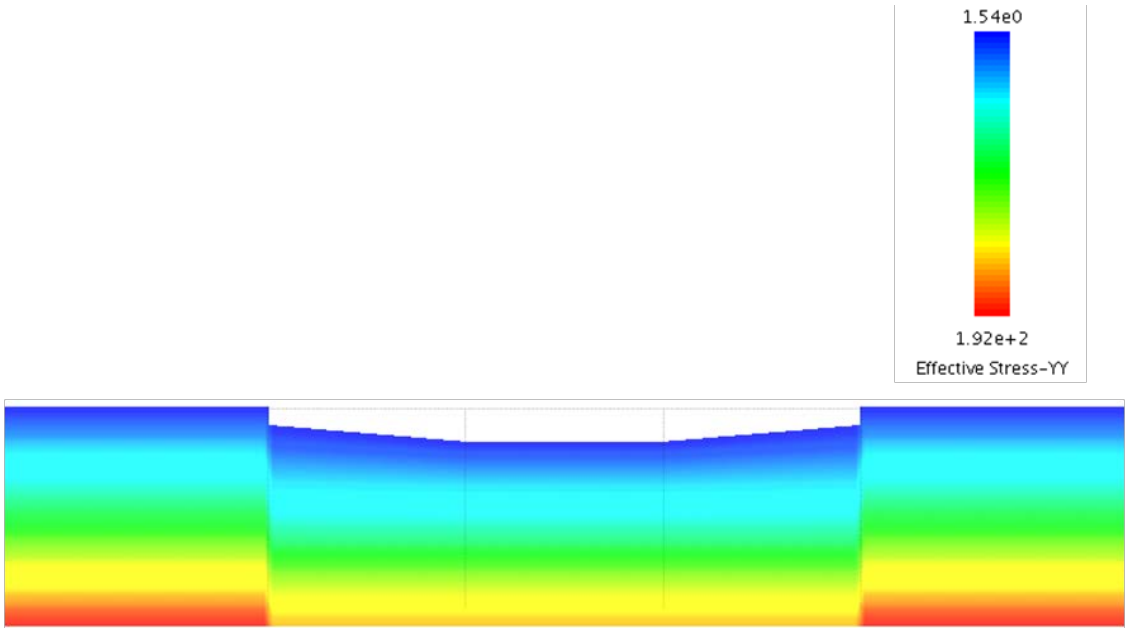

Figure 4.22: Initial Stress State (kPa) for Elastoplastic Analysis

4.6.2 Temperature Increase

The temperature increase was also applied to the bounding surface model. A comparison between the abutment and abutment pile deformations in the two analyses (linear elastic and bounding surface soils) is given in Figure 4.23. The abutment translation in the two analyses is nearly the same. The superstructure is very stiff compared to the backfill soil, and when thermally loaded it is almost behaving as it would in a free expansion. The more important behavior to study in Figure 4.23 is the abutment rotation and the pile response. Knowing the soil stratigraphy (see Figure 4.21), the results from the bounding surface model agree with expected pile behavior at depth. The clay layer (highlighted in Figure 4.23) is located between depths of 3.96 m and 5.49 m, with sand on either side. As the pile transitions from the soft clay layer to the sand layer, one would expect the pile deformation to markedly decrease. This is the case in the bounding surface model, but in the linear elastic model, the transition is not distinguishable.

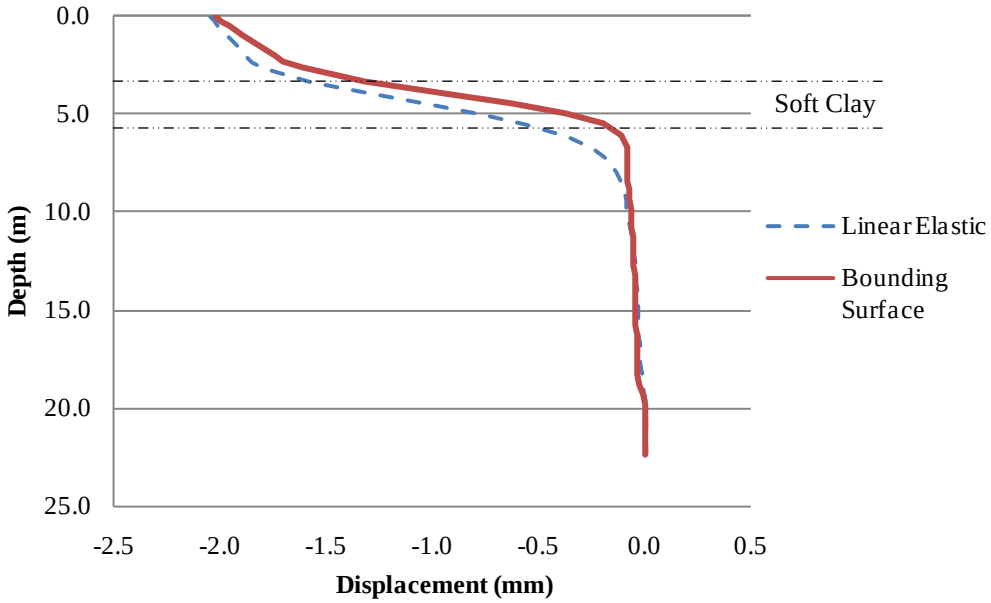

Figure 4.23: Abutment and Abutment Pile Deformation Comparison

The abutment displacements from both the linear elastic and bounding surface analysis are essentially the same. The superstructure in both cases was found to almost have a free expansion. The values of abutment rotation and pile curvature under the abutment were provided by the instrumentation study (Huang et al. 2004). The error magnitudes of the respective analyses are given in Table 4.5.

Table 4.6: Results and Error Estimates for Heating Analysis

Deformation Measure	True	Linear Elastic	% Error	Bounding Surface	% Error
Rotation (°)	0.014	0.0048	65.7	0.0079	43.6
Pile Curvature ($\frac{\mu\varepsilon}{m}$)	866	552	36.3	784	9.5

The error calculations show the bounding surface analysis to be more accurate. The pore pressure developed during the loading is shown in Figure 4.24. The

noticeable band of pore pressure is the clay layer. Part of the pore pressure developed in this layer is from the specified K_0 condition and OCR. The specified OCR (1.5) in this layer forms a relatively small initial bounding surface and as the initial stress state is brought into the bounding surface there is pore water pressure development. In the deep clay layer (OCR = 3), the pore pressure development is not nearly as defined as in the top layer.

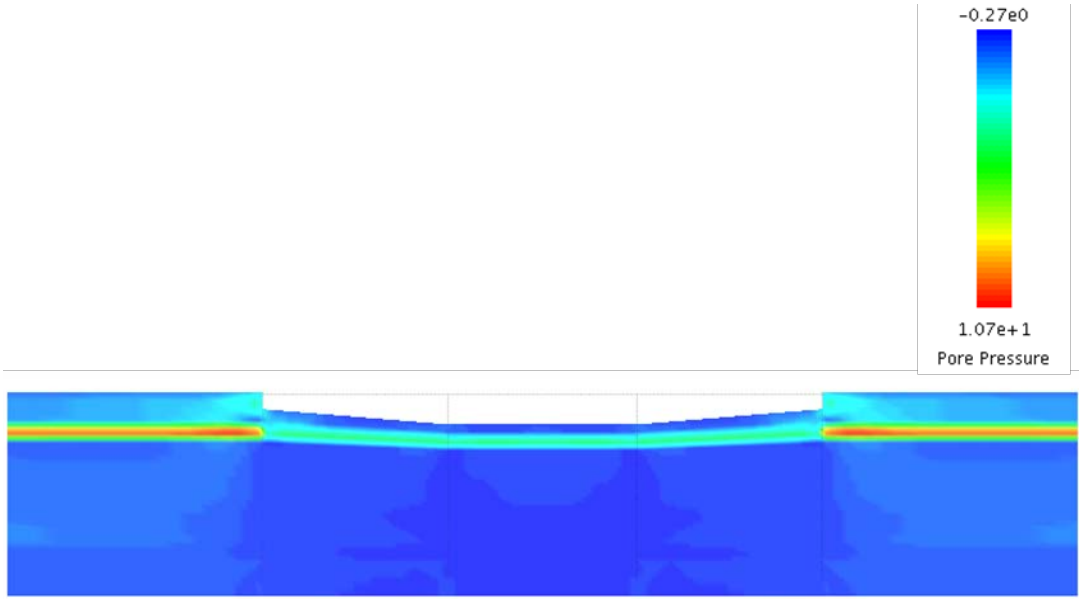

Figure 4.24: Bounding Surface Pore Pressure Development (kPa)

4.6.3 Temperature Decrease

The temperature decrease was also applied to the bounding surface model. A comparison between the abutment and abutment pile deformations in the two analyses (linear elastic and bounding surface soils) is given in Figure 4.25. Again, the abutment translation in the two analyses is nearly the same.

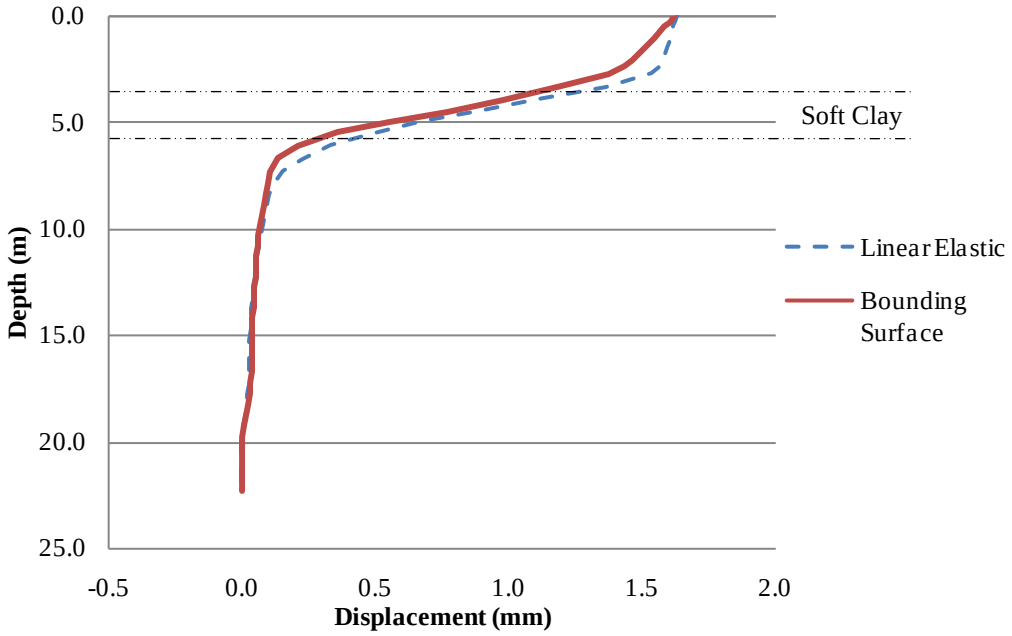

Figure 4.25: Abutment and Abutment Pile Deformation Comparison

The results comparison and error values are given in Table 4.6.

Table 4.7: Results and Error Estimates for Cooling Analysis

Deformation Measure	True	Linear Elastic	% Error	Bounding Surface	% Error
Rotation (°)	0.01	0.0015	85.0	0.0045	55.0
Pile Curvature ($\frac{\mu\varepsilon}{m}$)	709	515	27.4	687	3.1

The error calculations show the bounding surface analysis to be more accurate.

4.7 THREE-DIMENSIONAL ANALYSIS

Full 3D models of the Minnesota bridge and 15° skewed version of it were made in TeraDysac. To save on computational cost, these models were reduced to a size capable of running on a single processor machine. By removing the piles from the

models, a substantial number of elements in the vertical direction could be eliminated. And because the bridge girders rest on elastomeric pads over the piers, no elements were modeled in the pier regions either. These models consist only of the superstructure (girders and deck), the abutments, and the top two soil layers. They are small enough to be analyzed on a single processor in a reasonable amount of time. The meshes have 918 quadrilateral elements (deck and abutments), 256 line elements (girders), and 1344 hexagonal elements (soil), for a total of 2518 elements. The soil was modeled with the linear elastic elements and Γ was set to zero. Setting Γ = 0.0 kPa does not allow pore water pressure generation, but it permits a larger time step (and subsequently less computational effort). The 3D model (non-skewed) is shown in Figure 4.26.

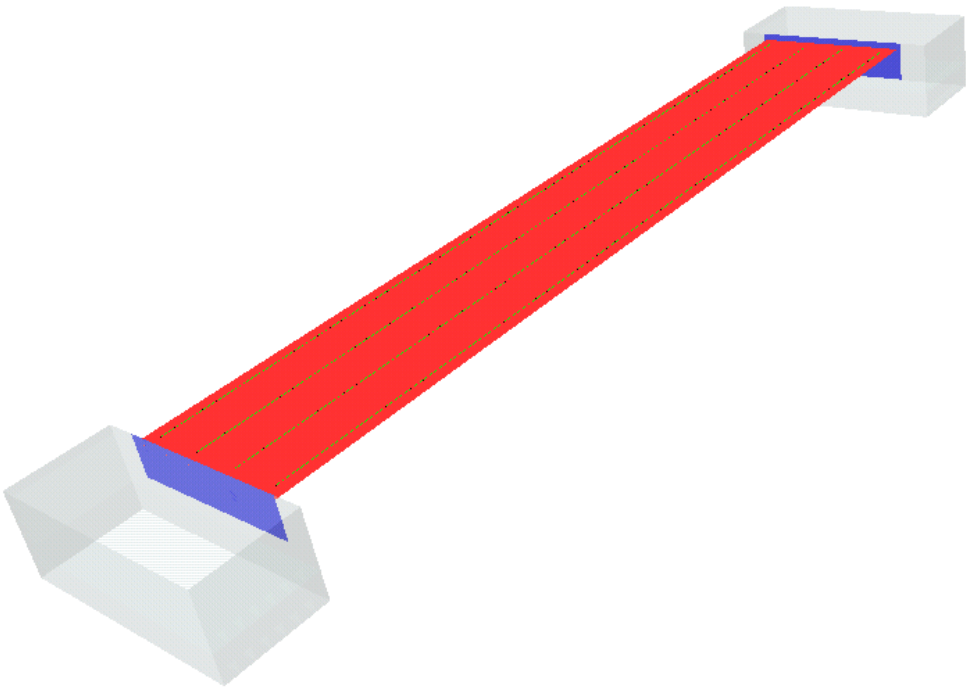

Figure 4.26: 3D Superstructure Model (Non-Skewed)

A plan view of the two 3D models is shown in Figure 4.27.

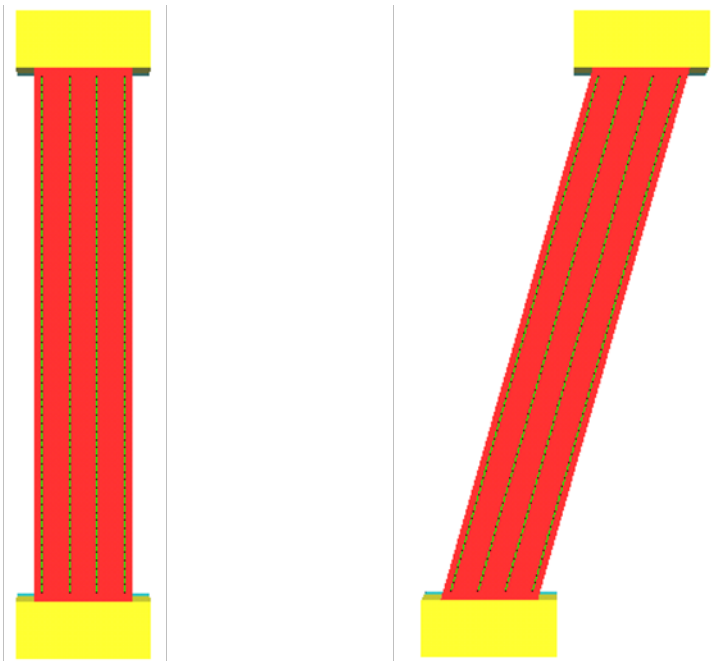

Figure 4.27: Plan View of 3D Superstructure Models

The bridges are both 66.0 m long and have a linear coefficient of thermal expansion of 6.162 * 10^{-6}/°F. The coefficient of thermal expansion was calculated using the weighted average approach described earlier. Both models were subjected to uniform temperature increase of 10°F. In addition to heating the superstructure, the abutments were also heated by the global temperature increase. This was done to strip away any interaction between the deck and the abutments. A plot showing the deformed shapes of the abutments is given in Figure 4.28. The line of nodes at the deck-abutment connection is used for the plot. The displacements correspond to the abutments at the top of Figure 4.27. Therefore, for the skewed bridge the obtuse corner is at a 'Position' of 0.0 m.

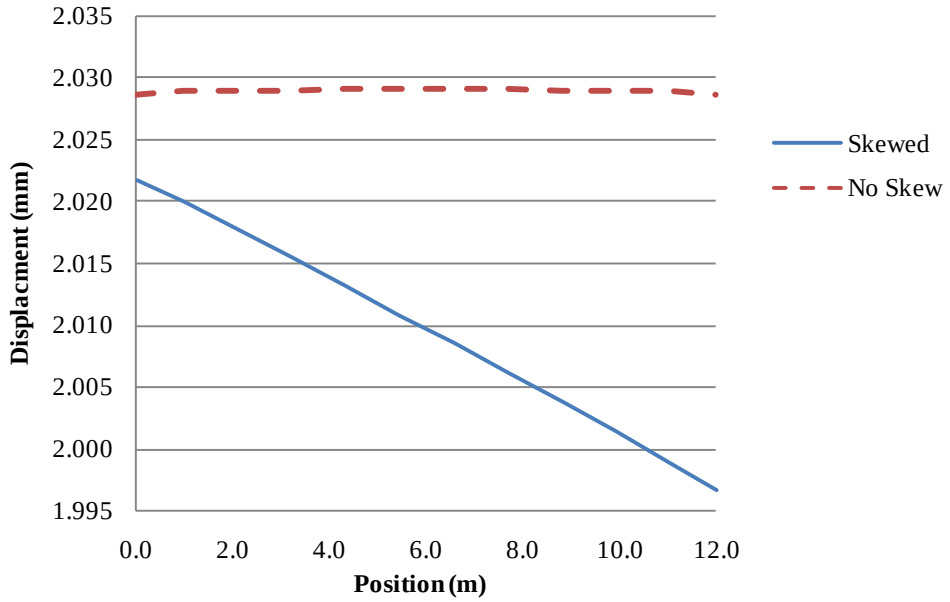

Figure 4.28: Abutment Deformations from 3D Analyses

A hand calculation of a free expansion of the non-skewed superstructure reveals abutment displacements of 2.03 mm, so it is evident that the implemented finite element technology and thermal loading scheme are working properly. It is also apparent that the backfill soils are not providing significant resistance, similar to what was observed in the 2D analyses. In studying Figure 4.28, it is clear that the bridge with no skew has a uniform displacement into the backfill soil. There is variation between the abutment corners in the skewed case though. The obtuse corner ('Position' = 0.0 m), is pushed farther into the backfill than the acute corner. The difference between the two corners is minor for this particular case, but the results provide insight into the general behavior of skewed IABs. In the obtuse corner, where the abutment has more displacement, the backfill pressure and stress in the superstructure will all be higher than in the acute corner. Figure 4.29 shows the forces at the abutment corners obtained from the analysis.

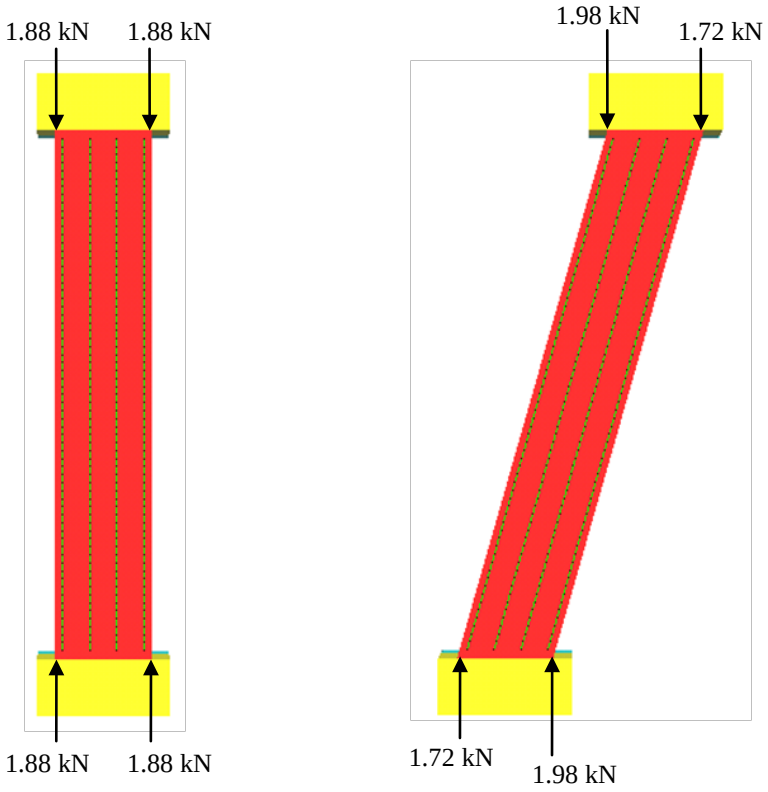

Figure 4.29: 3D Superstructure Corner Forces

The corner forces are equal in the non-skewed superstructure. In the skewed version, the forces in the obtuse corners are higher than the forces in the acute corners. This agrees with expected results and previous instrumentation results (e.g. Sandford and Elgaaly 1993).

5 INSTRUMENTATION OF AN OKLAHOMA IAB

The bridge that was instrumented is a 210-feet-long, integral abutment bridge with a 10° skew angle. The location of the bridge over Medicine Bluff Creek in reference to the State of Oklahoma and Comanche County is shown in Figure 5.1. This bridge was selected for instrumentation in consultation with the ODOT Bridge Division.

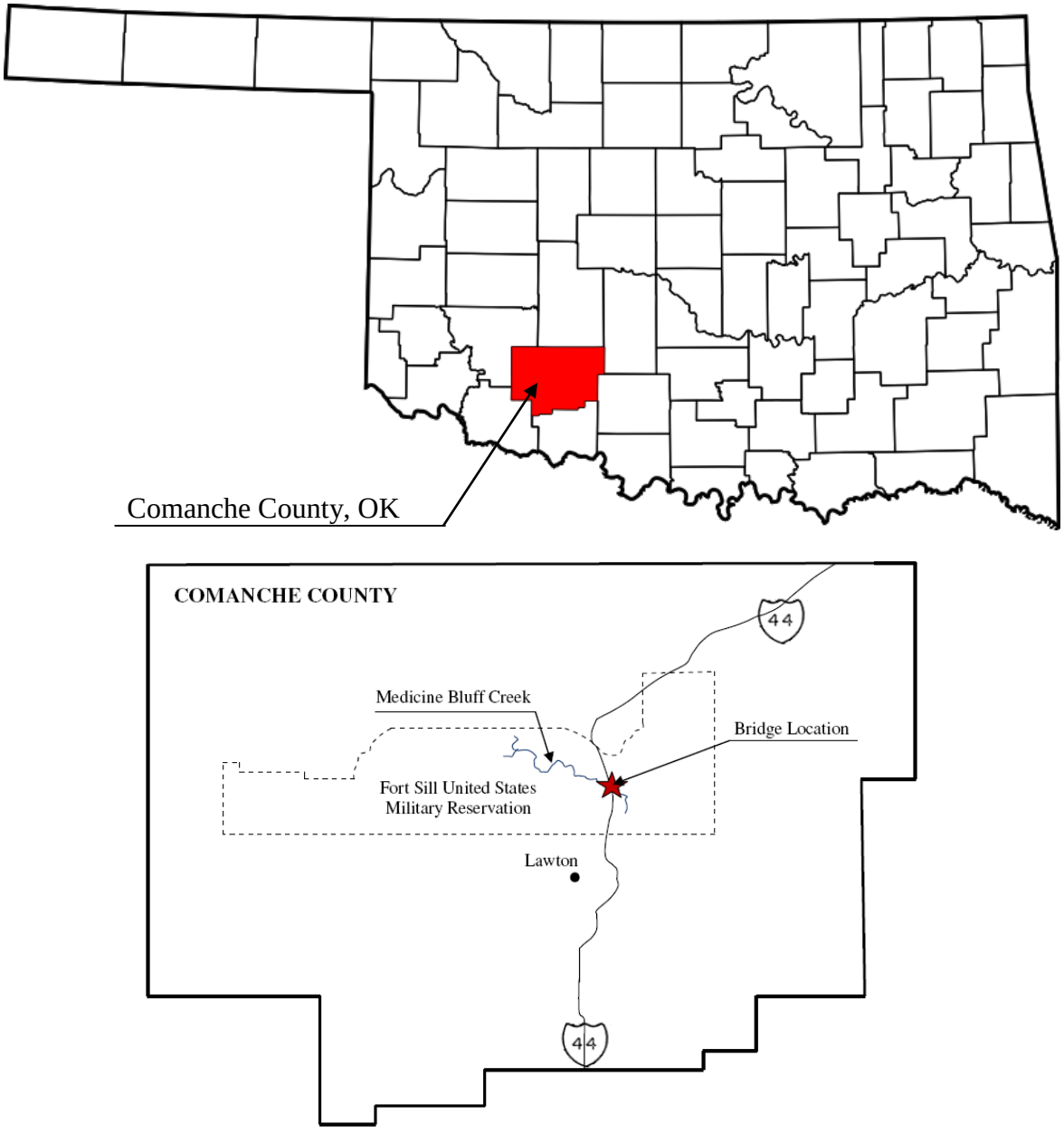

Figure 5.1: Location of the Oklahoma IAB

Before the instrumentation of the bridge could commence, the type, amount, and location of the instrumentation necessary to properly monitor the effect of thermal loading on the bridge had to be determined. The dimensions of the instrumented bridge are shown in Figure 5.2.

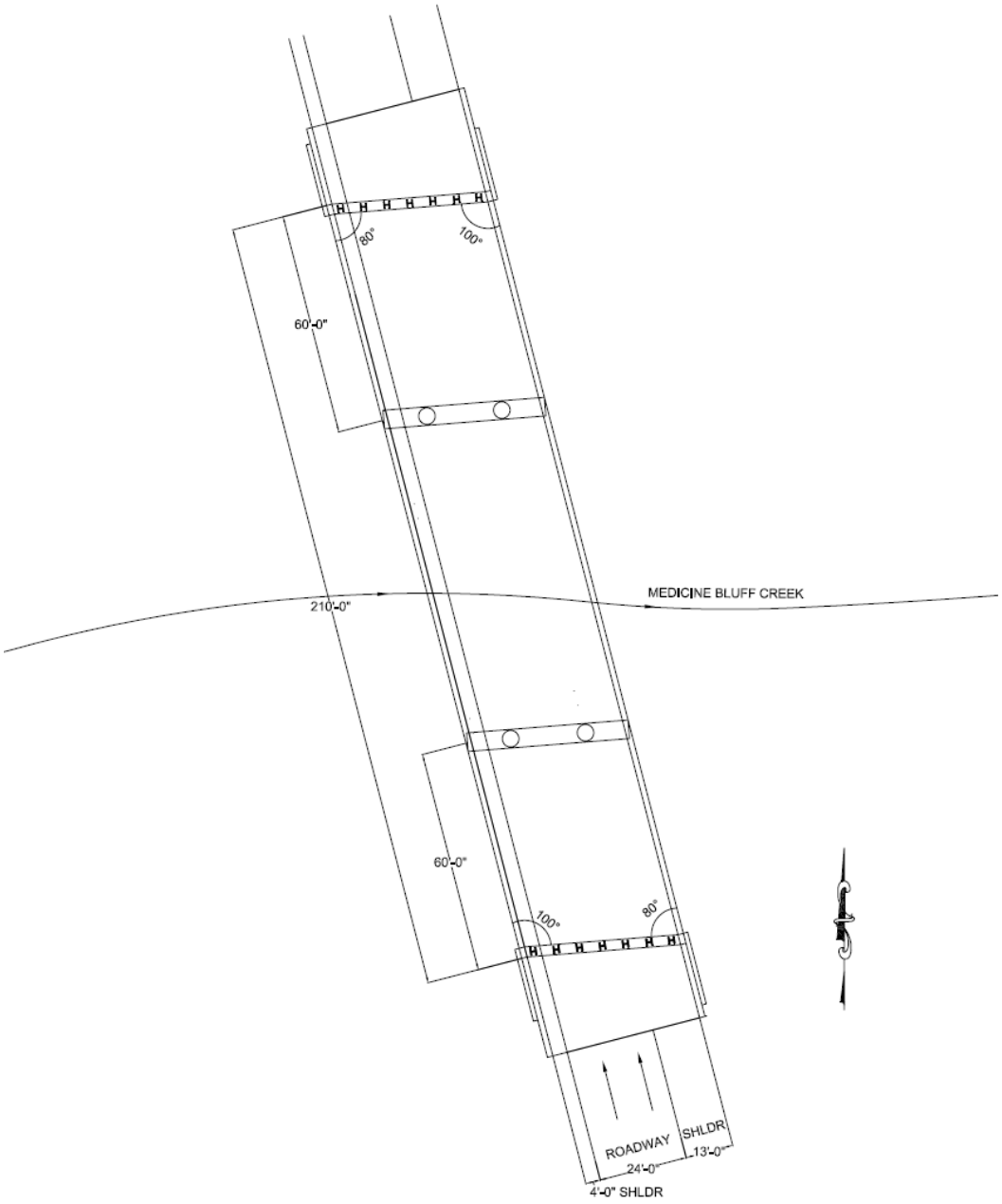

Figure 5.2: Dimensions of the Oklahoma IAB

The main goal when selecting the instruments was choosing appropriate ones that would provide an overall assessment of the bridge's movement due to thermal loading at various times. The following instruments were decided upon and installed as part of this project: strain gages, earth pressure cells, crackmeters, tiltmeters, and thermistors. The following sections detail the purpose of each instrument type, the installation of each instrument, and the locations of the instruments used for this study. While the following sections detail the installation and reasons for selecting the instrument locations, it must be kept in mind that for each instrument type, the number of instruments used was constrained by budget and the need to avoid delaying construction activities.

5.1 INSTRUMENTATION DETAILS

5.1.1 Strain Gages

The strain gages used for this research are Geokon Model 4000 arc weldable vibrating wire strain gages. These strain gages are designed to measure both long and short-term strain measurements on structural steel members, such as driven piles. The Geokon Model 4000 Strain Gages are not designed to be used for dynamic or rapidly changing strain measurements. The strain gages were installed on three of the fourteen driven abutment HP 10x42 piles at three depths spaced 3 feet apart on each pile. The gages were installed at three different depths to see if there is a variation in strain with depth. The locations of the instrumented piles are shown in Figure 5.3. The gages were installed on both sides of the piles at the same depths to measure bending moment in the piles. The vibrating wire strain gage consists of a length of steel wire tensioned between two mounting blocks that are welded to the steel pile. When the

piles have changes in length, the tension in the wire is altered. When a reading is taken, the wire is plucked, and its frequency is measured. The frequency change is proportion to the change in wire length. The frequency of the wire is converted to a strain measurement using calibration data.

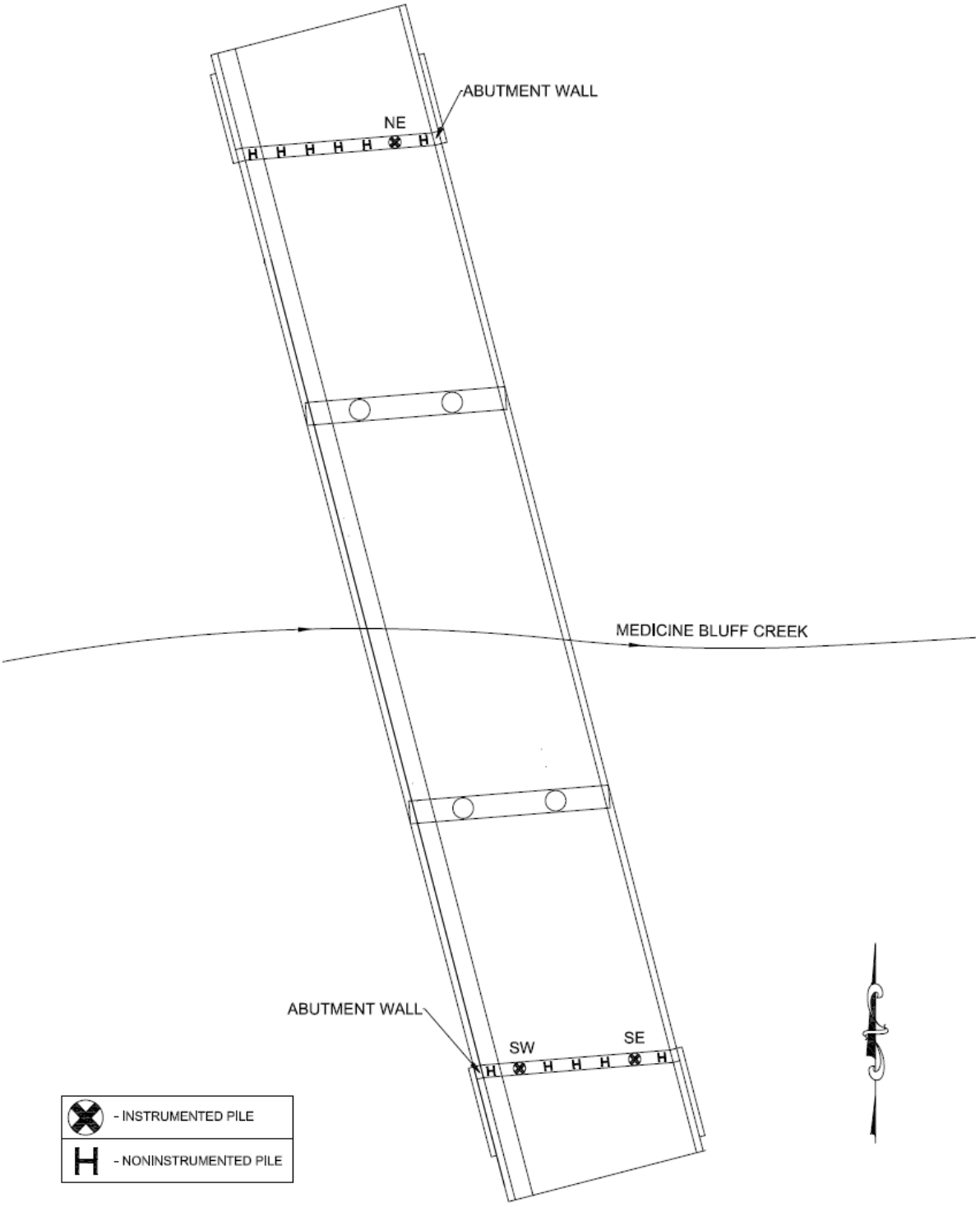

Figure 5.3: Locations of the Instrumented Piles

The piles that were instrumented were selected so that the largest expected variations in strain could be monitored. Thus, three piles near the corner of the abutment were chosen for instrumentation. Piles at the far abutment edge were not selected because of the lack of symmetry with respect to adjacent piles. Edge piles involve more complex loading, which complicates the analysis.

Instrumenting the steel HP 10x42 piles was the first required step to properly monitor the bridge movement because pile driving is one of the first steps of constructing an integral abutment bridge. Because gages could not be attached after the piles were driven, the depth of embedment had to be estimated using boring logs provided by ODOT to choose what locations to attach the gages to the piles. To insure that the strain gages will not move both during and after pile driving, the strain gages were attached to mounting blocks that are arc welded to the steel of the pile. The following figure shows the mounting block being welded to the piles.

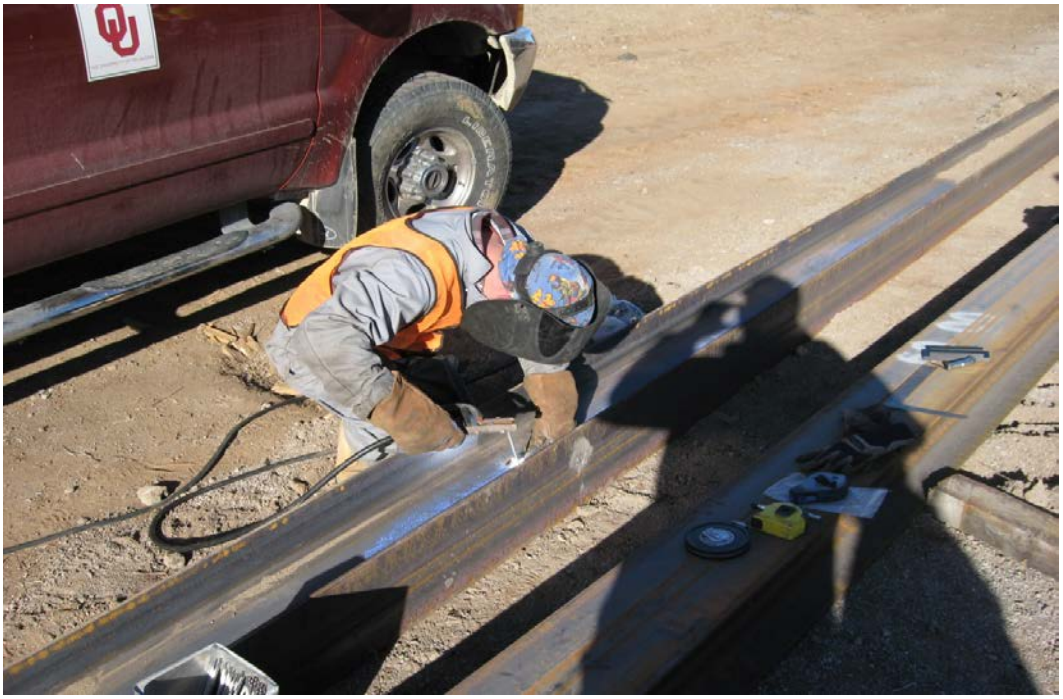

Figure 5.4: Mounting Blocks Being Welded to Pile

Once the mounting blocks were welded to the pile, the strain gages were placed in the mounting blocks and then secured by 3 screws. The screws were hand tightened and covered in epoxy to insure a tightened bond to the mounting blocks. Lastly the coil housing was clipped to the strain gage and is secured with epoxy and a hose clamp. Figures 5.5 and 5.6 show a finished strain gage both after being secured in the mounting blocks and after being secured with the hose clamp.

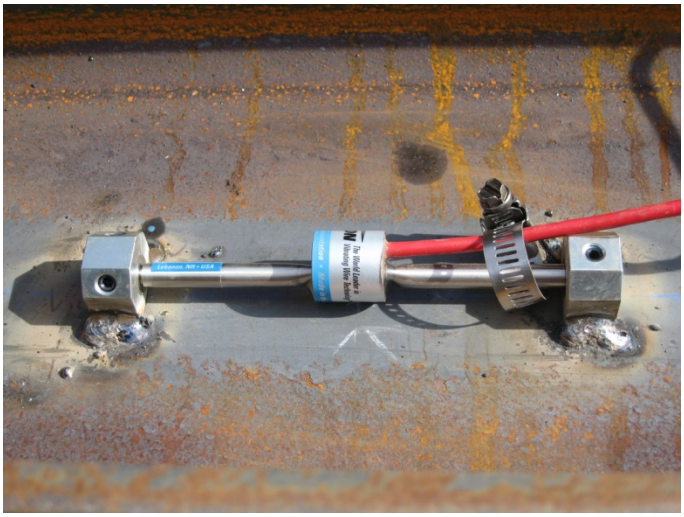

Figure 5.5: Strain Gage Attached to the Pile

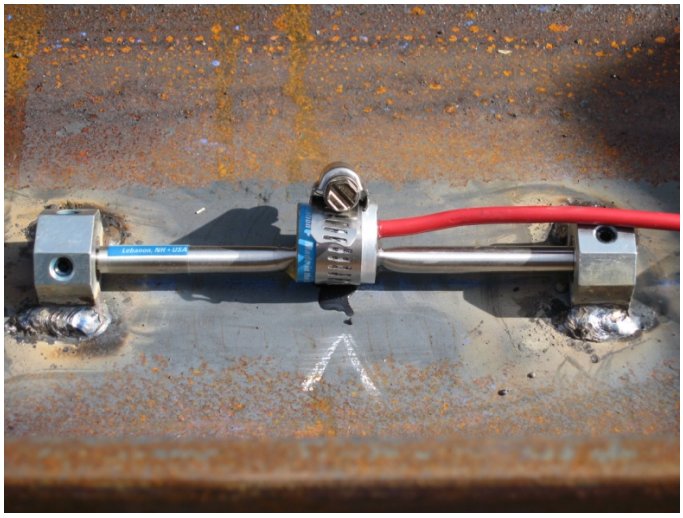

Figure 5.6: Strain Gage after Being Secured

Once the strain gages were secured, the gages were then covered by angle iron. The angle iron's purpose is to protect the gages both during and after pile driving. Because pile driving is such a severe dynamic loading on the pile, the maximum amount of protection was used to ensure that the gages don't get damaged during driving. The angle iron, like the mounting blocks, was welded to the pile to ensure high strength and durability. Figure 5.7 shows the gages both before and after the angle iron is attached.

Figure 5.7: Strain Gages before (Left) and after (Right) Angle Iron is Attached

The last measures of safety included covering the exposed sensor cables with ½ inch plastic conduit and using foam to plug the hole at the top of angle iron. The conduit was used to help protect the cables from corrosion and damage. The foam prevents soil from falling into the angle iron both during and after pile driving and potentially corroding the cables and holds the cables in place during pile driving so that they don't get damaged. Figure 5.8 shows the foam and conduit used for protection.

Figure 5.8: Angle Iron after Foam and Conduit are Installed

After all the gages were attached to piles and all the safety measures were installed, initial strain readings were taken using the Canary Systems Multilogger software, Geokon Model 8021-1 Micro-1000 Datalogger, and Geokon Model 8032 16

Channel Multiplexer. Details of all the data acquisition equipment are described in the Data Collection section of the chapter.

Once the piles were instrumented, the next step was to make sure the piles were installed at the proper locations and facing the proper directions. Piles were labeled so the construction workers knew where to install piles, and what direction each pile faced. This was critical to ensure that the readings can be properly interpreted to provide the actual pile stresses. The piles were oriented so that they would be in weak-axis bending to facilitate the effects of thermal loading on the bridge. The first instrumented pile to be driven was the northeast pile as shown in Figure 5.3. Only one pile was chosen for the north side of the bridge, because predicting the depth of embedment was difficult since the pilot holes were not used on the north side. Pilot holes were required for the south side, because a hard layer was present that was above the required bearing material (see Chapter 8 for detail discussion of the soil profiles). To avoid trying to drive the pile through the hard layer, pilot holes were used to drill below the hard layer to ensure proper embedment depth. On the north side, the boring logs showed no hard layer, so simple driving was satisfactory. As was feared, during pile driving, the appropriate bearing level ended up being approximately 14 feet deeper than was expected for the northeast instrumented pile. So the construction workers had to splice on two more 10 foot pile sections on top of our instrumented piles. In order to protect the wiring and the gages during the deeper driving, approximately 14 more feet of the angle iron had to be welded onto the pile. Figures 5.9 – 5.12 show the sequence of events to adapt to the deeper penetration depth.

Figure 5.9: NE Pile before Driving

Figure 5.10: NE Pile after Initial Pile Driving

Figure 5.11: Adding More Angle Iron to Spliced Sections

Figure 5.12: Pile after Splicing and Attaching Angle Iron

Once all the pile splicing and angle iron addition was complete, the pile was driven to a suitable bearing depth, which ended up being approximately 14 feet below the anticipated bearing level. This affected the results because it is expected that much less strain and bending will occur at deeper depth below the ground surface when compared to near the surface. The final depths for the gages were 15'-3", 18'-3", and 21'-3" below the bottom of the abutment. After the piles were driven, they were cut to a height of 2 feet above the ground surface. Figures 5.13 and 5.14 show the pile being cut and the height of the pile afterward.

Figure 5.13: NE Pile Being Cut

Figure 5.14: North Side Piles after Being Cut

It was decided that because the south side of the bridge was using pilot holes for the abutment piles, that two piles would be instrumented on the south side, due to the better predictability of bearing depth. The second most southeast and the second most southwest piles were chosen for instrumentation as shown in Figure 5.3. The same preparation was conducted for these piles, except the piles were placed in the pilot holes. Figures 5.15 and 5.16 show the pilot holes and piles inside the pilot holes.

Figure 5.15: A Pilot Hole on South Side

Figure 5.16: Piles in Pilot Holes

During the pile driving on the south side, the depth of embedment was more accurately predicted than on the north side of the bridge. The southeast instrumented pile was driven to approximately the ideal depth with the gages being at depths of 1'-2", 4'-2", and 7'-2" below the bottom of the abutment. The southwest pile on the other hand reached the necessary bearing capacity at a depth approximately 9 inches higher than planned. The reason this was a problem is because when the piles were cut to their finished elevation, the cut occurred near the top gage locations. With the amount of heat required to cut the steel piles, the gages and wires would have been damaged and unusable if left on the pile. To avoid damage, the top strain gages had to be removed from the southwest pile. Figures 5.17 and 5.18 show the southwest pile before and after removing the top strain gages from the pile.

Figure 5.17: SW Pile before Top Gage Removal

Figure 5.18: SW Pile after Top Gage Removal

Because the top gages were removed from the southwest pile, only four gages remained which means only two depths could be analyzed for the southwest pile. The gages are near the surface, so a relatively high amount of strain was expected to be observed. The final depths of the gages on the southwest instrumented pile were 2'-3" and 5'-3" below the bottom of the abutment.

The strain gages are also constructed with built in thermistors so that temperature readings can be taken at the gage installation locations, though it is not expected that there will be a large temperature variation below the ground surface. Figure 5.19 shows the final depths of all the strain gages with respect to the ground surface and the total pile lengths of all the instrumented piles.

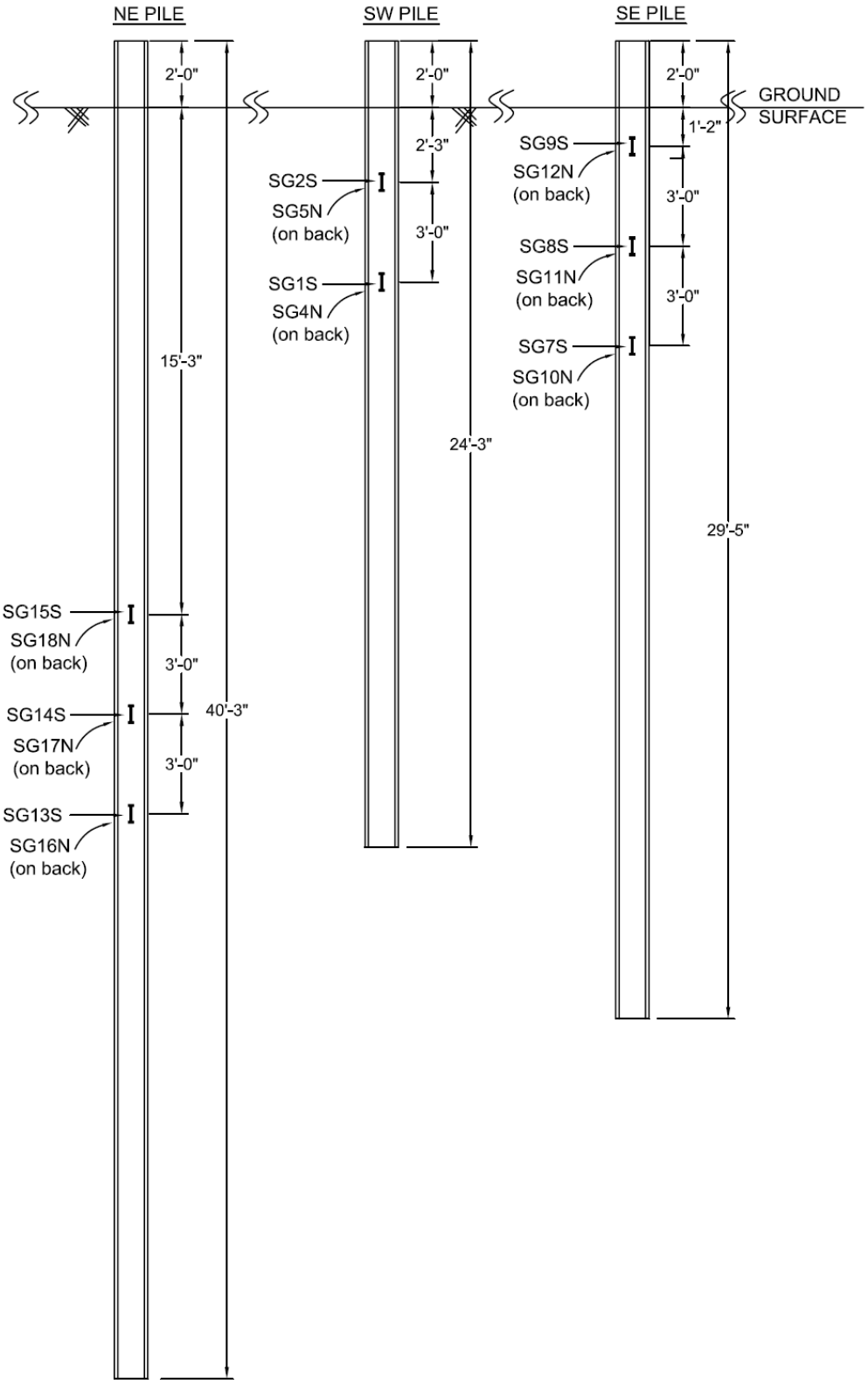

Figure 5.19: Strain Gage Depths for Each Pile

5.1.2 Earth Pressure Cells

After the abutment piles were installed, the abutment walls were constructed. Approximately 2 feet of the piles were embedded into the abutment walls. Once the abutment walls were completed, the earth pressure cells were installed on the outside faces of the abutment walls. The earth pressure cells used in this project were Geokon Model 4800 Earth pressure cells (EPC). The cells consist of two 9 inch diameter flat plates welded together around their perimeter and are separated by a small gap filled with hydraulic fluid. Whenever earth pressure squeezes the two plates together, the pressure inside the fluid increases. Figure 5.20 shows the components of the earth pressure cells.

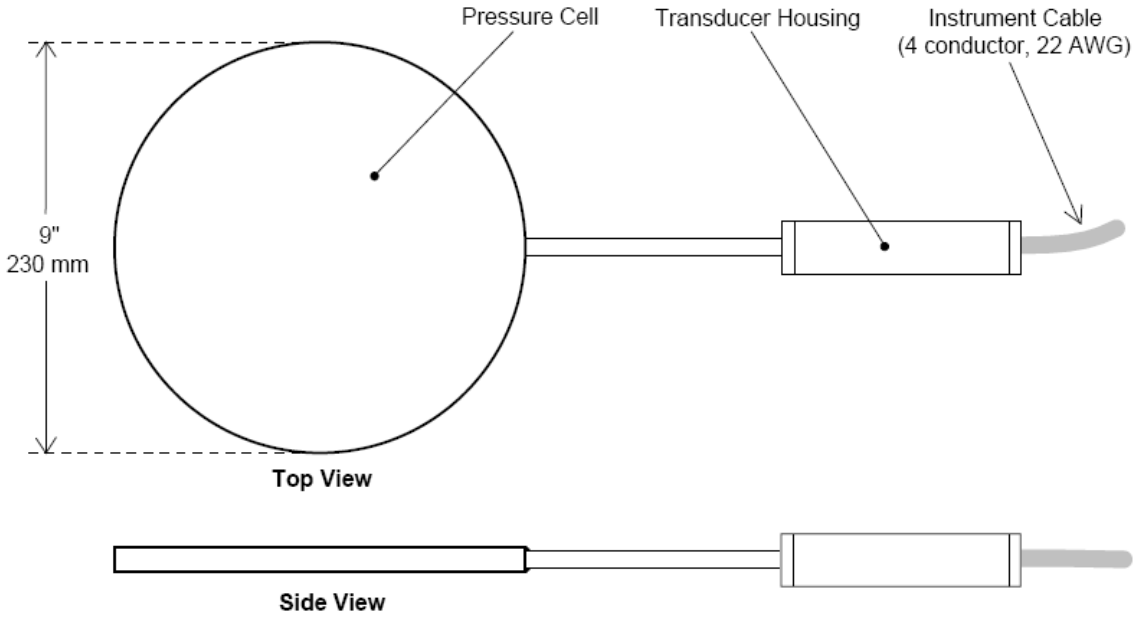

Figure 5.20: Geokon Model 4800 Circular Earth Pressure Cell

The earth pressures cells were calibrated by Geokon before they were shipped. The calibration factors were used to determine the pressures being applied to the abutment walls by the soil in units of either psi or kPa.

The locations of the earth pressure cells were chosen to determine the variation of earth pressure on the abutment walls. On both the north and the south abutment walls, cells were positioned across the horizontal length of the wall at the same height on the wall to measure the variation in pressure along the length of the wall. On the north wall, a cell was placed directly below the middle cell to see if there is a variation with respect to height along the wall. Four earth pressure cells were installed on the north abutment and two were installed on the south abutment. The locations of the earth pressure cells are shown in Figures 5.21 - 5.23.

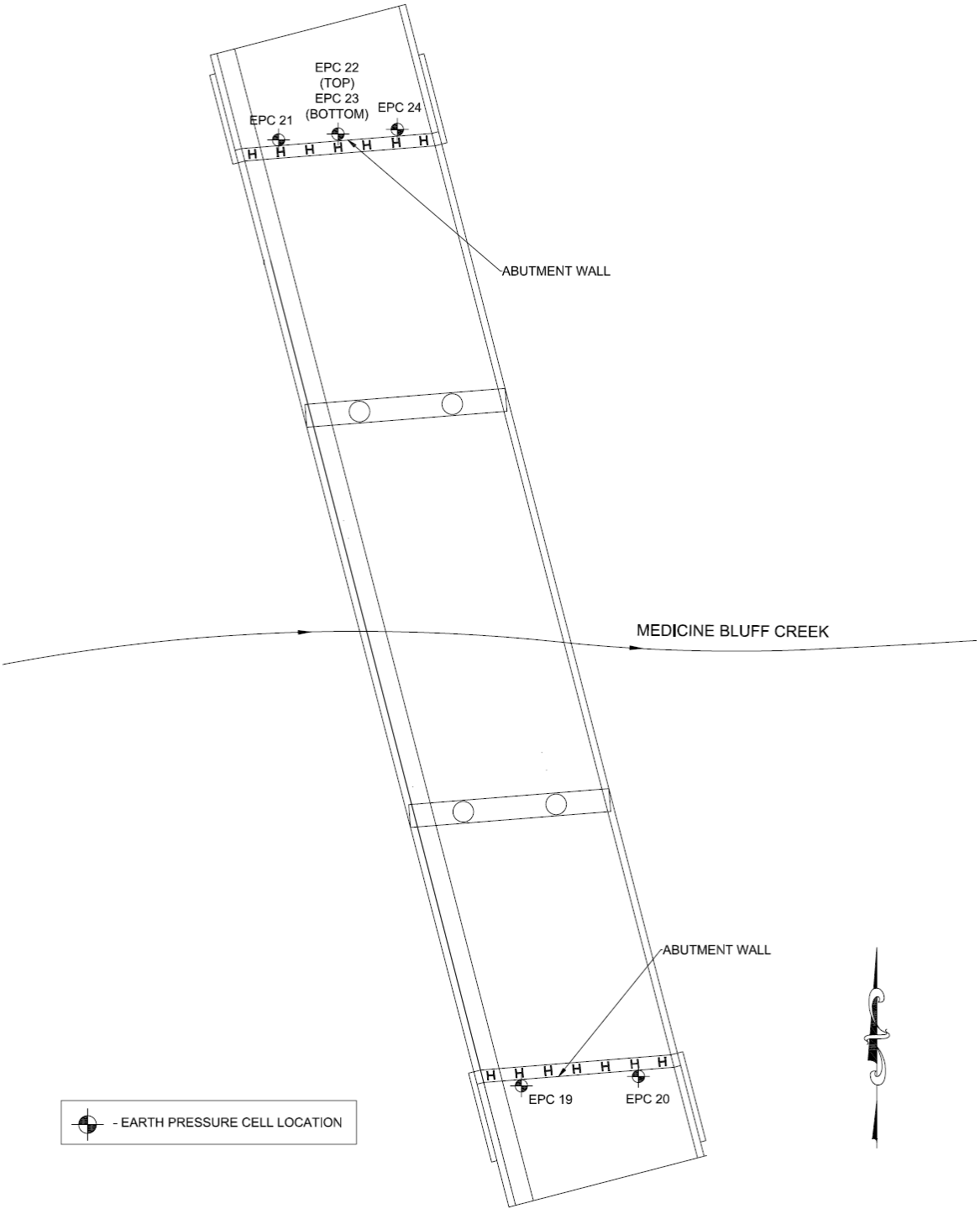

Figure 5.21: Locations of the Earth Pressure Cells

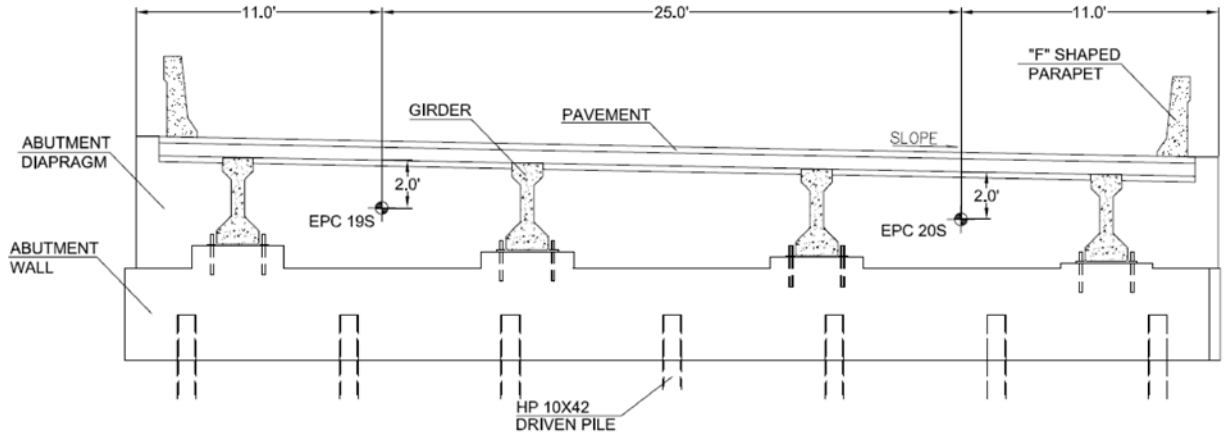

Figure 5.22: Locations of the Earth Pressure Cells on the South Abutment (Facing North)

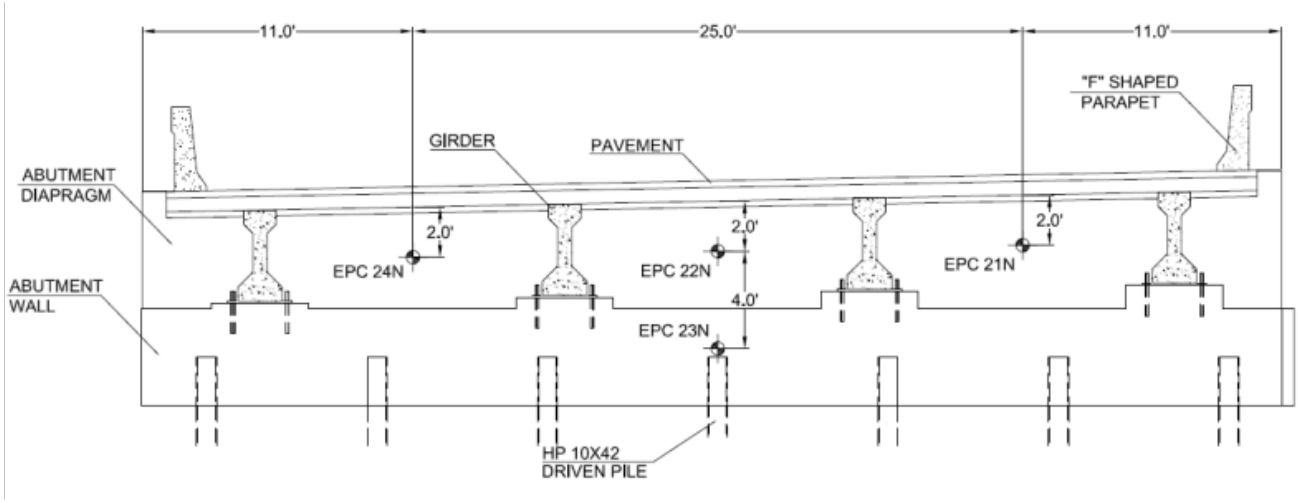

Figure 5.23: Locations of the Earth Pressure Cells on the North Abutment (Facing South)

During the installation, the cells were mounted directly onto the concrete abutment on the backfill side of the walls. To secure the earth pressure cells at their assigned locations, the cells were attached to the walls using plastic concrete screw anchors. By securing the cells directly on the concrete wall with four anchors, the amount of pressure being applied to the abutment wall can be consistently measured. To protect the instrument cables during the backfill compaction, ½ inch plastic conduit was used and secured against the abutment walls using ½ inch metal brackets. This was intended to prevent bending or breaking of the cables during and after the sand backfill placement and compaction. Initial baseline readings were taken with the data acquisition system before the backfill was placed. Figures 5.24 to 5.27 detail the installation of the earth pressure cells

Figure 5.24: Earth Pressure Cells Mounted on the South Abutment

Figure 5.25: Mounted Earth Pressure Cell on the Abutment Wall

Figure 5.26: South Abutment Wall after the Placement of the First Lift of Sand Backfill

Figure 5.27: Earth Pressure Cells on the North Abutment Wall

Similar to the strain gages, the earth pressure cells are constructed with built in thermistors so that temperature readings can be taken at the pressure cell locations.

5.1.3 Tiltmeters

The strain gages and the earth pressure cells were the only instruments that required installation before the construction of the bridge was completed. The remainder of the instrumentation, including the tiltmeters, was installed after the bridge construction was completed. The tiltmeters used were Geokon Model 6350 Vibrating Wire Tiltmeters. These tiltmeters are designed to monitor changes in tilt in degrees on structures such as abutment walls. These sensors are composed of a pendulous mass supported by a strain gage and an elastic hinge. When the tiltmeter begins to tilt, the strain gage senses the change in gravitational force caused by the rotation of the gage's center of gravity. These tiltmeters can be mounted so that either uniaxial (one direction) or biaxial (two directions) tilt measurements can be made. Because tilt was primarily

expected perpendicular to the abutment wall or parallel to the direction of traffic, the uniaxial mounting setup was used. Figure 5.28 details the setup for the uniaxial tiltmeter installation.

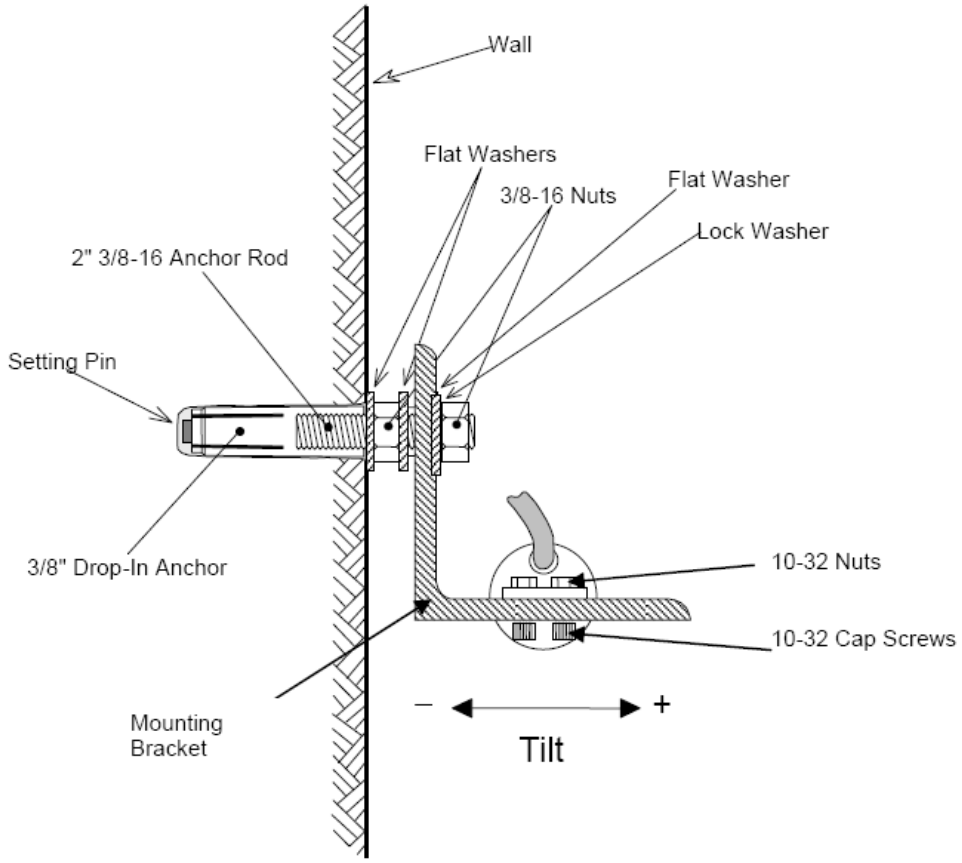

Figure 5.28: Top View of the Geokon Uniaxial Tiltmeter Setup

Two tiltmeters were installed at the same locations on both the north and south abutment walls. Figures 5.29 to 5.31 show the locations of the tiltmeters with respect to the bridge and the abutment walls.

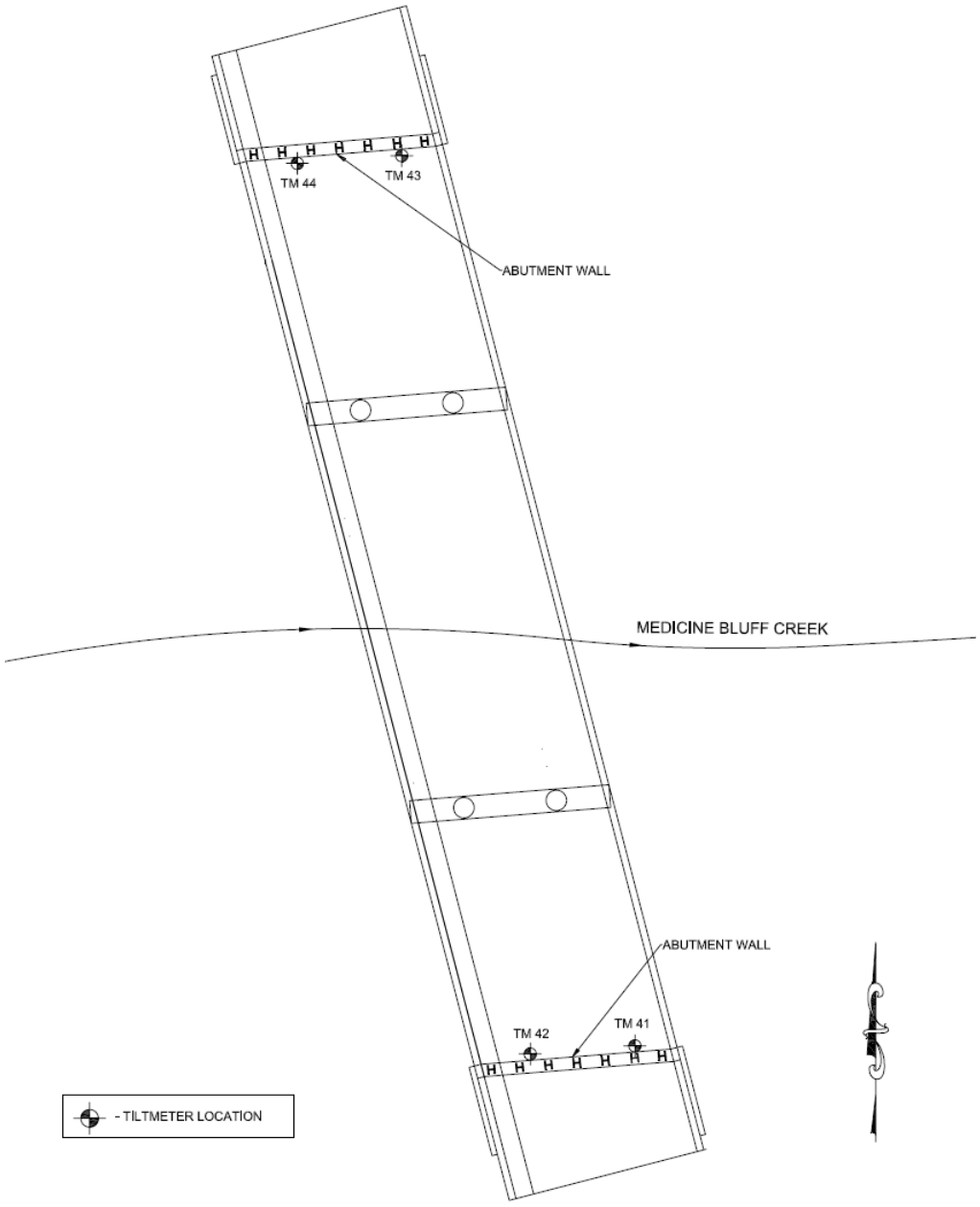

Figure 5.29: Locations of the Tiltmeters

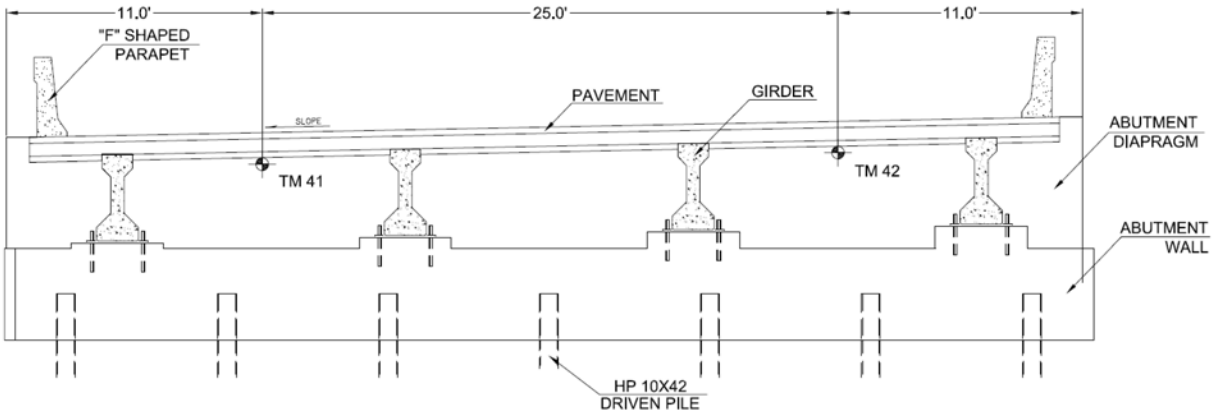

Figure 5.30: Locations of the Tiltmeters on South Abutment (Facing North)

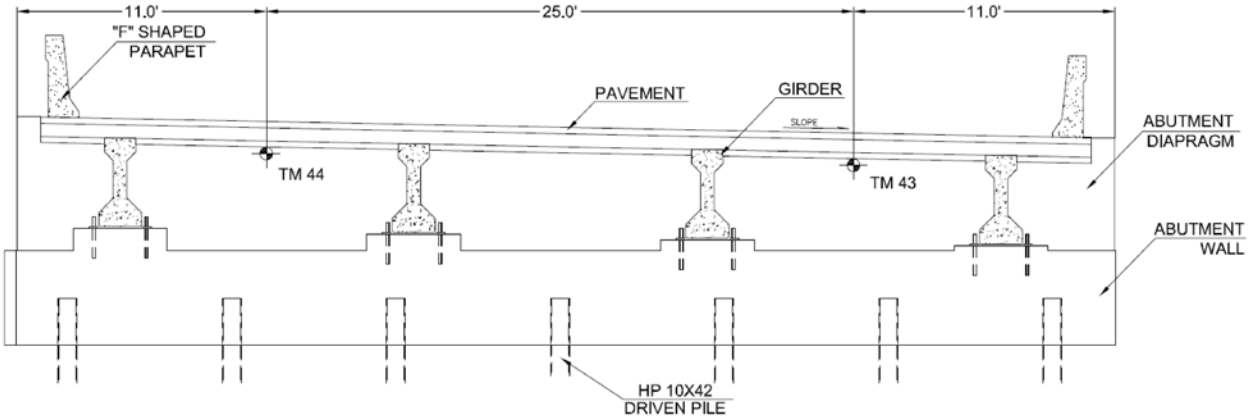

Figure 5.31: Locations of the Tiltmeters on North Abutment (Facing South)

The tiltmeters were mounted using 3/8 inch drop-in anchors to the inside facing walls (towards the creek) of the abutments. First a 2 ½ inch deep, 3/8 inch diameter hole had to be drilled near the bottom of the bridge deck at the assigned locations. Once the holes were drilled, the anchors were placed in the holes and expanded using a setting pin tool. Next the mounting bracket was screwed to the anchor and tightened so that the tilt measurements are consistent. Lastly, the tiltmeter was screwed to the mounting bracket and tightened. Initial reading were taken and used as the baseline to measure the change in tilt of the sensors. Because the tiltmeters are directly exposed to ambient temperature change, the tilt readings had to be temperature corrected. Figures 5.32 and 5.33 show the tiltmeters installed on the abutment walls.

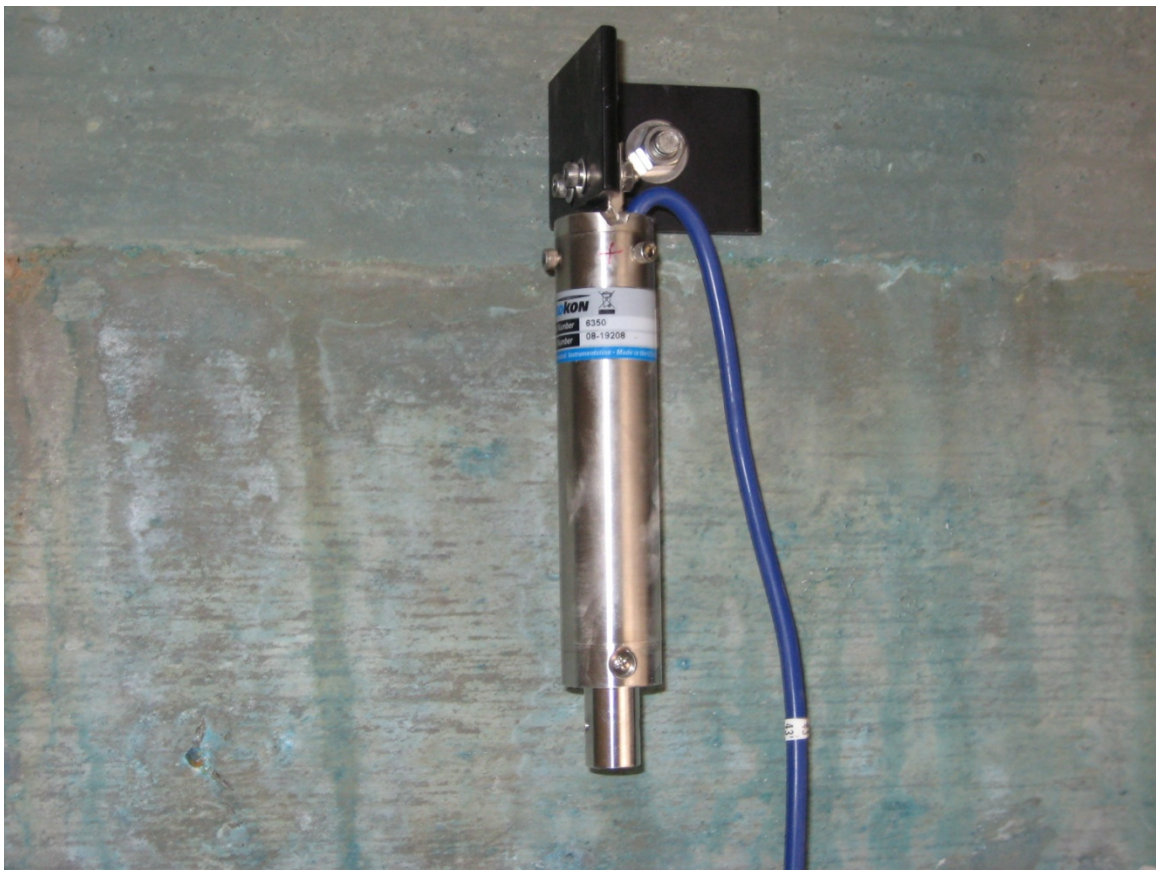

Figure 5.32: Tiltmeter Mounted on Abutment Wall

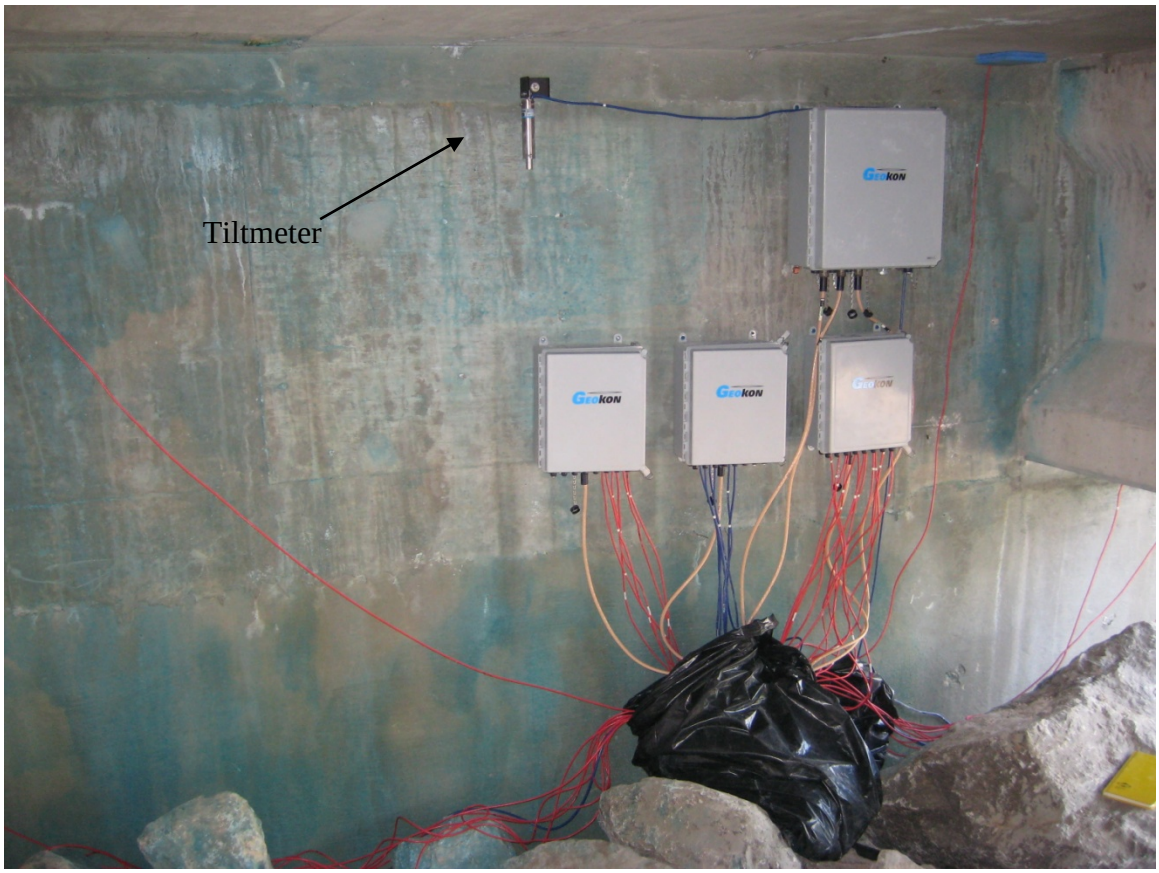

Figure 5.33: Mounted NE Tiltmeter on the North Abutment Wall

From the results of the tiltmeters, a variation in tilt across the abutment walls can be measured. Additionally, the tiltmeters are constructed with built in thermistors to measure temperature at those locations.

5.1.4 Crackmeters

The last instruments that measured bridge movement to be installed were the crackmeters. The crackmeters used for this project are Geokon Model 4420 Vibrating Wire Crackmeters. These crackmeters are designed to measure the movement across joints such as the thermal expansion joints located between the approach slabs and the pavement on integral abutment bridges. The instrument consists of a vibrating wire sensing element in series with a stress relief spring that is connected to the wire on one

end and a connecting rod on the other. As the connecting rod is elongated as the joint expands, the spring is elongated causing an increase in tension that is measured by the vibrating wire. The tension of the wire is proportional to the elongation of the joint, which allows for the measurement of the expansion or contraction of a joint in units of length.

The mounting hardware provided by Geokon could not be used for this project, because there was no place to attach the crackmeter directly to the pavement and approach slab across the expansion joint. So to measure the expansion and contraction of the joints, a modified system was created as shown in Figures 5.35 to 5.38. Two crackmeters were installed on each side of the bridge (one per corner) to see if there is a variation in bridge movement across the bridge. Figure 5.34 shows the locations of the crackmeters with respect to the bridge.

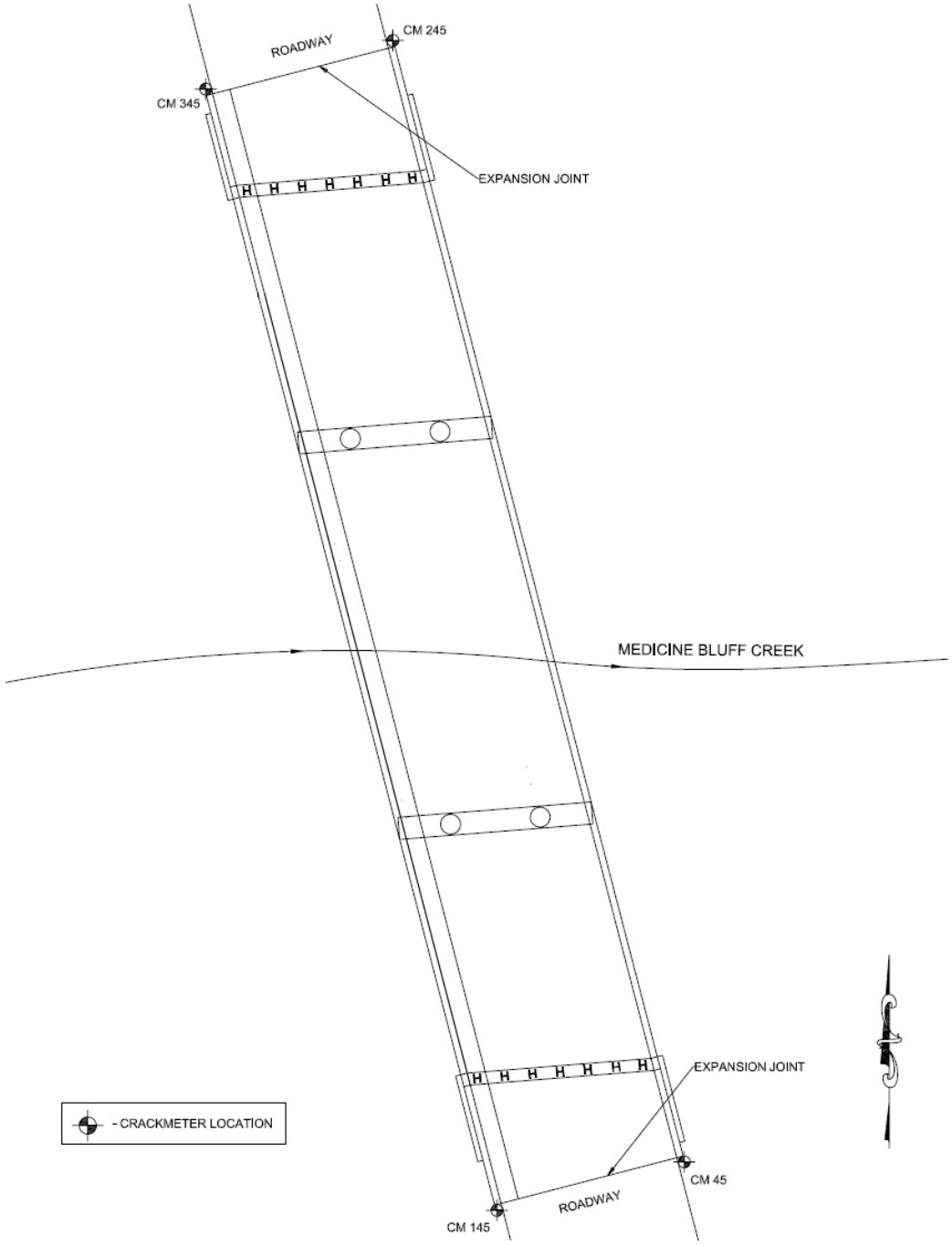

Figure 5.34: Locations of the Crackmeters

At the locations the crackmeters were installed, they were exposed directly to the heat of the sun. To avoid overheating, the crackmeters were covered by 2-inch diameter foam tubing. The foam is designed to protect the gage from direct sunlight, rain, and debris. Even though the instruments are covered by the foam tubing, the reading still had to be corrected for being exposed to the ambient temperature.

Figure 5.35: South Abutment Crackmeter Setup

Figure 5.36: North Abutment Crackmeter Setup

Figure 5.37: Installed Crackmeter Prior to Foam Installation

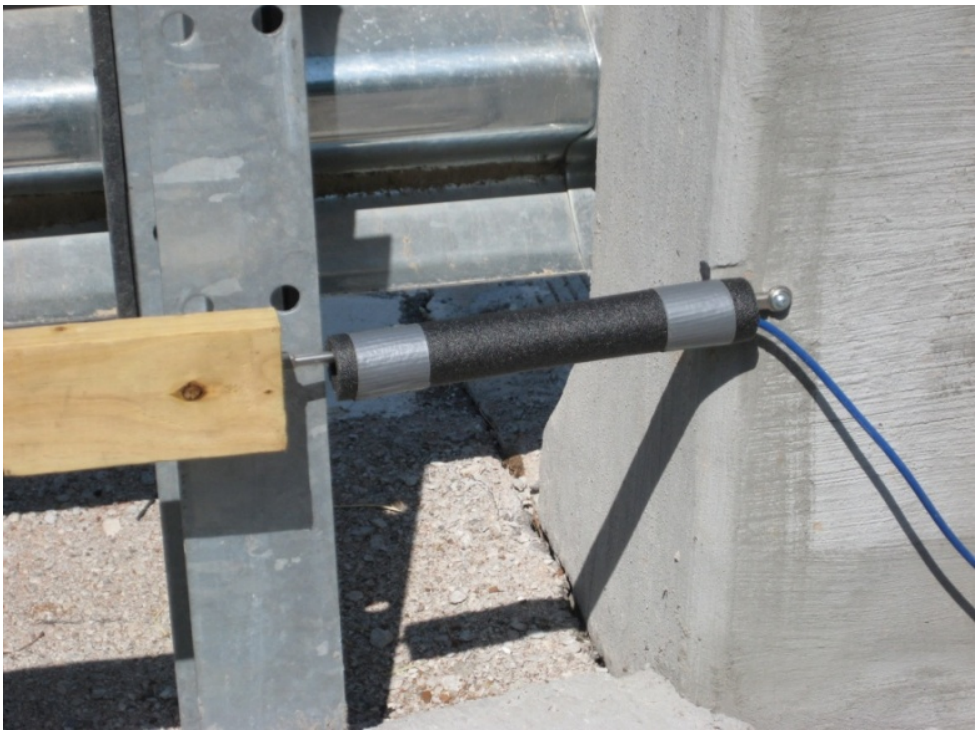

Figure 5.38: Installed Crackmeter after Foam Installation

Additionally, the crackmeters are constructed with built in thermistors to measure temperature.

5.1.5 Thermistors

Though all the instruments previously discussed have built in thermistors, the main use for that feature on those instruments was that the tiltmeters and crackmeters needed to be corrected for the temperature read by the thermistors. The actual temperature of the bridge was not being measured by these instruments. To measure the variation in temperature across the bridge, 16 Geokon Model 3800 Thermistors were positioned at various locations across the bridge. The thermistors are thermal resistors made from a mixture of metal oxides encased in epoxy. These temperature gages have an accuracy of ± 0.5°C. The locations of the thermistors included the top of the bridge deck, underneath the bridge deck, and various locations on the bridge

girders. Thirteen thermistors were installed on the north side of the bridge, while only three were installed on the south side. The main reason for more number of thermistors on the north side is that the data acquisition system was located on the north abutment and hence north side instruments would require shorter cable lengths than the south side. The north side locations covered the bridge cross-section well. The south locations were used to compare to the north side measurements. Figure 5.39 shows the locations of the thermistors with respect to the plan view of the bridge and Figures 5.40 and 5.41 show the profile locations of the thermistors on the north and south sides of the bridge

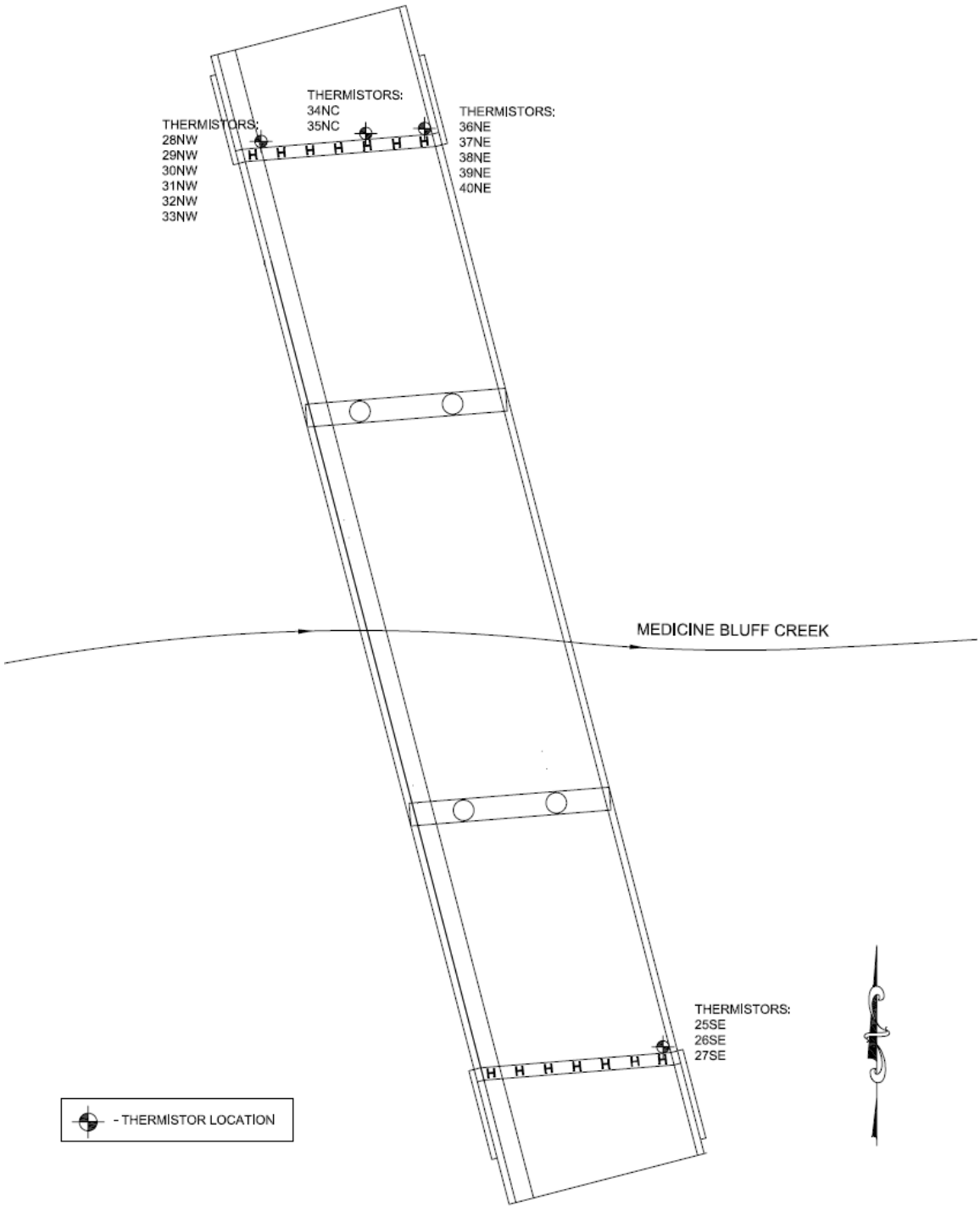

Figure 5.39: Locations of the Thermistors

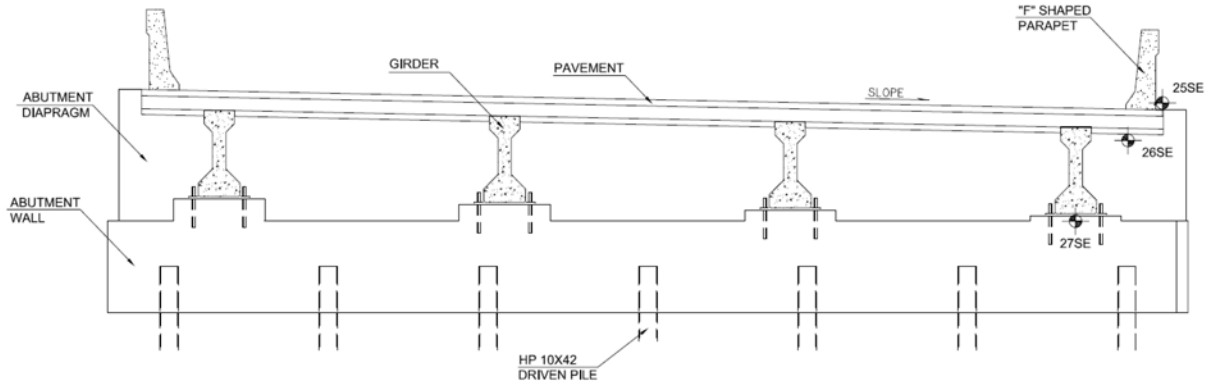

Figure 5.40: Locations of Thermistors on South Side of the Bridge (Facing North)

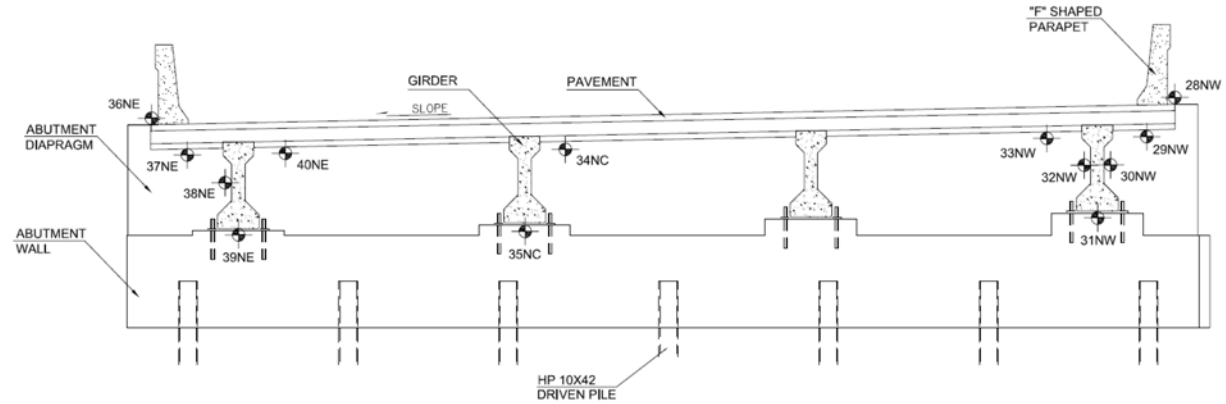

Figure 5.41: Locations of Thermistors on North Side of the Bridge (Facing South)

To make sure the temperatures of the bridge were being measured at the thermistor locations and not the ambient temperatures, the thermistors were covered in ½ inch thick foam insulation. The foam ideally protects thermistors from the ambient temperature, and allows them to only pick up the temperatures of the concrete of the bridge. Both the thermistors and the foam were attached to the bridge at the desired locations using an epoxy. To make the attachment of the thermistors to the concrete simpler, one side of each thermistor was flattened using sandpaper. This gave a flat surface to bond the thermistors to the bridge with adhesive. Figures 5.42 to 5.45 detail the installation of the thermistors.

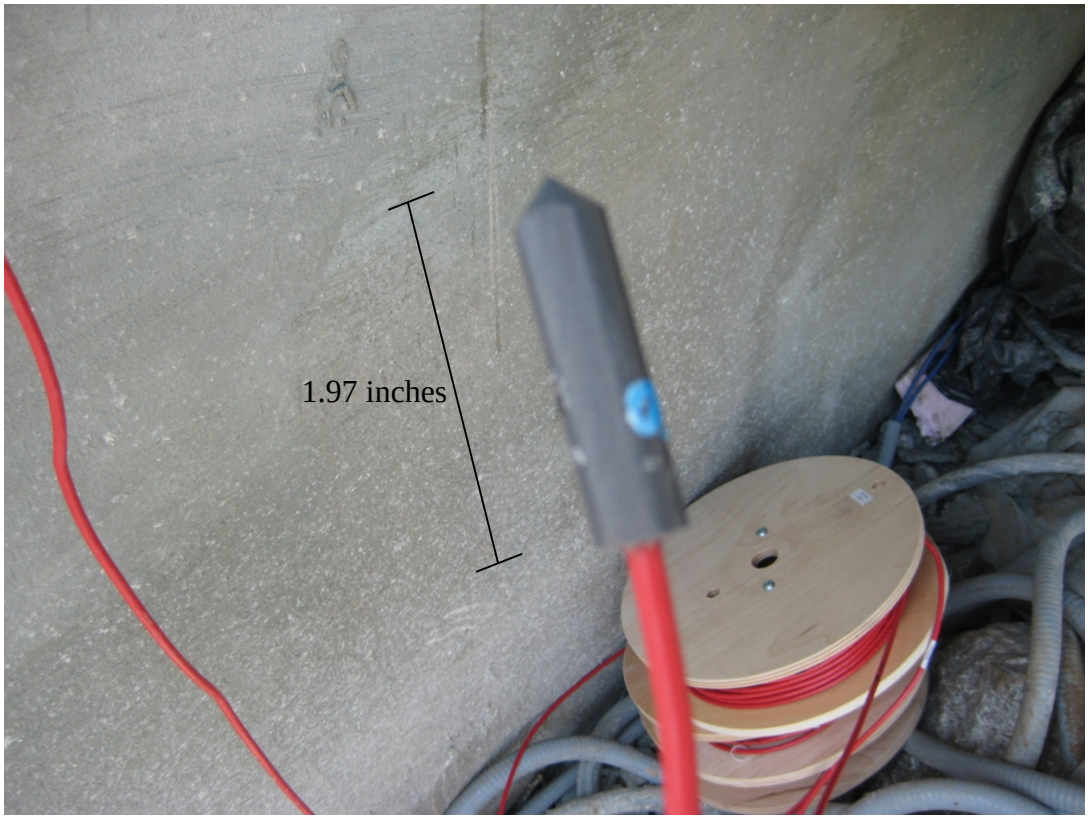

Figure 5.42: Thermistor with Flattened Surface on One Side

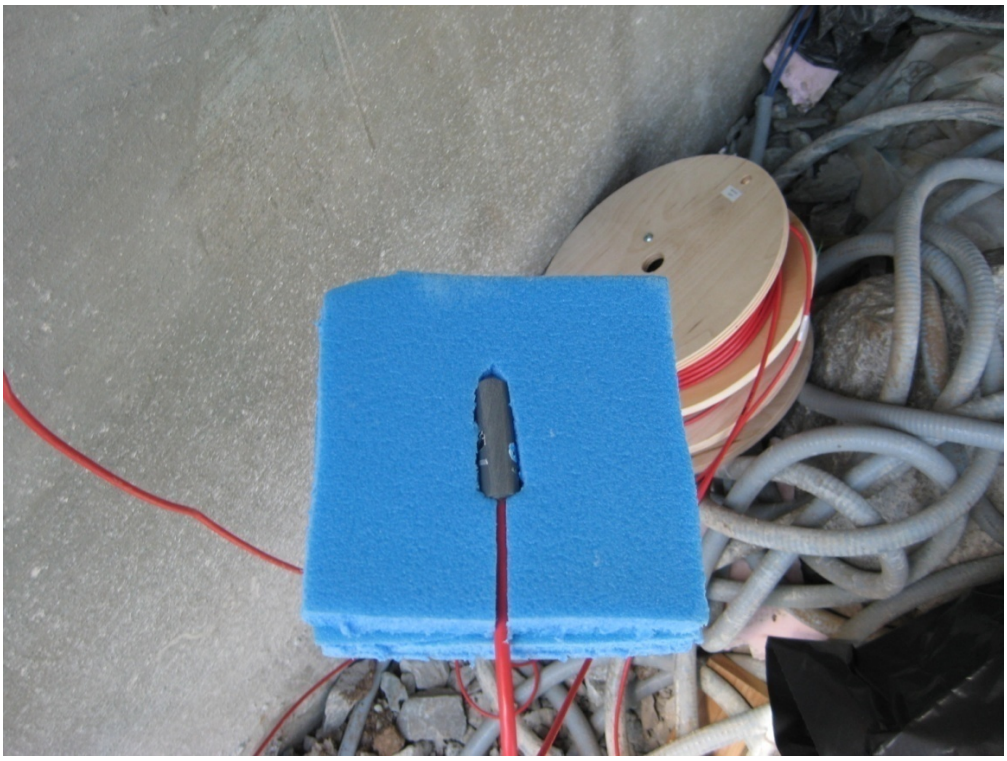

Figure 5.43: Thermistor inside Foam Protection

Figure 5.44: Thermistor after Being Installed on the Bridge

Figure 5.45: Installed Thermistors on the Top and Bottom of the Bridge Deck

5.1.6 Data Collection

Once all of the instruments were installed, the data collection began. To collect the data transmitted from the 46 installed instruments, a Geokon Model 8021-1 Micro-1000 Datalogger and 3 Geokon Model 8032 16 Channel Multiplexers were used. The Datalogger is designed to support the readings of a large quantity of vibrating wire instruments through the use of the 16 Channel Multiplexers. Each multiplexer can handle 16 different instruments, thus the 46 (originally 48, but 2 strain gages were removed) instruments could be monitored by 3 Multiplexers connected to the Datalogger. The Datalogger and Multiplexers were installed on the inward facing abutment wall on the north side of the bridge. Figure 5.46 shows the installed data collecting hardware.

Figure 5.46: Installed Datalogger (Top) and Three Multiplexers (Bottom)

Every time a reading is taken, the Datalogger sends a signal to the Multiplexers to pluck the vibrating wires. The frequency of the plucked wire when it returns from the instrument back to the Multiplexer is stored in the Datalogger and converted to the appropriate unit for the corresponding instrument to attain a reading. The process is repeated at whatever reading rate is chosen. Originally data was collected every 10 minutes. This reading frequency was used from June 23, 2009 to July 22, 2009. The problem with taking readings at this frequency was that the life of the 12-Volt battery of the Datalogger was only approximately 2 weeks. The reading frequency was changed to once an hour from August 12, 2009. This reading frequency provided a battery life of approximately 2 months. A reading frequency of once an hour was deemed adequate to provide insight into the behavior of the bridge while limiting the visits to the bridge site

that was located 90 miles from the University of Oklahoma. During each site visit, the battery was changed and the data was downloaded on to a laptop.

Monitoring of the north side strain gages, earth pressure cells, and tiltmeters started on June 23, 2009. The data collection began on the south side began on July 3, 2009 after securing the south side cables to the bridge using a steel cable and anchors. The last instruments to be monitored were the crackmeters, because they were not installed until July 9, 2009. Starting on July 9, 2009, data from all installed instruments are being collected.

5.2 INSTRUMENTATION SUMMARY

Table 5.1 summarizes the numbers, locations, and purposes for all the instruments discussed in the Section 5.1:

Table 5.1: Instrumentation Summary

Instrument Type	Amount	Locations	Purpose
Strain Gage	16 (10 South and 6 North)	Welded on Abutment Piles	Determine the strain, axial load, and bending moment in the piles
Earth Pressure Cell	6 (2 South and 4 North)	Mounted on Backfill Side of Abutment Walls	Determine the change in earth pressure on the abutment wall
Tiltmeter	4 (2 South and 2 North)	Mounted Under the Bridge Deck on the Abutment Walls	Determine the tilt of the bridge at the locations
Crackmeter	4 (2 South and 2 North)	Mounted between 2x4 and Parapet Wall over the Expansion Joint	Determine the relative displacement between the approach slab and the pavement
Thermistor	16 (3 South and 13 North)	At various locations such as on top of the deck, bottom of the deck, and at various positions on the girders	Measure the temperature at the assigned locations

6 BEHAVIOR OF OKLAHOMA IAB FOR DAILY TEMPERATURE VARIATIONS

In this chapter, the instrumentation results for daily temperature variations for the strain gages, earth pressure cells, tiltmeters, crackmeters, and thermistors are presented and discussed.

6.1 STRAIN GAGE RESULTS

In order to study the behavior of the bridge for daily temperature variations, the period of July 14 to July 18, 2009 was selected. After long periods of Oklahoma summer heat right after the installation of the instruments, this period had days where the temperatures greatly decreased when compared to the adjoining days. On July 15, 2009 the high and low temperatures at the Fort Sill Military Base were 103°F and 75°F respectively, then on July 17, 2009, the high and low temperatures dropped to 91°F and 68°F, respectively.

To examine the temperature of the bridge versus time, readings at six different thermistor locations, 28NW, 29NW, 34NW, 36NE, 37NE, and 40NE (see Figure 5.40), were used to compute the average bridge temperature. These locations are spread across the bridge and can be used to develop the most representative average bridge temperature possible. The average temperature variation of the bridge during this period is shown in Figure 6.1. Figures 6.2 - 6.4 show the change in axial strains for the three instrumented piles during the selected time period. The variations in axial strains within the South West (SW), South East (SE) and North East (NE) abutment piles are presented in Figures 6.2, 6.3 and 6.4, respectively. It should be noted that the S or N

located next to a strain gage number refers to what side of the pile that gage was installed on. S stands for South and N stands for North. Figure 5.19 should be used as a reference for the depth of installation for all the strain gages. The changes in axial strains are based on the readings at a specific time minus the initial reading for each instrument. The initial readings are used as a baseline for comparisons.

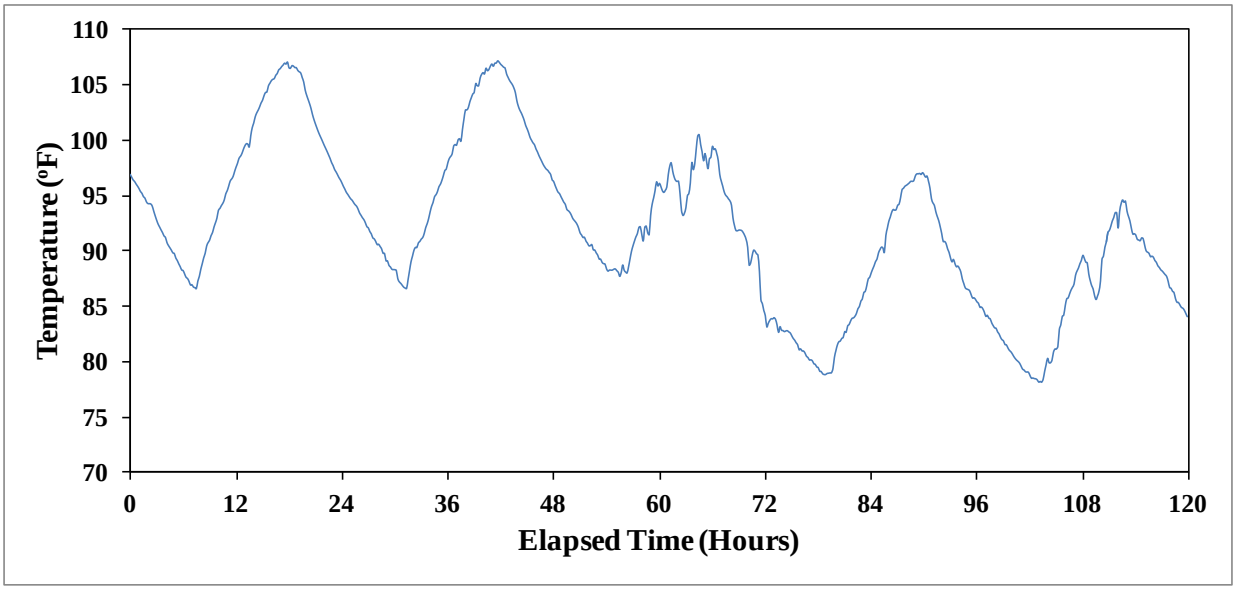

Figure 6.1: Variation of Average Bridge Temperature

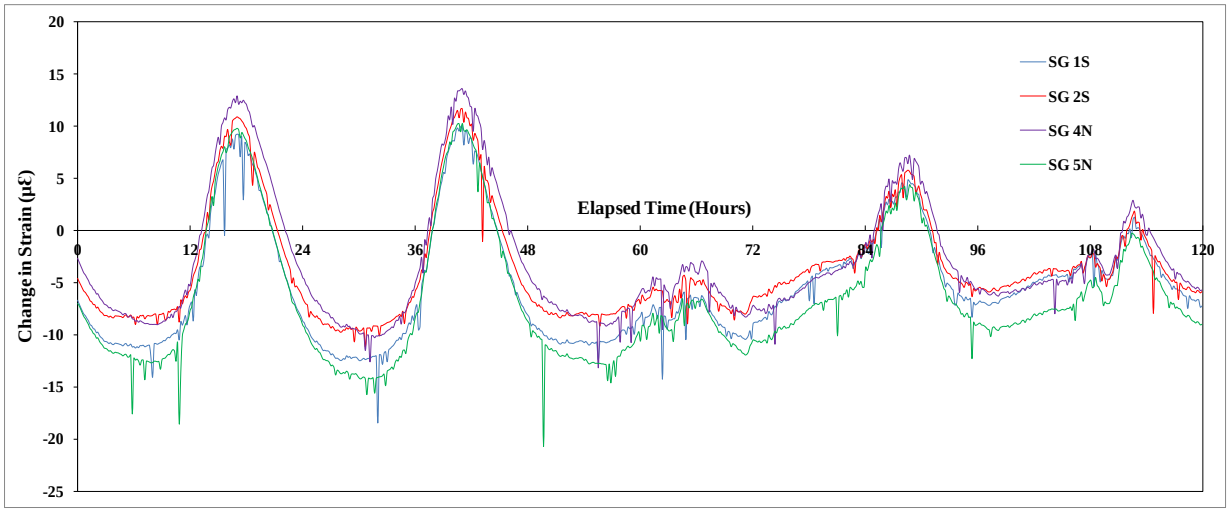

Figure 6.2: Changes in Axial Strains in SW Abutment Pile

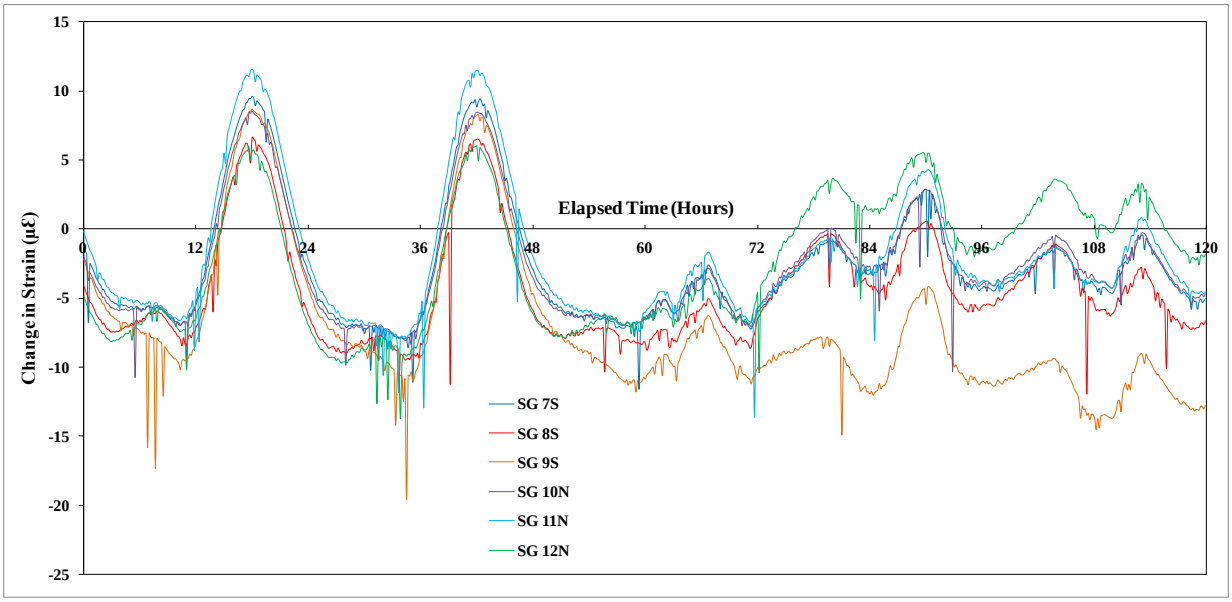

Figure 6.3: Changes in Axial Strains in SE Abutment Pile

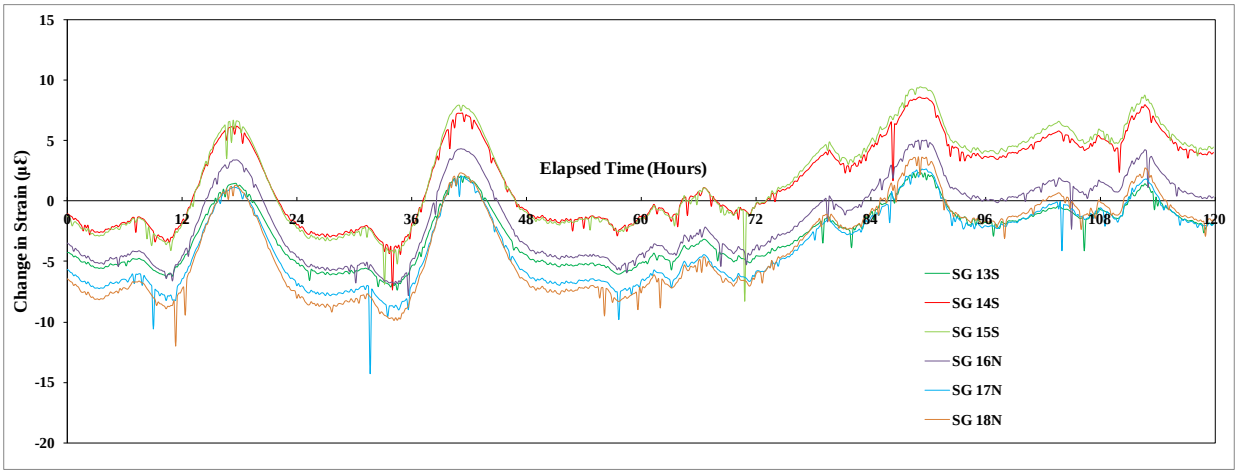

Figure 6.4: Changes in Axial Strains in NE Abutment Pile

The axial strains can be interpreted as follows; if the axial strain is decreasing with time (i.e. sloping downward), that means the strain gage is being compressed, which also means the compressive axial strain is increasing. The opposite is true when the change in axial strain is increasing with time, which means the strain gage is elongating or the axial compressive strain is decreasing. It should be noted here that the initial baseline reading of all the strain gages correspond to compressive stresses caused by the axial loads on the piles. According to the strain measurements, it appears that as the temperature of the bridge increases, the axial strain on the piles decreases or becomes less compressive. When the temperature decreases on the other hand, the gage readings decrease, thus the axial compressive strain on the pile is increasing with time. The results appear to show that as the bridge is expanding due to the increase in temperature, the downward strain on the piles decreases, which may be caused by the increased horizontal load created by the expansion. The increased horizontal loads appear to decrease the axial loads on the piles. The effect of the depth

of the strain gages can also be noticed in Figures 6.2 - 6.4. Table 6.1 presents change in axial strain for July 15, 2009 for all the strain gages at various depths.

Table 6.1: Daily Change in Axial Strain for All Strain Gages for 7/15/09

Strain Gage	Pile	Side of Pile	Position	Depth	Change in Bridge Temperature (°F)	Approximate Daily Change in Axial Strain (με)
1	SW	South	Bottom	2'-3"	28	22.0
2	SW	South	Middle	5'-3"	28	21.3
4	SW	North	Bottom	2'-3"	28	23.7
5	SW	North	Middle	5'-3"	28	24.3
7	SE	South	Bottom	1'-2"	28	17.7
8	SE	South	Middle	4'-2"	28	16.3
9	SE	South	Top	7'-2"	28	19.3
10	SE	North	Bottom	1'-2"	28	16.7
11	SE	North	Middle	4'-2"	28	19.7
12	SE	North	Top	7'-2"	28	15.3
13	NE	South	Bottom	15'-3"	28	9.0
14	NE	South	Middle	18'-3"	28	11.0
15	NE	South	Top	21'-3"	28	12.3
16	NE	North	Bottom	15'-3"	28	11.0
17	NE	North	Middle	18'-3"	28	10.7
18	NE	North	Top	21'-3"	28	12.0

For the most part, on each individual pile, the axial strain tended to be higher for the higher positioned gages when compared to the ones below it. It was expected that the higher the gage is on the pile, the more strain would be observed. Also, when near the top of the pile, more bending should occur due to the bridge expanding or contracting when compared to a deeper position. The changes in axial strain were found to be higher in the two south piles that had strain gages closer to the surface when compared to the north east pile.

The strain gages ended up not being good indicators of whether the skew would affect the thermal loading on the bridge, due to the fact that all the gages were installed at different depths. However the results can be used to show that the thermal induced strains on the piles tend to be higher the closer to the surface the gages are located.

6.2 EARTH PRESSURE CELL RESULTS

Figure 6.5 presents the changes in earth pressure and temperature versus time for the selected time period. Refer to Figures 5.21 to 5.23 for locations.

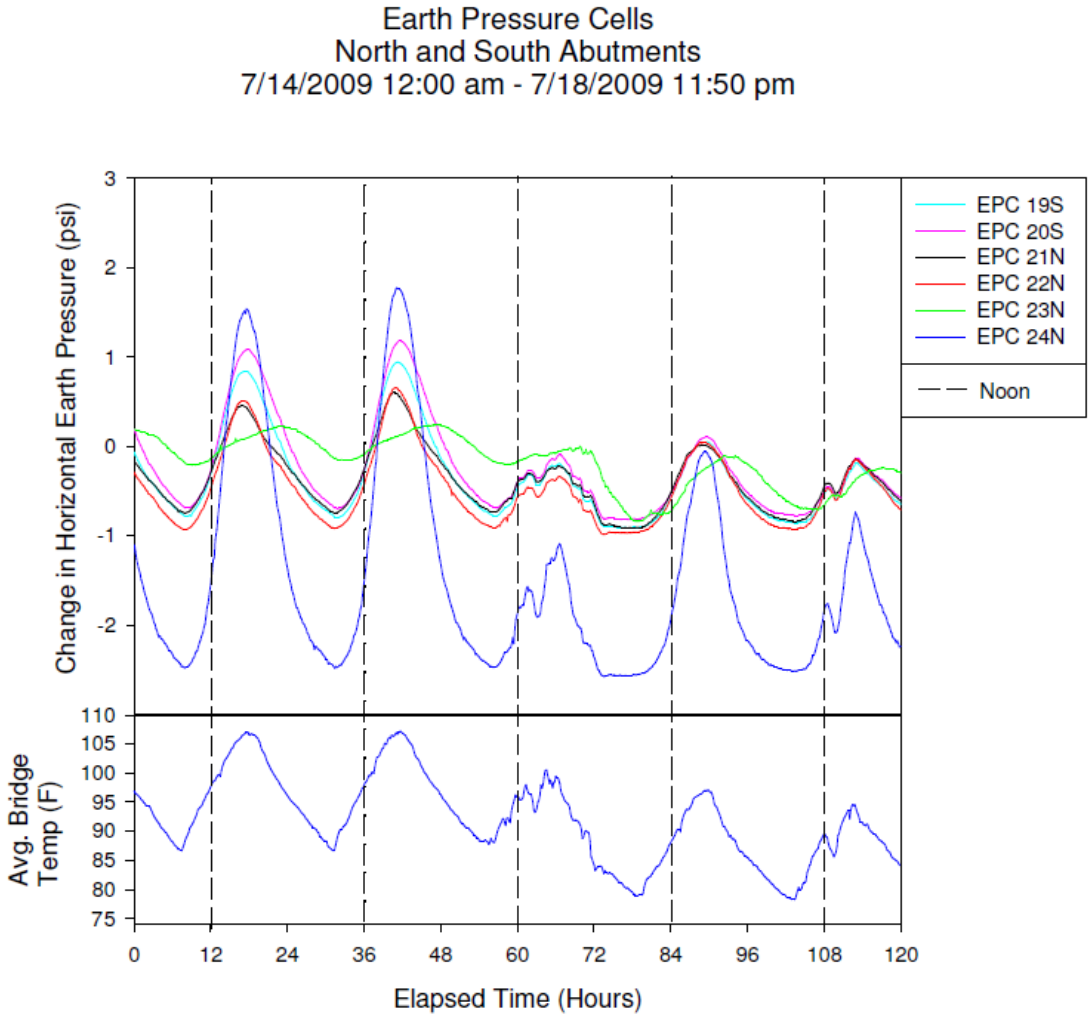

Figure 6.5: Earth Pressure Cell Readings from 7/14/09 through 7/18/09

Based on the results, it appears that the readings for the earth pressure cells are consistent and tend to follow what was expected. The earth pressure cells show a distinct pattern that follows the change in temperature versus time. As the temperature increases, the pressures increase, just as expected. As the bridge expands due to heating, the abutment walls tend to push on the soil backfill, thus increasing the earth

pressure on the wall. Table 6.2 shows the daily change in earth pressures at the cell locations.

Table 6.2: Earth Pressure Cell Readings for 7/15/09

EPC	Abutment Wall Position	Acute Obtuse or Middle	Change in Temperature (°F)	Approximate Change in Earth Pressure (psi)
19	Top South-West	Obtuse Corner	28	1.75
20	Top South-East	Acute Corner	28	1.88
21	Top North-West	Acute Corner	28	1.35
22	North Top	Middle	28	1.59
23	North Bottom	Middle	28	0.38
24	Top North-East	Obtuse Corner	28	4.25

The earth pressure cells on the north abutment wall provided interesting results. The pressure changes were higher on the obtuse corner location when compared to the middle and acute corner locations. The pressure changes measured in the obtuse corner were more than three times as high as any of the other pressure changes measured on the north wall. The top middle cell pressures were higher than the acute corner cell pressures. Also the middle bottom cell pressure change was much lower than middle top cell pressure change. This is consistent with the abutment wall rotating about its bottom. On the other hand, the earth pressure cells on the south abutment did not clearly align with the expectations. The change in earth pressure for the two south abutment cells was basically similar for both the acute corner and the obtuse corner. Both corners had less change in pressure than was observed at the obtuse corner of the north abutment wall. These results translate to there being less earth pressure transmitted to the south abutment than the north abutment. This may be due to backfill

being compacted differently on the south side than the north side. If one side of the backfill was compacted differently than the other, the pressures being measured may not directly correlate with the bridges movement. One side of the wall with greater backfill stiffness may result in higher measured pressures. Without a detailed analysis of the backfill compaction, it is difficult to conclude whether or not this is a factor. Another possible explanation for the variation in earth pressures from one side of the bridge to the other may be the fact that the piles on the north side were driven down to bedrock while the south side used pilot holes to get down to bedrock. The pilot holes were backfilled with sand, thus possibly providing less lateral resistance when compared to the driven piles in the naturally compacted native soil. Because the method of pile driving and length of piles were different on both sides of the bridge, this may help to explain the lack of symmetry in the results from North to South and East to West. Detailed analysis of bending of piles presented in Chapter 8 also supports this observation.

The earth pressure cells on the north abutment indicate that the skew of the bridge may affect the pressures across the wall. The pressures on the obtuse corner were more than three time higher than the pressure on the acute corner possibly because of the 10° skew of the bridge. The south abutment readings, however, seemed to show no affect due to the skew angle. Figure 6.6 shows the pressures across the north abutment wall at three different times on July 15, 2009.

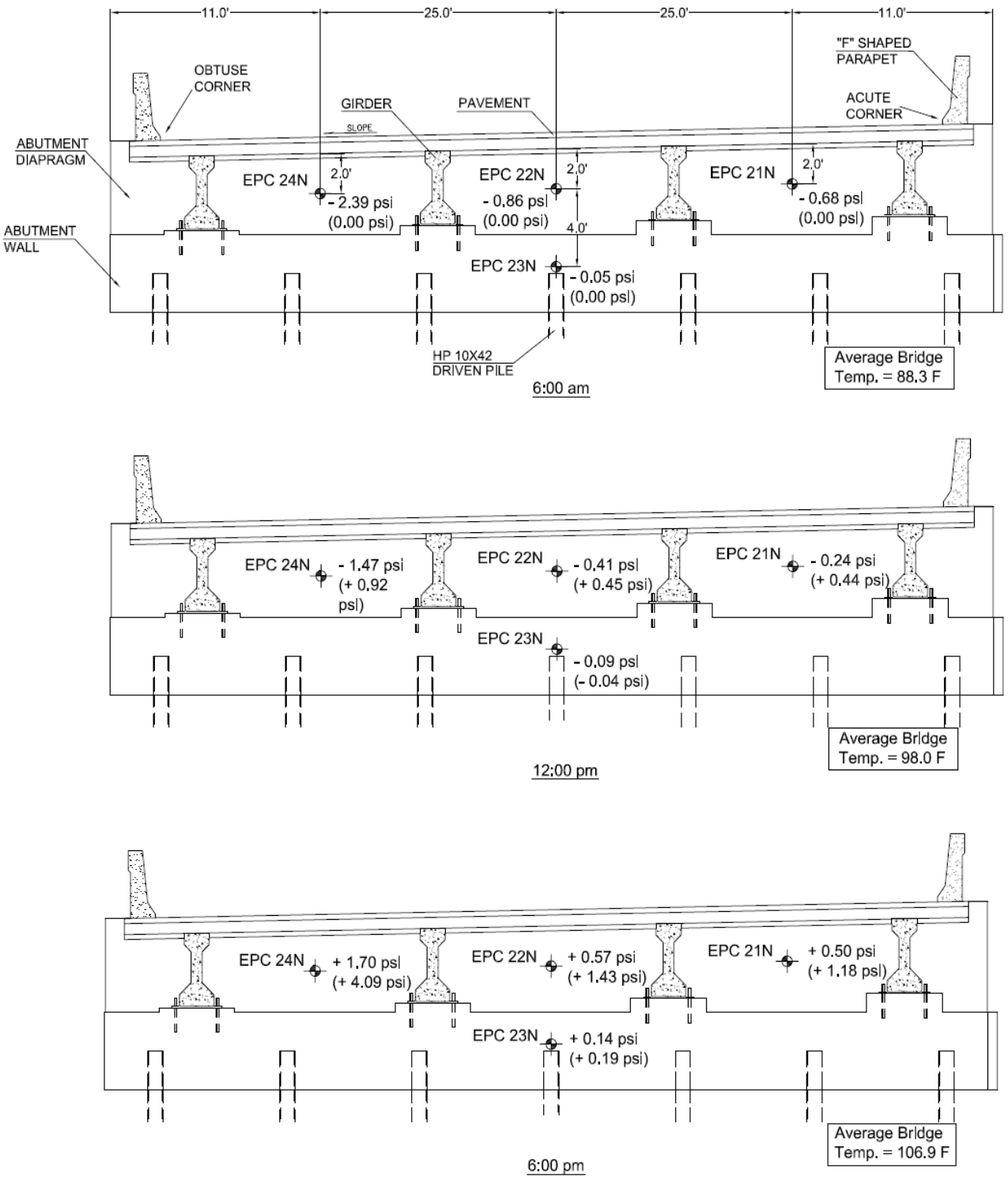

Figure 6.6: Earth Pressure Cell Readings for the North abutment at Various Times on July 15, 2009

(Numbers in Parentheses Indicate Change Relative to 6.00 AM)

From Figure 6.6, it can be concluded that the changes in pressures between the backfill and the abutment wall are higher on the obtuse side of the wall when compared to the acute side for the entire day. Figure 6.7 shows how the earth pressure varies with temperature over the entire day of July 15, 2009.

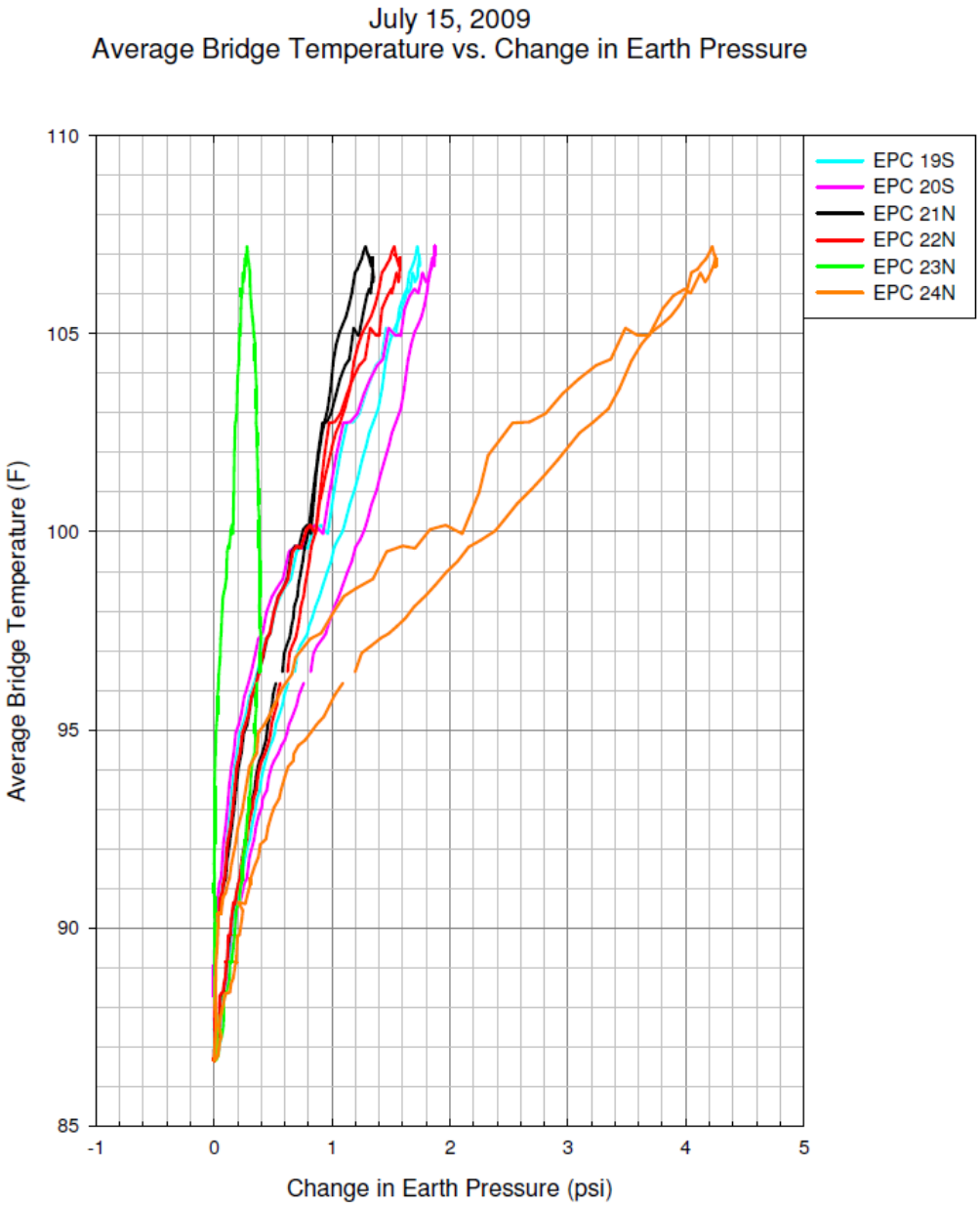

Figure 6.7: Change in Earth Pressure vs. Average Bridge Temperature on July 15, 2009

From Figure 6.7 it appears that the earth pressure varies with temperature similarly for all the earth pressure cells. EPC 24, located on the obtuse corner of the north wall showed the highest variation with temperature, while EPC 23, located in middle bottom of the north wall, showed the lowest variation with temperature.

6.3 TILTMETER RESULTS

Figures 6.8 and 6.9 show the readings for the tiltmeters from July 14 to July 18, 2009.

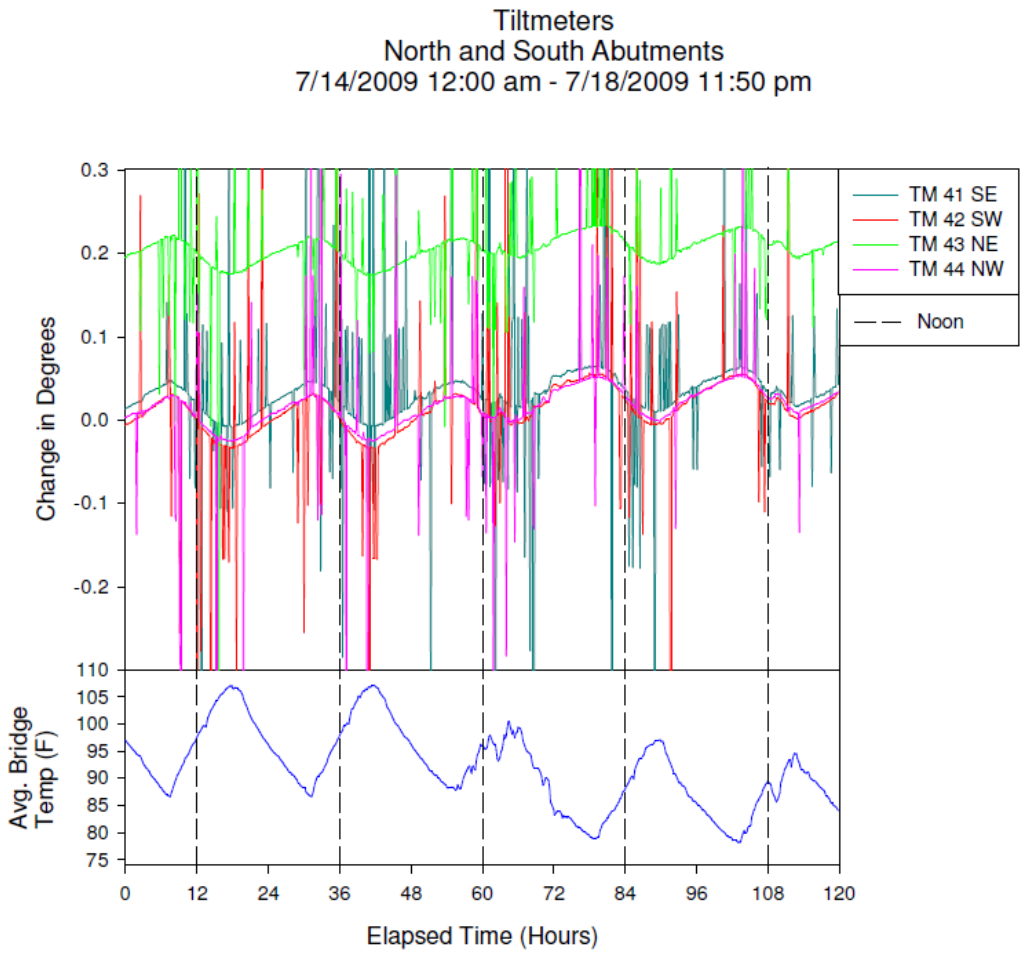

Figure 6.8: Tiltmeter Readings from 7/14/09 through 7/18/09

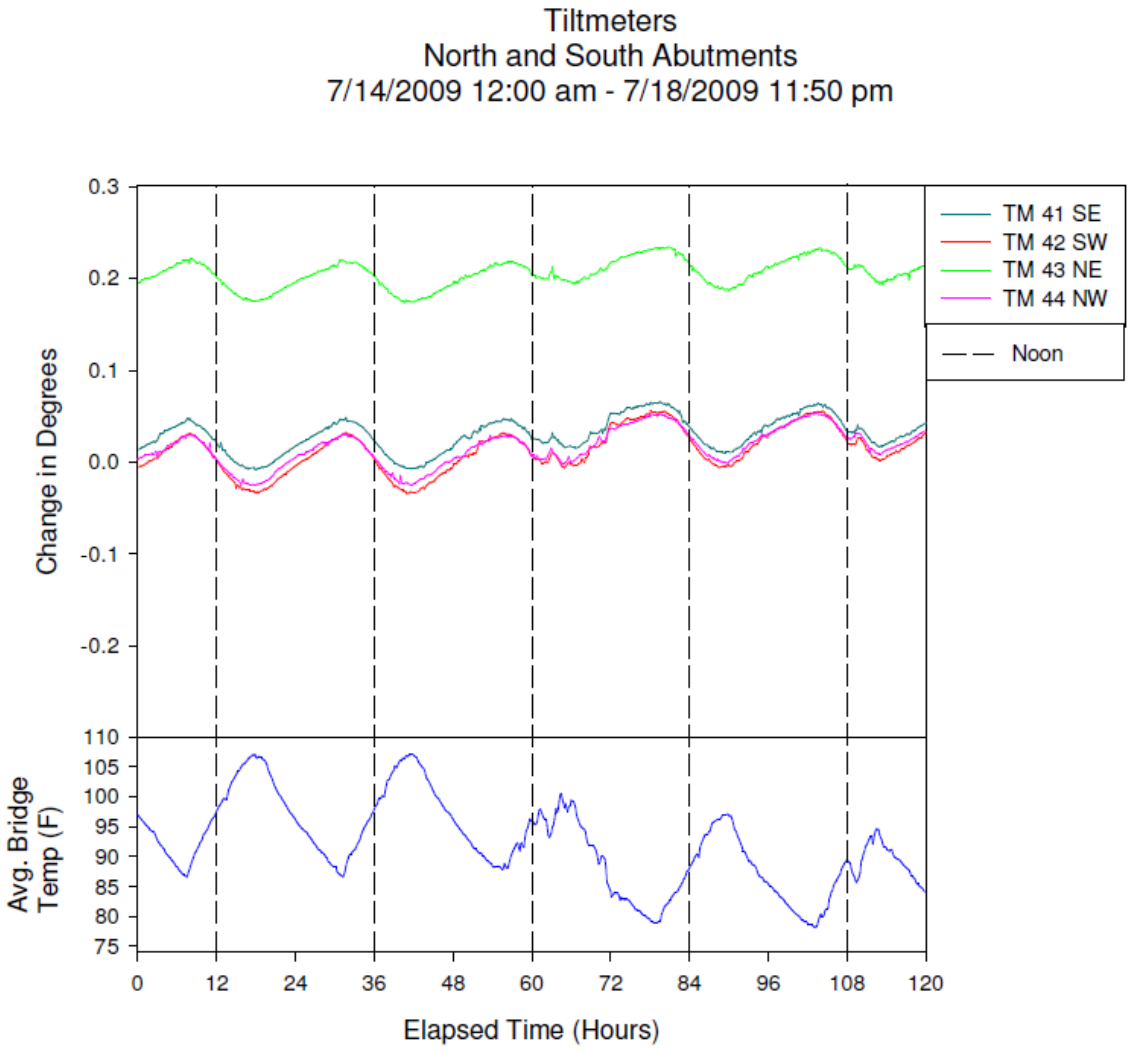

Figure 6.9: Basic Trend in Tiltmeter Readings from 7/14/09 through 7/18/09

Based on the results, it appears that the readings for the tiltmeters are consistent from day to day and show a distinct pattern that follows the shape of the change in temperature versus time. The tiltmeters are very sensitive to movement, so whenever a large vehicle drives over the bridge as the datalogger takes a tiltmeter reading, the reading may be affected. That could be a reason there are so many spikes in the data. After removing the spikes, a basic trend of the data can be observed. It has a curve that is similar in shape to the temperature versus time plot as shown in Figure 6.9. A positive

change in tilt means that the wall is rotating into the backfill and a negative change in tilt means that the wall is rotating away from the backfill. This parallels the finding of the strain gages and earth pressure cells that the bridge is expanding when heated and pushing on the top of the abutment walls, and vice versa when the bridge is cooled. The following table shows the change in tilt at the tiltmeter locations.

Table 6.3: Tiltmeter Readings for 7/15/09

Tiltmeter	Abutment Wall	Position	Change in Temperature (°F)	Approximate Change in Tilt (Degrees)
41	Southeast	Acute Corner	28	0.053
42	Southwest	Obtuse Corner	28	0.066
43	Northeast	Obtuse Corner	28	0.044
44	Northwest	Acute Corner	28	0.057

The abutment wall is approximately 9 feet tall (including bridge deck thickness). If the wall tilts 0.05 degrees, that correlates to the top of the wall moving 2.4 mm or 0.094 inch assuming the bottom is stationary. So in general, the wall moves between 2 to 4 mm a day based on the readings from July 15, 2009.

The changes in tilt at the tiltmeter locations were pretty consistent. The south obtuse corner saw the highest changes in tilt, followed by the north acute corner, the south acute corner, and the lowest tilts were observed at the north obtuse corner location. Based on the results, it seems the bridge is tilting more on the west side of the bridge when compared to the east side. These results do somewhat parallel the findings with the other instruments. The lowest daily tilt variation occurred at the north obtuse corner of the bridge, which is where the highest earth pressures are being measured. Maybe the backfill behind the wall is more compacted at the corner which

lowers the movement of the abutment wall while increasing the earth pressure against the wall. On each side of the bridge, the corner with the lower tilt had a higher earth pressure.

6.4 CRACKMETER RESULTS

Figure 6.10 shows the readings for the crackmeters from July 14 to July 18, 2009.

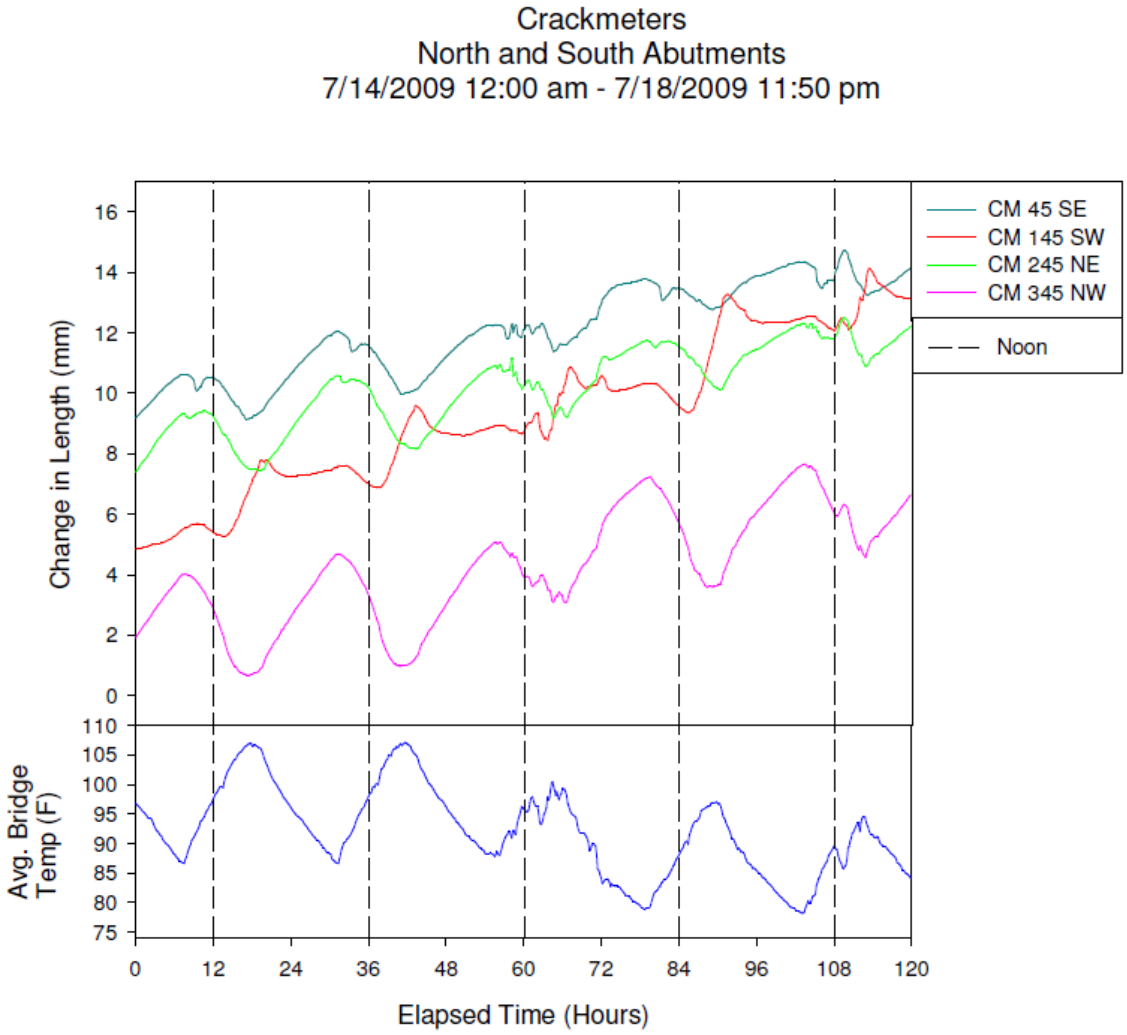

Figure 6.10: Crackmeter Readings from 7/14/09 through 7/18/09

Based on the results, it appears that the readings for the crackmeters are consistent from day to day and show a distinct pattern that follows the shape of the change in temperature versus time. The results for CM 145 SW should be used with caution. A wrong wire length was used for this crackmeter and the original wire length was not sufficient to reach the multiplexer. To extend the wire, a splicing technique suggested by Geokon was used. It appears the change in joint width measured by CM 145 SW is similar to the other crackmeters, but the results are flipped upside down. This may have been caused by the wires being crossed during the splicing process. The readings for CM 145 SW should only be used analyzing the change in width of the expansion joint. The trend of the data for the other crackmeters goes down as the temperature goes up, which means the gap in the expansion joint is closing as the bridge is expanding due to thermal loading. This parallels the finding of the other instruments that show the bridge is expanding when heated and thus pushing out on the top of the abutment walls and the approach slab causing the expansion joints to close. Table 6.4 shows the change in readings at the crackmeter locations.

Table 6.4: Crackmeter Readings for 7/15/09

Crack-meter	Side of Bridge	Position	Change in Temperature (°F)	Approx. Change in Expansion Joint Gap (mm)
45	Southeast	Acute Corner	28	2.06
145	Southwest	Obtuse Corner	28	2.71
245	Northeast	Obtuse Corner	28	2.41
345	Northwest	Acute Corner	28	3.70

The results show that the change in expansion joint width was higher on the west side of the bridge when compared to east side. These results parallel the results from the tiltmeters. Both the crackmeters and tiltmeters indicated between 2 to 4 mm of bridge movement a day.

6.5 THERMISTOR RESULTS

To present the temperature variation through the bridge deck, through the girders, and across the abutment wall, temperatures are shown at 5 different times of the day at various locations across the north abutment wall. Figure 6.11 shows how temperature varied across the north abutment wall on July 14, 2009.

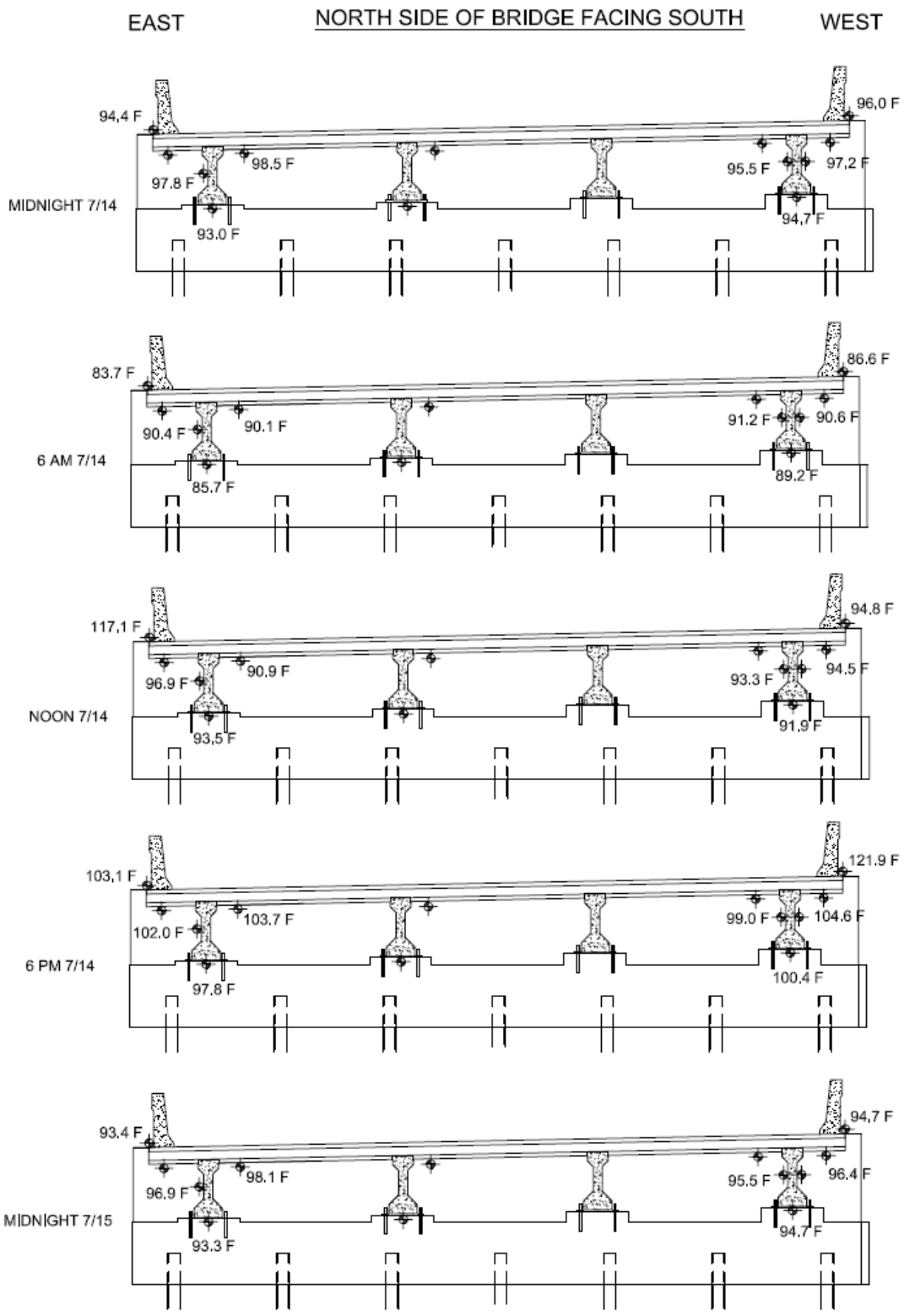

Figure 6.11: Temperature Readings for North Side of Bridge: 7/14/2009

All the temperature readings are shown from the perspective of north abutment wall facing south. This would mean when looking at the abutment wall in Figure 6.11, left would be east and right would be west. The results of the temperature readings were as expected. At midnight, the concrete maintains some of the heat from the day, and then the concrete cools down from midnight to 6:00 AM. As the sun rises in the east, the east side of the bridge heats up due to direct sunlight exposure from 6:00 AM to noon. During the warmest times of the day, the sun is directly over the bridge and works its way to the west side of the bridge as it sets. The 6:00 PM gradient plots show the shift of the highest temperatures from the east side of the bridge to the west. Once the sun sets, the concrete retains some heat from the day, but greatly decreases in temperature from the 6:00 PM to midnight. Figure 6.12 shows how the temperature varies at all the thermistor locations on July 15, 2009. For locations of the thermistors, refer to Figures 5.39, 5.40, and 5.41.

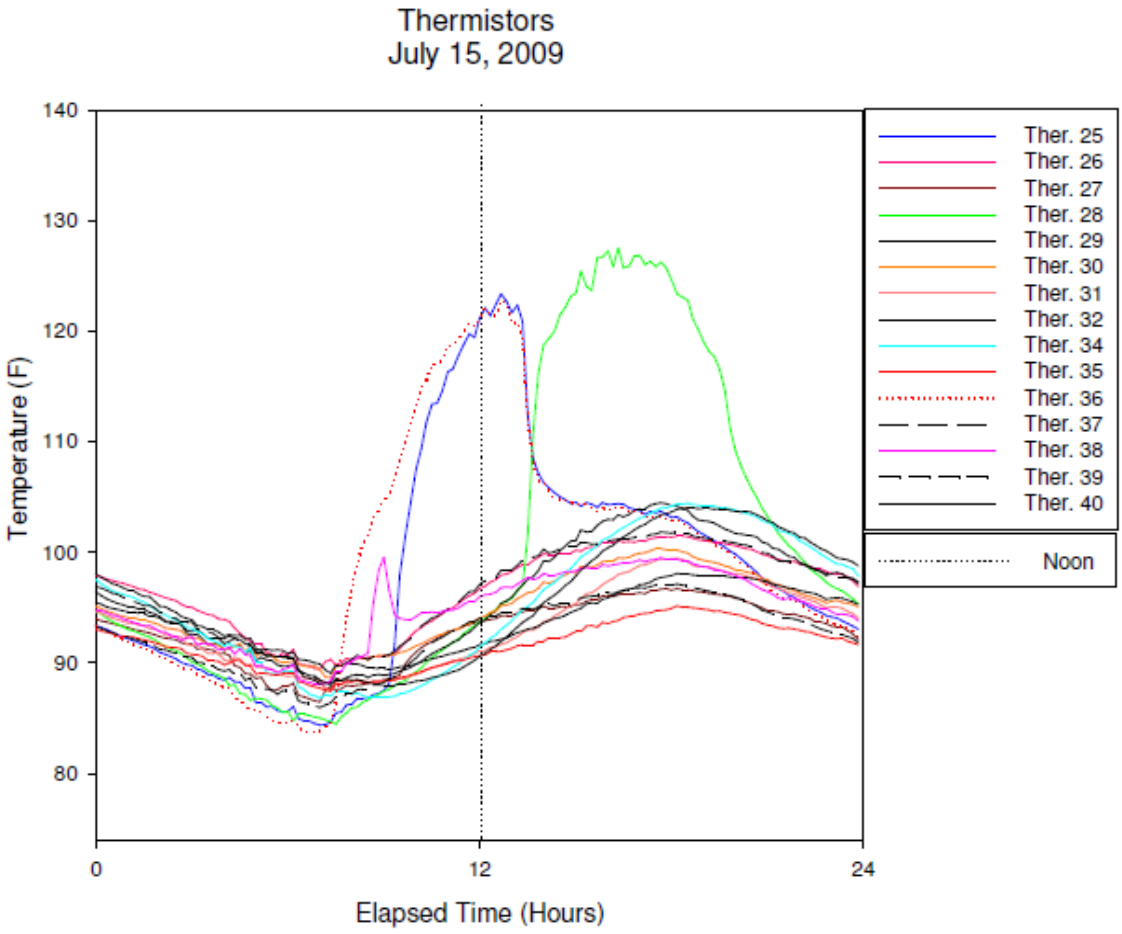

Figure 6.12: Thermistor Readings for July 15, 2009

All the readings seemed to follow the same path, except for the gages installed on top of the bridge deck. The readings for the gages on the east side of the bridge increase before the readings on the west side for comparable locations. This trend can be seen in Figure 6.12 when comparing Thermistor 36 (NE corner) to Thermistor 28 (NW corner). Thermistor 36 peaks earlier in the day when compared to the gage at a comparable location (Thermistor 28) on the other side of the bridge. This is because the sunlight directly shines on the east side of the bridge before the west side.

Table 6.5 compares the variations in temperature from the north side of the bridge when compared to the south side by presenting the readings from the same

positions on each side of the bridge at the same times. Table 6.6 compares the variation in temperature across the north abutment wall at the same positions on both the east and west sides.

Table 6.5: South vs. North Thermistor Reading Comparison for 7/15/09

Time and Date	Southeast Side Temperature (°F)			Northeast Side Temperature (°F)		
	Top of Deck 25 SE	Bottom of Deck 26 SE	Bottom of Girder 27 SE	Top of Deck 36 NE	Bottom of Deck 37 NE	Bottom of Girder 39 NE
Midnight 7/15/09	93.4	97.9	94.0	93.4	96.9	93.3
6 AM 7/15/09	85.6	90.7	87.9	84.5	90.4	87.5
Noon 7/15/09	121.1	96.7	93.7	121.3	97.1	94.0
6 PM 7/15/09	103.2	101.4	96.6	102.9	101.8	97.1
Midnight 7/16/09	92.8	96.5	91.8	91.8	97.3	91.6

Table 6.6: West vs. East Thermistor Reading Comparison for 7/15/09

Time and Date	Northwest Side Temperature (°F)			Northeast Side Temperature (°F)		
	Top of Deck 28 NW	Bottom of Deck 29 NW	Bottom of Girder 31 NW	Top of Deck 36 NE	Bottom of Deck 37 NE	Bottom of Girder 39 NE
Midnight 7/15/09	94.7	96.4	94.7	93.4	96.9	93.3
6 AM 7/15/09	85.6	89.7	88.7	84.5	90.4	87.5
Noon 7/15/09	93.8	93.7	91.1	121.3	97.1	94.0
6 PM 7/15/09	124.7	104.2	99.4	102.9	101.8	97.1
Midnight 7/16/09	95.2	97.2	94.1	91.8	97.3	91.6

Table 6.5 shows that there is very little variation between the temperatures on the south and north sides of the bridge. This means the temperatures across the north abutment wall can generally be assumed to be the same across the entire bridge length. However, Table 6.6 shows that the bridge experiences highest temperatures on

the east side around noon, while the west side experiences its highest temperatures at 6:00 PM.

The temperature loading of the bridge is very complex. The east side of the bridge is thermally loaded in the morning at a higher rate than the west side because it is directly exposed to the sun. During the middle of the day, when the sun is directly above the bridge, both sides may be heated equally but the east side may retain some heat from the morning exposure that was not experienced on the west side, so even though both sides are being exposed to the same temperature, the loading on the east side is higher than the west side at that particular time. Once the sun starts moving westward, the heat on the east side of the bridge begins to dissipate as the west side is heated up. So the west side is exposed to more extreme heat when it is directly loaded between 5:00 and 6:00 PM, compared to when the east side was directly loaded in the morning.

7 BEHAVIOR OF OKLAHOMA IAB FOR SEASONAL TEMPERATURE VARIATIONS

7.1 INTRODUCTION

The connections between the superstructure and abutments for IABs are rigid joints. As a result of the restrained displacements of the bridge superstructure that are caused by the integral construction, thermal expansion and contraction, and concrete creep and shrinkage of the bridge superstructure induces strains in the bridge members. Primary concern of IAB is related to the forces and displacements that are induced in the abutments and abutment piles during the expansion and contraction of the bridge superstructure and therefore the behavior of Oklahoma IAB for seasonal temperature variations is presented in this chapter. Furthermore, seasonal behavior of bridge will indicate the long term performance of the bridge. The data collection started on June 23, 2009 and so far more than 30 months of high quality data from this bridge has been collected, and presented in this discussion. This is the first time such a comprehensive set of data is being collected for an Oklahoma IAB.

Data collection from the north side abutment pile strain gages, earth pressure cells and tiltmeters started on June 23, 2009. Monitoring of the south side abutment pile strain gages, earth pressure cells and tiltmeters started on July 3, 2009. Data collection from the crackmeters started on July 9, 2009. The data from July 23-August 11, August 28-September 7, and October 10-11 in 2009 is not available due to a malfunction in the data acquisition system. Although earth pressure cells EPC 19S and EPC 21N, and abutment pile strain gages SG 1S, SG 4N, SG 7S and SG 10N stopped providing reliable readings after some time, sufficient data has been collected from these gages.

All other instruments are continuing to provide reliable and valuable data. Erroneous data was identified and eliminated before the measured data were presented in this report.

7.2 TEMPERATURE VARIATIONS

Average temperature variation for the bridge is shown in Figure 7.1. The temperature readings at six different thermistor locations (28NW, 29NW, 34NC, 36NE, 37NE, and 40NE) are averaged to calculate a representative bridge temperature that is shown in Figure 7.1. The average temperature change that the bridge superstructure experienced over a six month period of time is 90 – 95 ^{0}F. As shown in Figure 7.1, the bridge temperature decreases for a six-month duration (from July to January) and then increases for the next six-month duration (January to July). This repetitive pattern (cyclic behavior) continues from year to year within the measurement time frame. As will be discussed below, these temperature variations are reflected in other instruments and provide a valuable and complete set of data for an Oklahoma IAB over a 30-month time period. The data collection from these instruments is continuing and additional data will be reported elsewhere.

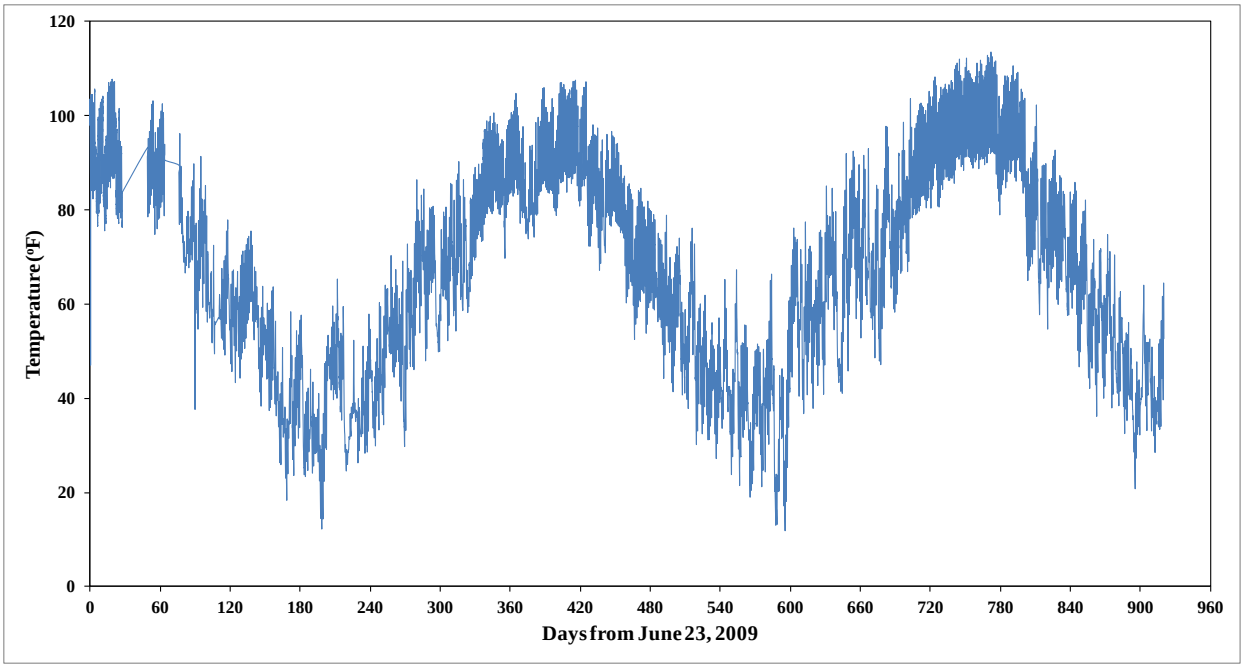

Figure 7.1: Variation of Average Bridge Temperature

The American Association of State Highway and Transportation Officials (AASHTO) Load and Resistance Factor Design (LRFD) Bridge Design Specifications (2007) has been widely used by the bridge-design agencies in the design of IABs. It describes two procedures in Section 3.12 for the selection of design temperature range for IABs with concrete girders and deck, and steel girders and concrete deck. Either Procedure A or Procedure B can be employed for concrete deck bridges having concrete or steel girders. According to Procedure A, the temperature range for IABs with concrete girders in moderate climate condition is 10 ^{0}F to 80 ^{0}F. Procedure A is considered as the historic method that has been used for bridge design and the specified minimum and maximum temperatures are considered as $T_{minDesign}$ and $T_{maxDesign}$ for the bridge design. Therefore the temperature change considered for the design is 70 ^{0}F. According to Procedure B, the temperature range ($T_{minDesign}$ and $T_{maxDesign}$) for IABs with concrete girders and deck located in Lawton, OK is 15 ^{0}F to 115

^{0}F. Therefore the temperature change considered for the design is 100 ^{0}F. Contour maps for maximum and minimum design temperatures for bridges located throughout the U.S. with two different bridge superstructure conditions (concrete girders and deck, and steel girders and concrete deck) are presented in Procedure B. The field measured bridge temperatures for Oklahoma IAB agrees with the temperature range specified in Procedure B.

7.3 EARTH PRESSURES ON ABUTMENTS

The backfill soil pressure is measured with earth pressure cells behind the abutments. Changes in earth pressures recorded are shown in Figure 7.2. Vertical variations in earth pressures can be seen in Figure 7.3, where the recorded readings for EPC 22 and 23 are presented. The baseline reading for EPC 24N (Green curve in Figure 7.2) seems to have drifted after about 420 days and the data from this EPC should be used with caution. It can be observed that as the temperature decreases, earth pressures decrease and as the temperature increases, earth pressures increase. This is consistent with the expected behavior that as the temperature increases the bridge will expand and push the abutments outward resulting in positive changes in earth pressures. Similarly the earth pressures will decrease as the temperature decreases. The maximum earth pressure changes were recorded on the obtuse corner of the north abutment (EPC 24). At this EPC the maximum earth pressure change recorded in a single day was 7.4 psi (51.0 kPa). Krier (2009), using 3-dimensional TeraDysac (Muraleetharan et al. 2003) computer simulations, predicted that in a skewed IAB, obtuse corners will experience larger earth pressure changes for a given temperature increase. The primary reason for this difference is that the perpendicular

distance between the force vectors acting on the obtuse corners is smaller than that of the acute corners and hence the obtuse corners will carry larger loads for a given displacement of the abutments to keep the bridge in equilibrium. Why similar behavior is not seen in the obtuse corner of the south abutment (EPC 20) is not clear at this point. Moreover, as shown in Figure 7.3, larger changes in earth pressures were observed near the bridge deck (EPC 22) than at a depth (EPC 23). The abutments are expected to rotate and translate as a rigid body during heating and cooling of the bridge and hence the top of the abutments will undergo larger lateral displacements and hence larger changes in earth pressures. The observed earth pressures (Figure 7.3) confirm this expected behavior. Earth pressure measurements show that fairly significant amount of abutment back pressures have been recorded during summer and there is an increase in the earth pressures during summer 2011 when compared to summer 2010.

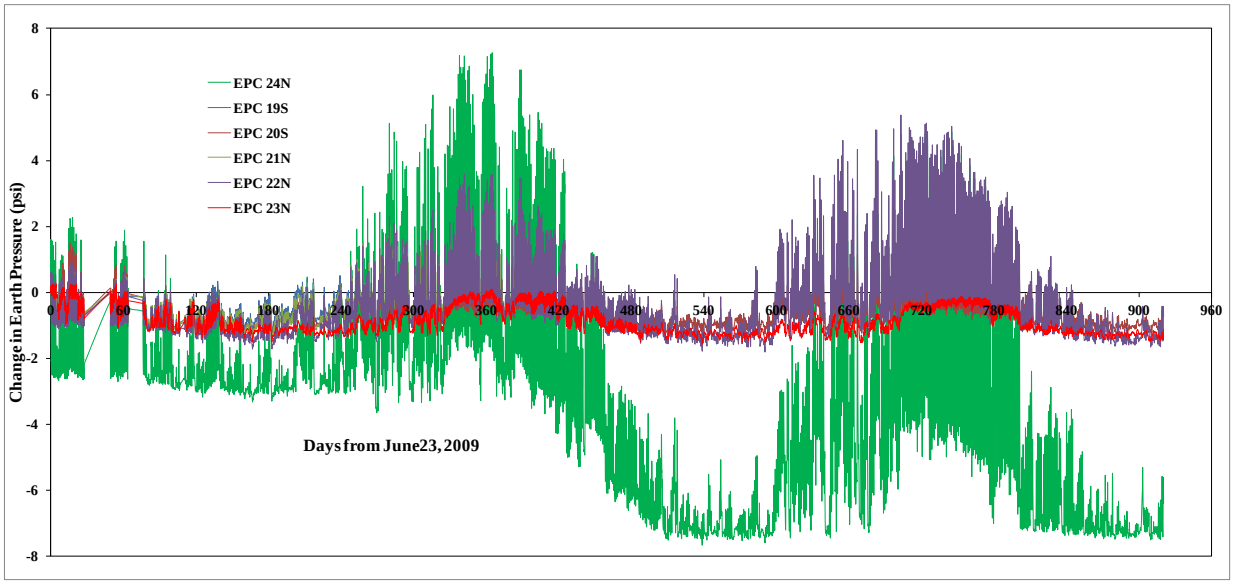

Figure 7.2: Changes in Earth Pressures behind Abutments

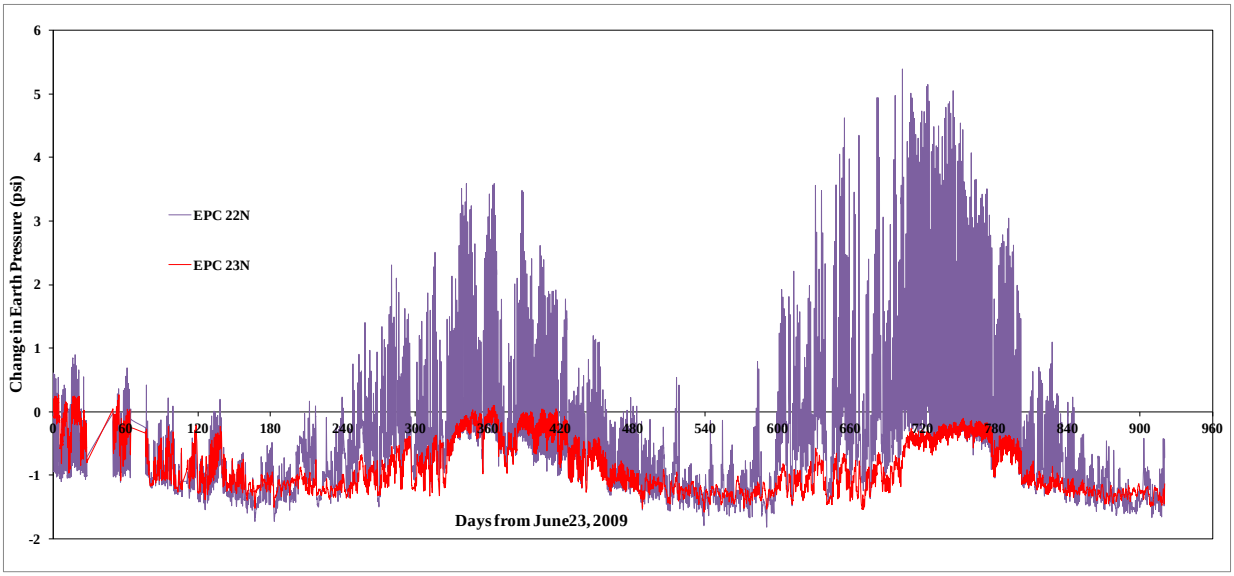

Figure 7.3: Changes in Earth Pressures with Depth on North Abutment

7.4 TRANSLATION OF THE BRIDGE

Crackmeters (CM) were attached between the pavement and the approach slabs to measure the translation of the bridge during heating and cooling. The measured approach slab movements are presented in Figure 7.4. Only crackmeter readings from June 23, 2009 through June 21, 2010 are presented in Figure 7.4 as the crackmeter readings indicate inconsistent behavior after June 21, 2010. As the temperature reduces from July 2009 through January 2010 the expansion joints open (a negative change in length) and as the temperature increases the expansion joints close (a positive change in length). The bridge undergoes 22 mm translation during this period. Independent field measurements confirm the readings from the crackmeters.

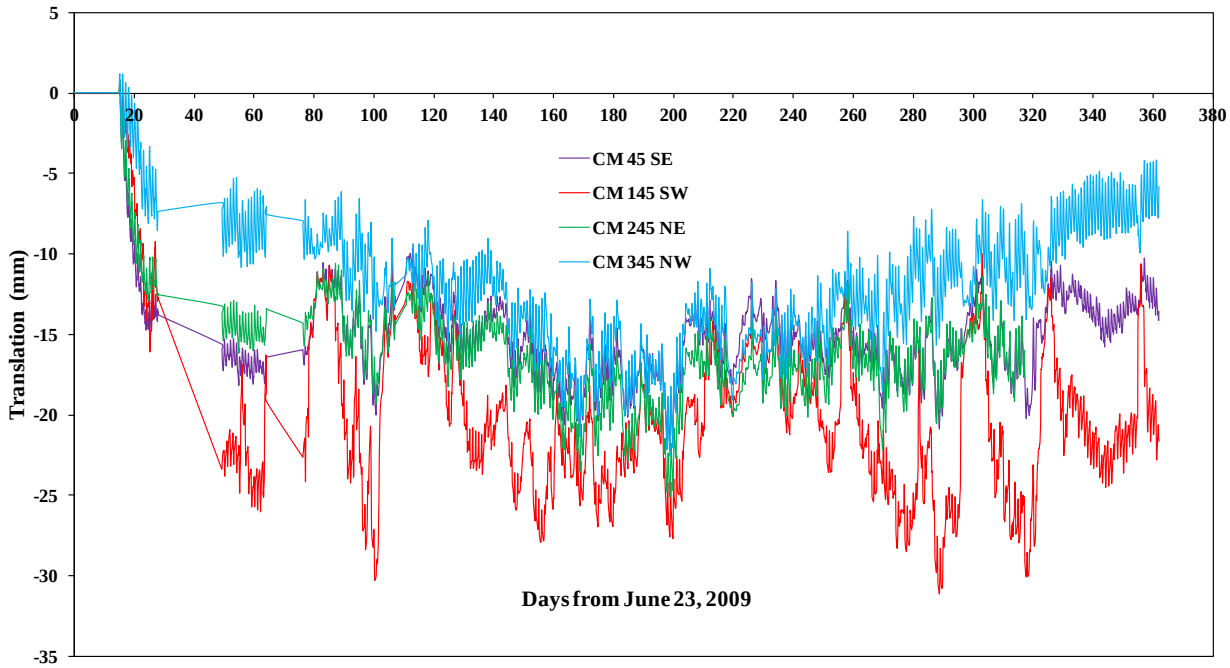

Figure 7.4: Crackmeter Measurements

7.5 ROTATION OF ABUTMENTS

Tiltmeters (TM) were attached to the abutments to measure the rotation of the abutments about a horizontal axis. The measured rotations are shown in Figure 7.5. Only tiltmeter readings from June 23, 2009 through June 21, 2010 are presented in Figure 7.5 as the tiltmeter readings indicate inconsistent behavior after June 21, 2010. Negative changes in rotations are measured during temperature decrease and positive changes in rotations are measured during temperature increase indicating that the abutments rotate inward when the bridge cools and rotates outward when bridge is heated. Tiltmeter data had spikes and they were traffic related vibrations of the tiltmeters and not actual rotations of the abutments. Therefore spikes are removed during the data processing and Figure 7.5 shows the actual rotations of the abutments. Sudden change in TM 43 NE around 20 days (blue curve in Figure 7.5) is suspicious

and the measurement from this tiltmeter should be viewed with caution. The abutment rotates 0.125^0 during this period and it is equivalent to 6 mm translation at the top of the abutment. Since the translation of bridge is 22 mm, rest of the translation (16 mm) is occurring at the top of the abutment piles. Therefore thr majority of translation is accommodated by the abutment pile movements in IABs.

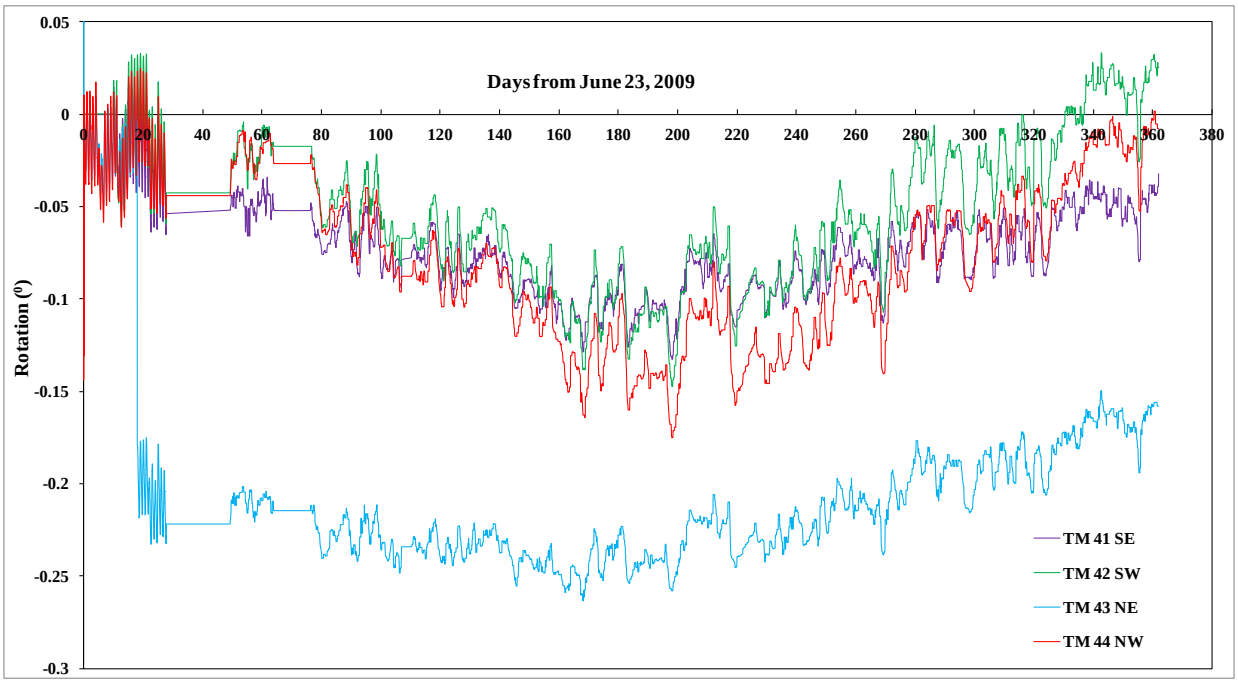

Figure 7.5: Rotations of Abutments

7.6 ABUTMENT PILE STRAINS

The variations in axial strains within the South West (SW), South East (SE) and North East (NE) abutment piles are presented in Figures 7.6, 7.7 and 7.8 respectively. A positive change in strain means an increase in tension at that location and a negative change in strain means an increase compression at that location. Strain gages in the SW and SE abutment piles are located at shallower depths compared to the strain

gages in the NE abutment pile. The abutment movements result in translation of the top of the piles and hence larger strains are expected at the shallower depths.

It can be seen from Figure 7.8 that after some accumulation, strains in NE abutment pile are stabilizing. Since strain gages in NE abutment pile are located at a greater depth, they are not showing larger variations in strains over time. However, strains in the SW and SE abutment piles are continuing to accumulate (Figures 7.6 and 7.7). This observation is further investigated in the next section.

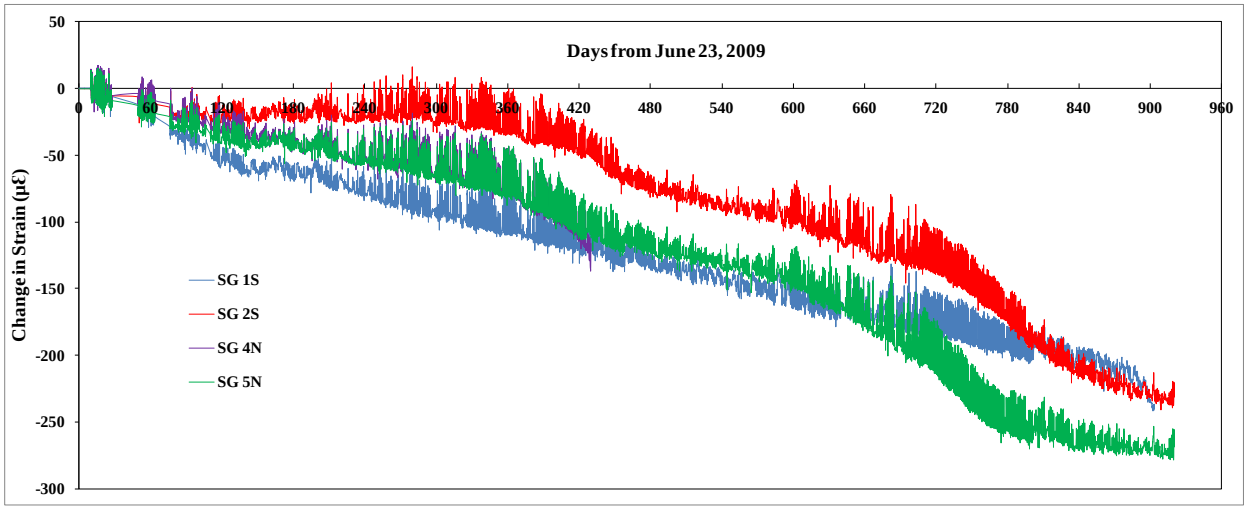

Figure 7.6: Changes in Axial Strains in SW Abutment Pile

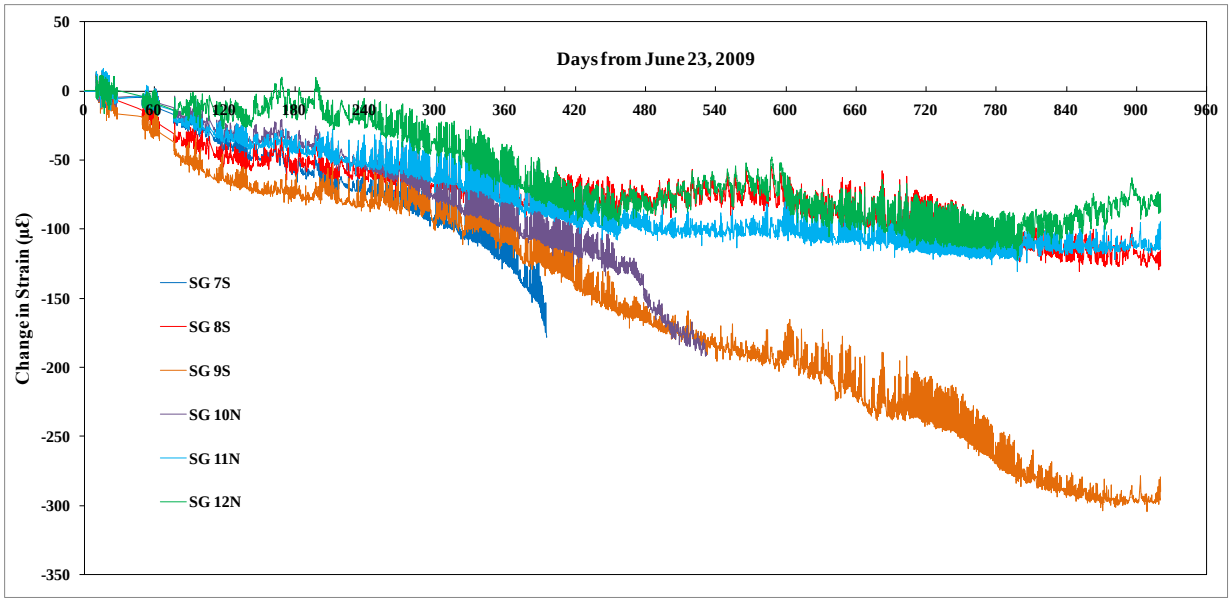

Figure 7.7: Changes in Axial Strains in SE Abutment Pile

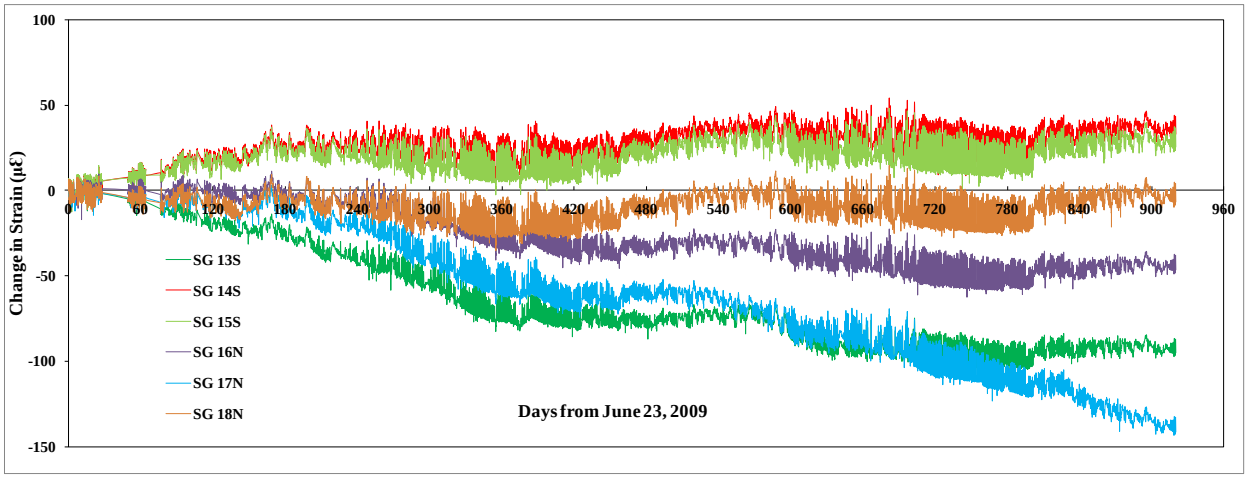

Figure 7.8: Changes in Axial Strains in NE Abutment Pile

7.7 BEHAVIOR OF ABUTMENT PILES

The long term behavior of abutment piles can be explained using the strain gage data. At each depth, two strain gages were placed on the web on the opposite sides (north and south sides) so that the bending strains can be calculated for that particular

location. The locations of strain gages are shown in Figure 5.19. The bending strain, $\Delta\varepsilon$ can be calculated from the difference between two opposite strain gage readings at a particular depth as shown in Equation 7.1. The bending moment, M can be calculated from Equation 7.2.

$$\Delta\varepsilon = \frac{\varepsilon_1 - \varepsilon_2}{2} \tag{7.1}$$

$$M = \frac{EI\Delta\varepsilon}{y} \tag{7.2}$$

where,

Young's modulus of steel, $E = 200GPa$

Moment of inertia, $I = 2.98x10^{-5} m^4$

Distance from neutral axis, $y = \frac{t_w}{2} = 5.27x10^{-3} m$

The seasonal variations in bending moment for SE and SW abutment piles are shown in Figures 7.9 and 7.10. Variations in bending moment for NE abutment pile are presented in Figure 7.11. It is interesting to notice that even though strain gages are located at a greater depth in NE abutment pile when compared to south abutment piles, they are also experiencing significant bending moment.

The yield bending moment, M_y and ultimate bending moment, M_{ult} of steel pile can be calculated from Equations 7.3 and 7.4 respectively.

$$M_y = f_y S \tag{7.3}$$

$$M_{ult} = fZ \tag{7.4}$$

Properties of steel HP 10x42 piles oriented in weak axis are listed below:

Elastic section modulus, $S = 2.33x10^{-4} m^3$

Plastic section modulus, $Z = 3.57x10^{-4} m^3$

Yield strength of steel, $f_y = 0.276GPa$

Ultimate strength of steel, $f = 0.414GPa$

The yield bending moment, M_y and ultimate bending moment, M_{ult} of steel HP 10x42 pile are 64.2 kN.m and 147.9 kN.m respectively.

If the effect of axial load on pile is considered, the yield bending moment, $M_y^{'}$ can be calculated from Equation 7.5.

$$M_y^{'} = M_y - t_w a^2 f_y \tag{7.5}$$

where, $a = \frac{P}{2t_w f_y}$, and axial load, $P = 136.6kN$ and $t_w = 0.0105m$.

Therefore the yield bending moment considering axial load, $M_y^{'} = 62.6kN.m$

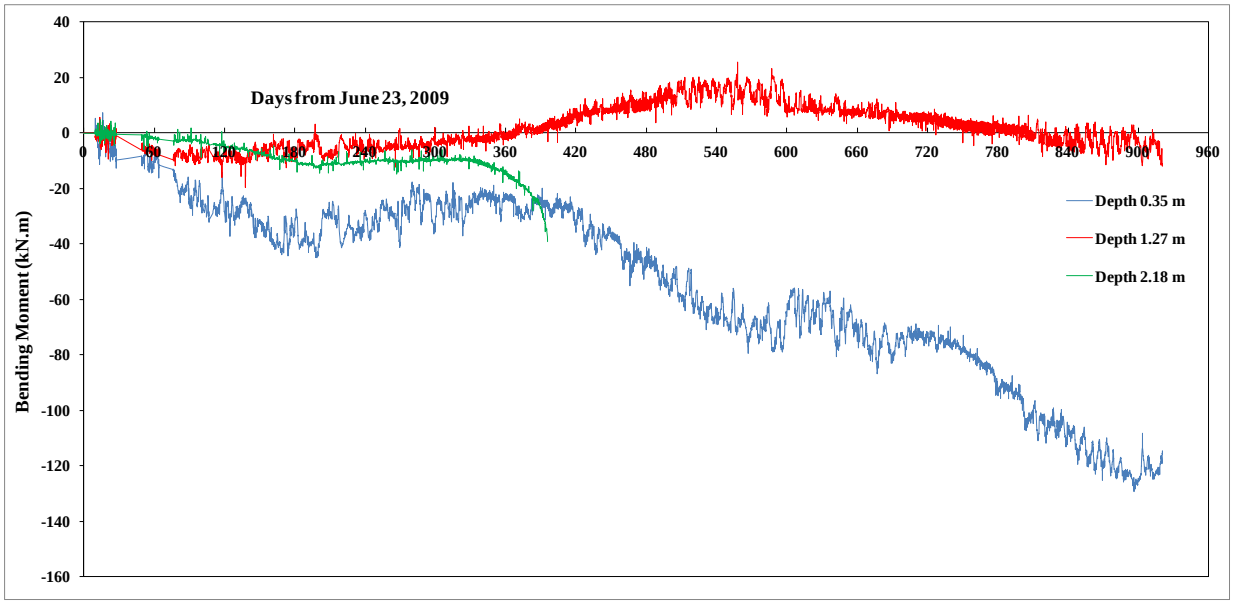

Figure 7.9: Bending Moment in SE Abutment Piles

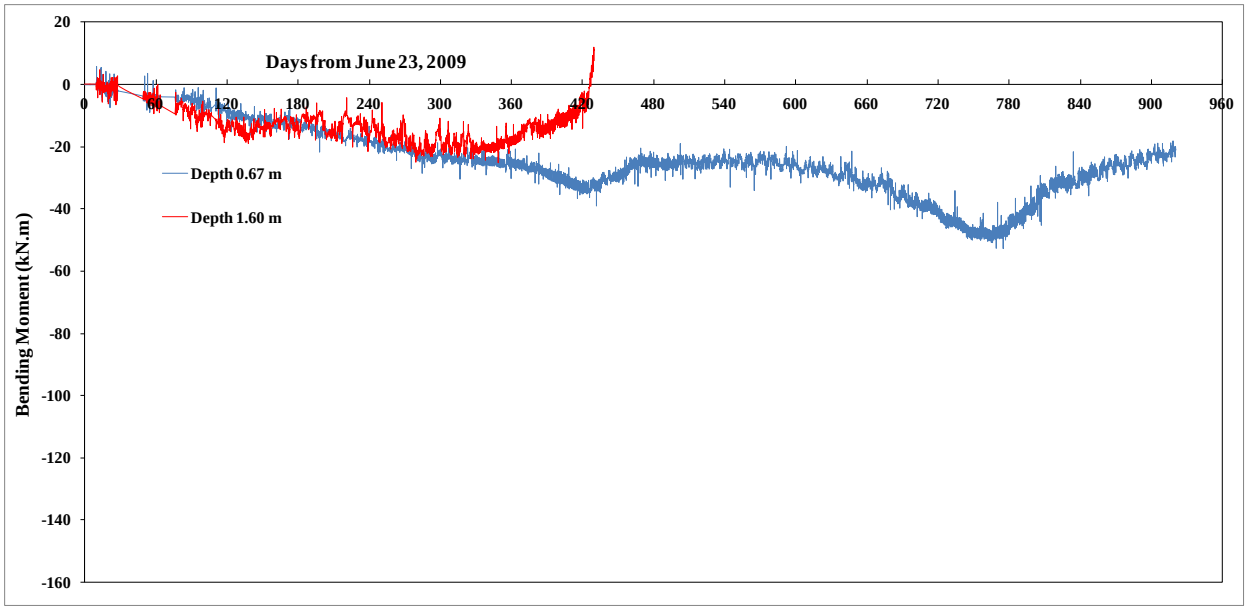

Figure 7.10: Bending Moment in SW Abutment Piles

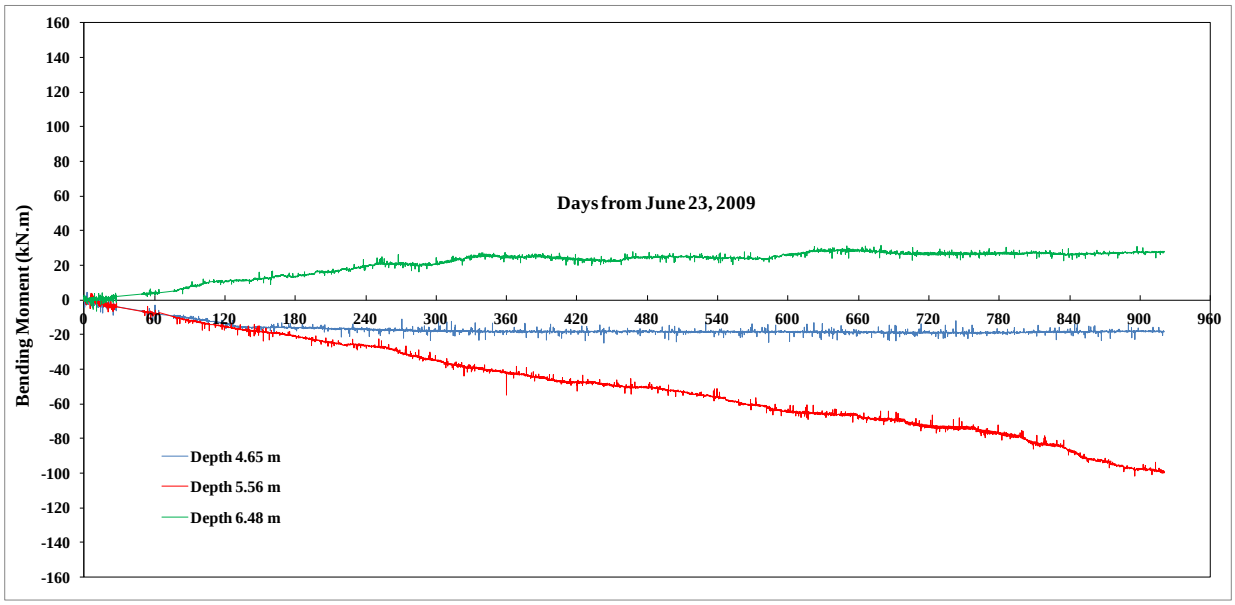

Figure 7.11: Bending Moment in NE Abutment Piles

As shown in Figure 7.9, the shallowest instrumented depth is 0.35 m and bending moment at this particular location is showing continuous increment over time. It confirms the strains in abutment piles are accumulating. Furthermore, it shows the induced bending moment due to thermal loading in the abutment pile is larger than the yield bending moment, however, it has not reached the ultimate bending moment. Similarly, bending moment at the depth of 0.67 m is showing continuous increase over time as shown in Figure 7.10. However, the induced bending moment is below the yield bending moment. The bending moments in north abutment pile have positive and negative values as shown in Figure 7.11 and they represent the change in curvature of the abutment pile. Furthermore, the abutment pile has reached yield bending moment at a depth of 5.56 m. The measured bending moments are on the webs and the bending moments on the tip of the flanges will be even higher. It can be concluded the abutment piles of IABs are experiencing bending moments beyond the yield bending moment along a portion of the flange at the shallow depth for seasonal temperature changes in the bridge superstructure. To accommodate these large bending moments, pile ductility demands have to be increased. Ideally, the upper portion of the pile length should be in a pre-bored hole that is filled with a material, which has a very low stiffness (such as bentonite slurry or loose sand). Analyses described in Chapter 8 provides further insight into bending of the abutment piles.

8 NUMERICAL MODELING OF THE OKLAHOMA IAB

8.1 INTRODUCTION

Computer programs LPILE (ENSOFT 2007) and GROUP (ENSOFT 2010) are used to study the long term behavior of the Oklahoma IAB. The thermal loading on abutment piles can be simulated using the above mentioned computer programs considering the connection between the abutment and superstructure as rigid. Simulation results are compared with field measurements to validate the computer programs and then these computer programs are used in a parametric study.

LPILE and GROUP consider the non-linear soil behavior by utilizing non-linear soil lateral resistance-displacement curves (p-y curves). These computer programs have built-in empirical curves to describe the soil behavior. Furthermore, user defined p-y curves can be specified to describe different soil behaviors. Pile behavior can be modeled as either elastic or plastic. The plastic behavior of the pile is modeled by either providing data to calculate non-linear moment-curvature relations for specified sections or considering user specified non-linear moment-curvature relations. LPILE models the behavior of a single pile under lateral loading while GROUP models the behavior of a group of piles subjected to axial and lateral loading. Two-dimensional and three-dimensional modeling of abutment piles can be performed in GROUP; however, LPILE only considers two-dimensional behavior of a single pile.

8.2 LPILE MODELING OF THE OKLAHOMA IAB

The long term behavior of the Oklahoma IAB was studied with the use of the computer program LPILE. Since LPILE can only handle two-dimensional modeling of soil-pile interaction for a single pile, the tributary superstructure dimensions corresponding to a single abutment pile is considered in the analyses. Furthermore, the Oklahoma IAB has a skew angle of 10^0 and it is not considered in LPILE analyses.

8.2.1 Properties of the Soil Layers

The soil profile at the bridge site is shown in Figure 8.1. The soil underneath the south abutment is a 3.35 m thick layer of stiff lean clay to fat clay with sand. This soil deposit is underlain by a 1.54 m thick layer of medium dense clayey sand, followed by a laminated sandstone rock interbedded with shale seams (very weak to weak rock). The soil underneath the north abutment is considered as a 3.35 m thick layer of stiff lean clay to fat clay with sand, followed by a 4.57 m thick layer of medium dense clayey sand. This layer is underlain by a 3.96 m thick layer of very stiff sandy lean clay, followed by the laminated sandstone interbedded with shale seams (very weak to weak rock).

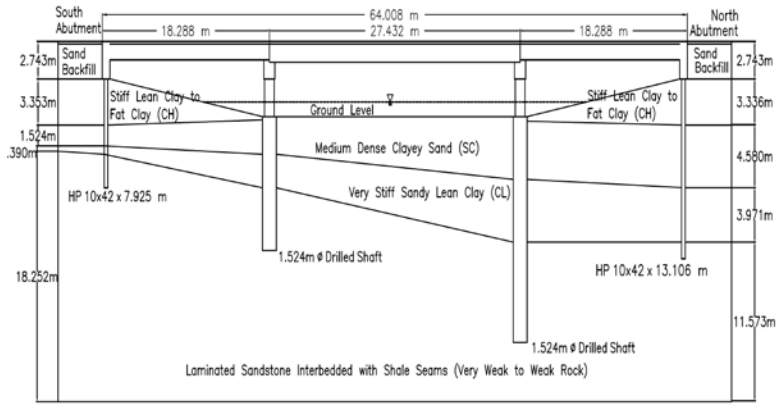

Figure 8.1: Soil Profile at the Bridge Site

The soil profiles at south and north abutments, considered for LPILE analyses are shown in Figures 8.2 and 8.3, respectively. The material properties of soil layers used for the analyses are shown in Tables 8.1 and 8.2, respectively. Ground water level is considered 1.397 m below the ground surface as shown in Figures 8.2 and 8.3. Both abutment piles are anchored into the weak laminated sandstone interbedded with shale seams. Material properties of weak rock are listed below:

Young's modulus of rock, $E_r = 15GPa$

Uniaxial compressive strength, $\sigma_c = 5000kPa$

Rock quality designation, $RQD = 50\%$

Dimensionless constant, $k_{ir} = 0.0005$

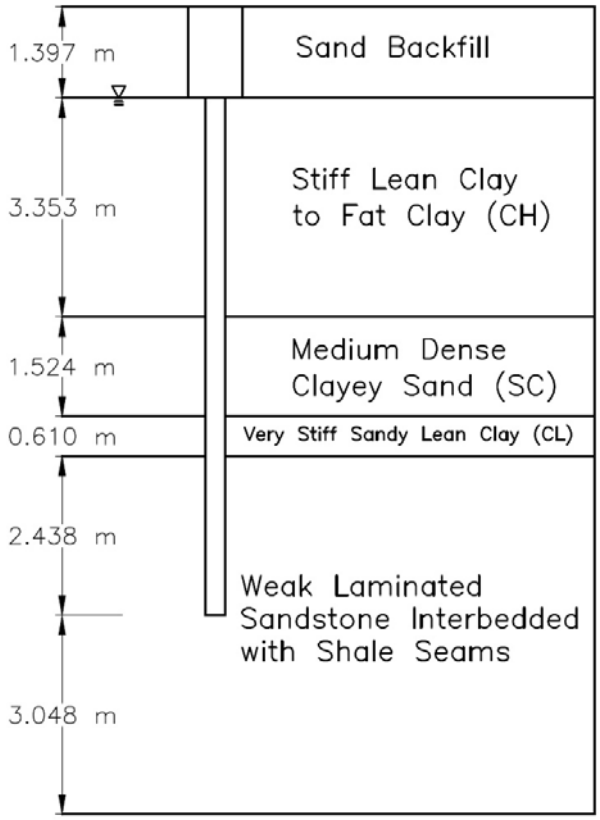

Figure 8.2: Soil Profile at the South Abutment

Table 8.1: Properties of Soil Layers at the South Abutment

Soil Layer	Unit Weight (kN/m^3)	Soil Lateral Stiffness, k (kN/m^3)	Undrained Cohesion, c (kN/m^2)	Internal Friction Angle (^{0})	Strain factor, ε_{50}
Sand backfill	19.95	61 000	-	38	-
Stiff lean clay to fat clay	18.85	136 000	60	-	0.007
Medium dense clayey sand	21.36	33 900	-	39	-
Very stiff sandy lean clay	19.63	271 000	100	-	0.005
Weak laminated sandstone interbedded with shale seams	24.35	-	-	-	-

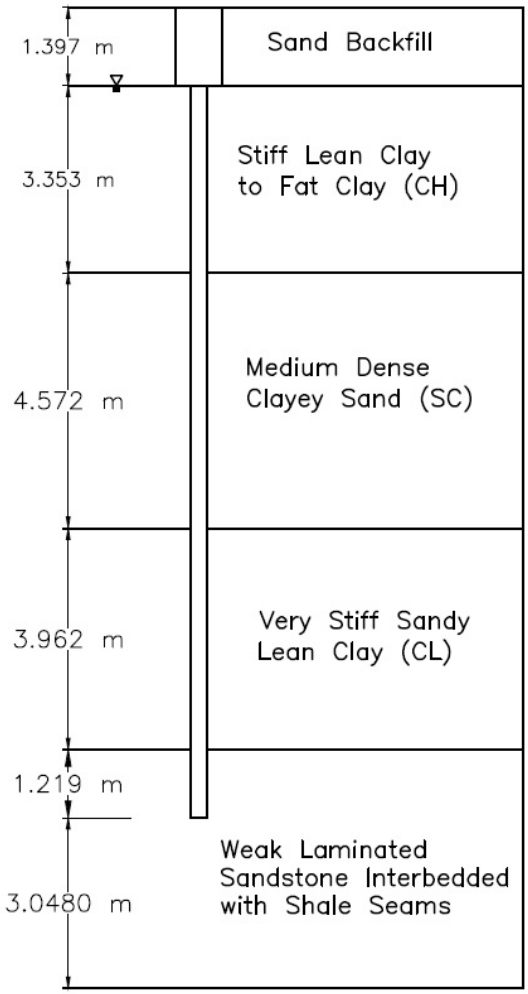

Figure 8.3: Soil Profile at the North Abutment

Table 8.2: Properties of Soil Layers at the North Abutment

Soil Layer	Unit Weight (kN/m^3)	Soil Lateral Stiffness, k (kN/m^3)	Undrained Cohesion, c (kN/m^2)	Internal Friction Angle (^{0})	Strain Factor, ε_{50}
Sand backfill	19.95	61 000	-	38	-
Stiff lean clay to fat clay	18.85	136 000	60	-	0.007
Medium dense clayey sand	21.36	33 900	-	39	-
Very stiff sandy lean clay	19.63	271 000	100	-	0.005
Weak laminated sandstone interbedded with shale seams	24.35	-	-	-	-

8.2.2 Properties of Abutment Piles

The abutment pile considered in LPILE analyses has two sections (see Figures 8.2 and 8.3). Top section is reinforced concrete representing the abutment backwall and the bottom section is HP 10x42 steel pile, oriented in weak axis bending. Average lengths of steel piles at south and north abutments are 7.925 m and 13.106 m, respectively.

Properties of the reinforced concrete section are:

Young's modulus of reinforced concrete, $E_c = 33.7GPa$

Moment of inertia, $I = 0.1032m^4$

Cross-sectional area, $A = 1.764m^2$

Properties of HP 10x 42 steel piles are:

Young's modulus of steel, $E_s = 200GPa$

Moment of inertia, $I = 2.98x10^{-5}m^4$

Cross-sectional area, $A = 0.008m^2$

8.2.3 Loading Condition

The superstructure of bridge undergoes an average temperature variation of 90 - 95 ^{0}F over a six month period. Assuming the thermal deformation of the bridge is symmetric about the center of the bridge, the thermal-induced deformation of the superstructure at the abutment due to the change in temperature of superstructure can be evaluated by Equation 2.1.

$$\Delta L = \alpha \Delta T L / 2 \qquad (2.1)$$

where, α is the coefficient of thermal expansion, ΔT is the change in temperature and L is the total length of the bridge. Thermal expansion coefficient of the reinforced

concrete superstructure, α is considered as $6.23x10^{-6}/^{0}F$ in the thermal movement calculation. Thermally induced deformation of the superstructure at the abutment is 0.019 m. The average movement of superstructure based on crackmeter readings is 0.022 m. Since the calculated superstructure movement is in the range of the measured readings from the crackmeters, thermally induced deformation at the abutment is considered as 0.022 m. The displacement of the abutment is directly applied as the boundary condition in LPILE modeling. The axial load on the pile due to the superstructure is 136.6 kN.

8.2.4 Behavior of Abutment Piles

The behaviors of steel HP piles for the south and north abutments due to the thermal-induced abutment deformation are shown in Figures 8.4 and 8.5, respectively. Even though north abutment piles are longer than the south abutment piles, the LPILE calculated bending moments are similar for both the north and south piles.

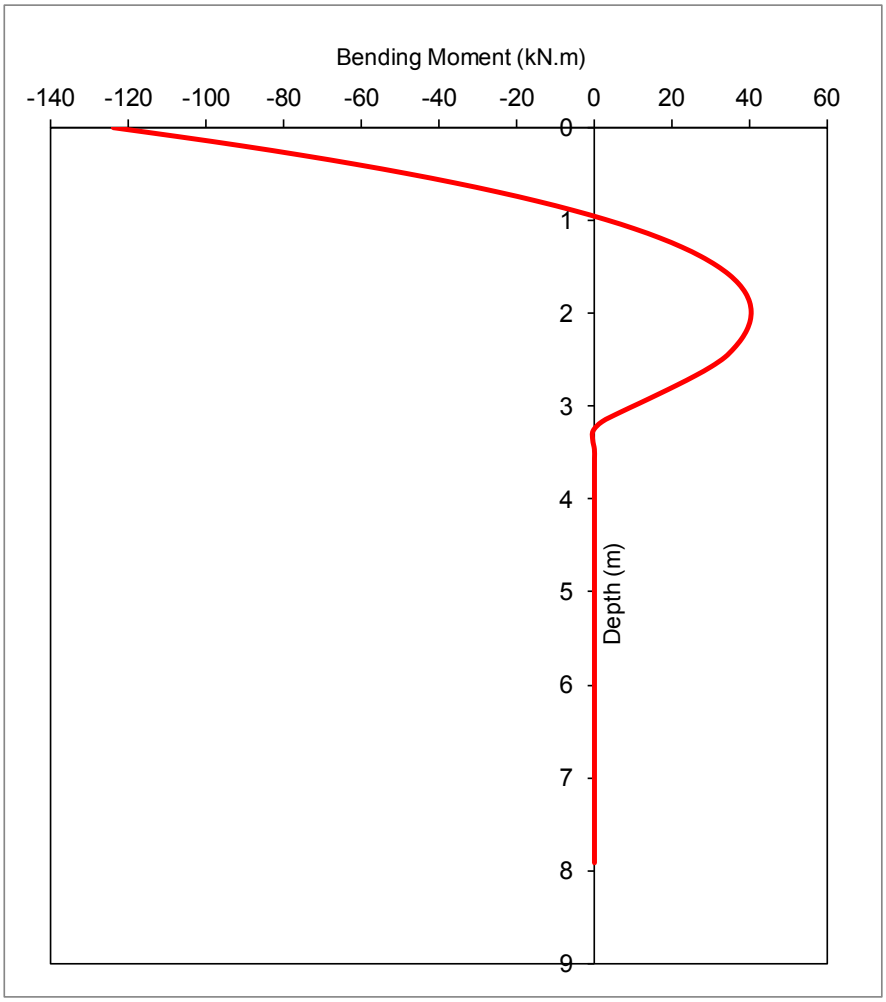

Figure 8.4: Bending Moments for the South Abutment Pile

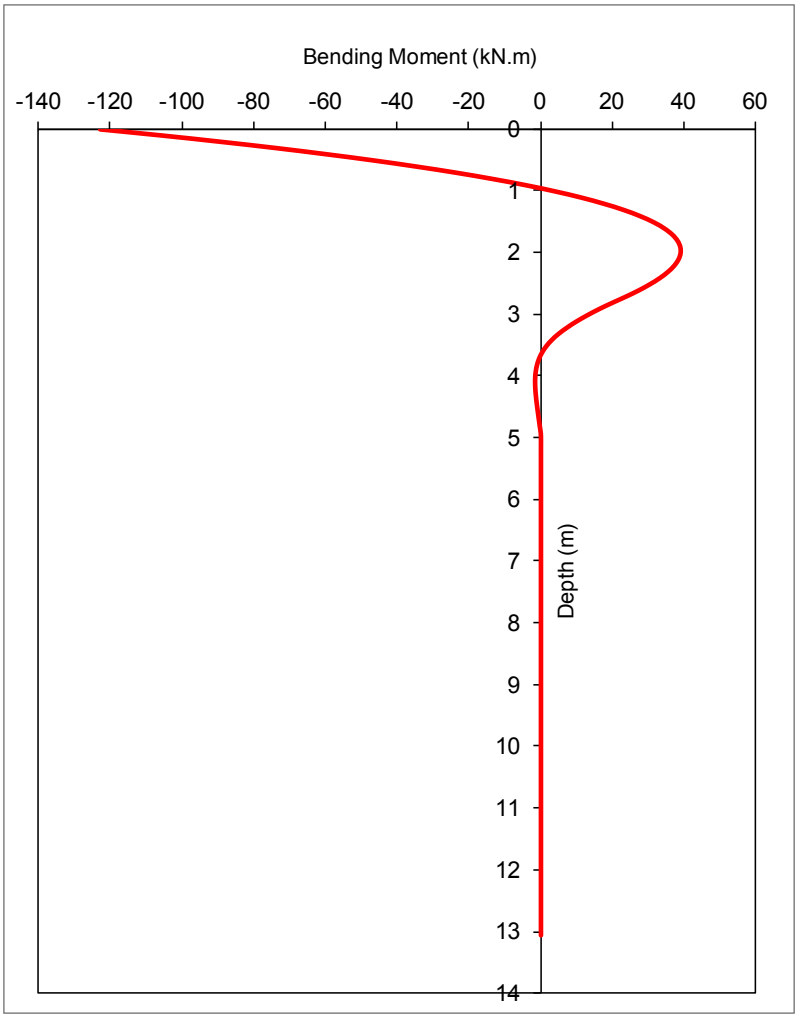

Figure 8.5: Bending Moments for the North Abutment Pile

The yield bending moment, M_y and ultimate bending moment, M_{ult} of steel HP 10x42 piles are 64.2 kN.m and 147.9 kN.m, respectively. The computed LPILE bending moment for abutment piles shows that the pile has yielded at shallow depths; however, it has not reached the ultimate bending moment.

8.2.5 Comparison of Field Measurements and LPILE Results

The steel HP piles of the Oklahoma IAB were instrumented with strain gages at different depths. Strain gages were placed at shallow depths in south abutment piles and they were placed at greater depths in the north abutment pile. The bending strain, $\Delta\varepsilon$ can be calculated from the difference between two opposite strain gage readings at a particular depth as shown in Equation 7.1. The bending moment, M can be calculated from Equation 7.2 as expressed in Section 7.7.

The comparison of field measured bending moments and computed LPILE bending moment based on thermally induced abutment deformation for south and north abutment piles are shown in Figures 8.6 and 8.7, respectively.

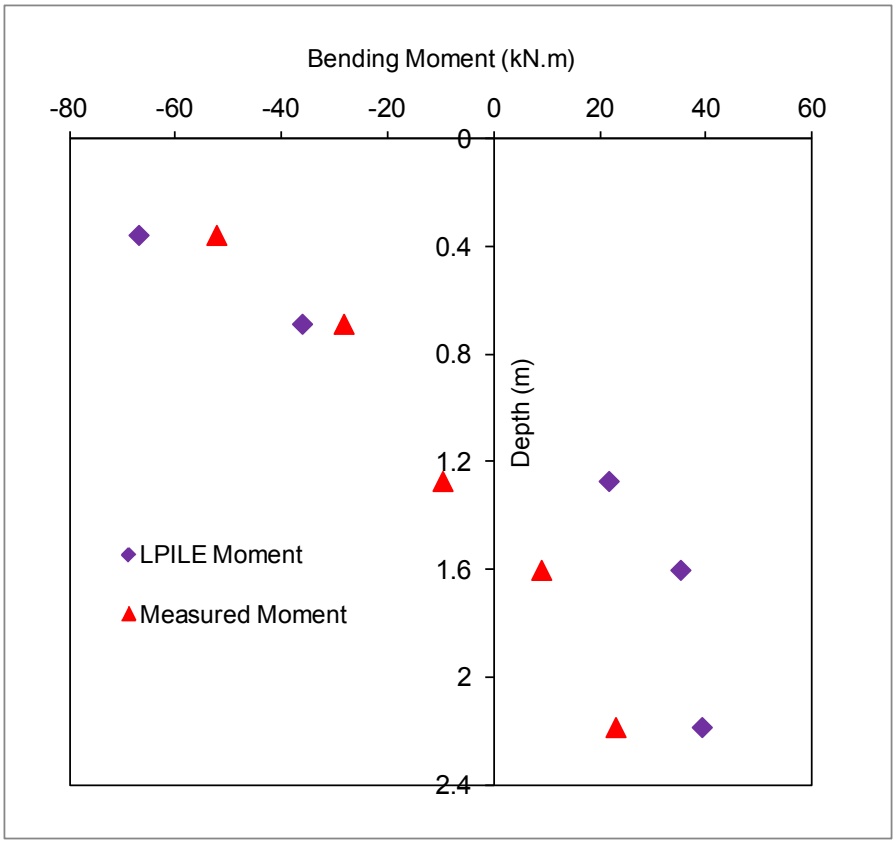

Figure 8.6: Measured and LPILE Bending Moments for the South Abutment Pile

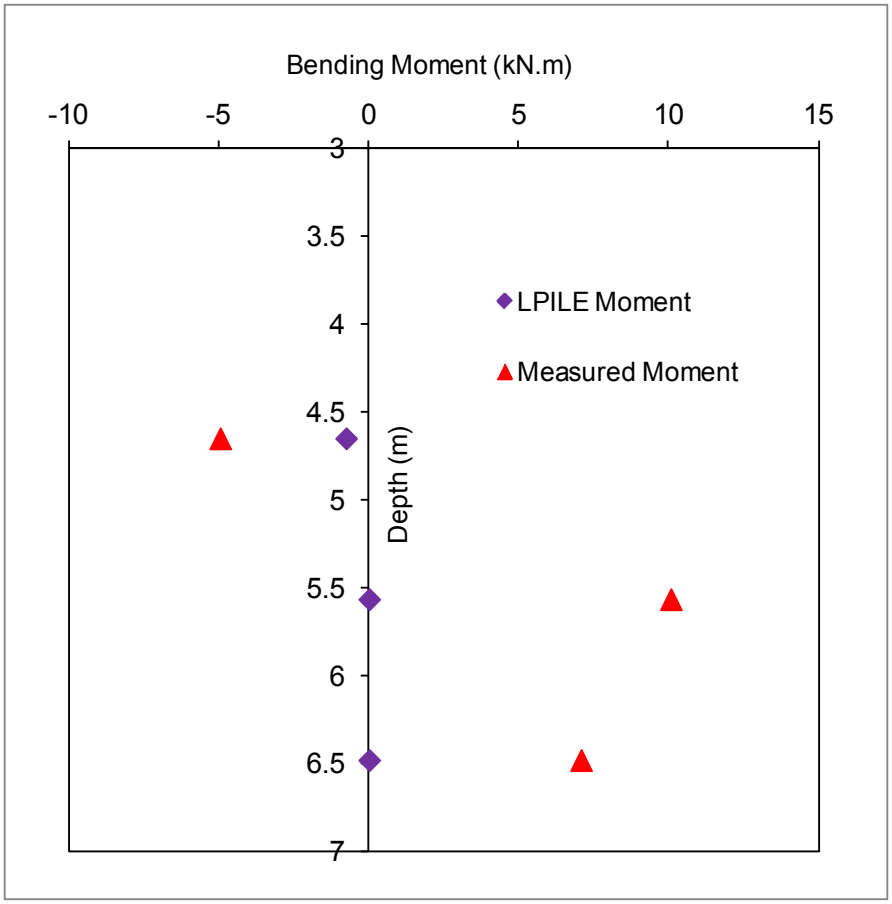

Figure 8.7: Measured and LPILE Bending Moments for the North Abutment Pile

The field measured bending moments for the south abutment pile shows lower values than the computed LPILE bending moments. The field measured bending moments for the north abutment pile, however, shows higher values than the computed LPILE bending moment. However, the variations in bending moment for the north abutment pile are not important in this discussion as strain gages are located at a greater depth in the north abutment pile and they do not experience significant bending moment.

The following reasons may be attributed for the difference between the field measured and computed values of bending moment. LIPLE considers simple two

dimensional modeling of single pile and skew of the Oklahoma IAB is not considered in the analysis. Furthermore, thermal movement of the bridge was calculated based on the average temperature variation within the superstructure, however, the temperature variation of superstructure is not uniform across the depth of superstructure. Pre-drilled holes were used to drive south abutment piles, however, this particular condition was not modeled in LIPLE and it would play a significant role in the computed bending moments being higher than the measured values.

8.3 GROUP MODELING OF THE OKLAHOMA IAB

The long term behavior of the Oklahoma IAB was also studied with the use of the computer program GROUP. Since GROUP can handle both two-dimensional and three-dimensional modeling of abutment piles subjected to axial and lateral loading, the entire abutment structure comprised of seven abutment piles was considered in the analyses. Furthermore, Oklahoma IAB has a skew angle of 10^0 and by incorporating three-dimensional modeling, the skew of the Oklahoma IAB is also considered in GROUP analyses.

The embedded pile cap option available in GROUP was used to model the entire abutment structure. Since the passive soil resistance against the abutment backwall plays a vital role in the modeling of abutment subjected to lateral loading, the passive soil resistance against the pile cap was considered in the GROUP modeling of the Oklahoma IAB. The soil-structure interaction for the pile cap under translational movement is similar to the soil resistance (p-y curves) on piles under lateral loading. The approach adopted in the computer program GROUP is to derive the soil resistance for the pile cap using the same p-y criteria for piles, but with the diameter equal to the

width of the front side of the concrete cap. The movements at the top and bottom of the pile cap are computed based on the translation and rotation of the cap.

8.3.1 Input Material Properties

The soil properties considered for the GROUP analyses remain the same as described in Section 8.2.1. The abutment piles considered in GROUP analysis have only one section. Single row of seven HP 10x42 steel piles oriented in weak axis bending are placed along the abutment with a spacing of 2.134 m. The width of the abutment is 14.289 m. The cross-section of the abutment considered for GROUP analyses is shown in Figure 8.8. Average lengths of steel piles at south and north abutments are 7.925 m and 13.106 m, respectively. Properties of abutment pile remain the same as described in Section 8.2.2.

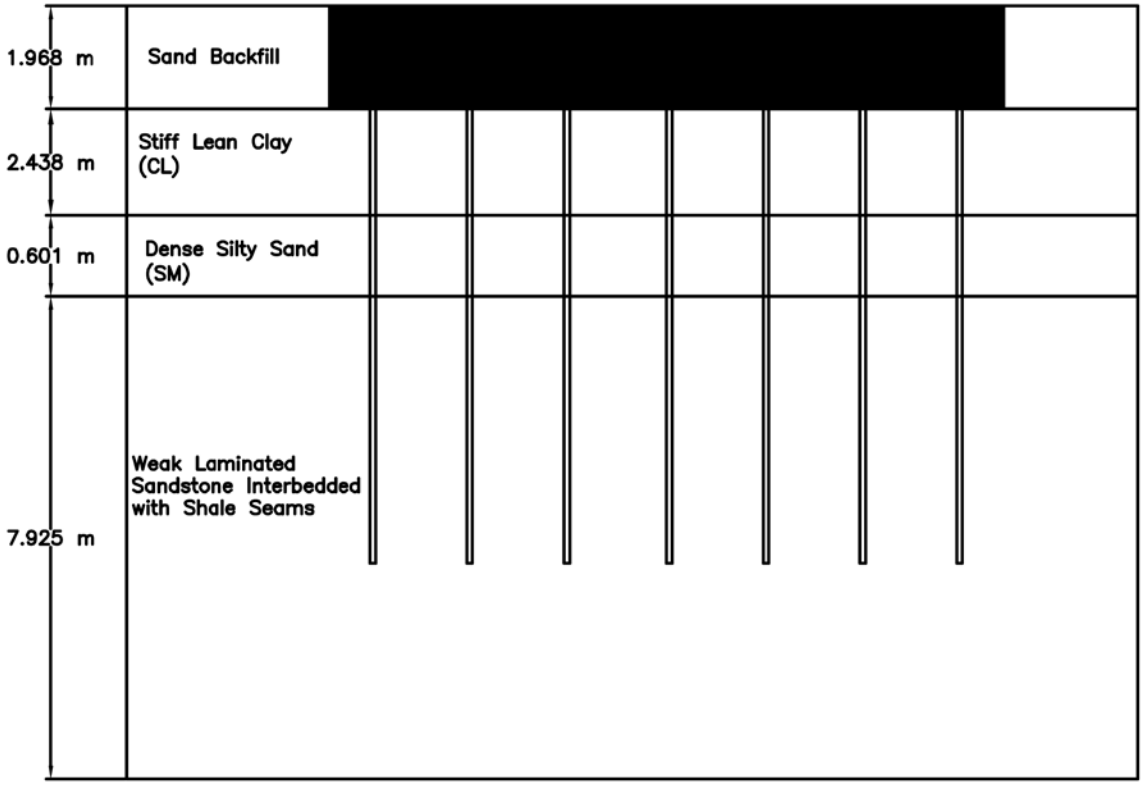

Figure 8.8: Cross-section of the Abutment

8.3.2 Loading Condition

Thermally induced deformation at the abutment is considered as 0.022 m as described in Section 8.2.2, but the displacement of the abutment cannot be directly applied as a boundary condition in GROUP. An alternative procedure was used to calculate the forces and moments acting on the abutment for the thermally induced deformation. The forces and moments at the top of the abutment obtained in LPILE analysis were used to calculate the forces and moments required for GROUP analysis. The forces and moments at the top of the abutment obtained in LPILE analysis were based on the tributary superstructure dimensions corresponding to a single abutment pile. Thus, total forces and moments acting on the entire abutment were calculated

based on the number of piles and their corresponding superstructure dimensions. Since the skew of the bridge is considered in GROUP analysis, the longitudinal and transverse components of forces and moments were calculated based on the skew of the bridge. The axial load on the piles due to the superstructure is 871.8 kN. During the analysis, the displacement of the abutment for the above loading condition was checked against with the actual deformation of the abutment and these values matched. Therefore, no further adjustments for forces and moments were needed.

8.3.3 Behavior of Abutment Piles

Since the thermal loading of the superstructure is not symmetric in a skewed IAB, biaxial bending (bending in longitudinal and transverse directions) of abutment piles occurs in the Oklahoma IAB. Due to the rigidity of the abutment during deformation, there was not a significant difference among the calculated GROUP bending moment for each abutment pile (interior and exterior piles) even though the exterior piles have a reduced superstructure dimension than the interior piles.

The bending moments in longitudinal and transverse directions for the south abutment piles are shown in Figures 8.9 and 8.10, respectively. Similarly, the bending moments for the north abutment piles are shown in Figures 8.11 and 8.12. Computed longitudinal GROUP bending moments are higher than LPILE bending moments. The friction between the abutment and backfill material becomes very important in the skewed IAB in addition to the normal pressure acting against the surface of the abutments. The longitudinal component of the passive backfill soil pressure in a skewed IAB is smaller than that in a straight IAB. Thus, in a skewed IAB, the reduction in backfill

soil pressure increases the amount of abutment pile bending in the longitudinal direction and larger longitudinal bending moments were observed in GROUP when compared to LPILE bending moments.

Furthermore, even though north abutment piles are longer the than south abutment piles, the GROUP calculated bending moments are similar for both north and south abutment piles.

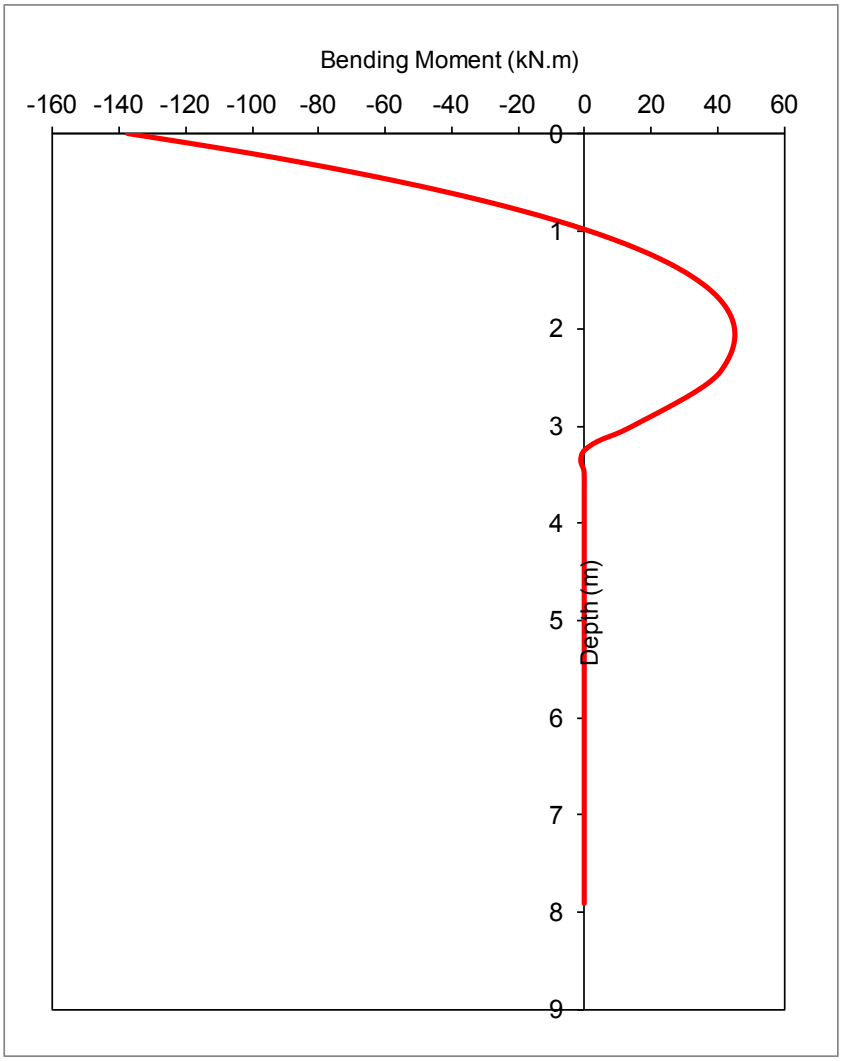

Figure 8.9: Bending Moment in Longitudinal Direction for the South Abutment Pile

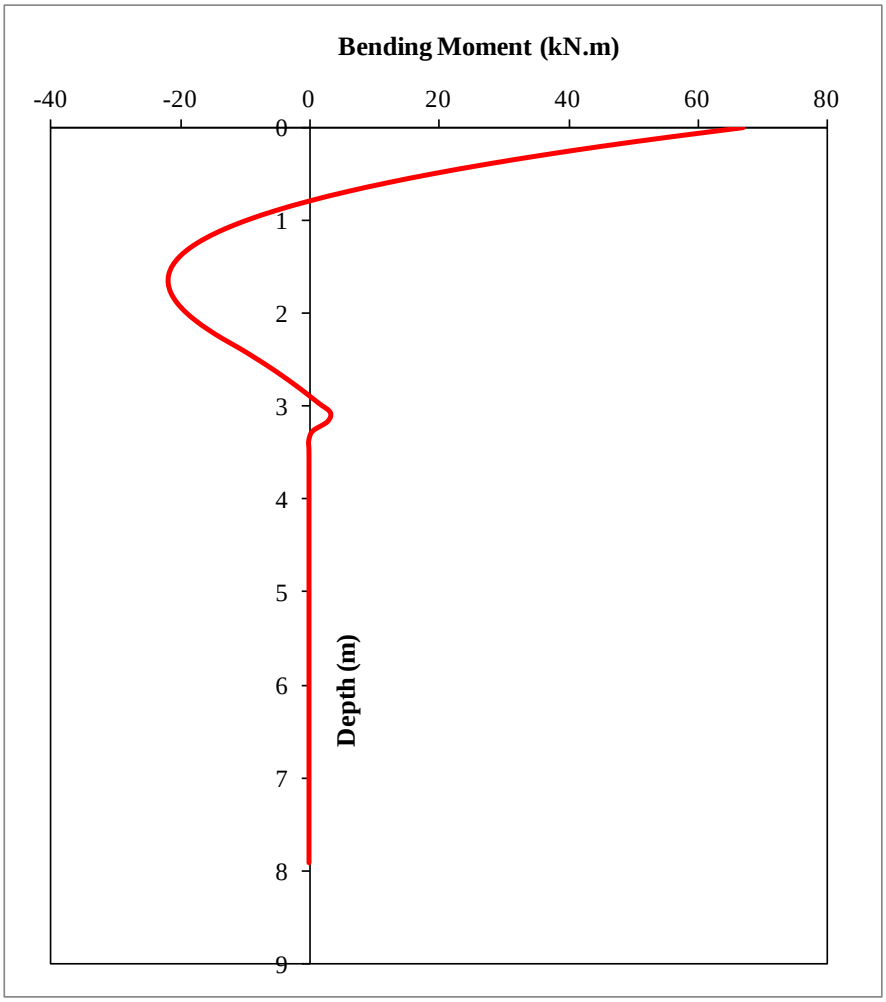

Figure 8.10: Bending Moment in Transverse Direction for the South Abutment Pile

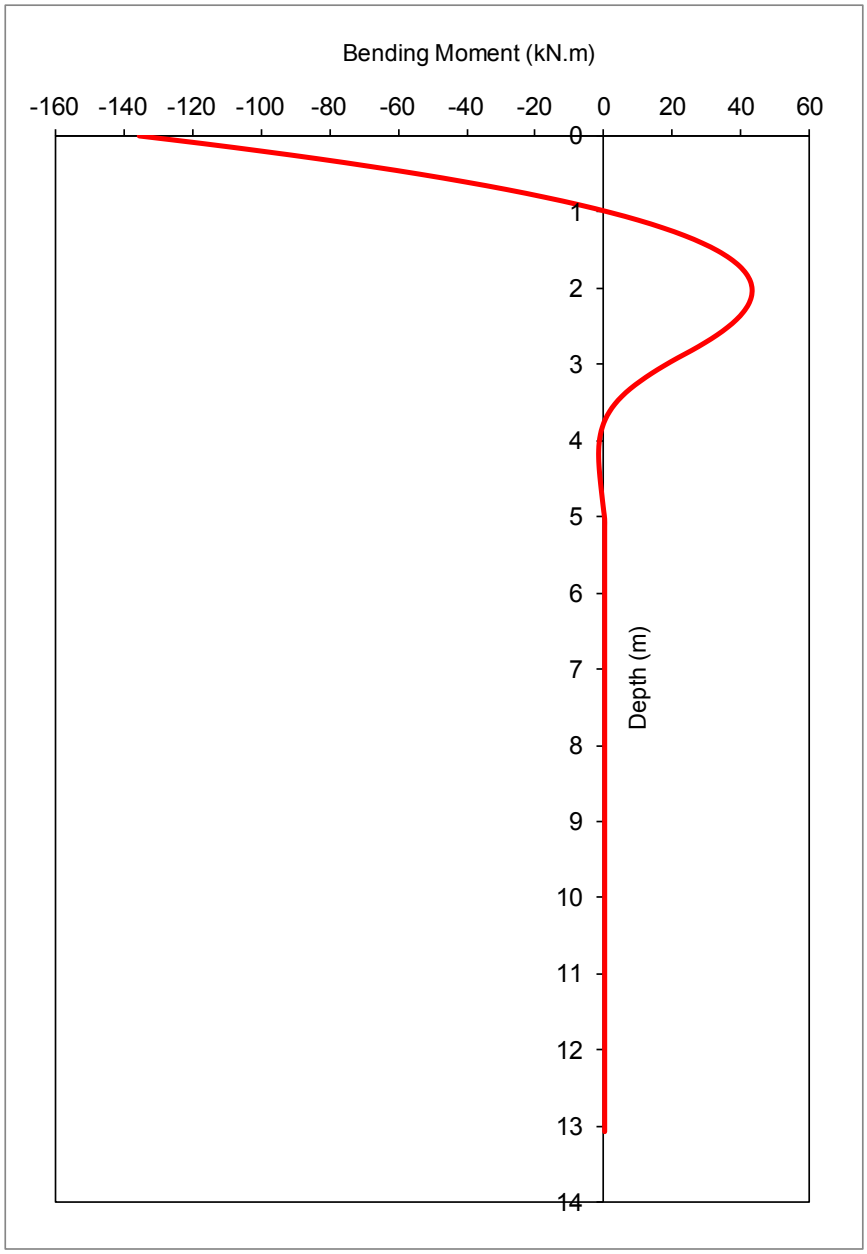

Figure 8.11: Bending Moment in Longitudinal Direction for the North Abutment Pile

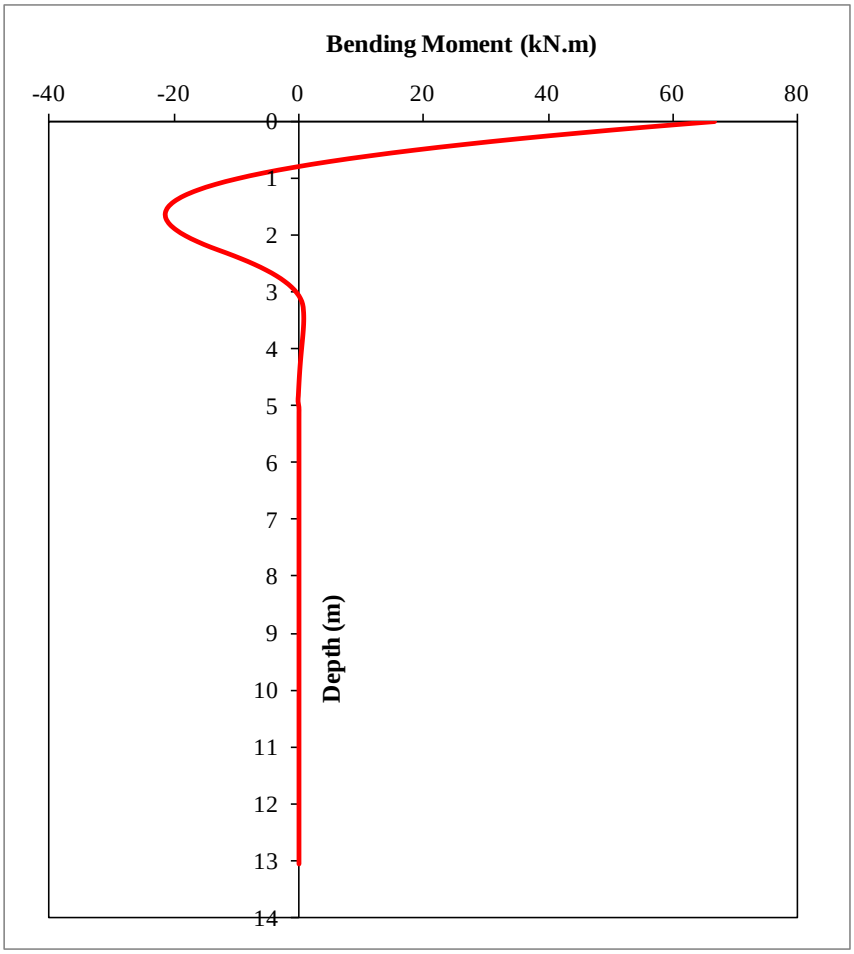

Figure 8.12: Bending Moment in Transverse Direction for the North Abutment Pile

The yield bending moment, M_y and ultimate bending moment, M_{ult} of steel HP 10x42 pile for weak axis bending are 64.2 kN.m and 147.9 kN.m, respectively. The computed longitudinal GROUP bending moment for abutment piles also shows that the pile has yielded at shallow depths, however, it has not reached the ultimate bending moment. Abutment piles are oriented in strong axis bending in the transverse direction and therefore should be able to easily accommodate the bending in the transverse direction.

8.3.4 Comparison of Field Measurements and GROUP Results

The comparison of field measured bending moments and computed longitudinal GROUP bending moments for south and north abutment piles are shown in Figures 8.13 and 8.14, respectively.

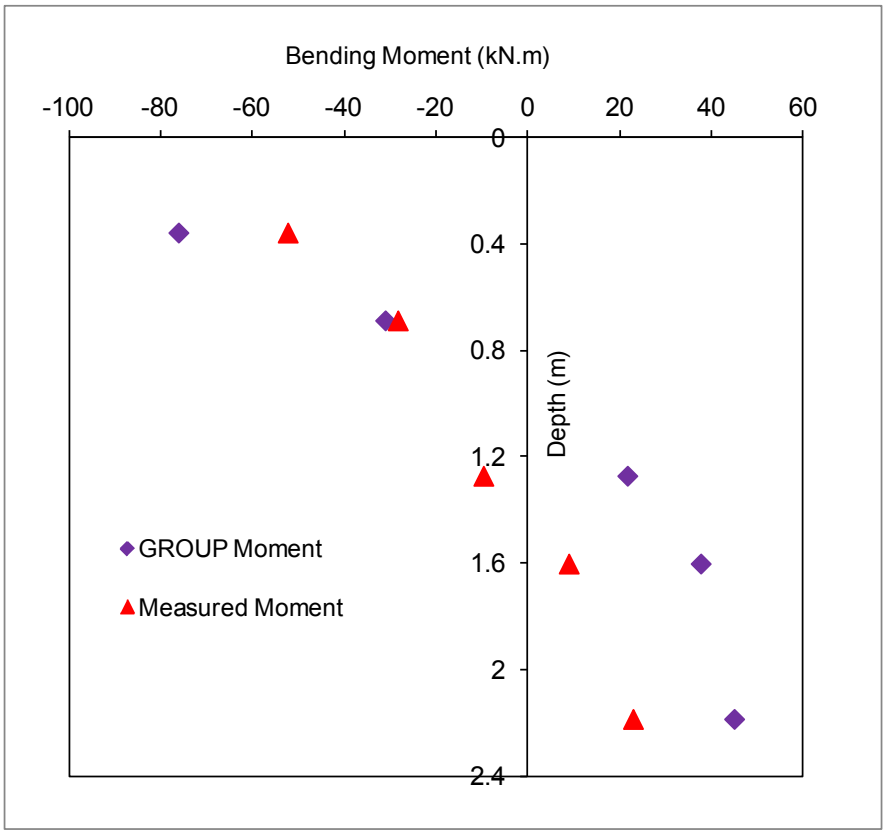

Figure 8.13: Measured and GROUP Bending Moments for the South Abutment Pile

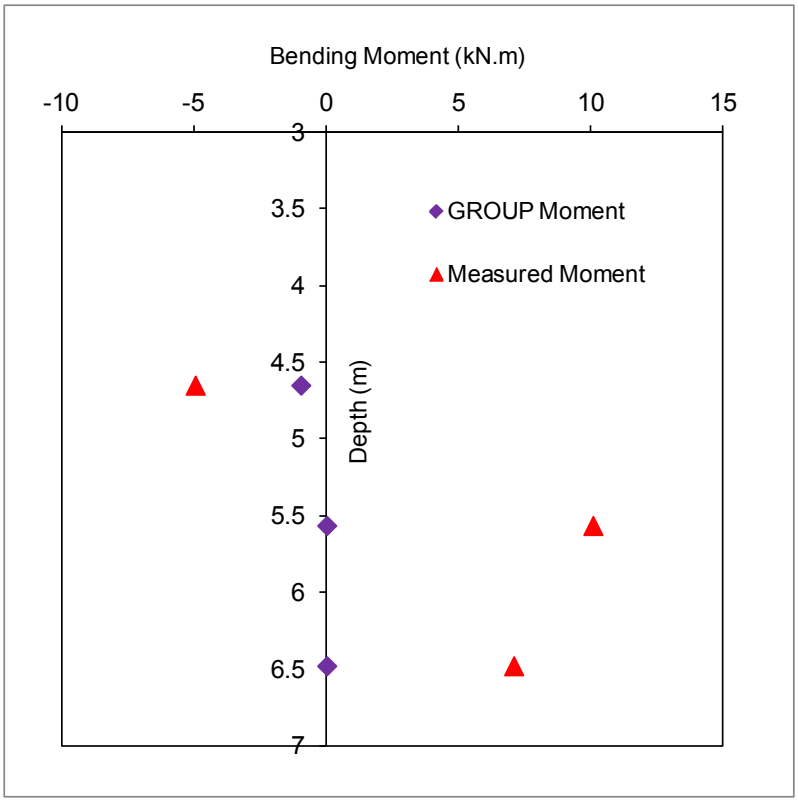

Figure 8.14: Measured and GROUP Bending Moments for the North Abutment Pile

Similar to LPILE simulations, the field measured bending moments for the south abutment pile shows lower values than the computed GROUP bending moments. The field measured bending moments for the north the abutment pile, however, shows higher values than the computed GROUP bending moments. The differences in bending moment for the north abutment pile are not that important in this discussion as strain gages are located at a greater depth in the north abutment pile and they do not experience significant bending moment.

Even though the skew of the bridge is incorporated in GROUP modeling, differences are observed in between the field measured and computed values of bending moments. The reasons for the differences between the field measured and computed values of bending moments are explained in Section 8.2.4.

9 A PARAMETRIC STUDY FOR IABS

9.1 INTRODUCTION

Only limited studies have been found in the literature regarding the parametric studies of IABs. One of the objectives of this research was to extend the results of the Oklahoma IAB to general IABs and propose design guidelines to build new IABs with longer lengths and larger skew angles. The computer code GROUP was used to understand the long-term behavior of IABs in this parametric study. The base case was taken as the numerical models developed for the Oklahoma IAB in the computer program GROUP. Thermally induced deformation of the abutment and the bending moment in the abutment piles were studied to understand the long-term behavior of IABs.

9.2 VARIABLES CONSIDERED IN THE PARAMETRIC STUDY

Abutment pile type, size and orientation, type of soil surrounding the abutment piles, bridge length and girder depth, and bridge skew angle are the variables considered in the parametric study to simulate various conditions of IABs. The variables are selected based on the literature review and the behavior of the Oklahoma IAB.

9.3 ABUTMENT PILE TYPE, SIZE, AND ORIENTATION

In the literature, a range of discussions have been presented regarding the type of abutment piles designed for IABs. Steel HP piles were most frequently used in the design of IABs, however, cast-in-place (CIP), prestressed and pipe piles had also been used by the design agencies. HP piles have been used in a wide range of bridge spans and soil conditions with two types of pile orientations: weak axis bending and strong

axis bending. CIP piles utilize driven steel pipes which are later filled with concrete, and steel reinforcement is placed in the top section of the piles. Prestressed concrete and pipe piles are sometimes used for short span IABs.

In this parametric study, the behavior of HP 10x42 steel piles, HP 12x53 steel piles and 12-inch diameter CIP piles are investigated for seasonal temperature changes. HP 10x42 piles were oriented in both weak axis bending and strong axis bending, however, HP 12x53 piles were oriented only in weak axis bending. The behavior of CIP piles with a 12-inch diameter was also investigated and compared to that of HP piles. A 210 feet long, three-span straight IAB (Bridge A) was considered in this parametric study. Variables considered in this parametric study are summarized in Table 9.1.

Table 9.1: Different Types of Abutment Piles

Description	Abutment Pile Type	Bending Axis	Number of Piles	Pile Spacing (ft)
Case 1	HP 10x42	Weak	7	7
Case 2	HP 10x42	Strong	7	7
Case 3	HP 12x53	Weak	7	7
Case 4	12-inch CIP	-	7	7

The sectional properties of the considered piles are given below:

Properties of HP 10x 42 steel piles in weak axis bending:

Young's modulus of steel, $E_s = 200\ GPa$

Moment of inertia, $I = 2.98x10^{-5}\ m^4$

Cross-sectional area, $A = 0.008\ m^2$

Properties of HP 10x 42 steel piles in strong axis bending:

Young's modulus of reinforced concrete, $E_s = 200\ GPa$

Moment of inertia, $I = 8.741x10^{-5}\ m^4$

Cross-sectional area, $A = 0.008\ m^2$

Properties of HP 12x 53 steel piles in weak axis bending:

Young's modulus of steel, $E_s = 200\ GPa$

Moment of inertia, $I = 5.286x10^{-5}\ m^4$

Cross-sectional area, $A = 0.01\ m^2$

Properties of 12-inch diameter CIP piles:

Young's modulus of reinforced concrete, $E_c = 31.3\ GPa$

Moment of inertia, $I = 0.0025\ m^4$

Cross-sectional area, $A = 0.0845\ m^2$

The number of piles under the abutments was selected based on the vertical load carrying capacity of the abutment piles. The axial load due to the superstructure was considered in calculating the number of piles required for the abutments. The

computed GROUP pile bending moment with different pile types and sizes are shown in Figure 9.1. According to Figure 9.1, the largest bending moment occurred when CIP piles were used. From the computed results, CIP piles may be used only in short IABs. Except for CIP piles, HP 10x42 piles oriented in strong axis bending caused larger bending moments in the abutment piles than the other pile configurations considered in the modeling. The computed bending moment for HP 12x53 piles oriented in weak axis bending were larger than the bending moments for HP 10x42 piles oriented in weak axis bending.

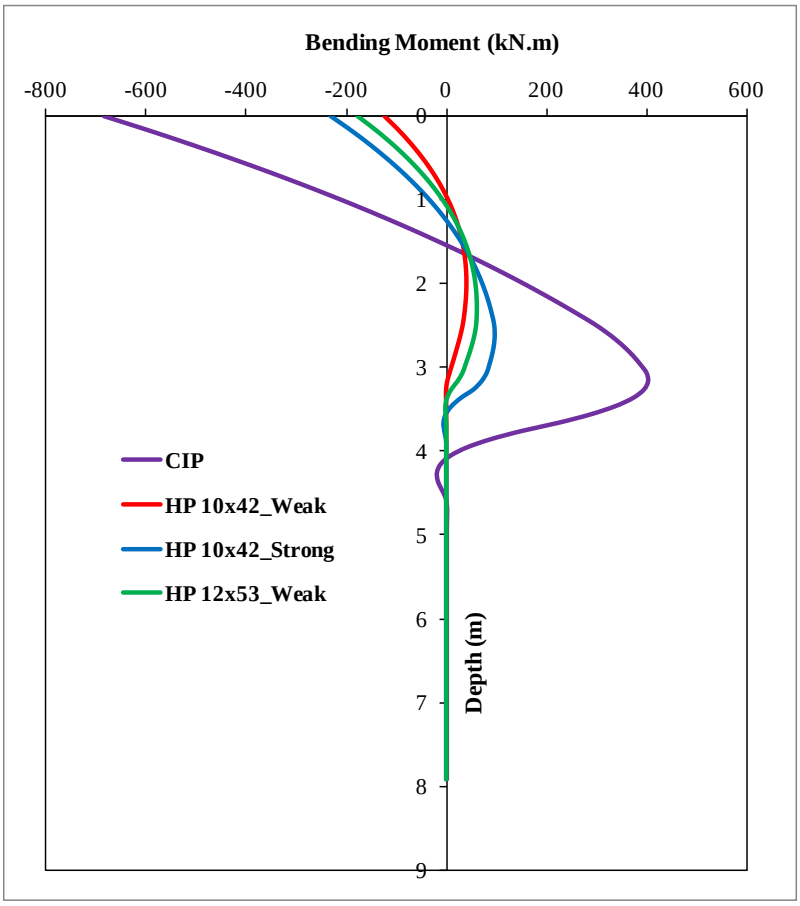

Figure 9.1: Variation in Pile Bending Moments for Different Pile Configurations

The orientation of HP piles with reference to the bridge's longitudinal axis affected the thermally induced bending moments in the abutment piles since the stiffness of the HP piles varies according to the bending axis. The weak axis bending helped to reduce the bending moment that occurs in the abutment piles while providing the required flexibility to the bridge. The orientation of weak axis bending will also help to reduce the thermally induced concrete stresses in the superstructure. The length of the bridge and the type of soil surrounding the abutment piles also play an important role in the behavior of abutment piles.

According to this parametric study, steel HP piles are most suitable to support abutments in IABs. The inherent flexibility of steel HP piles allow them to endure constant flexure induced by the cyclic thermal strains of the superstructure. Using a smaller HP pile section sufficient to carry vertical loads and orienting HP piles in weak axis bending will ensure the effective performance of IABs for seasonal temperature changes.

9.4 BRIDGE LENGTH AND GIRDER DEPTH

In practice, the length of an IAB is often limited. Girder depth and bridge length are often related and in general, deeper girders are used for longer bridges. For multi-span bridges, to reach the same bridge length, the bridges may consist of more short-span shallow girders or fewer long-span deep girders.

In this study, three combinations illustrated as Bridge A, Bridge B and Bridge C were investigated. Bridge A and Bridge B had the same girder depths (Type III PCB) and different bridge lengths. Bridge B (420 feet, 6 spans) was twice as long as Bridge A (210 feet, 3 spans). Bridge B (6 spans) and Bridge C (3 spans) had the same total

bridge length (420 feet) and different girder depths. Bridge C had Type IV PCB girders, which was deeper than that of Type III PCB girders used in Bridge B. To reach the same total length, six spans of girders were required in Bridge B and three spans in Bridge C. Bridges considered in this parametric study were straight IABs. Abutment piles were oriented in week axis bending. Different types of bridge configurations considered in this parametric study are summarized in Table 9.2. Except for the varied parameters described above, other bridge parameters and soil conditions were kept constant.

Table 9.2: Different Types of Bridge Configurations

Description	Bridge A	Bridge B	Bridge C
Total Bridge Length (ft)	210	420	420
Number of Spans	3	6	3
Girder Type	Type III PCB	Type III PCB	Type IV PCB
Girder Length (ft)	60	60	120
Abutment Pile Type	HP 10x42	HP 10x42	HP 10x42
Number of Piles	7	7	12
Pile Spacing (ft)	7	7	3.9

The computed GROUP pile bending moment for different bridge and superstructure configurations are shown in Figure 9.2.

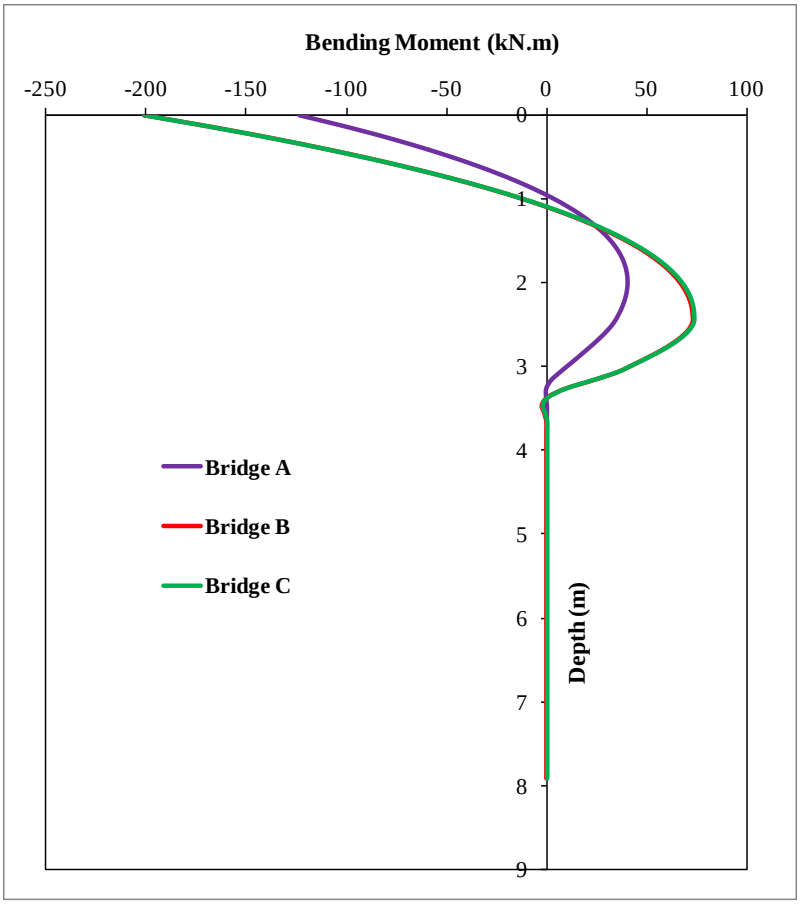

Figure 9.2: Variation in Pile Bending Moments for Different Bridge Configurations

According to Figure 9.2, the bending moment occurring in the abutment piles depends on the total bridge length. For the same bridge length, the computed bending moments are similar. The expansion and contraction of the superstructure were closely related to the total bridge length. The expansion and contraction of Bridge A was approximately half of that of Bridge B.

From the analyses, with the increase of total bridge length from 210 feet to 420 feet; the expansion and contraction of the superstructure and the bending moment in abutment piles increased correspondingly. There is not much variation in the bending moment for Bridge B and Bridge C, however, using longer spans with larger girders (Bridge C) will increase the axial load on the abutment piles. Furthermore, larger

thermal gradients will exist across the depth of superstructure when longer span girders are used for the bridge. Greater thermal gradient will increase the concrete stresses within the superstructure due to the larger depth of girders. Therefore long-span IABs should be designed with caution ensuring that thermally induced abutment pile bending moments and concrete stresses are limited within the allowable ranges.

9.5 TYPE OF SOIL SURROUNDING THE ABUTMENT PILES

Since the abutment piles were rigidly connected to the bridge superstructure, the type of soil surrounding the abutment piles has a direct effect on abutment pile behavior and an indirect effect on the behavior of superstructure. The following types of soils were investigated in the parametric study: loose sand, dense sand, soft clay, stiff clay and very stiff clay. A 210 feet long, three-span straight IAB (Bridge A) was considered in this parametric study. Abutment piles (7 HP 10x42 piles) were oriented in weak axis bending.

Types and properties of soils surrounding the abutment piles are listed in Table 9.3 (Reese et al. 1974, 1976; Kamel et al. 1996). Computed GROUP pile bending moments for different types of soils are presented in Figure 9.3.

Table 9.3: Properties of Different Types of Soils

Soil Layer	Unit Weight (kN/m^3)	Soil Lateral Stiffness, k (kN/m^3)	Undrained Cohesion, c (kN/m^2)	Internal Friction Angle (o)	Strain Factor, ε_{50}
Loose sand	15.63	6 790	-	30	-
Dense sand	20.72	61 000	-	40	-
Soft clay	17.1	8 140	20	-	0.02
Stiff clay	20.5	136 00	90	-	0.007
Very stiff clay	22.1	271 000	240	-	0.004

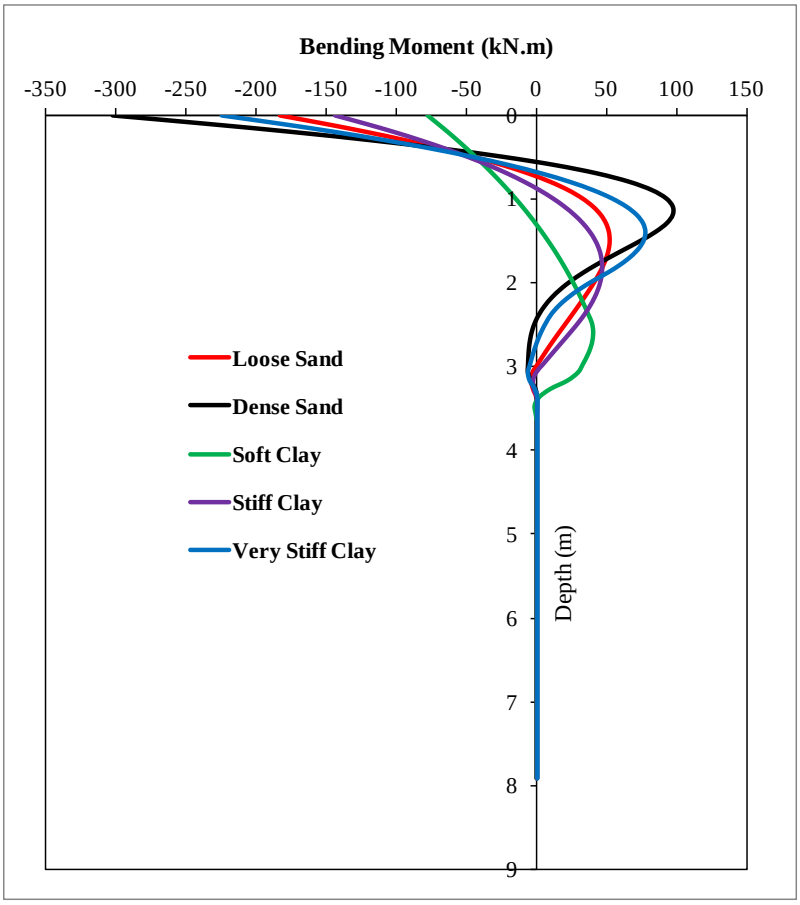

Figure 9.3: Variation in Pile Bending Moments for Different Types of Soils Surrounding the Piles

Soil surrounding the pile had a significant effect on the behavior of the abutment piles. According to Figure 9.3, dense sand and very stiff clay layers surrounding the piles created the largest bending moments in the piles. The stiffness of soil directly affects the abutment pile behavior. When the stiffness of soil is increased, partial flanges of the pile cross section near the pile head will yield and the plastic hinges may occur for longer IABs and larger temperature variations. Pre-drilled holes should be used to improve the behavior of the abutment piles when a stiffer soil layer is located surrounding the piles at shallow depth.

9.6 BRIDGE SKEW ANGLE

In practice, skewed bridges are sometimes unavoidable due to the terrain at the bridge site or road alignment. Behavior of skewed IABs is much more complicated than straight IABs due to the uncertainly of soil-structure interactions. Soil pressure variation behind the abutment backwall is affected by the skew of bridge as the thermal loading of the superstructure is not symmetric in skewed IABs. Changes in soil pressure will also affect the behavior of the abutment piles in skewed IABs.

Very few articles have been found in the literature regarding the behavior of the skewed IABs. The behavior of skewed IABs is not fully understood and design agencies are reluctant to build IABs with larger skew angles. Different from straight IABs, in addition to the normal pressure acting against the surface of the abutments, the friction between the abutment and backfill material becomes very important.

In this study, a 210 feet long three-span IAB with three different skew angles (10^o, 20^o, 30^o) was investigated. Abutment piles (7 HP 10x42 piles) were oriented in week axis bending. The computer program GROUP was used for this parametric study.

The variations of pile bending moment in the longitudinal and transverse directions for different skew angles are shown in Figures 9.4 and 9.5, respectively.

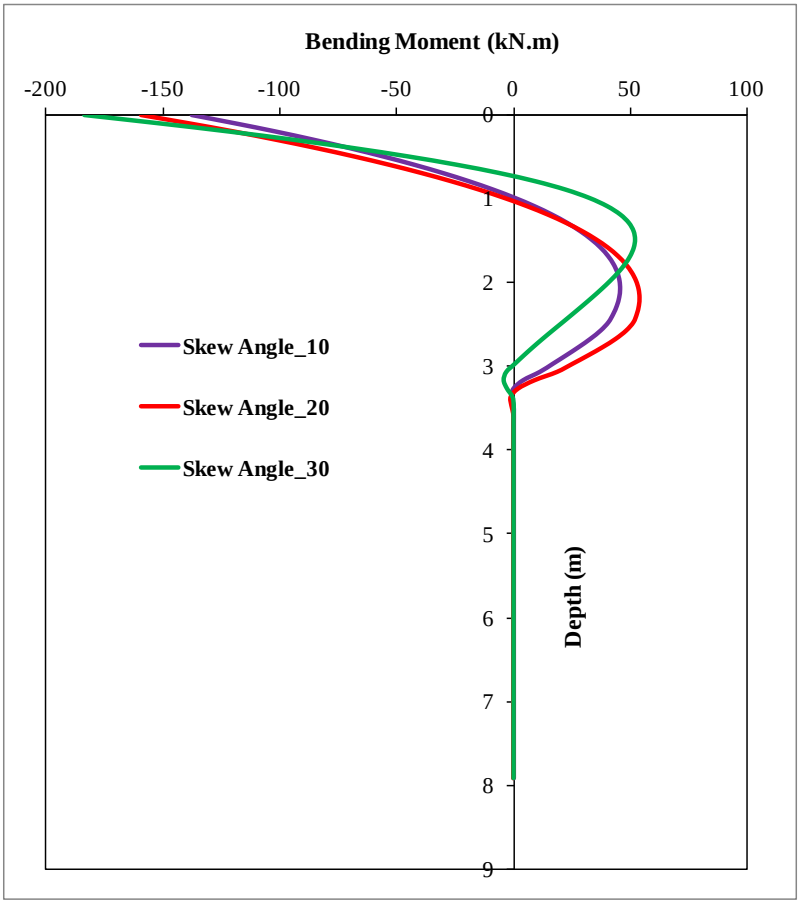

Figure 9.4: Bending Moment Variation in Longitudinal Direction for Different Skew Angles

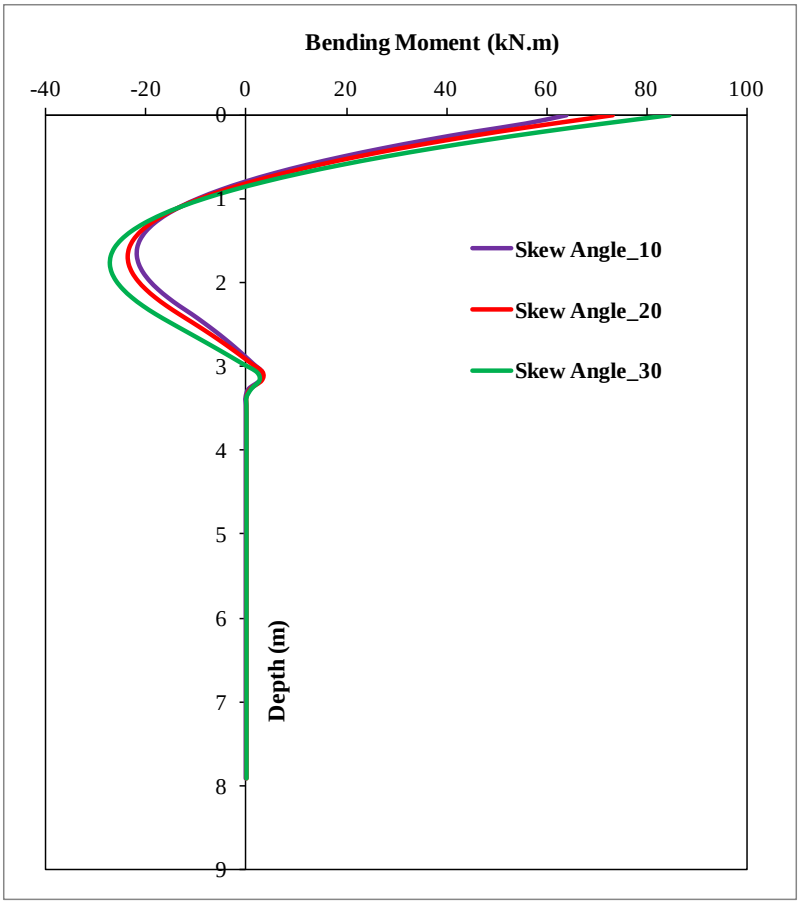

Figure 9.5: Bending Moment Variation in Transverse Direction for Different Skew Angles

According to Figures 9.4 and 9.5, there was an increase in the bending moment in the longitudinal and transverse directions when the skew angle of the bridge is increased. It may be explained that for the skewed bridge, the total force due to the backfill soil pressure was smaller than that of the straight IABs. In the skewed IAB, the reduction in the backfill soil pressure increased the amount of abutment pile bending and thus, larger bending moments were observed. Biaxial bending of abutment piles takes place in the skewed IABs as the thermal loading of the superstructure is not symmetric in skewed IABs.

The biaxial bending of the abutment piles in skewed IABs increases the stresses in the concrete superstructure, especially for long-span IABs and larger seasonal temperature changes. When the bridge skew angle becomes larger, the bending moment in the transverse direction becomes larger than the bending moment in the longitudinal direction. With skewed IABs, the soil passive pressure developed in response to thermal movement has a component in the transverse direction as well. Within certain limits of the skew angle, soil friction on the abutment will resist the transverse component of passive pressure, however, for larger skew angles, the soil friction is insufficient and significant bending moments in transverse direction are generated. Furthermore, the structural components for the IABs with larger skew angles have to be designed with caution to accommodate the thermally induced deformations in the superstructure and avoid distresses within the superstructure.

This page is intentionally blank

10 CONCLUSIONS AND RECOMMENDATIONS

10.1 CONCLUSIONS

10.1.1 Validation of Computer Simulation Tools

A series of finite element analyses of the Minnesota IAB superstructure were performed using the program TeraGrande. The advanced reinforced concrete analyses which model rebar accurately and use a smeared crack model to study nonlinear concrete behavior showed that for the deformations experienced during the thermal loading modeled in this project, the linear structural elements developed for TeraDysac are adequate. Significant concrete cracking was not observed in the superstructure and stresses and strains were low enough that the linear elastic assumptions embedded in beam and plate formulations available within TeraDysac are acceptable.

The Minnesota IAB has no skew angle. Because the bridge abutment translates and rotates uniformly across the bridge width, a 2D analysis can approximate the field behavior. The 2D soil analysis in TeraDysac uses a plane strain assumption for the soil elements. A procedure for obtaining structural properties (area and moment of inertia) based on a unit width of bridge was presented. The structural components of the bridge consist of steel and concrete. Using a weighted-average approach, material parameters such as Young's modulus, linear coefficient of thermal expansion, and Poisson's ratio were determined. The series of 2D TeraDysac analyses showed reasonable agreement with the field measurements results. There were four analyses performed: a temperature increase and decrease using linear elastic and bounding surface soils. In each loading case, the bounding surface models provided more

accurate results. The results for the temperature decrease analysis were generally better than for the heating analysis. This is attributed to the fact that in winter (January in this case), thermal gradients are minimal through the superstructure depth. Therefore, the deck temperature change can be applied directly to the model without having to estimate what the thermal gradient might be (as was done in the summer heating analysis).

Full 3D models of the Minnesota IAB and a skewed version of it were developed. These models were not analyzed in their entirety, but reduced models considering the superstructures and the top two soil layers were studied. Each model was subjected to a uniform temperature increase and the behavior at the abutments was observed. In the non-skewed bridge, the abutment deformation was uniform across its width. The skewed superstructure (15°) had a non-symmetric response at the abutments. The deformation at the obtuse corner was greater than at the acute corner. The difference was minor, but the analysis revealed that the abutment deformation and subsequently the developed pore water pressure and earth pressure behind the abutments will be varied. For small skew angles, a 2D approach may be acceptable. Not capturing the variation in response behind the abutments may be worth the computational savings. A 3D model is more demanding computationally and requires more effort to build, but is required for accurate results, especially for large skew angles in IABs.

10.1.2 Behavior of the Oklahoma IAB for Daily Temperature Variations

The following conclusions were developed based on the behavior of the Oklahoma IAB for daily temperature variations. The piles experience higher daily variation in axial strains closer to the ground surface. The north abutment wall

experienced higher change in earth pressures on the obtuse corner of the wall when compared to the acute corner. Higher changes in earth pressures were observed within the abutment walls closer to the bridge deck. The south abutment wall experienced nearly the same daily change in earth pressures across the entire length of wall. Higher changes in tilt occurred on the west side of the abutment walls when compared to the east side. Higher changes in expansion joint width occurred on the west side of the bridge when compared to the east side. Higher temperature readings were measured on the east side of bridge in the morning hours because as the sun rises that side is directly exposed to the sunlight. As the day progressed, higher temperatures shifted with the sun to the west side of the bridge. The temperatures were similar when comparing the north side of the bridge to the south, but the temperatures varied from east to west across the bridge. Typically the west side of the bridge had higher daily variation in temperature readings when compared to the east side of the bridge. During the hottest parts of the day, the west side of the bridge is directly exposed to the sunlight, while the east side of the bridge is not, thus a much higher load is enacted on the west side of the bridge than when the east side of the bridge is directly exposed to the sunlight in the cooler mornings.

10.1.3 Behavior of the Oklahoma IAB for Seasonal Temperature Variations

From the interpretation of the field data, the following conclusions can be drawn for the seasonal behavior of the Oklahoma IAB. The bridge temperature decreases for six month duration (from July to January) and then increases for the next six month duration (January to July). This cyclic behavior continued from year to year within the time period of the measurements. The average temperature change that the bridge

superstructure experienced over a six month period of time is 90 – 95 ^{0}F. The field measured bridge temperatures for the Oklahoma IAB agrees with the temperature range specified in AASHTO LRFD Bridge Design Specifications.

Earth pressures on the abutments increases as the temperature increases and decreases as the temperature decreases. Maximum changes in earth pressures are recorded at the obtuse corner of the north abutment. Earth pressure measurements show that fairly significant amount of abutment back pressures have been recorded during summer. Recorded readings from the earth pressure cells, tiltmeters, and crackmeters are consistent with the expected behavior of abutments rotating outward during heating and rotating inward during cooling. Crackmeter and tiltmeter measurements show majority of bridge translation is accommodated by the abutment pile movements in IABs. Recorded abutment pile strains show that strains in the piles seem to be accumulating and then stabilizing after a certain time. Furthermore, the abutment piles of IABs are experiencing bending moments beyond the yield bending moment.

10.1.4 Numerical Modeling of the Oklahoma IAB

The long term behavior of Oklahoma IAB was studied with the use of computer programs LPILE and GROUP. Computed longitudinal GROUP bending moments are higher than LPILE bending moment since the skew of the Oklahoma IAB is incorporated in the three-dimensional model developed in GROUP. Since the thermal loading of the superstructure is not symmetric in a skewed IAB, biaxial bending (bending in longitudinal and transverse directions) of abutment piles occurs in the Oklahoma IAB. The computed LPILE and GROUP bending moments for abutment piles shows that the

steel HP piles have yielded at shallow depths, however, they have not reached the ultimate bending moment. The comparisons of field measured bending moments and computed LPILE and GROUP bending moments show field measured bending moments for the south abutment pile have lower values than the computed LPILE and GROUP bending moments. Several reasons may be attributed for the differences between the field measured and computed bending moments and the most important reason among them is that the south abutment piles were installed in pre-drilled holes.

The results of the Oklahoma IAB were extended to general IABs in order to propose design guidelines to build new IABs with longer lengths and larger skew angles. The computer code GROUP was used to understand the long-term behavior of IABs using a parametric study. Steel HP piles are most suitable to support abutments in IABs. The inherent flexibility of steel HP piles allows them to endure constant flexure induced by the cyclic thermal strains of the superstructure. Using a lighter pile section and orienting HP piles in weak axis bending will ensure the effective performance of IABs for seasonal temperature changes. The expansion and contraction of the superstructure are closely related to the total bridge length. Using longer spans with larger girders will increase the axial load on the abutment piles and therefore long-span IABs should be designed with caution to ensure that thermally induced abutment pile bending moments are limited within the allowable ranges.

Types of soil surrounding the abutment piles had a significant effect on the behavior of IABs. Stiffer soils created larger bending moments in the abutment piles. When the stiffness of soil is increased, partial flanges of the pile cross section near the pile head will yield and the plastic hinges may occur for longer IABs and larger

temperature variations. Pre-drilled holes should be used to improve the behavior of the abutment piles when a stiffer soil layer is located surrounding the piles at shallow depth.

Soil pressure variation behind the abutment backwall is affected by the skew of bridge as the thermal loading of the superstructure is not symmetric in skewed IABs. Changes in soil pressure will also affect the behavior of the abutment piles in skewed IABs. There was an increase in the bending moment in the longitudinal and lateral directions when the skew angle of the bridge was increased. Biaxial bending of the abutment piles increases the stresses in the concrete superstructure, especially for long-span IABs and larger seasonal temperature changes. When the bridge skew angle becomes larger, the bending moment in transverse direction becomes larger than the bending moment in longitudinal direction and the orientation of the bending axes of the piles should be reevaluated. Furthermore, the structural components for the IABs with larger skew angles have to be designed carefully to accommodate the thermally induced deformations in the superstructure.

10.2 RECOMMENDATIONS

The following recommendations are provided for design and construction of IABs. The deign temperature range of IABs should be selected based on the location of the bridge as specified in AASHTO LRFD Specifications. In order to accommodate the thermal movement in IABs, the upper portion of the abutment pile length should be in a pre-bored hole that is filled with a material, that has a very low stiffness (such as bentonite slurry or loose sand) and the piles should be placed in weak axis bending. The temperature variation of superstructure is not uniform along its cross-section and this temperature gradient should be considered in the design of IABs. Comparing IABs

with equal total lengths, short spans with shallow girders are recommended over long span deep girders.

Larger differences exist in the design of abutment piles for IABs and not all designers consider lateral loads due to thermal loading. The magnitude of the lateral loads depends on the total length of the bridge, the size and orientation of the piles, the soil condition at the bridge site and the climate. The abutment piles for IABs should be checked for the capacities under combined axial force and bending moments.

Biaxial bending of the abutment piles takes place in skewed bridges. Since the bending moments in both directions increase with the increase of skew angle of the bridge, it causes an increase in stresses in the concrete superstructure, especially for long-span IABs and larger seasonal temperature changes. When the bridge skew angle becomes larger, the bending moment in transverse direction becomes larger than the bending moment in longitudinal direction and the orientation of the bending axes of the piles should be reevaluated. The structural components for the IABs with larger skew angles have to be designed carefully to accommodate the thermally induced deformations in the superstructure.

This page is intentionally blank

11 REFERENCES

American Association of State Highway and Transportation Officials (AASHTO) Load and Resistance Factor Design (LRFD) Bridge Design Specifications, Fourth Edition, Washington, D.C. (2004).

American Concrete Institute. Building Code Requirements for Structural Concrete (ACI 318-02) and Commentary (ACI 318R-02). Page 318/318R-89.

ANATECH Corporation (formerly TeraScale, LLC). TeraGrande: A multi-physics finite element program. Albuquerque, NM. 2005.

ANATECH Corporation (formerly TeraScale, LLC). TeraGrande User's Manual, Version 1.0. Albuquerque, NM. 2005.

ANATECH Corporation (formerly TeraScale, LLC). The TeraScale Framework. Albuquerque, NM. 2001.

Alampalli, S. and Yannotti, A.P. In-service performance of integral bridges and jointless decks. Transportation Research Record 1624. 1998. Pages 1-7.

Arockiasamy, M., Butrieng, N., and Sivakumar, M. State-of-the-art of integral abutment bridges: design and practice. Journal of Bridge Engineering (ASCE) 9 n5. 2004. Pages 497-506.

Beer, G. An isoparametric joint/interface element for finite element analysis. International Journal for Numerical Methods in Engineering 21. 1985. Pages 585-600.

Canary Systems, Inc, (2008). *MultiLogger Software User's Guide Version 4.3.* New London, New Hampshire.

Comstock, L. and Dagher, H. Physical testing of two R/C skewed slab bridges with integral wall abutments. Structural Engineering in Natural Hazards Mitigation. Proceedings of Papers Presented at the Structures Congress '93. Volume 2. 1993. Pages 969-974.

Dafalias, Y.F., and Herrmann, L.R. Bounding surface formulation of soil plasticity. Soil Mechanics – Transient and Cyclic Loads (in G.N. Pande and O.C. Zienkiewicz eds). Wiley. Chichester, England. 1982. Pages 253-282.

Dafalias, Y.F., and Herrmann, L.R. Bounding surface plasticity II: application to isotropic cohesive soils. Journal of Engineering Mechanics 112 n12. December 1986. Pages 1263-1291.

Dameron, R.A. and Dunham, R.S. Continuum F.E. analyses of concrete bridge outrigger cyclic loading tests with a new rebar bond-slip model. Report to the Third NSF Workshop on Bridge Engineering Research in Progress. November 16-17, 1992.

Day, R.A., and Potts, D.M. Zero thickness interface elements – numerical stability and application. International Journal for Numerical and Analytical Methods in Geomechanics 18. 1994. Pages 689-708.

Desai, C.S., Zaman, M.M., Lightner, J.G. and Siriwardane, H.J. Thin-layer elements for interfaces and joints. International Journal for Numerical and Analytical Methods in Geomechanics 8. 1984. Pages 19-43.

Dunham, R.S. et al. Predictive analysis of outrigger knee-joint hysteresis tests: a torsion/flexure test at UCB and two flexure tests at UCSD. Caltrans First Annual Seismic Research Workshop. November 1991.

ENSOFT, Inc. Computer program LPILE^{PLUS} 5.0 for Windows. Austin, TX. 2007.

ENSOFT, Inc. Computer program GROUP 8.0 for Windows. Austin, TX. 2010.

ENSOFT, Inc. LPILE^{PLUS} 5.0 for Windows Technical Manual. Austin, TX. July 2004. Page 3-33.

Fennema, J.L., Laman, J.A., and Linzell, D.G. Predicted and measured response of an integral abutment bridge. Journal of Bridge Engineering (ASCE) 10 n6. 2005. Pages 666-677.

Geokon, Inc. (2005). *Instruction Manual for Model 4000 Vibrating Wire Strain Gage.* Lebanon, New Hampshire.

Geokon, Inc. (2007). *Instruction Manual for Model 6350 Vibrating Wire Tiltmeter.* Lebanon, New Hampshire.

Geokon, Inc. (2007). *Instruction Manual for Model 8032 Terminal Board and 16/32 Channel Multiplexer.* Lebanon, New Hampshire.

Geokon, Inc. (2007). *Instruction Manual for Model 8021-1 Micro-1000 Datalogger.* Lebanon, New Hampshire.

Geokon, Inc. (2008). *Instruction Manual for Model 3800 Thermistors & Thermistor Strings.* Lebanon, New Hampshire.

Geokon, Inc. (2008). *Instruction Manual for Model 4420 VW Crackmeter.* Lebanon, New Hampshire.

Geokon, Inc. (2008). *Instruction Manual for Models 4800, 4810, 4815, 4820, and 4830 VW Earth Pressure Cells.* Lebanon, New Hampshire.

Goodman, R.E., Taylor, R.L. and Brekke, T.L. A model for the mechanics of jointed rock. Journal of the Soil Mechanics and Foundations Division, ASCE 94. May 1968. Pages 637-659.

Greimann, L.F., Wolfe-Tinsae, A.M., and Yang, P.S. Skewed bridges with integral abutments. Transportation Research Record 903. 1983. Pages 64-72.

Hanlon, B. Instrumentation to study thermal loading of a skewed integral abutment bridge. M.S. thesis, School of Civil Engineering and Environmental Science, University of Oklahoma, Norman, Oklahoma. 2010.

Hassiotis, S., and Roman, E.K. A survey of current issues on the use of integral abutment bridges. Bridge Structures 1 n2. June 2005. Pages 81-101.

Horvath, J.S. Integral-abutment bridges: a complex soil-structure interaction challenge. Geotechnical Special Publication, n 126 I, Geotechnical Engineering for Transportation Projects: Proceedings of Geo-Trans 2004. 2004. Pages 460-469.

Huang, J., French, C.E., and Shield, C.K. Behavior of concrete integral abutment bridges: final report. November 2004.

Jorgenson, J.L. Behavior of abutment piles in an integral abutment in response to bridge movements. Transportation Research Record: Journal of the Transportation Research Board 903. 1983. Pages 72-79.

Krier, D. Modeling of integral abutment bridges considering soil-structure interaction effects. Ph.D. dissertation, School of Civil Engineering and Environmental Science, University of Oklahoma, Norman, Oklahoma. 2009.

Kunin, J. and Alampalli, S. Integral abutment bridges: current practice in United States and Canada. Journal of Performance of Constructed Facilities 14 n3. August 2000. Pages 104-111.

Lai, J.Y., and Booker, J.R. A residual force finite element approach to soil-structure interaction analysis. International Journal for Numerical and Analytical Methods in Geomechanics 15. 1991. Pages 181-203.

Muraleetharan, K.K. VELACS extension project: constitutive model calibration and predictions. Research report. University of Oklahoma. October 1995.

Muraleetharan, K.K., Mish, K.D., and Arulanandan, K. A fully coupled non-linear dynamic analysis procedure and its verification using centrifuge results. International Journal for Numerical and Analytical Methods in Geomechanics 18. 1994. Pages 305-325.

Muraleetharan, K.K., Ravichandran, N., and Taylor, L.M. TeraDysac: TeraScale Dynamic Soil Analysis Code. Computer Code. School of Civil Engineering and Environmental Science, University of Oklahoma. Norman, Oklahoma. 2003.

Naval Facilities Engineering Command. Design Manual 7.01. 1986. Page 7.1-220.

Nickerson, R.L. Jointless steel bridges design and retrofit. Proceedings of Structures Congress XIV 1. 1996. Pages 313-320.

Paul, M., Laman, J.A., and Linzell, D.G. Thermally induced superstructure stresses in prestressed girder integral abutment bridges. Transportation Research Record: Journal of the Transportation Research Board. 6th International Bridge Engineering Conference. 2005. Pages 287-297.

Rashid, Y.R. Ultimate strength analysis of prestressed concrete pressure vessels. Nuclear Engineering and Design 7. 1968. Pages 334-344.

Ravichandran, N. A framework-based finite element approach for solving large deformation problems in multi-phase porous media. Ph.D. dissertation, University of Oklahoma, Norman, OK. 2005.

Sandford, T.C., and Elgaaly, M. Skew effects on backfill pressures at frame bridge abutments. Transportation Research Record: Journal of the Transportation Research Board 1415. 1993. Pages 1-11.

Sandford, T.C., Davids, W.G., Hartt, S.L., and DeLano, J.G. Construction-induced stresses in H-piles supporting an integral abutment bridge. Transportation

Research Record: Journal of the Transportation Research Board 1975. 2006. Pages 39-48.

Steinberg, E., Sargand, S.M., and Bettinger, C. Forces in wingwalls of skewed semi-integral bridges. Journal of Bridge Engineering 9 n6. November/December 2004. Pages 563-571.

Soltani, A. (1990). *Design and Application of Integral Abutment Bridges.* Master's thesis, University of Oklahoma, Norman, Oklahoma.

Wolde-Tinsae, A.M., and Greimann, L.F. General design details for integral abutment bridges. Civil Engineering Practice 3 n2. 1988. Pages 7-20.

Tokimatsu, K. and Seed, H.B. Evaluation of settlements in sands due to earthquake shaking. ASCE Journal of Geotechnical Engineering 113 n8. August 1987. Pages 861-878.

Yang, P.S., Wolde-Tinsae, A.M., and Greimann, L.F. Effects of Predrilling and Layered Soils on Piles. Journal of Geotechnical Engineering 111 n1. 1985. Pages 18-31.

Yogachandran, C. Numerical and centrifugal modeling of seismically induced flow failures. Ph.D. dissertation. University of California, Davis. 1991.